NOBLE METAL ENTRAPPED HYDROGEL NANOCOMPOSITES

THESIS SUBMITTED TO THE

UNIVERSITY OF KERALA

FOR THE DEGREE OF

DOCTOR OF PHILOSOPHY

IN

CHEMISTRY

UNDER THE FACULTY OF SCIENCE

BY

ROHINI K. N.

CHEMICAL SCIENCES AND TECHNOLOGY DIVISION

CSIR-NATIONAL INSTITUTE FOR INTERDISCIPLINARY SCIENCE

AND TECHNOLOGY (CSIR-NIIST)

TRIVANDRUM, KERALA-695019

March 2016

DECLARATION

I hereby declare that the content of the thesis entitled as "**NOBLE METAL ENTRAPPED HYDROGEL NANOCOMPOSITES**" is the result of investigations carried out by me at Chemical Sciences and Technology Division, CSIR–National Institute for Interdisciplinary Science and Technology (CSIR-NIIST), Trivandrum under the supervision of Dr J. D. Sudha and Dr T. Prasada Rao. The same has not been submitted elsewhere for any other degree.

Thiruvananthapuram

Rohini K.N.

27 March 2016

CERTIFICATE

This is to certify that the work embodied in the thesis entitled as **"NOBLE METAL ENTRAPPED HYDROGEL NANOCOMPOSITES"** has been carried out by   Ms. Rohini K.N. under our supervision and guidance at Chemical Sciences and Technology Division, CSIR- National Institute for Interdisciplinary Science and Technology (CSIR-NIIST), Trivandrum and the same has not been submitted elsewhere for any other degree.

Dr T. Prasada Rao
Chief Scientist (Retired)
CSIR- NIIST
Trivandrum

Dr J. D. Sudha
Principal Tech. Off /Assoc. Prof. (AcSIR)
CSIR- NIIST
Trivandrum

ACKNOWLEDGEMENTS

CONTENTS

CHAPTER 1   NOBLE METAL ENTRAPPED HYDROGEL NANOCOMPOSITES

CHAPTER 4 DEVELOPMENT OF FUNCTIONAL LIQUID CRYSTALLINE LAPONITE-AMIDODIOL GEL THROUGH SELF-ASSEMBLY APPROACH

CHAPTER 5 DEVELOPMENT OF NANOSILVER PATTERNED LIQUID CRYSTALLINE GEL AND ITS APPLICATION AS ELECTROCHEMICAL SENSOR

List of Tables

List of Schemes

List of Figures

List of Abbreviations

AA	Acrylic Acid
AMD	Amidodiol
APS	Ammonium persulfate
CPE	Constant Phase Element
CV	Crystal Violet
DPV	Differential Pulse Voltammetry
EIS	Electrochemical Impedance Spectroscopy
FCC	Face Centred Cubic
FLAG	Functionalized Laponite- Amidodiol Gel
FT-IR	Fourier Transform – Infra Red
GCD	Galvanostatic Charge discharge
GCE	Glassy Carbon Electrode
LAP	Laponite Gels
LCP	Liquid Crystalline Polymer
LCST	Lower Critical Solution Temperature
MAP	meta-aminophenol
MB	Methylene Blue
MEF	Metal Enhanced Fluroscence
MNP	Meta nitrophenol
OAP	orthoaminophenol
ONP	orthonitrophenol
PAA	Polyacrylic Acid
PAG	Polyacrylic Acid-Amidodiol Gel
PAM	Polyacrylamide
PAP	Para aminophenol
PEG	Polyethylene glycol
PHEMA	Poly (2-hydroxyethylmethacrylate)
PLA	Polylactic acid
PLM	Polarised Light Microscope
PNIPAM	Poly(N-isopropylacrylamide)
PNP	Para nitrophenol

PVA	Poly vinyl alcohol
PVP	Poly(N-vinyl-2-pyrrolidone)
R6G	Rhodamine 6G
R_{ct}	Charge Transfer Resistance
R_S	Solution Resistance
SEM	Scanning Electron microscope
SERS	Surface enhanced Raman Scattering
SFLAG	Silver Nanoparticles Entrapped Functionalized Laponite Amidodiol Gel
SPAG	Silver Nanoparticles Entrapped Polyacrylic Acid-Amidodiol Gel
SPRE	Surface Plasmon Resonance Energy
TEM	Transmission electron Microscope
TLC	Thin Layer Chromatography
UCST	Upper Critical Solution temperature
UV	Ultra Violet
XRD	X–Ray Diffraction
1D	One dimensional
2D	Two dimensional
3D	Three dimensional

PREFACE

In recent years, there has been considerable interest in hydrogel-stabilized metal nanocomposites which respond to various stimuli in the bulk phase. They were used in responsive artificial muscles, switches, memory devices, catalysis, tissue engineering, etc. Hydrogels are three-dimensional fibrillar networks of hydrophilic polymers or low molecular weight gelators which can imbibe large amount of water with stimuli responsive swelling and de-swelling properties. Covalent and non-covalent interactions such as hydrogen bonding, π-π stacking, and van der Waal's interactions are involved during the organization of these molecules into 3D architectures. The unique properties of metal nanoparticles are different from their bulk counter parts and they find promising applications in the areas such as nano electronic devices, catalysis, sensors, bio-chemical tagging reagents, optical switches and so forth. Among the metal nanoparticles, silver is easily reducible and has high excitation efficiency, surface plasmon resonance energy in the visible region and unique electrical, optical and catalytic properties. Silver-catalyzed reactions such as Diels Alder reaction, epoxidation, hydrogenation of aldehydes, hydroformylation, carbonylation, reduction of dyes, nitrophenol, etc. have been reported earlier. Metal nanoparticles tend to aggregate during the catalytic process due to their van der Waal's forces of attraction and high surface area. A wide range of capping agents such as block copolymers, polysaccharides, latex particles, hydrogels and surfactants have been used to enhance the stability and dispersion of metal nanoparticles. Among these stabilizers, hydrogels with three-dimensional fibrillar networks are receiving importance. The hydrophilic ionic groups present in the hydrogel network can potentially serve as nanoreactors for the synthesis of metal nanoparticles and provide cage effect for its stabilization and speed up the diffusion of metal ions through the

hydrogel networks. Apart from this, the size and shape of metal nanoparticles could be tuned by controlling the amount of monomer, cross-linker and metal ions.

In the present investigation, we have explored an extensive literature survey on the development and applications of hydrogel entrapped metal nanocomposites. The different synthetic procedure for hydrogel metal nanocomposites and their application in the field of catalysis and sensing was discussed. An introduction about the significance of metal entrapped polymeric and supramolecular hydrogel nanocomposite was presented in chapter1. In the subsequent chapters, preparation, evaluation of properties and application of the various systems of hydrogel/ silver nanoparticle entrapped hydrogel nanocomposites were discussed.

The preparation of robust polyacrylic acid hydrogel (PAGs) by the insitu polymerization of acrylic acid using amidodiol as cross-linking agent and their application was discussed in chapter 2. PAGs were characterized for its chemical structure, rheology, swelling, diffusion, and adsorption studies. Kinetics and mechanism of adsorption of dyes were investigated by UV–Visible spectroscopy. Results suggested pseudo second order and multilayer adsorption of the dyes by PAGs. Extent of interaction between adsorbate– adsorbate and adsorbent–adsorbate was studied using Gile's model. Finally, we have demonstrated its application for the removal of dyes from waste water collected from textile and paper industries. The generated results may provide a low cost simple technology for the development of robust polymeric hydrogel for the removal of impurities from waste water.

Description on the preparation and characterization of silver nanoparticle entrapped polyacrylic acid-amidodiol hydrogels (SPAGs) and their application as a catalyst for reduction process is discussed in the chapter 3. SPAGs were prepared by in situ polymerization of acrylic acid and reduction of silver nitrate using amidodiol as cross-linking

cum reducing agent under ambient conditions. SPAGs were characterized by UV–Visible spectroscopy, SEM, TEM, XRD and rheology. Further, catalytic activities of SPAGs were studied using dyes and nitro phenols. Reduction process in the presence of SPAG exhibited a first order reaction and the reduction mechanism is found to be obeying the Langmuir−Hinshelwood model. In addition, SPAGs showed excellent reusability, easy separation, high rate constant and absence of induction period. All these results suggested SPAGs as a promising catalyst for the reduction of organic molecules.

Studies on the design and development of liquid crystalline supramolecular hydrogels are receiving importance in academia and high-tech applications. In the fourth chapter of this thesis describes the preparation of functional liquid crystalline gels by multi-scale hierarchical self-assembly of laponite and amidodiol (FLAGs) and its application as a gel electrolyte. Liquid crystalline physical gels of FLAGs exhibited anisotropic ordering as evidenced from microscopic and rheological analysis. They showed enhanced conductivity, viscoelastic properties, good electrochemical stability window, mechanical strength and faster response and they find application in electrochemical devices and sensors. Further, we have fabricated super capacitor device using FLAG as an electrolyte. The electrochemical studies of the FLAG showed excellent electrochemical window (-0.4V – 1V) and symmetrical triangular charge discharge profile with the specific capacitance of 1856 mF/g at a constant current density of 0.02 A/g. The device gave 99% retention of specific capacitance even after 100th cycle revealing high cycling stability.

The fifth chapter of the thesis illustrated the development of silver nanoparticles patterned liquid crystalline supramolecular hydrogel (SFLAGs) by the simultaneous reduction of silver ions and supramolecular organization of laponite and amidodiol. SFLAGs were characterized with SEM, TEM, XRD, UV-Visible spectroscopy and rheology. The

glassy carbon electrode modified with SFLAG showed good electrocatalytic activity towards the oxidation of L-Tyrosine with a high current response and lower detection limit of 10 nM. The interference studies showed good selectivity of SFALG/GCE towards oxidation of tyrosine and the better recovery values with human blood serum samples propose its analytical applications. In terms of ease of fabrication, long term stability, reusability and selectivity, SFLAG/GCE can be exploited as an electrochemical sensor for tyrosine in clinical diagnostics.

In the final chapter, we have summarized the conclusions and made a proposal for the future perspectives of this program.

CHAPTER 1

NOBLE METAL ENTRAPPED HYDROGEL NANOCOMPOSITES
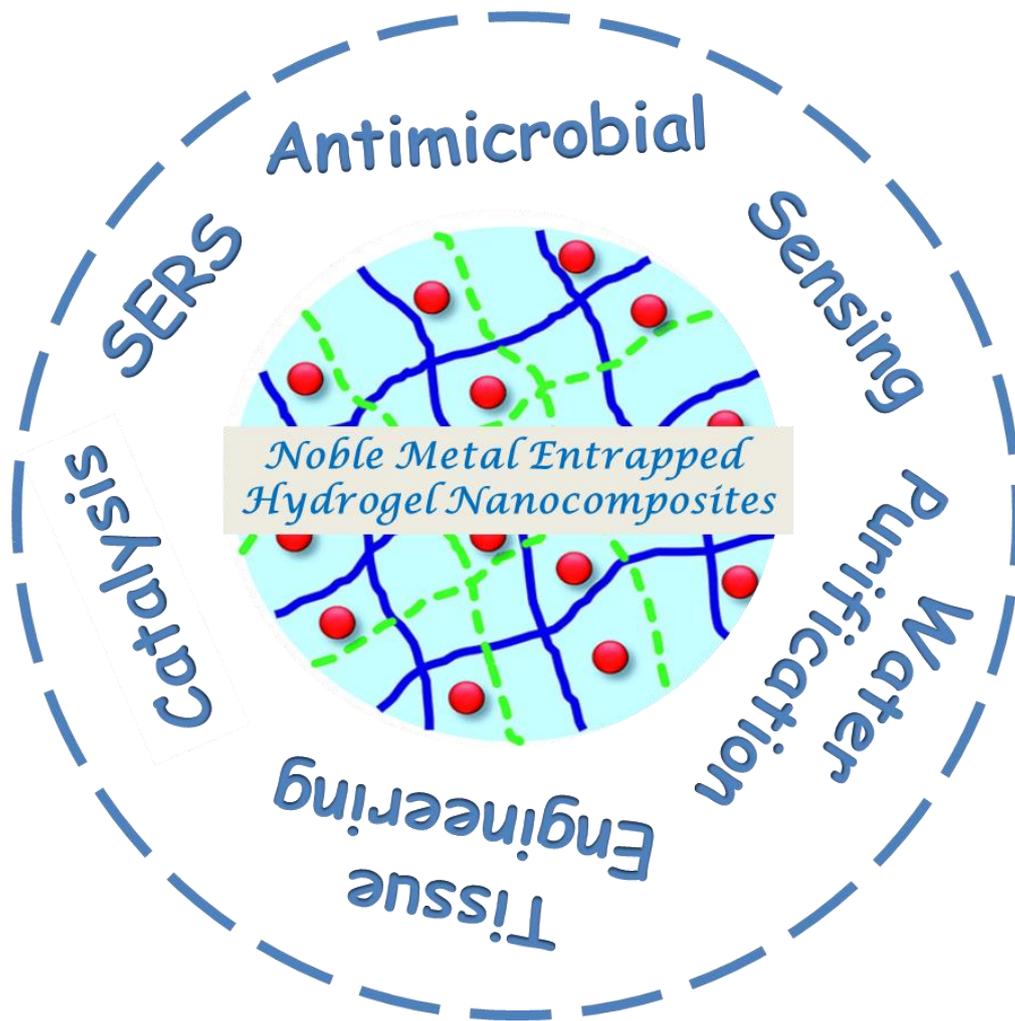
1.1.   Abstract

Hydrogels are three-dimensional fibrillar networks composed of hydrophilic polymer chains or low molecular weight gelators which can imbibe a large amount of water and exhibit stimuli responsive swelling and de-swelling properties. The hydrophilic groups present in the hydrogel network can potentially serve as nanoreactors for the synthesis of metal nanoparticles and provide cage effect for its stabilization and can speed up the diffusion of metal ions through the hydrogel networks. Noble metal nanoparticles are easily reducible, and have high excitation efficiency, surface plasmon resonance energy in the visible region, unique electrical, optical and catalytic properties. They are potential candidates in catalysis and sensing because of their high surface area and size and shape-dependent catalytic properties. The low molecular weight liquid crystalline hydrogels offer more flexibility in tailoring the functionality and mechanical properties of the gels and exhibit multifunctional applications. Thus, incorporation of metal nanoparticles inside the hydrogel network expected to exhibit the synergistic properties of three dimensionally ordered stimuli responsive hydrogel and optoelectronic properties of noble metal nanoparticles. They find applications in responsive artificial muscles, switches, memory devices, catalysis, tissue engineering, sensors and so forth. This chapter encompasses an introduction to noble metal entrapped hydrogel nanocomposites, general preparation strategies, properties, application and scope and objective of the program.

1.2.   Introduction

Gels are substantially cross-linked systems which possess the properties of both solids and liquids. Scottish chemist Thomas Graham coined the word gel from gelatine, a gelling agent used in photography, food, pharmaceuticals, etc. They are commonly seen in our everyday life in commercial products such as soaps, shampoo, toothpaste, hair gels, cosmetics, contact lenses and gel pens, etc. The crosslinking

present in gels may be either physical or chemical interactions. Depending upon the dispersion medium, they are classified into hydrogels and organogels. The dispersion medium of three- dimensional gel network is swollen with water in a hydrogel and composed with an organic solvent in organogels.

1.3.   Hydrogels

Hydrogels have been received considerable attention due to their wide range of applications in biological, medical, pharmaceutical, environmental and industrial areas due to their characteristic properties such as high swelling in water and lack of toxicity (Pal et al., 2009). Hydrogel is a chemically or physically cross- linked three-dimensional network constitutes of hydrophilic polymers or low molecular weight gelators which can imbibe a large amount of water. The hydrophilicity of these materials is due to the hydrophilic functional groups such as $-OH, -COOK, -CONH_2, -CONH$ and $-SO_3H$ along the polymeric chains which can absorb and store water. If enough interstitial space exists within the network, water molecules become trapped and immobilized, filling the available free volume. Chemically cross-linked hydrogels have strong permanent interactions while the physical network is made up of physical interactions such as hydrogen bonding, van der Waal's interactions, dipole- dipole interaction and ionic interactions (Hacker et al., 2011). Raghavan et al. reported the formation of chemically cross-linked gel by free-radical polymerization of acrylamide in the presence of bis (N, N'-methylene-bis-acrylamide) cross-linker and a physically cross-linked gel by combining alginate and Ca^{2+} ions along junction zones (Raghavan et al., 2012). Schematic representation for chemical and physical hydrogel is given in Figure 1.1.

(a) Chemically cross-linked gel   **(b) Physically cross-linked gel**

PAM	BIS	Alginate	Ca²⁺ ion

PAM chains   **BIS cross-links**   **Alginate chains**   **Ca $^{2+}$ ion junctions**
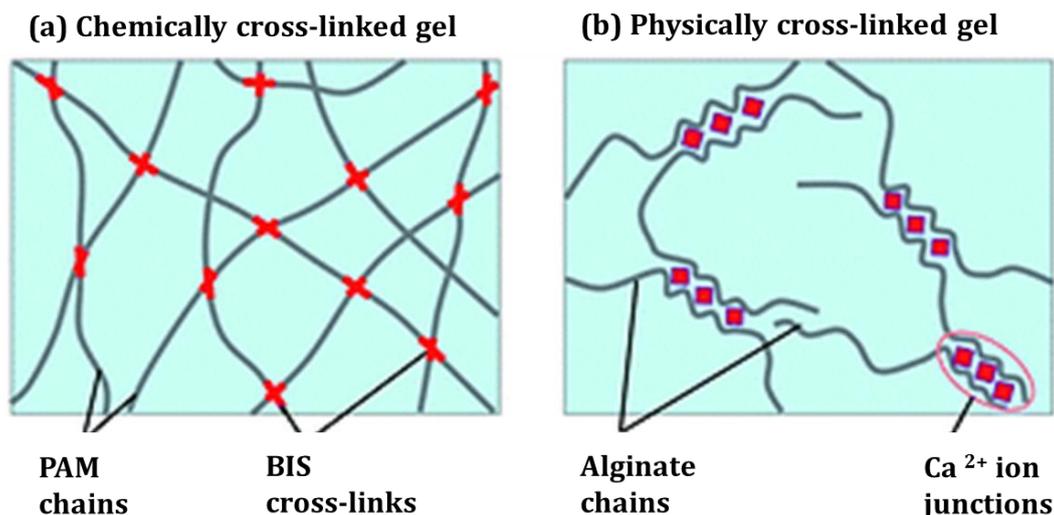
Figure 1.1. (a) Chemically cross-linked gel (b) Physically cross-linked gel

1.4.   Polymeric hydrogels

Polymeric hydrogels are three dimensionally cross-linked networks of hydrophilic polymer chains. Polymeric hydrogels may be physical or chemical hydrogels depending on the interaction. They can be synthesized with tailored properties such as biodegradation, mechanical strength, and stimuli responsiveness by controlling the cross-linking density, nature of monomer, equilibrium water content etc. Based on composition, they are classified as homopolymeric, copolymeric, as well as semi-interpenetrating polymeric hydrogel. In homopolymeric hydrogels, the basic structural unit comprising of the polymeric network is derived from a single monomer. Copolymer hydrogel is made up of two different types of monomers. Hydrogels may be again classified into natural or synthetic based on their origin. Hydrogels forming natural polymers include collagen, gelatin, starch, alginate, agarose, etc. Nowadays natural polymers were gradually replaced by synthetic hydrogels due to their long life, high strength and high capacity of water absorption. The first hydrogel synthesized with potential biomedical use is poly-2-hydroxyethyl methacrylate (PHEMA) by Professors Lim and Wichterle of Prague, The Czech

Republic in 1955. This was stable under varying pH, temperature and used in contact lens production (Wichterle et al., 1960). Most commonly known hydrogels are polyvinyl alcohol (PVA), poly(ethylene glycol) (PEG), polyacrylic acid (PAA), poly(methylmethacrylic acid) (PMMA) and polyacrylamide (PAM) and poly(N-isopropylacrylamide) (PNIPAM) and their copolymers. The chemical structures of the commonly used synthetic polymers were given in Figure 1.2.
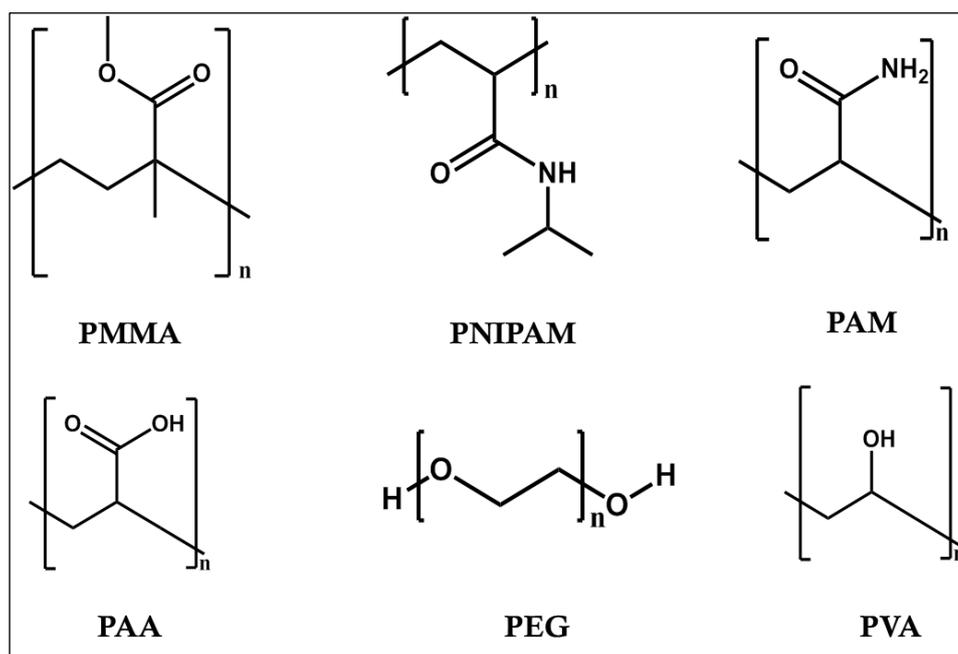
Figure 1.2. The chemical structures of the commonly used polymers for the synthesis of hydrogels

PHEMA is widely used in biomedical applications such as production of contact lenses, wound dressing material, tissue engineering and scaffolds due to its non-toxicity, biocompatibility etc. It is soft and flexible on swelling and the mechanical strength of PHEMA hydrogels can be increased by crosslinking with natural and synthetic polymers. PEG hydrogel is one of the mostly used hydrogels in medicine and biomedicine. The biocompatibility, nontoxicity and stimuli responsiveness make them highly suitable for drug delivery applications. Chemically cross-linked PEG hydrogels are used in the manufacture of synthetic, biologically

active hydrogel scaffolds for protein recombination and functional tissue production. PEG hydrogels are used as matrices for controlling drug delivery and as cell delivery vehicles for promoting tissue regeneration. PVA hydrogels are also highly biocompatible, possess good water permeability, provides a moist environment and can be used in wound dressing materials. PVA hydrogels can also be used in contact lens production, cartilage reconstruction, artificial organs and for catalytic applications. Lu et al. reported a nanotree type polystyrene-PVA hydrogels for the catalytic reduction of nitrophenols (Lu et al., 2007).The largest group comprises of synthetic polymers behave as hydrogels are the homo and copolymer derivatives of Acrylic acid (AA). AA and its sodium or potassium salts often used in the industrial preparation of hydrogels. PAA hydrogels are receiving interest due to their wide range of application in the biomedical field, agriculture, sensors, and catalysis. They are widely employed in breast implants due to their excellent biocompatibility, non-toxicity, optimal viscosity, elasticity and stability. The chitosan-silica-PAA was reported for tissue engineering applications (Lin et al., 2014). Adsorption is considered as efficient method to remove the contaminants of water due to its low cost and high potential for regeneration and reuse. PAA hydrogels are reported as good adsorbents. The chitosan- PAA- attapulgite was used to adsorb Cd (II) from waste water (Crane et al., 2010). The covalently cross-linked attapulgite/poly(acrylic acid-co-acrylamide) was reported for the selective adsorption of Pb^{2+} and Cu^{2+} (Liu et al., 2015). PAA based hydrogels were employed in the adsorption of cationic dyes.

Polymeric hydrogels can be prepared by simultaneous copolymerization and cross- linking of monofunctional or multifunctional monomers using chemical reagents or irradiation. They can also be prepared either by cross linking the reactive functional groups of water soluble linear polymer or by copolymerizing vinyl

monomers with multifunctional cross linking monomers. Several polymerization techniques have been employed to synthesize polymeric hydrogels such as bulk polymerization, solution polymerization, radiation polymerization, suspension/emulsion polymerization, (Ahmed et al., 2012).

The bulk polymerization is taking place in the presence of monomers and monomer soluble initiators and is initiated with UV or thermal irradiation or with catalysts. The rate of polymerization increases with the amount of monomers. Bulk hydrogels can be formed with one or more types of monomers and usually, a small amount of cross-linking agent is added in any hydrogel formulation. The polymerized hydrogel may be produced in a wide variety of forms including films and membranes, rods, particles, and emulsions. The bulk polymerization of monomers yields a homogeneous hydrogel. In solution polymerization, the ionic or neutral monomers were mixed with multifunctional cross linking agents and is initiated thermally or UV radiation or by the use of a redox initiator. The solution polymerization is employing solvent as a heat sink and helps in the formation of the homogeneous hydrogel. The prepared hydrogels were washed with distilled water to remove excess monomer, cross linking agent, initiator and other impurities. Suspension/emulsion polymerization can be successfully used for the synthesis of spherical polymeric hydrogel micro particles. In this technique, the monomers and the initiators were dispersed in a hydrocarbon solvent and form fine monomer droplets and then the polymerization initiated by thermal decomposition of the initiator. The formed hydrogel was washed to remove unreacted monomers, initiator, cross linking agent and the other impurities. The particle size and shape of the hydrogel particles is affected by the viscosity of monomers, agitation speed, nature of dispersant, etc. In the radiation polymerization, the high energy radiations such as gamma rays,

electron beams were used in the formation of hydrogels. The radicals formed by the irradiation of aqueous polymer solution and the hydroxyl radicals formed by the radiolysis of water, attack the polymer chains and initiate the polymerization. The recombination of the formed macroradicals yields a cross- linked structure. PVA, PEG, and PAA hydrogels can be produced by radiation polymerization. This type of polymerization gives pure and initiator free hydrogels. The mechanical strength of the hydrogel could be increased by the use of graft polymerization. In this technique, monomers are grafted on to a stronger support and then polymerized to form hydrogels. A schematic representation for the different strategies of preparation of hydrogels such as photopolymerization, physical and chemical cross-linking of polymers and block copolymers is given in Figure 1.3 (Khan et al., 2015).
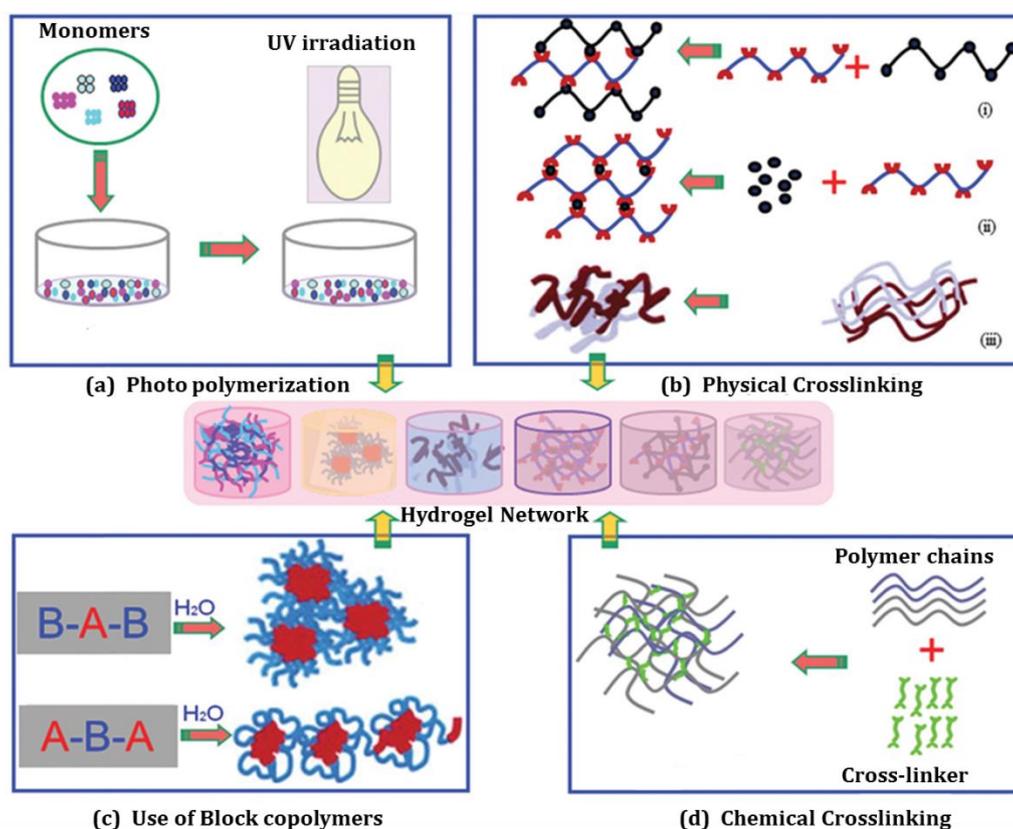
Figure 1.3. Schematic representations for the preparation process of polymer hydrogels using different methods

1.5.   Supramolecular hydrogels

Supramolecular hydrogels have been developed using a wide variety of supramolecular motifs, such as hydrogen bonding, metal–ligand coordination, host–guest recognition, π-π interactions, and electrostatic interaction (Kato et al., 2006). The schematic representation of supramolecular assembly is shown in Figure 1.4.
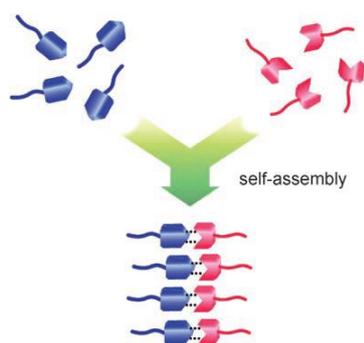
Figure 1.4. Supramolecular assembly of low molecular weight gelators through specific non-covalent interactions

Based on the types of building blocks, they are classified into molecular hydrogels, supramolecular polymeric hydrogels and supramolecular hybrid hydrogels (Dong et al., 2015).The low-molecular-weight building blocks such as peptide, bile acids, sugar, amino acids etc. have been reported earlier for the synthesis of molecular hydrogels. Cholic acid derivatives are reported to form hydrogels and could be used as a template to synthesize inorganic nanotubes of metal oxides and metal sulphates (Gunidiah et al., 2003). Cationic and anionic analogues of bile acids form thermo reversible gels in the presence of water and organic solvents and exhibited different aggregation behaviour (Sangeetha et al., 2002). There are many reports in which sugar based moieties were used to form hydrogels in which the sugar part of the molecule helps to increase the solubility and the aromatic part promote the π-π aggregation in water and exhibit highly flexible gelation properties (Jung et al., 2002;

Yoza et al., 1999). Amino acids such as alanine, aspartic acid, glutamic acid forms hydrogel at low concentrations and exhibit pH dependent hydrogel formation due to the presence of carboxylic acid (Imae et al., 1992; Imae et al; 2000). Supramolecular polymeric hydrogels can be formed by the multivalent non-covalent cross-linking between conventional polymer chains functionalized with multiple complementary supramolecular motifs (Yoshii et al., 2014). Supramolecular hybrid hydrogels contain inorganic components such as carbon nanotubes, graphene, quantum dots, clays, metal nanostructures (Ma et al., 2014 ; Zhou et al., 2014).These rigid inorganic and metal substances generally serve as multivalent cross-linking sites, thus greatly improving the mechanical properties (Ogoshi et al., 2014, Tan et al., 2014).Wang et al. reported a freestanding gel film with laponite and a dendritic molecule with enhanced mechanical strength and self-healing capacity (Wang et al., 2010). Polymer – clay nanocomposites were reported for biocompatible adhesive films, self-healing materials, fast thermo responsiveness, pH responsiveness, cancer treatment (Shen et al., 2014; Haraguchi et al., 2011; Zhang et al., 2014; Stempfle et al., 2014 ; Chen et al., 2014; Li et al., 2011; Nagahama et al., 2015; Strachota et al., 2015; Li et al., 2015, Shikinaka et al., 2011).

1.6.   Liquid crystalline hydrogels

Liquid crystals are anisotropic molecules which can self-organize into various mesophases, such as micellar, columnar, layered, and bicontinuous cubic phases. The mesophase segregated dynamically functional materials exhibit superior mass transport and find application in a wide variety of technological areas such as sensing, catalysis, templates, and electro-optical displays (Kato et al., 2006). The liquid crystalline polymers have been used to fabricate liquid crystalline hybrid

materials which can replicate the anisotropy to fabricate synthetic polymers with ordered structures. Liquid crystalline polymers (LCPs) incorporate mesogens in a variety of ways, most commonly along the main-chain, in a segmented configuration, or as dangling side-chains. There have been three main approaches for developing liquid crystalline hydrogels. The first approach was crosslinking lyotropic liquid crystalline materials into hydrogel form; however, the produced networks do not demonstrate complete liquid crystalline structure or hydrogel-like behaviour. The second approach is to utilize liquid crystalline organogels and convert them to liquid crystalline hydrogels without destroying the liquid crystalline structure, which can be challenging. The third approach is to use lyotropic liquid crystalline phases as a template to synthesize hydrogels. The thermoreversible change of the liquid crystalline physical gel is reported by kato et al. and is shown in Figure 1.5 (Kato et al., 2007).The non-covalent interactions such as hydrogen bonds, ionic bonds, and charge-transfer interactions are utilized during the formation of self-assembled systems. The lamellar lyotropic systems of polymers and low molecular weight gelators used in the formation of liquid crystalline physical gels show potential for the development of new types of supramolecular bioactive materials for drug delivery or tissue engineering and wound healing applications (Ungar et al., 2011; Mehl et al., 2005). Liquid-crystalline physical gels are soft solids and exhibit liquid-crystalline properties which consist of liquid crystals and self-assembled fibrillar network of low-molecular-weight compounds driven by hydrogen bonding or π-π interactions. Organic and inorganic nanoparticles have been incorporated into low-molecular-weight liquid crystals to develop switchable electro-optical materials. Liquid crystalline gels can be considered as a versatile medium for the synthesis of nanoparticles. The homogeneous dispersion of the nanoparticle aggregates effectively

induces the formation of liquid-crystalline polydomains (Kato et al., 2007). Laponite water interaction and the lyotropic liquid crystalline phases of laponite gels were extensively reported (Ruzicka et al., 2004; Gabriel et al., 1996; Pujala et al., 2010). The self-assembly of laponite with pluronic F27 is reported through thermogleation and photogelation strategies (Juggernauth et al., 2011; Sun et al., 2010).
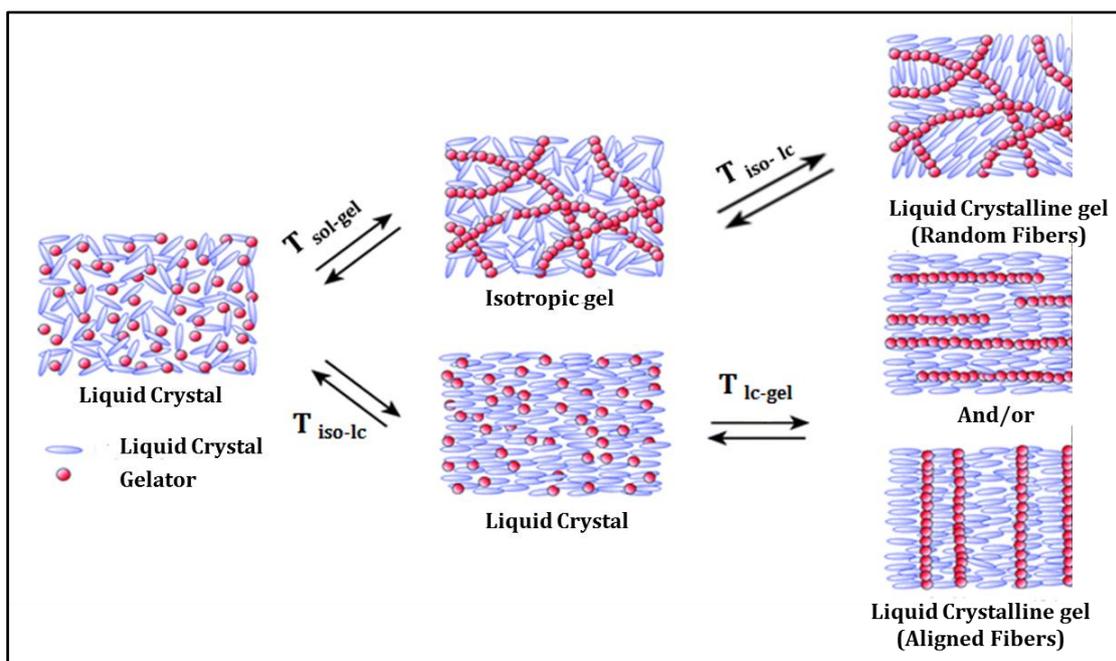
Figure 1.5. Schematic illustration of two types of thermoreversible structural changes of liquid crystalline physical gels

1.7. Properties of hydrogels

Exact information about the structure and properties of hydrogels are required to employ them in various fields. The interesting molecular features of the hydrogel can control their properties. Swelling is the most important property of hydrogels. While swelling, the volume of the hydrogel increases up to equilibrium. As the network swell, the polymer chains are elongated and exert a force in opposition to swelling. The osmotic pressure attributed to the polymer is the driving force of swelling. The swelling characteristics of a gel are affected by the external stimuli such

as pH, temperature, electric field, magnetic field etc. In the case of PAA based hydrogels, at lower pH, the ionization of the AA is very slow and hence the swelling takes place slowly. While at higher pH, AA ionizes and the repulsive forces between the like charges increases which tend to open up the matrix. This tendency of the matrix may facilitate a faster rate of swelling. The rate of diffusion overtakes the rate of relaxation of polymer chains and water will enter into the gel matrix until the chemical potential of the hydrogel matches with the environment.
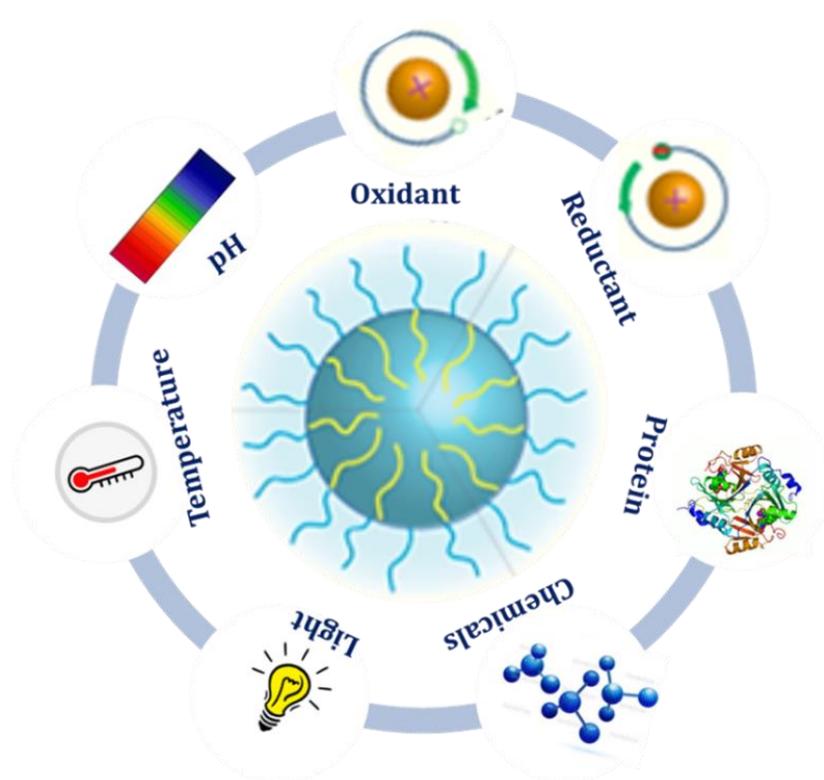
Figure 1.6. Schematic representation of multi stimuli responsive swelling and shrinking of hydrogels

Hydrogels can be stimuli-sensitive and respond to surrounding environment like temperature, pH, chemicals, electric field, magnetic field and light. The volume phase transition of the hydrogel induced by external stimuli such as variation in pH, temperature or electrical field can modify the relative distance of the functional groups and given in Figure 1.6. The fast environment response of the hydrogel makes

them smart materials. Thermo-sensitive hydrogels exhibit temperature dependent swelling and deswelling behaviour. These temperature sensitive hydrogels are classified into three. Negative temperature hydrogels will shrink when the temperature increases above low critical solution temperature (LCST) and show swelling behaviour at lower LCST. The LCST of polymer with more hydrophobic constituent will shift to a lower temperature. The LCST of a hydrogel can be tuned by varying the percentage ratio of hydrophilic to hydrophobic components. At temperature lower than LCST, water interact with the hydrophilic part of the polymer chain and form hydrogen bonding and hence the swelling of gel occurred. At temperature greater than LCST, the hydrophobic – hydrophobic interaction strengthens and the shrinking of the sample takes place due to inter polymer chain association.
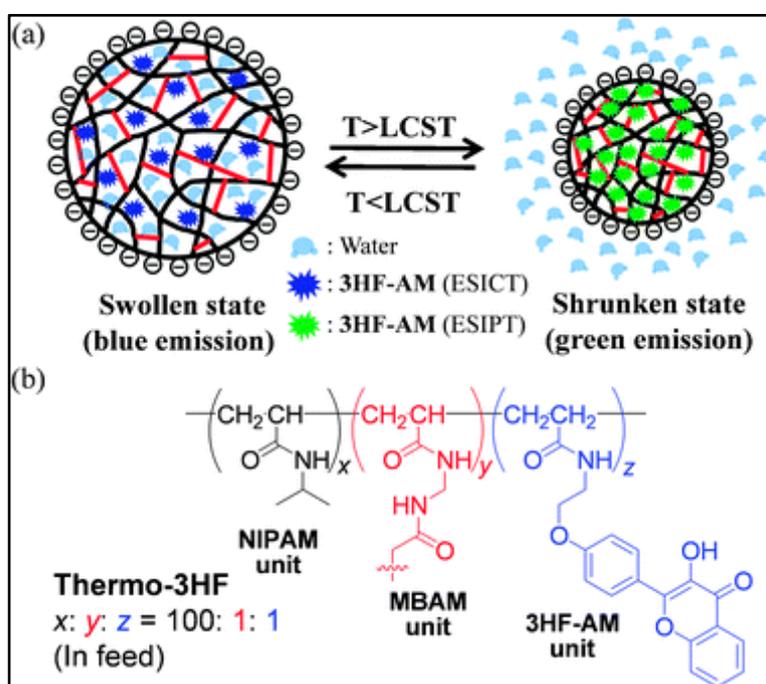
Figure 1.7. (a) The temperature responsive fluorescence emission of 3HF-nanogel and (b) The chemical compositions of components

In positive temperature hydrogels swelling takes place at temperature higher than upper critical solution temperature (UCST). Positive temperature hydrogel undergo shrinking at low temperature because of the formation of complex structure by hydrogen bonds. At high temperature, the bonds will break and swelling occurs above UCST.A PNIPAM-based fluorescent nanothermometer with ratiometric readout is reported by Chen et al. which exhibits blue fluorescence on swelling and green fluorescence on shrinking and is given in Figure 1.7 (Chen et al., 2011). The hydrogels of PNIPAM, pluronics and tetronics exhibit thermo reversible shrinking and swelling (Ruel et al., 2004; Guo et al., 2007).

The pH sensitive hydrogels have swelling and deswelling behaviour according to the pH of the environment. The anionic pH sensitive hydrogels comprises of carboxylic or sulphonic groups and they undergo swelling when the pKa is higher than the pH of the surrounding medium (Dong et al., 1991; Park et al., 1999).The cationic hydrogels have pendant group such as amine and exhibit swelling property when the pH of the surrounding medium is lower than the pKb. Chitosan hydrogels were reported for the pH responsive drug delivery and the schematic diagram is shown in Figure 1.8. (Zou et al., 2015). Electric sensitive hydrogels are made up of poly electrolytes and undergo swelling and deswelling depending on the applied electric signal.   The typical photoresponsive groups are azobenzene and spyropyranogroups. The photoresponsive hydrogels are widely used in drug delivery applications (Tomatsu et al., 2011).
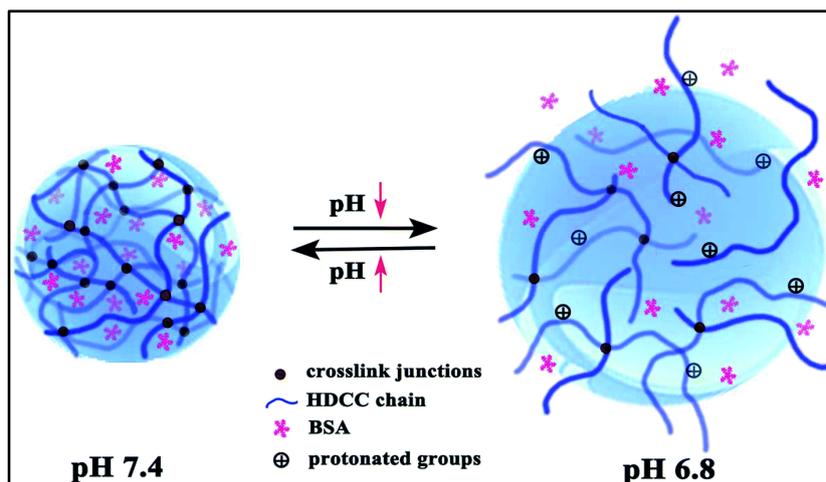
Figure 1.8. Schematic mechanism of pH-responsive behaviour of the modified chitosan hydrogels

1.8.   Applications of hydrogels

1.8.1. Agriculture

Hydrogels find application in the agricultural field as soil conditioning materials, they may be considered as water retention granules. Most of the hydrogels marketed in the agriculture are using cross-linked PAM and acrylamide - acrylate copolymers. Hydrogels enhance the water holding capacity of the soil, infiltration rates and soil permeability as well as reduces the soil erosion, water run-off and fertilizer leaching. Hydrogels are called as miniature water reservoirs, and water can be taken from these upon root demand through osmotic pressure difference. Hydrogels can also act as a controlled release system for the uptake of nutrients for plants (Ahmed et al., 2012; Chatzoudis et al., 1998).

1.8.2. Water purification

Recently, hydrogel based adsorbents were developed for the removal of toxic pollutants such as heavy metals, dyes, radioactive wastes, etc. due to the high adsorption capacity, high mechanical strength, good recyclability, low cost and green

approach. Different techniques were developed for the removal of toxic pollutants from water such as flocculation, ion exchange, membrane filtration, adsorption, coagulation etc. Among these, adsorption is considered to be more convenient, cheap and effective process. Hydrogels were reported for the water treatment applications (Jing et al., 2013; Rudzinski et al., 2002). Radioactive waste is a major concern, they seriously affect the environment. Polyelectrolyte hydrogels developed from acrylamide and bentonite reported for the sorption of uranyl ion (Kundakci et al., 2011).Textile industry produced highly coloured toxic and carcinogenic dye wastes. The PAM hydrogels were reported as a sorbent for dyes in the textile industries (Bocos et al., 2014).

1.8.3. Biomedical applications

Hydrogels are widely used for biomedical applications. The use of hydrogel for biomedical applications dates back to 1960 when Wichterle and Lim developed cross-inked poly (hydroxyethyl methacrylate) (pHEMA). Hydrogel can absorb and hold large amount of water and hence they can be used in disposable diapers, sanitary pads, wound dressings and so forth. The most commonly used hydrogels in diapers are sodium polyacrylate and PAM. Blood-glucose detection kit and insulin delivery were reported using pH sensitive hydrogels. Electric field sensitive hydrogels have been used for artificial muscles, and controlled drug delivery systems (Kim et al., 2005). Petelin and co-workers reported Orabase®, Carbopol 934P and neutralized poly (MAA-co-methyl methacrylate) for the delivery of liposomes (Peppas et al., 2000; Petelin et al., 1998). Alginate-chitosan hydrogels was developed by Hari et al. for the controlled release of bioactive peptides (Hari et al., 1996). Polymethacrylic acid and PVA based hydrogel was reported to deliver ibuprofen into the intestine

(Mundargi et al., 2008). Hydrogel act as moist wound dressing material and they can promote fibroblast proliferation by reducing the fluid loss from the wound surface and promote rapid wound healing. PVA and chitosan based hydrogels were reported as wound dressing material. Tissue engineering is a useful tool for replacing the damaged tissues. Polymers like polylactic acid (PLA), polyglycolic acid (PGA), and their copolymers (PLA-co-PGA; PLGA) are being used as scaffolds for tissue engineering (Atala et al., 2006).

1.9.   Metal nanoparticles

Metal nanoparticles possess large surface to volume ratio, high surface area, plasmon excitation, quantum confinement, short-range ordering, increased number of coordination sites. Noble metal nanoparticles find many applications in different technological areas due to their exceptional optical, electronic, magnetic and chemical properties and are different from those of the corresponding bulk materials. In the ancient days, noble metal nanoparticles were used as decorative pigments because of their bright and fascinating colour. The Roman Lycurgus Cup, a bronze cup lined with coloured glass which dates to the fourth Century AD was the first recognition of nanoparticles (Evanoff et al., 2005). The glass is an alloy of silver and gold and it scatters dull green light and transmits red. Gold and silver nanoparticles were used to create coloured patterns in glasses in the later centuries. The efficient photo physical properties of metal nanoparticles and the fast advances in the nanoparticle synthesis directed them towards a wide range of applications in the field of photonics, sensors, catalysts, biomedicine etc. Light interacts with metal nanoparticles resulting a collective oscillation of the metal free electrons with respect to the nanoparticle lattice in resonance with the light field is termed as surface

plasmon resonance (SPR) and it was first pointed out by Gustav Mie in 1908 (Mie et al., 1908). Schematic representation for SPR of metal nanoparticles is given in Figure 1.9. The SPR of metal nanoparticles will enhance the spectroscopic signal of molecules present in the neighbourhood of metal nanoparticles. This exciting property of metal nanoparticles can be used in metal plasmon enhanced fluorescence, surface enhanced Raman scattering and hence they can act as sensing platforms and allows single molecule detection. Metal nanoparticles have been prepared using different techniques such as laser ablation, thermal decomposition of organometallic compounds, pulse radiolysis, electrochemical reduction and chemical reduction (Rao et al., 2000; Thomas et al., 1966; Esumi et al., 1992; Henglein et al., 1993). Metal nanoparticles have a tendency to agglomerate and hence protecting agents such as surfactants, polymers, micelles, quaternary ammonium salts are employed in the synthesis of nanoparticles (Reetz et al., 1994; Reetz et al., 2001). Incorporation of nanoparticles into polymers can be resulting the formation of polymer-nanocomposites has long been established. Hydrogel-metal nanocomposites have many fascinating potential uses, including quantum dots, chemical sensors, light-emitting diodes, 'ferrofluids' for cell separations, industrial lithography and photochemical pattern applications such as flat-panel displays (Oral et al.,2004; Mayol et al., 2015).
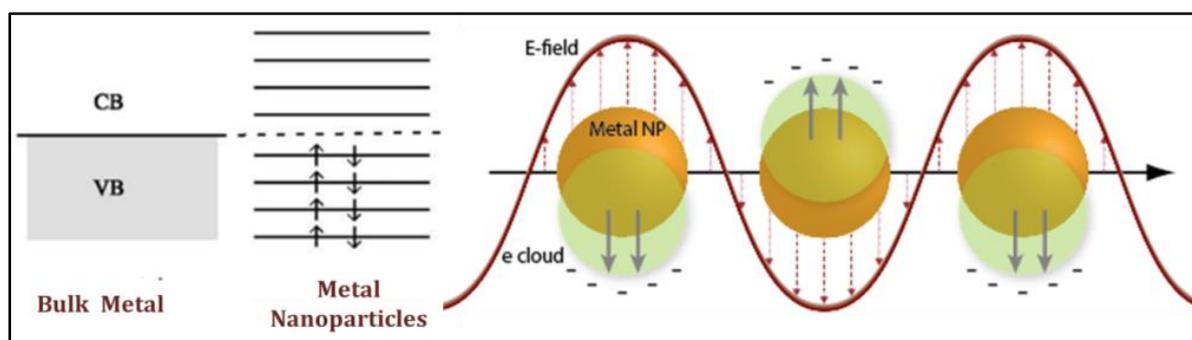
Figure 1.9. Schematic representation for surface plasmon resonance of metal nanoparticles

1.10. Silver nanoparticles

Among the metal nanoparticles, silver is easily reducible, exhibit strong SPRE in the visible region and has high excitation efficiency, unique electrical, optical, magnetic, and thermal properties and finds application in nanoscale electronic and information storage devices, plasmonic waveguides, and biomedical and chemical sensing via surface-enhanced Raman scattering and surface-enhanced fluorescence. The good electrical conductivity, photophysical properties, and antimicrobial effects make them superior to other metal nanoparticles (Abou El-Nour et al., 2014; Sarkar et al., 2007).

There are different methods for the preparation of silver nanoparticle such as chemical and physical approaches. Various methods are used to synthesize silver nanoparticles such as photochemical, sonochemical and electrochemical reduction. Many reports are available in the literature for the solution synthesis of silver nanoparticles. Chemical reduction with strong reducing agents, such as sodium borohydride, hydrazine, tetrabutylammonium borohydride, N, N–dimethylformamide can be carried out at room temperature. In the presence of weak reducing agents such as glucose, sodium citrate, dimethyl formamide, potassium bitartrate, ascorbic acid and alcohols, prolonged refluxing is required. A variety of stabilizers or coating agents has been used in the preparation methods to prevent the aggregation and for controlling the size, shape and stability of silver nanoparticles (Oliveira et al., 2005; Bai et al., 2007). Single crystal cubes and tetrahedrons of silver with truncated edges were synthesized by reducing silver nitrate with ethylene glycol in the presence of polyvinyl pyrrolidone and trace amount of sodium chloride (Wiley et al., 2004). Polygonal silver nanoprisms were reported by boiling silver nitrate with

dimethylformamide in the presence of polyvinyl pyrrolidone (Pastoriza-Santos et al., 2002). Ohde and co-workers demonstrated the synthesis of silver and copper nanoparticle using supercritical carbon dioxide in the presence of sodium cyanoborohydride and tetramethyl-p-phenylenediamine (Ohde et al., 2001). Highly surface roughened silver nanoflowers were reported with the reduction of silver nitrate with ascorbic acid (Liang et al., 2009). Photochemical reduction is another approach for the synthesis of silver nanoparticles. A light assisted synthesis of silver nanoparticles in polyurethane matrix exhibited good antimicrobial property (Saez et al., 2014). Henglein and co-workers reported silver nanoparticles with narrow optical absorption band are synthesized by the UV illumination of aqueous solution containing silver perchlorate, acetone and 2-propanol with different stabilizers polyethyleneimine, sodium polyphosphate, sodium polyacrylate, and PVP (Henglein et al., 1998). Highly fluorescent silver nanoparticles have been prepared by the use of photogenerated ketyl radicals that reduce Ag^+ from silver trifluoroacetate in the presence of amines (Maretti et al., 2009). Starowicz et al. reported an electrochemical synthesis of silver nanoparticles based on the dissolution of the metallic anode. They carried out the electro-reduction of anodically solved silver ions in acetonitrile containing tetrabutylammonium salts and silver nanoparticles ranging from 2 to 7 nm obtained by changing the current density (Starowicz et al., 2000). The stable organosols of silver nanoparticles without any capping agent have been reported by Wadkar et al., by electrochemical dissolution of silver electrode in dimethyl sulphoxide (Wadkar et al., 2006). Living organisms such as bacteria, fungi and plants may be exploited as potential biofactories for the synthesis of metallic nanoparticles. Enzymes like silver reductase and the aminoacids can be used for the reduction of metal ions. Klaus et al. reported the formation of triangular, hexagonal and spherical

silver nanoparticles at different cellular binding sites of the bacterium, Pseudomonas stutzeri AG259 (Klaus et al., 1999). Vigneshwaran et al. reported the reduction of silver nanoparticles on the surface of the fungus, Aspergillusflavus by accumulating silver nitrate solution on its cell wall (Vigneshwaran et al., 2007).

Silver nanoparticles possess a broad range of applications and can be employed in different technological areas such as biomedical labels, sensors, catalysts and detectors (Bosetti et al., 2002; Cho et al., 2005; Gupta et al., 1998; Jain et al., 2005; Chavan et al., 2015). Silver nanoparticles are used to efficiently harvest light and for enhanced optical spectroscopies including metal-enhanced fluorescence (MEF) and surface-enhanced Raman scattering (SERS). They can increase the emission intensity of fluorescein, a common biological label, and can be made use in the ultra-level detection of biological assays like proteins. Silver nanoparticles can be efficiently functioning as optical antennas in collectors. The electrical conductivity of materials like plastics, composites, adhesive can increase by the addition of silver nanoparticles. The excellent electrical conductivity of silver nanoparticles was made use in the applications like conductive inks, pastes, fillers etc. The silver nanoparticles have found diverse application in wound dressing, coatings for medical devices, etc. (Fateixa et al., 2014). The burn wounds treated with silver nanoparticles shows better cosmetic appearance and scarless healing. The silver nanoparticles are capable of inactivating the vital enzymes and also help in the prevention of the replication of DNA. Silver nanoparticles were used to target the bacterial membrane to destabilize the plasma membrane potential that leads to the depletion of the levels of intracellular adenosine triphosphate, resulting in the death of bacterial cells. The antibacterial activity of antibiotics like penicillin G, amoxyicillin, erythromycin, and vancomycin are enhanced in the presence of silver nanoparticles against E-coli and S aureus.

Silver nanoparticles are attracting the present scenario due to its high catalytic efficiency. The catalytic activity of these nanoparticles is also dependent on their size, shape and chemical–physical environment. Silver has been extensively reported for styrene epoxidation, oxidation of hydrocarbons, alcohols, ammonia, carbon monoxide, and volatile organic compounds, hydrogenation of nitro-aromatics and aldehyde, reduction of nitric oxide, decomposition of H_2O_2, aza-Diels-Alder reaction, asymmetric aldol reaction, addition, coupling, cyclization and allylation have been reported (Xu et al., 2006; Woo et al., 2006; Jiang et al., 2005; Zheng et al., 2012; Lu et al., 2007). The silver nanomaterial modified electrodes act as an appropriate alternative in sensing applications because of their advantages as a high surface reaction activity, high catalytic efficiency, large surface-to-volume ratio, strong adsorption ability, stability and convenience of electron transfer and hence provide faster response time and lower detection limits.

1.11. Hydrogel metal nanocomposites

The synergistic combination of organic soft hydrogels and metal nanoparticles enhances the properties of both components which may result in improved opto-electronic properties, mechanical strength and stimuli responsiveness. The benefits of the combination of two different materials produce advanced materials with unique properties and catalyzed intense research activity in the field of nanoparticle hydrogel composites. The innovative combination of nanoparticles and hydrogels create synergistic, unique and potentially useful properties that are not found in the individual components. The hydrogel-nanoparticle composites respond to various stimuli in the bulk phase and exhibit improved properties than polymers and nanoparticles with increased modulus strength, barrier properties and conferring good

kinetic stability to the nanoparticles. The stabilization of nanoparticles in the hydrogel matrix overcomes the limitation of bare nanoparticles and decreases the health hazards.The three- dimensional cross- linked network of the hydrogel is formed by either chemical or physical interaction. The physical interactions are non-covalent interactions and are due to hydrogen bonding, hydrophobic or dipole – diploe interactions. The covalent bonds present in the polymeric chain are responsible for the chemical interactions. The picture showing the synthesis of silver entrapped hydrogels is given in Figure 1.10.
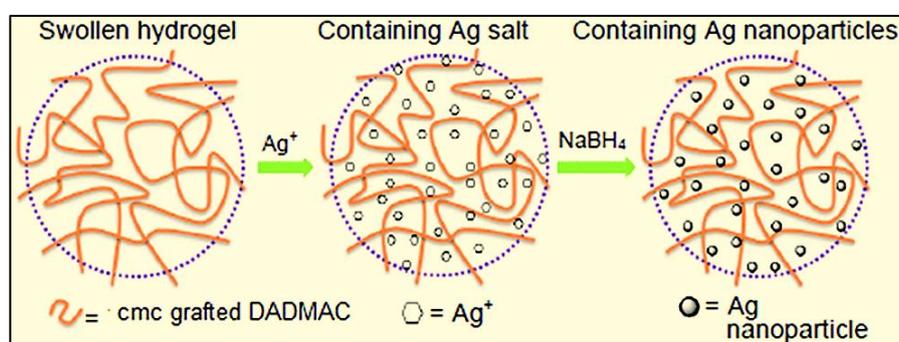
Figure1.10. Schematic representation for the synthesis of hydrogel silver nanocomposite

The unique properties of hydrogels such as absorption, swelling- deswelling response to various stimuli and hydrophilicity make them a good candidate for wide range of applications. Recently hydrogel based networks are tailored in different designs to meet a wide range of applications. The nanoparticles can efficiently entrap in the hydrogel networks and enhance the cross linking property of the hydrogel. The nanoparticles add unique properties to the hydrogel matrix such as response to mechanical, optical, thermal, magnetic and electric properties. They find application in the field of electronics, optics, sensors, actuators, catalysis, separation devices, drug delivery, and many other biotechnological areas (Wang et al., 2004; Yoshida et al., 1995; Dong et al., 1991; Fuhrer et al., 2009).

There are different techniques to prepare polymer metal nanocomposites, in situ and ex-situ method. In the in situ technique, nanoparticles are generated inside polymer matrix by decomposition of metal precursors. Polymerization of the monomer is performed with metal nanoparticle precursors, and then metal nanoparticles are formed using chemical, thermal or photolytic reduction methods. In the ex situ technique, first nanoparticles are produced by chemical methods then are distributed into a polymer solution or monomer solution to polymerize (Thoniyot et al., 2015).

1.12.   Applications of hydrogel metal nanocomposites

1.12.1. Biomedical applications

The integration of hydrogels and nanocomposites lead to the efficient synthesis of biomaterials which mimic the structure and properties of native tissues used in drug delivery, tissue engineering and scaffolds. The combination and formulation of synthetic and natural polymers with nanoparticles and biomolecules synergistically combines advantageous chemical, physical, and biological properties to produce nanocomposite hydrogels that support the repair and regeneration of human tissues and body functions (Schexnailder et al., 2009). The in vitro and in vivo biocompatibility, the anti-thrombogenicity, as well as the thermo sensitivity of these materials suggest applications as biomaterials for contact lenses or implants. In addition, the mechanical toughness is useful for development of elastic biomaterials such as sutures and artificial tendons. Stronger polymer–nanoparticle interactions that are induced, e.g., by the attachment of gold reactive thiol groups to the PNIPAM hydrogel, may change thermo sensitivity and swelling behaviour (Wang et al., 2004). Hydrogels containing magnetic nanoparticles could be used for inducing non-invasive

focused hyperthermia, for controlled drug release, and for triggering thermo sensitive changes in hydrogel volume or shape. Magnetic hydrogels thus offer ways to selectively target, detect, and potentially treat cancer tissue via magnetic resonance imaging and inductive heating. Besides the biomedical applications mentioned above, magnetic hydrogels are potentially attractive to the development of other technologies including nanometres, sensors, robot-like soft actuators, and a variety of separation devices (Ramanujan et al., 2006).
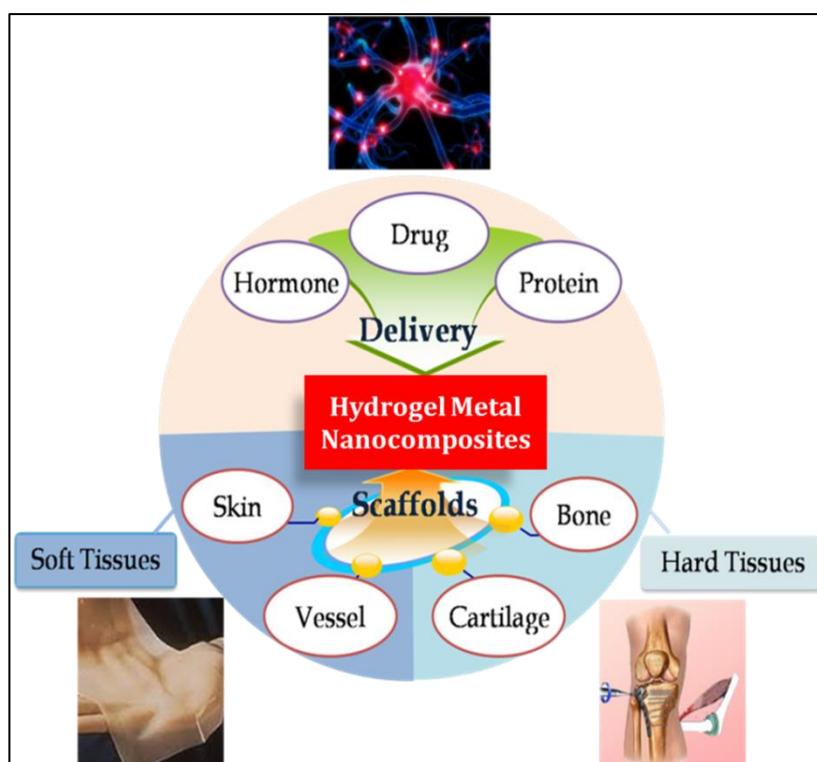
Figure 1.11. Biomedical applications of hydrogel metal nanocomposites

There are many examples of nanocomposite hydrogels being used as biomaterials in drug delivery, tissue engineering. Functionalization of polymer hydrogels with finely dispersed calcium phosphate nanocrystals for bone repair was reported (Leeuwenburgh et al., 2007). Homogeneous hydrogels were fabricated by synthesizing calciumphosphate nanocrystals directly inside a poly (ethylene glycol) fumarate hydrogel, and used in the tissue engineering applications (Webb et al.,

2007). The applicability of these composites can be enhanced by increasing the mechanical stability, biodegradability and stimuli responsiveness. The biomedical applications of hydrogel nanocomposite are given in the Figure 1.11.

Silver nanoparticles are known for their antimicrobial properties and have been widely used in dental fillings and recently in the wound and burn dressings to prevent infections. The design of silver nanoparticle- hydrogel composites expected to provide functional coatings for various applications. The silver nanoparticles with unique chemical and physical properties are providing an alternative path for development of new antibacterial agents. The silver nanoparticles have also found diverse application in form of wound dressing, coatings for medicinal devices, silver nanoparticles impregnated textile fabrics etc.
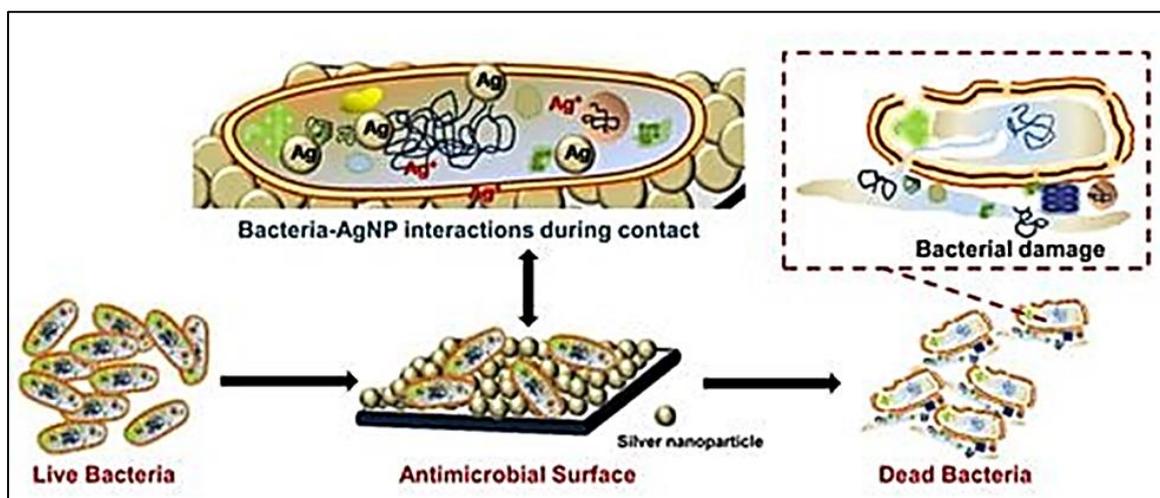
Figure 1.12. Contact killing mode of antibacterial action of immobilized silver nanoparticles

The advantage of using silver nanoparticles for impregnation is that there is a continuous release of silver ions and the devices can be coated by both the outer and inner side, hence enhancing its antibacterial efficiency and the schematic representation for the antimicrobial action is given in Figure 1.12 (Agnihotri et al., 2013). The burn wounds treated with silver nanoparticles shows better cosmetic

appearance and scarless healing. The silver nanoparticle/poly (N-vinyl-2-pyrrolidone) composite functioned as a bactericide is applied in infected burns and purulent wounds.

The antibacterial properties of silver nanoparticle entrapped hydrogels were extensively reported. Hydrogels such as gum acacia – poly sodium acrylate (Bajpai et al., 2015), PNIPAM (Bajpai et al., 2011), cellulose-PAA (Bajpai et al., 2013), poly (acrylamide-co-acrylic acid) (Thomas et al., 2007), PAM-PVP (Murthy et al., 2008) were reported the insitu preparation of silver nanoparticles and their antibacterial activities. Recently, gum acacia/poly (sodium acrylate) semi interpenetrating hydrogel network was reported via free radical initiated polymerization of sodium acrylate in the presence of gum acacia. Silver nanoparticles were synthesized using a green approach with extract of bacteria, and the antibacterial activity of silver nanoparticles against E. coli is tested (Bajpai et al., 2015). In another report, temperature sensitive poly (NIPAM) has been exploited for the in situ synthesis of silver nanoparticles and demonstrated the fair antibacterial activity against E. coli (Bajpai et al., 2011). Cellulose- PAA hydrogels were reported for antibacterial applications. The free radical polymerization of AA is carried out in cellulose solution. These gels were loaded with silver ions and reduced with sodium borohydride and demonstrated the fair antibacterial activity against E. coli (Bajpai et al., 2013). A versatile breathing out/breathing in mechanism were utilized for the synthesis of silver nanoparticle loaded with poly(acrylamide-co-N-vinyl pyrrolidone) hydrogels. As the number of breathing in- breathing out cycles increases, more amount of silver nanoparticles can be loaded to the hydrogels. The antibacterial activity against E. coli. was studied with respect to number of breathing in- breathing out cycles and degree of cross-linking (Murthy et al., 2008). Bajpai and Mohanaraju

et al. reported the tuning of silver nanoparticles in a hydrogel network. They have synthesized hydrogels of poly acrylamide and its copolymers such as Poly (acrylamide)/poly(ethylene glycol), Poly(acrylamide)/ poly(vinyl sulfonic acid), Poly(acrylamide-co-AA) (PAM - AAc). Depending upon the monomers and crosslinking density, the size of the silver nanoparticles can be regulated between 1 to 10 nm and in different shapes such as nanospheres, nanorods, and nanocubes (Murali Mohan et al., 2013). The nanoparticles can be released from the network and find promising antibacterial applications. The antibacterial application of hydrogels can be increased by incorporating natural curcumin. Ravindra et al. reported a silver entrapped protein based hydrogels and the improved antibacterial efficacy is observed by including curcumin to the matrix (Ravindra et al., 2013). Inorganic nanocomposite hydrogels may be considered as a novel platform for stabilizing silver nanoparticles and for the inactivation of bacteria. An inorganic nanocomposite hydrogel was reported using PAM for synthesizing uniform sized silver and gold nanoparticles in the hydrogel matrix (Vimala et al., 2014). The silver zeolite–poly (acrylamide-co-AA) nanocomposite synthesized via radical graft copolymerization exhibited inhibition on bacterial growth against Bacillus subtilis (as Gram-positive bacteria), Pseudomonas aeruginosa (Gram negative bacteria), and is comparable to standard drugs (Zendehdel et al., 2015).

1.12.2. Catalytic applications

The catalytic reduction with heterogeneous catalysts has received much attention due to its easy operation, high efficiency, simple processing, and low cost. The catalytic reduction and decolouration of dye pollutants and the conversion of aromatic nitro compounds to beneficial amino counterparts have been widely reported. The

metal based reductions highly depend on noble metals such as silver, gold, palladium, platinum. The nanostructured metal catalysts aggregate easily and reduce their catalytic efficiency and lifetime (Chaudhari et al., 2011; Elias et al., 2014). The aggregation of metal nanoparticles can be arrested by the use of capping agents such as organic surfactants, ligands and etc. The solution based catalysts are difficult to separate and reuse. Solid supported metal nanoparticles may passivate the active sites and reduce the catalytic efficiency. The catalytic reduction of 4-nitrophenol with boron nitride/silver nanocomposite is reduced by the addition of PVP as a stabilizer (Huang et al., 2013). Surfactants and ligands may poison or deactivate the catalyst due to tight packing and hence adversely affect the accessibility and catalytic activity of a catalyst molecule.
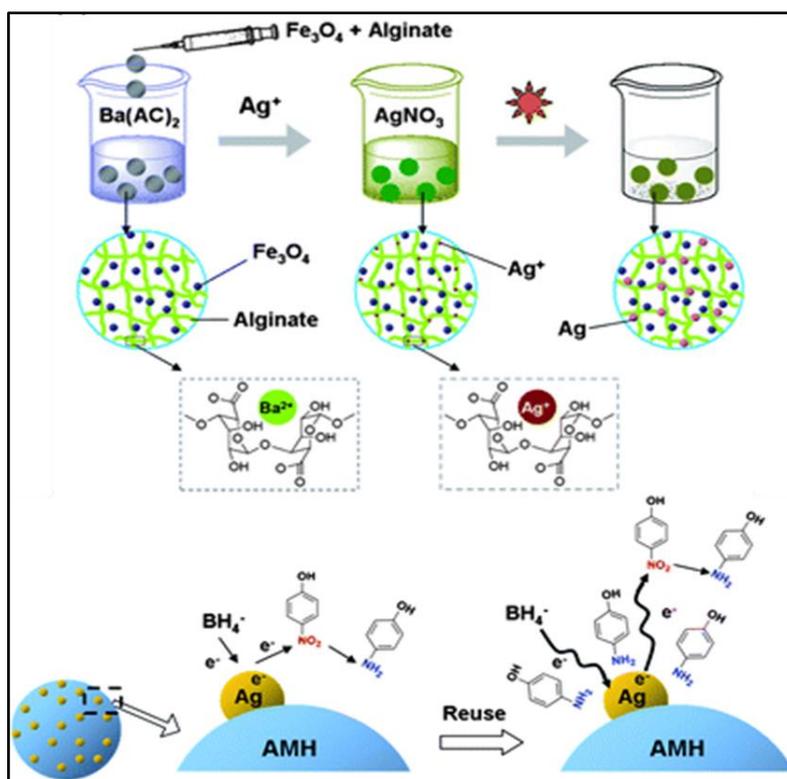
Figure 1.13. A highly reusable alginate-silver hydrogel catalyst for the reduction of nitrophenols

Among the stabilizers, hydrogels with three-dimensional fibrillar networks are receiving importance due to its better stabilization of metal nanoparticles (Butun et al.,

2011). The ionic hydrophilic groups present in the hydrogel network can potentially serve as nanoreactors for the synthesis of metal nanoparticles and provide cage effect for its stabilization. Moreover, the fibrillar network can speed up the diffusion of metal ions through the hydrogel networks. Apart from this, the size and shape of metal nanoparticles could be tuned by controlling the amount of monomer, cross-linker and metal ions. Polymeric hydrogel metal nanocomposites are viable catalysts because they prevent aggregation of nanoparticles, and the loosely bound dynamic structure will give easy access to the nanoparticles. Zhang and co-workers reported reduced graphene oxide silver composites catalysts for dye degradation in water treatment plants. Reduced graphene oxide based silver composites were prepared by insitu through the simultaneous reduction of graphene oxides in polyethylene imine with silver acetate as the precursor of silver ions and studied the photocatalytic degradation of organic dyes such as rhodamine B (RhB) and methylene blue (MB) (Jiao et al., 2015). They also reported a Chitosan/silver/gaphene oxide hydrogels for the photocatalytic degradation of dyes (Jiao et al., 2015). Wang et al. reported a biomimetic nanowire structured recyclable catalyst with PHEMA and applied for the conversion of o-nitroaniline, 1,2-benzenediamine (Mao et al., 2015). A ternary hydrogel based on PAM, graphene and silver hydrogel was developed as highly reusable catalyst for the reduction of dyes and nitrophenol (Hu et al., 2015). Silver immobilized alginate based magnetic hydrogel were reported and used for the repeated catalytic reduction of nitrophenols as shown in Figure 1.13 (Jiang et al., 2014). Much effort has been devoted in developing silver immobilized polymeric hydrogel catalytic systems such as poly (acrylamide-co-AA) (Hu et al., 2015) poly aspartic acid (Patwadkar et al., 2015), poly(ethylene oxide propylphosponamidate) (Zhang et al., 2013), poly alginate, (Ai et al., 2013; Otari et al., 2013) chitosan (Zheng

et al., 2012) polyvinyl alcohol, (Lu et al., 2007) and dextran (Ma et al., 2009) for the catalytic reduction of organic compounds.

1.12.3. Surface enhanced Raman scattering

Surface enhanced Raman scattering (SERS) is highly sensitive and selective technique which increase the magnitude of the Raman signal upto 10^{14-15} times which allows single molecule detection. They find applications in different areas such as biomedical, environmental monitoring, and food quality assurance. Enormous amount of research has been focused on the development of reproducible and cost effective SERS substrates. Noble metal nanoparticles are powerful SERS substrates due to the strong signals exhibited by the coupling of between surface plasmon resonance and local electromagnetic field. Incorporation of metal nanoparticles in polymers and inorganic substrates can control the morphology and aggregation of metal nanoparticles. Polymers with stimuli responsiveness add complementary functionalities to the SERS substrate. Hydrogels are considered as SERS substrate which gives a greatly enhanced SERS signal due to the synergistic action of plasmonic metal nanoparticles and stimuli responsive polymers. Hydrogels possess advantages such as tunable dimensions of metal nanoparticles, fast responsiveness and potential biocompatibility. Silver nanoparticles have been extensively used as SERS substrates such as rough electrodes, or as nanocomposites. It exhibit dominant SERS properties due to high extinction coefficient. Silver nanoparticles incorporated kappa- carrageenan hydrogels have been reported as SERS substrates. They show enhancement in the SERS signal depending on the strength of silver/polysaccharide hydrogel. This may be due to the formation of more number of hot spots due to the formation of increased number of silver nanoparticles nanojunctions as the

biopolymer rearranges to a stronger gel (Fatexia et al., 2014). The PNIPAM hydrogels loaded with silver and gold nanoparticles produced much higher SERS intensities in the detection of analytes (Contreras et al., 2010). Silver nanoparticles loaded with an interpenetrating polymer network of PAA and PNIPAM with pH and temperature responsiveness. These hybrid hydrogels exhibit pH and temperature responsive SERS signal enhancement and can be utilised for measuring the pH and temperature values of the surrounding (Liu et al., 2014). Gong et al synthesized silver nanoparticle s loaded PVA hydrogel and utilized for the detection of triazophos, isocarbophos, and methyl parathion, and Sudan red III from different substrates (Gong et al.,2014).

1.12.4. Electrochemical sensing

Electrochemical sensors represent the most rapidly growing class of chemical sensors. Electrochemical sensor transforms electrochemical information into an analytically useful signal with a transduction mechanism. Electrochemical sensors usually composed of two basic components, a chemical recognition system which is the most important part of a sensor and a physicochemical transducer which is a device that converts the chemical response into a signal that can be detected by modern electrical instrumentations. In electrochemical sensors, modified electrodes are widely used as sensing elements. These modified electrodes can be formed on the basis of different inorganic or organic materials characterized by good electrical conductivity and catalytic properties. (Jackowska et al., 2013)

Recently, Hydrogels were developing as an efficient electrochemical platform for sensing the analytes. The three-dimensional networks of hydrogels provide a greater effective surface area and facilitate the transport of electrons and ions, lead to an improved conductivity. Polymerized crystalline colloidal array of

poly(acrylamide) hydrogels containing Benzo-18-crown-6 were reported for the electrochemical investigation of Pb^{2+} binding. (Geary et al., 2005). The hydrogels prepared from self-assembly methods have gained great interest because of its facile preparation process and functionalization flexibility. Glucose oxidase was successfully incorporated to ferrocene modified amino acid phenylalanine hydrogel. This was utilized for the detection of glucose in blood samples using amperometric technique. The prepared glucose biosensor exhibited good performance, high sensitivity, wide linear range, short response time, good stability and biocompatibility. (Qu et al., 2014)

The noble metal entrapped hydrogels can enhance the selectivity and sensitivity of the hydrogel substrate. Silver nanoparticles doped chitosan hydrogel film was utilized for the electrochemical sensing of trichloroacetic acid. Silver nanoparticles and chitosan were co deposited on to the surface of the glassy carbon electrode. The fast diffusion and electron transfer of the negatively charged trichloroacetic acid to the positively charged silver nanoparticles allows a low detection limit for the sensing of trichloroacetic acid (Liu et al., 2012). Nanostructured polypyrrole hydrogel/Au composite was used as enhanced electrochemical biosensor platform for the detection of a model protein, carcinoembryonic antigen. The polypyrrole/Au hydrogel exhibited excellent sensing performance and high sensitivity as an electrochemical platform (Rong et al., 2015).

1.13. Scope and objective

Noble metal entrapped hydrogel nanocomposites are receiving considerable research attention due to the combined properties of the stimuli-responsive hydrogels with unique optoelectronic properties of metal nanoparticles. The synergistic

properties arising from the molecular level self-assembly of this hybrid material is presently flourishing to satisfy a variety of applications in many technological areas. They find academic and technological interest in many interdisciplinary areas such as drug delivery, sensors, catalysts and super absorbent materials. Among the metal nanoparticles, silver is easily reducible, exhibit strong surface plasmon absorption in the visible region and has high excitation efficiency. Literature showed that hydrogel stabilized with metal nanoparticles can act as efficient nanoreactors because of their three dimensional porous network and provides better stabilization and easy access to the active nanoparticles. They have been used in a wide range of biological, medical, pharmaceutical, and environmental applications.

PAA and its derivatives are popular thickening, dispersing, suspending and emulsifying agents in pharmaceuticals, cosmetics and paints. The mechanical stability of PAA hydrogels can be enhanced by the use of a physical crosslinking agent such as amidodiol. The colour removal from waste water is important for solving the ecological, biological and industrial problems associated with the dyes. Polymeric adsorbents particularly hydrogels with different functional groups can complex with the dyes and used for water purification. Apart from this, studies on the mechanism of adsorbent--adsorbate interaction is also receiving importance for utilizing gel as an adsorbate. Nitro-aromatic compounds hold a significant role in the industrial chemistry and are generally produced as a by-product from pharmaceuticals, agrochemicals, urethanes, dyes and are also toxic organic species. Therefore, to reduce aromatic nitro compounds to their corresponding useful amines, various catalysts have been developed. The utilization of environmentally benign hydrogels nanocomposite in such a catalytic reduction reaction is a reasonable goal.

A hierarchically structured liquid crystalline domain offers excellent flexibility in tailoring the functionality of the gels. Layered materials such as clay having high aspect ratio are amenable for further modification receives importance as an ordered linker for generating liquid crystalline phase. Laponite is made up of discoid platelets of lithium magnesium silicate ($Si_8[Mg_{5.5}Li_{0.4}O_{24.0}]H_4O_{24}Na_{0.7}$) with a thickness of about 1 nm, and diameter of about 30 nm having partial positive charges at the edges and negative charges on the surface. Laponite clay can act as a physical cross linker due to its nanoscale dimension and high aspect ratio which can enhance ordering as well as thermo-mechanical stability. They can form ordered network structures through various non-covalent interactions such as hydrogen bonding and ion-dipole interactions. Ruzika et al. studied the liquid crystalline phase formation of laponite based systems in water. Design of self-assembled liquid crystalline functional materials using tailor made functional cross linkers offers new features. In this respect, utilization of amidodiol (1,6-bis (hydroxybutyramido) hexane) as a cross-linking agent is receiving interest since it is endowed with two amide groups and two hydroxyl groups and can enhance mechanical stability of the hydrogel apart from providing functional groups to the liquid crystalline gels. Liquid crystalline phase can act as structure directing agents and also can stabilizes the metal nanoparticles at the interface between domains.

The liquid crystalline soft molecular hydrogels significantly enhances the electrical conductivity, faster response to chemical and electrochemical reactions apart from increasing the mechanical strength. Hence its utilization as a gel electrolyte is receiving importance for the fabrication of energy storage systems.

Metal nanoparticles can be patterned inside the channels of liquid crystalline phase and expected to act as efficient nanoreactors. Because of their porous channel network, they may provide better stabilization and easy access to the active nanoparticles. Hence studies on the silver nanoparticle patterned liquid crystalline hydrogels modified electrode as an electrochemical sensor will be interesting.

So, the objectives of the present research program involve the collection and anthology of the latest developments in the area of polymeric hydrogel - metal nanoparticles, properties and applications. Then, hydrogels based on PAA-amidodiol was prepared and demonstrated its application in the dye removal. This system is further modified by entrapping silver nanoparticles and studied its application as catalyst for the reduction of nitrophenol to aminophenol. Further, studies were carried out the on the design and development of laponite-amidodiol based liquid crystalline gel and its application as an electrolyte. Later, preparation and property evaluation of silver entrapped liquid crystalline laponite-amidodiol gel were studied and demonstrated its application as an electrochemical sensor for the detection of L–tyrosine.

CHAPTER 2

STUDIES ON THE PREPARATION AND PROPERTIES OF POLYACRYLIC ACID-AMIDODIOL HYDROGEL AND ITS APPLICATION AS A DYE ADSORBENT
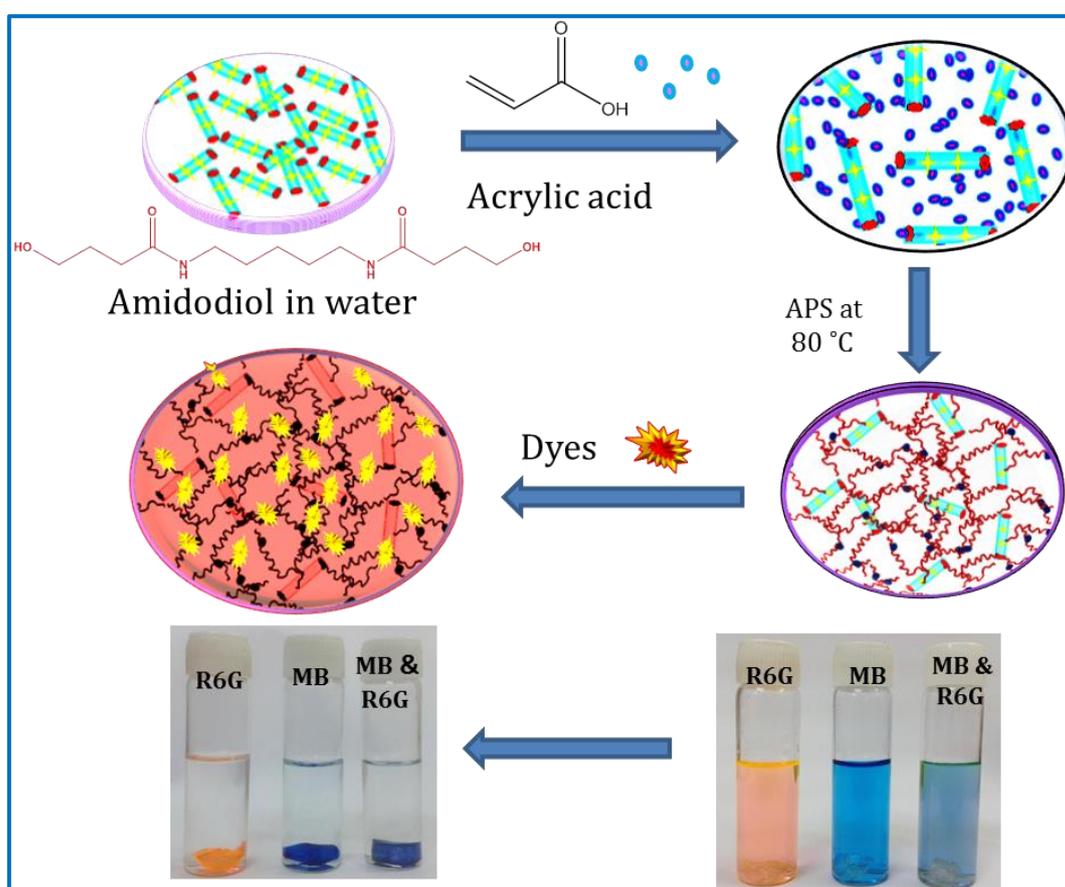
2.1. Abstract

Herein, we report the preparation of polyacrylic acid-amidodiol hydrogel (PAG) through the polymerization of acrylic acid (AA) using ammonium persulphate (APS) as the radical initiator in presence of amidodiol (AMD). Chemical structure, rheology, swelling, diffusion and adsorption properties of PAGs were studied. Kinetics and mechanism of adsorption were investigated using dyes such as rhodamine 6G (R6G) and methylene blue (MB) as the adsorbate. Effect of AMD on the adsorption of dyes was investigated. The extent of interaction between adsorbate-adsorbate and adsorbent-adsorbate was studied using Gile's model. Further results suggested a multilayer adsorption and pseudo second order kinetics. Finally, its application is demonstrated for the removal of dyes present in waste water collected from textile and paper industries.

2.2. Introduction

Polymeric hydrogels are composed of three-dimensional networks of flexible hydrophilic polymeric chains which can absorb and retain water and solute molecules. They find applications in the area of medicine, water treatment, food industry and agriculture (Kim et al., 2003; Nho et al., 2005). The higher water content and porous structure of the hydrogel network allows solute to diffuse into the interstices of the hydrogel (Jeon et al., 2008). Various non-covalent interactions include hydrogen bonding, π- π stacking, van der Waals interactions are involved during the organization of these molecules into 3D architectures that enable the solute molecules to be trapped inside the gel matrix. Polyacrylamide, polyvinyl pyrrolidone, chitosan, polyacrylic acid and its derivatives are the most commonly used systems for developing hydrogels due to their nontoxicity, presence of long flexible chains and capacity in preserving their shape. A large number of investigations have been reported for improving the mechanical and chemical properties of these hydrogels

through reinforcing with nanofillers such as inorganic nanoclays, metal nanoparticles, cellulosic particles and carbon nanotubes and so forth (Haraguchi et al.,2002; Saravanan et al.,2007; Zhou et al.,2011; Xia et al.,2010).

A large amount of dyes and toxic organic molecules are discharged into the aquatic systems from various textile and paper industries. MB is a thiazine type cationic dye and R6G is a cationic amine type fluorescent xanthene dye and are included in the category of hazardous dyes since they are not biodegradable and mainly aromatic in structures. Removal of dyes is important since they affect life due to its carcinogenic and mutagenic effects (Wong et al., 1999; Panswad et al., 2000). Various strategies such as adsorption, chemical oxidation, chemical flocculation, froth flotation, ultrafiltration, reduction, chemical destruction, membrane filtration have been employed for the color removal (Ong et al., 2011;Valdes et al.,2010; Jian-Xiao et al.,2009; Wang et al.,2008; Zidane et al.,2008; Wong et al.,2008). Among these, adsorption process is considered to be highly efficient due to its sludge free clean operation, simplicity of design and complete removal of dyes. Crini et al. reviewed adsorbents such as activated carbon, clays, siliceous materials and agricultural wastes for the removal of dyes (Crini et al., 2006). Literature showed a number of reports on the adsorptive removal of cationic dyes using various polymeric hydrogels as adsorbents (Liu et al.,2010; Gholam Reza Mahdavinia et al., 2012; Zhu et al., 2010; Guven et al., 2009; Saraydin et al., 2001; Rosa et al.,2008; Zendehdel et al., 2010).

Thus, the development of adsorbent based on robust polymeric hydrogel and studies on its adsorption/diffusion characteristics and mechanism is receiving importance. AMD is a simple organic molecule prepared by the aminolysis of γ-butyrolactone at room temperature. It is endowed with two terminal hydroxyl groups

and diamide linkage connected through hexamethylene bridge. The liquid crystalline properties attributing from the rigidity of this rod shaped molecule is reported earlier (Sudha et al., 2000). The rigidity along with the presence of functional groups such as amide and hydroxyl moieties are expected to adsorb solute molecules through various van der Waals' interactions apart from acting as reinforcing agent. In the present study, we have developed robust polymeric hydrogel based on polyacrylic acid (PAA) physically cross-linked by multifunctional AMD through the simultaneous polymerization of AA and cross-linking with AMD at room temperature using APS as the initiator. Thus, the prepared PAG is endowed with hydrophilic groups such as hydroxyl, carboxyl and diamide groups which can enhance the adsorbate- adsorbent interaction through extensive hydrogen bonding and electrostatic and ionic interactions. The mechanism of swelling and diffusion has been studied. The adsorption efficiency of the hydrogels was monitored by measuring the decrease in absorption intensity by using UV-Visible spectroscopy and fitted the generated data in different isotherms and kinetic model equations. Effect of AMD, pH and temperature on the adsorption efficiency was studied and also experiments were performed with the mixture of dyes.

2.3. Results and discussion

2.3.1. Preparation and characterization of PAGs

PAG hydrogels were prepared by the simultaneous polymerization of AA and physical cross-linking with AMD. The interactions among PAA and AMD were studied by FT–IR spectroscopy. FT–IR spectra of PAA, PAG and AMD are shown in Figure 2.1.
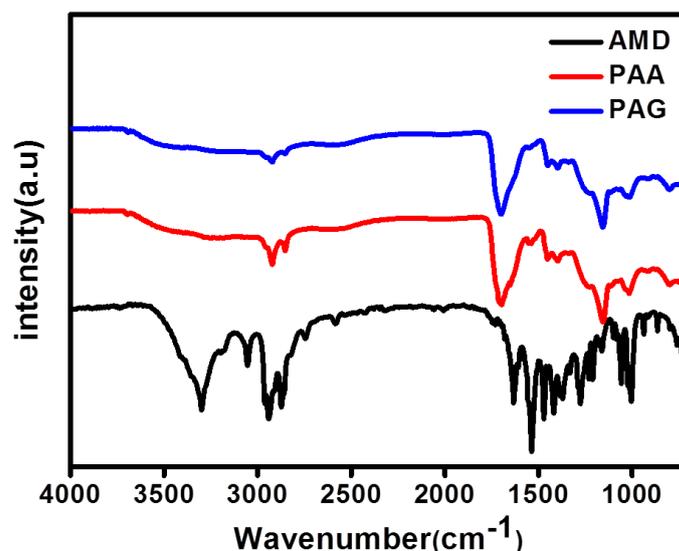
Figure 2.1. FT–IR spectra of AMD, PAA and PAG

FT–IR spectra of AMD exhibited the characteristic amide band of amide I and amide II at 1636 cm^{-1}, 1545 cm^{-1} respectively and the –OH stretching frequency at 3300 cm^{-1}. FT–IR spectra of PAA exhibited a broad band at 3600 cm^{-1} and 3100 cm^{-1} due to the –OH and –CH stretching. The band observed at 1714 cm^{-1} corresponds to – C=O stretching vibration of the carboxylic acid and band at 1399 cm^{-1} matches with – C–H stretching vibrations which are distinct to the varying microenvironments in PAA. The broad band of the hydroxyl group observed at 3600–3200 cm^{-1} in PAG revealed the formation of extensive hydrogen bonding interaction among PAA and AMD molecules. The –C=O band shifted to 1700 cm^{-1} in PAG also attributed to the formation of hydrogen bonding. The observed band at 2930 cm^{-1} and 1450 cm^{-1} in PAG is due to the –CH$_2$ and –N–H stretching vibrations. Thus, the observed shift in the positions of bands in PAG compared to the characteristic bands of the PAA revealed the formation of extensive hydrogen bonding among AA and AMD. Thus, the PAG hydrogel is endowed with numerous carboxyl and hydroxyl group which can interact with the cationic groups of the dyes and may enhance the adsorption process. The characteristic band of the hydroxyl group at 3600–3200 cm^{-1} observed in PAG

broadened during adsorption of dyes, revealing the formation of extensive hydrogen bonding between the PAG and the dye molecules. These observations were further confirmed the presence of ionic and hydrogen bonding interactions between the hydrogel and dye molecules. The scheme showing the formation of PAG and the adsorption of dyes is given in scheme 2.1.
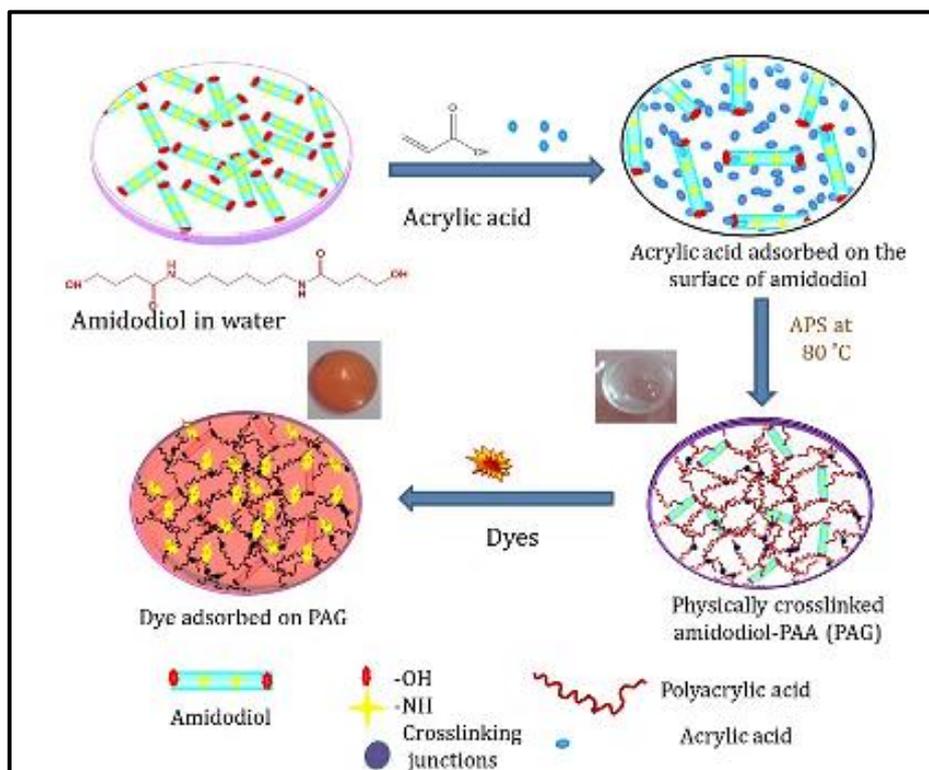
Scheme 2.1. Scheme showing the formation of PAG and adsorption of dyes

Further, the visco-elastic properties of the hydrogels were studied and the rheogram for the same is given in 2.2 (a). It was observed that at the low frequency region, the variation of storage modulus (G′) and loss modulus (G″) is independent of angular frequency. The applied frequency does not affect considerably the three-dimensional structure of the gels and is the signature for the gels. The storage modulus, loss modulus and complex viscosity of the PAG5 is observed as 3130 Pa, 792 Pa, and 427 Pa, respectively at a constant strain of 1%. The gap between the storage and loss modulus was measured as 2338 Pa suggesting solid like behaviour of

gels. The value of storage modulus augmented with increasing percentage of AMD in PAG and is shown in Figure 2.2 (b). It is confirmed that rod like AMD molecules possessing both hydroxyl and amide functional group and effectively physical cross-link with PAA and hence enhances the strength of the gel.
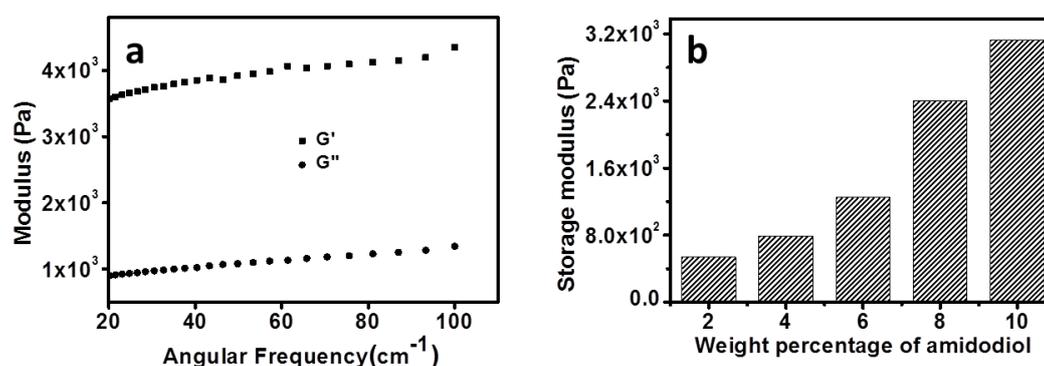
Figure 2.2. (a) Rheogram showing angular frequency versus storage modulus and loss modulus of PAG5 and (b) Variation of storage modulas with increasing concentration of AMD

Equilibrium swelling values of the hydrogel in distilled water and dye solutions were calculated and the graph showing the variation of percentage of swelling against time is shown in Figure 2.3 (a). From the graph, it is observed that swelling percentage is increased with time and reached a plateau after a particular time. The swelling behaviour observed could be associated with adsorption mechanism, which in turn, is determined by the diffusion process. When PAG hydrogel is brought in contact with water, water molecules diffused into the hydrogel and it swells. The equilibrium swelling percentage of hydrogel was measured as 76 % in water, and 120 % and 140 % in aqueous solutions of MB and R6G respectively. In dye solutions, PAG exhibited an enhancement in the equilibrium swelling index due to their interaction with the amino group present in the dye molecules which can form hydrogen bond interaction with the functional moieties present in the hydrogel. However, diffusion process depends upon the rate of solvent diffusion (R_{diff}) and rate of relaxation (R_{relax}) of molecular

chains in the polymer. This behaviour is classified as Fickian and non-Fickian

diffusion (Saraydin et al., 1995). Fickian diffusion is characterized by a solvent

diffusion rate (R_{diff}), which is slower than the polymer relaxation rate, ($R_{diff} < R_{relax}$). In

non Fickian diffusion, the solvent diffusion rate is faster than the polymer relaxation

process ($R_{diff} > R_{relax}$), whereas in anomalous diffusion, the solvent diffusion rate and the

polymer relaxation are about the same order of magnitude ($R_{diff} \sim R_{relax}$).
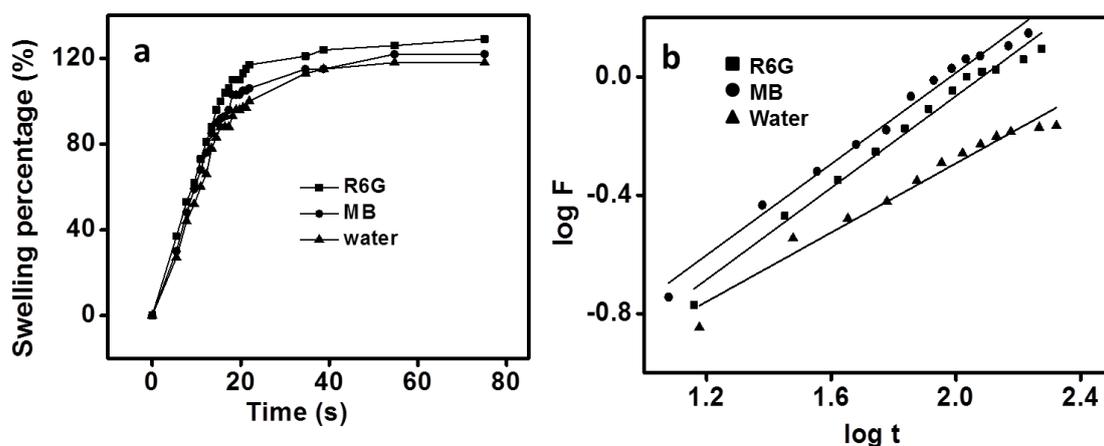
Figure 2.3. (a) Swelling percentage curves of PAG in dyes and distilled water with respect to time and
(b) Swelling kinetic curves of PAG5 in dyes and distilled water with respect to time

The following equation is used to determine the nature of diffusion rate

$$F = kt^n$$

Where, 'F' is the amount of solvent fraction in the gel at time t, 'k' is a constant related

to the structure of the network, and 'n' is called the diffusional exponent which is

indicative of the type of diffusion. The plot of log t versus log F of the PAG gels in

water and dye solutions are shown in Figure 2.3 (b). This equation is applied to the

initial stages of swelling and the plot of log F versus log t exhibited a straight line. The

exponent n and k values were calculated from the slope and intercept of the line,

respectively. It was observed that the value of n is 0.54, 0.72 and 0.74 for water, MB

solution and R6G solution respectively suggesting non-Fickian character (When n =

0.45 - 0.50 - Fickian diffusion, whereas $0.5 > n < 1$ indicates that diffusion is non-Fickian) (Mendizábal et al., 2010; Hu et al., 1996). When the polymer is in the rubbery state (elastic state), the polymer chains have a higher mobility that allows an easier penetration of the solvent and dye molecules.

2.3.2. Kinetics of adsorption studies

Dye adsorption and decolorization efficiency of PAG were studied by UV-Visible absorption spectroscopy. The chemical structure, molar mass, colour index number and absorption maxima for MB and R6G is given in Table 2.1.

Name	Chemical Formula	Molar mass	Colour index number	Λ_{max}
R6G		479.02	45160	525
MB		319.85	5201	665
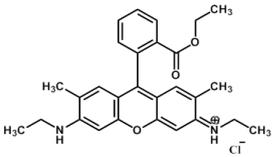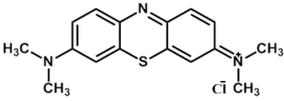
Table 2.1. Properties of dyes

Experiments were performed at 30 °C and at pH 7.5 using dye solutions for three days with PAG hydrogel and the decrease in the UV–Visible absorption intensity of the solution was measured at regular intervals of time. Representative spectra of dye solutions of R6G and MB at regular intervals of time are shown in Figure 2.4 (a) and (b), respectively. The photographs of the same before and after adsorption are shown in the inset. It has been observed that there is a decrease in the intensity of the

absorption band of MB at 665 nm and for R6G at 525 nm revealing the adsorption of

the dye by the PAG. It was also observed that as time lapses, gel swelled due to

diffusion of water and dye molecules. Since the hydrogel contains carboxyl groups

which can interact with the cationic group of dyes effectively and can also adsorb MB

and R6G dyes through electrostatic and hydrogen bonding interaction.
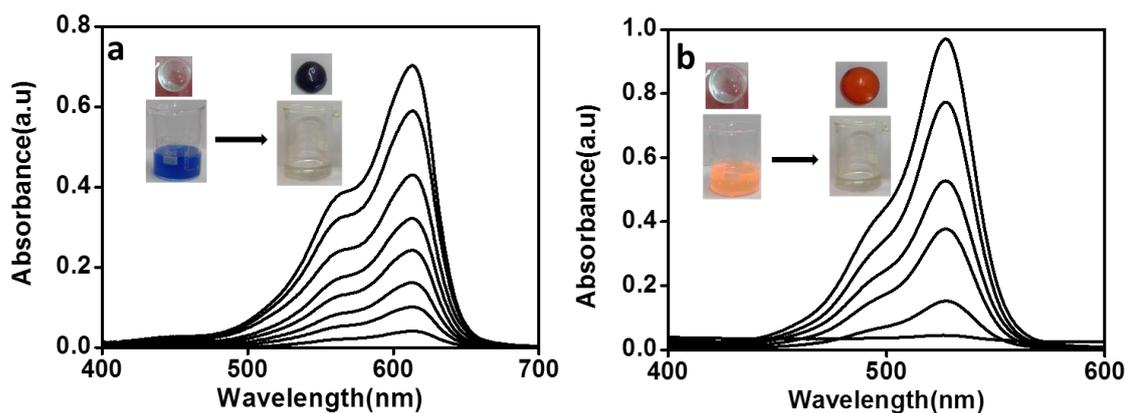
Figure 2.4. Time dependent absorption spectra of (a) MB and (b) R6G in the presence of PAG5

Kinetics of dye adsorption was studied with different model equations.

Adsorption of dyes R6G and MB (20 mg/L) onto PAG5 gel as a function of time was

studied by fitting these values in pseudo first order and pseudo second order equations.

The pseudo first order kinetics was studied using Lagergren equation (Perju et al.,

2010).

$$\log (q_e - q_t) = \log q_e - \frac{k_1\, t}{2.303}$$

Where q_e and q_t are the amounts of dyes adsorbed at equilibrium and at time t,

k_1 is the rate constant. Pseudo first-order model was checked by plotting $\log (q_e - q_t)$

versus time and is given in Figure 2.5. The rate constant and q_e were calculated from

the slope and intercept and were listed in Table 2.2. The values calculated from the

pseudo first order model differs considerably from the experimental values suggesting

that the pseudo first order model fails to describe the adsorption of dyes.
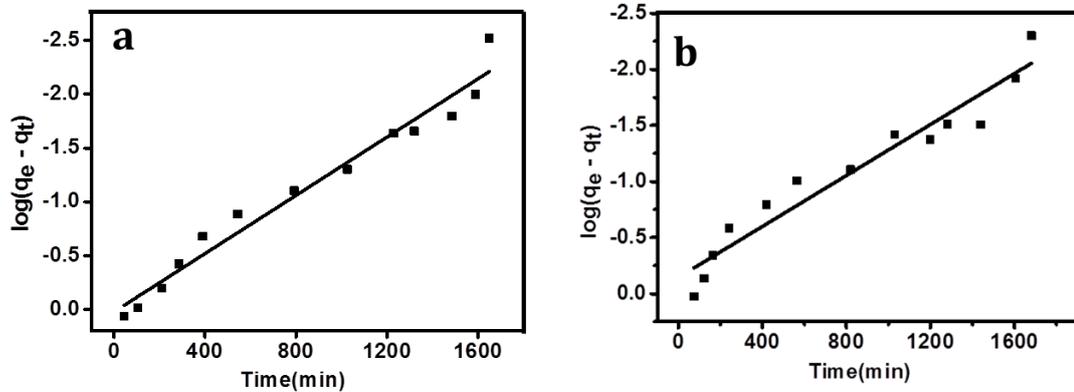
Figure 2.5. Pseudo first order model for dye adsorption of PAG5 (a) R6G and (b) MB

Then tested for the pseudo second order equation (Ho et al., 1999),

$$\frac{t}{q_t} = \frac{t}{k_2 q_e^2} + \frac{1}{q_e}$$

Where k_2 is the pseudo second order rate constant.
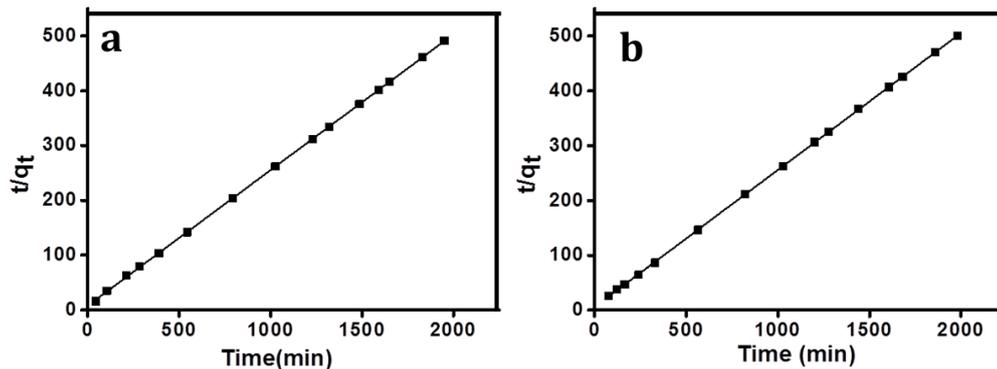
Figure 2.6. Pseudo second order model for dye adsorption of PAG5 (a) R6G and (b) MB

The pseudo second order model for R6G and MB were checked by plotting t/q_t

versus time (t) and are given in Figure 2.6 (a) and (b). The plot is obtained as a straight

line and the values of k_2 and q_e calculated from the slope and intercept and is depicted

in Table 2.2. Here, the calculated value of q_e matches well with the experimental

values. Further, the high value of regression coefficient obtained for pseudo second

order model compared with the pseudo first order also suggested the adsorption of

dyes onto PAG gel followed a pseudo second order kinetics.

Dye	q_e(mg/g) exptl	Pseudo first order parameters			Pseudo second order parameters		
		k_1 (min^{-1})	q_e(mg/g) calculated	R^2	k_2 (min^{-1})	q_e(mg/g) calculated	R^2
R6G	3.97	1.69×10^{-6}	1.05	0.983	7.78×10^{-3}	4.05	0.999
MB	3.958	1.38×10^{-6}	0.65	0.955	1.05×10^{-5}	4	0.999

Table 2.2. Dye adsorption Parameters of PAG for pseudo first order and pseudo second order model

Effect of amount of AMD in PAG on the adsorption efficiency was studied.

$$K_d = (C_0 - C)/C$$

Where, K_d is the empirical partition coefficient which relates the total

concentration of the dissolved species to the total concentration of adsorbed species

(Li et al., 2008). As the AMD content increased, PAG5 exhibited decolourization

efficiency of 99 % for R6G and 98% for MB. The decolourization efficiency and K_d

values for PAA and PAGs are listed in Table 2.3. The K_d values enhanced with

increasing AMD content indicating it as a better adsorbent. It has been observed that

adsorption efficiency initially enhanced with increasing amount of AMD due to the

presence of large number of free hydroxyl and amide groups available for interaction

with dye molecules. Adsorption efficiency showed decrease in value when AMD content increased to 10 wt %, due to the formation of physically cross-linked networks between the functional groups. Pure PAA showed decolourization efficiency of 83% for R6G and 81% for MB.

Hydrogel	Decolourization efficiency (%) of		k_d of	
	R6G	MB	R6G	MB
PAA	83.33	80.9	6	6
PAG1	85.71	84.05	6.63	6.6
PAG2	89.2	88.09	9.5	8.33
PAG3	92.8	91.6	11	10
PAG4	97	94.04	13	12.7
PAG5	99	97.62	22.3	20

Table 2.3. Decolourization efficiency and k_d of PAGs with varying AMD content

2.3.3. Mechanism of adsorption

Mechanism of adsorption of dye in hydrogels was studied by Langmuir and Freundlich adsorption isotherms and Gile's adsorption studies. Langmuir isotherm assumes monolayer adsorption while in Freundlich model, the mechanism of adsorption is multilayer sorption. Langmuir model can be represented by the equation (Al-Qodah et al., 2000).

$$\frac{C_e}{q_e} = \frac{C_e}{q_m} + \frac{1}{q_m b}$$

Where C_e, is the equilibrium dye concentration in the solution (mg/L), b is the Langmuir adsorption constant (L/mg), and q_m is the theoretical maximum adsorption

capacity (mg/g). Langmuir plot of C_e vs. (C_e/q_e) exhibited a correlation value of 0.88 for R6G and 0.75 for MB.

The Freundlich adsorption isotherm is mathematically represented by the equation

$$\log\left(\frac{x}{m}\right) = logK + \frac{1}{n}logC$$

$$lnq_e = K_f + \frac{1}{n}lnc_e$$

Where k_f is the equilibrium adsorption coefficient and n is the empirical constant.
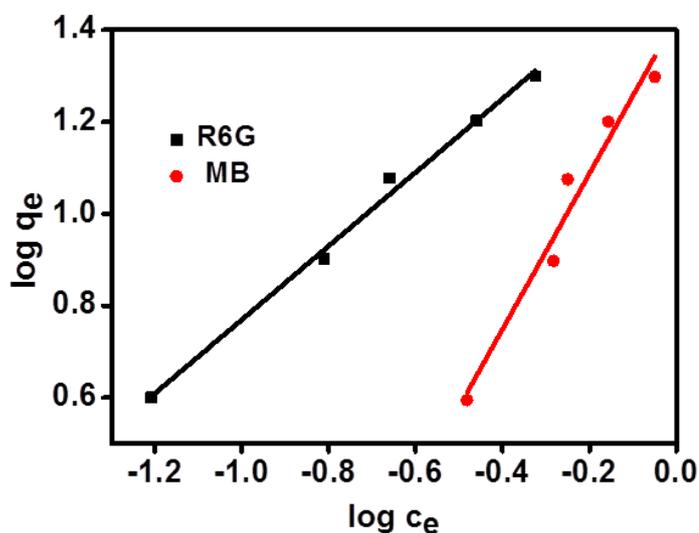
Figure 2.7. Freundlich adsorption isotherms of R6G and MB

The linear plot of the Freundlich isotherm for R6G and MB is shown in Figure 2.7. The k_f and n values can be calculated from intercept and slope. The values of n for MB and R6G are 1.7 and 1.1, respectively and k_f values are 1.42 and 1.6 for MB and R6G. The value of k_f for R6G is higher than MB which showed the PAG hydrogel has more affinity towards R6G than MB. The high value of the correlation coefficient obtained in the Freundlich isotherm for MB (0.98) and R6G (0.99) compared with the correlation coefficient of Langmuir isotherm (0.88 for R6G and 0.75 for MB)

suggested that Freundlich adsorption (multilayer adsorption) isotherm is the best fit for the adsorption of the dyes (Akpomie et al.,2012;Gholam Reza Mahdavinia et al.,2012).

The amount of dye adsorption and the adsorbate-adsorbent interaction of PAG was studied using Gile's classification system. The amount of MB and R6G adsorbed per dry mass of the hydrogel (q_e, mg of dye/g of hydrogel) as a function of the equilibrium concentration of dyes (c_e, mg/L) is shown in Figure 2.8.
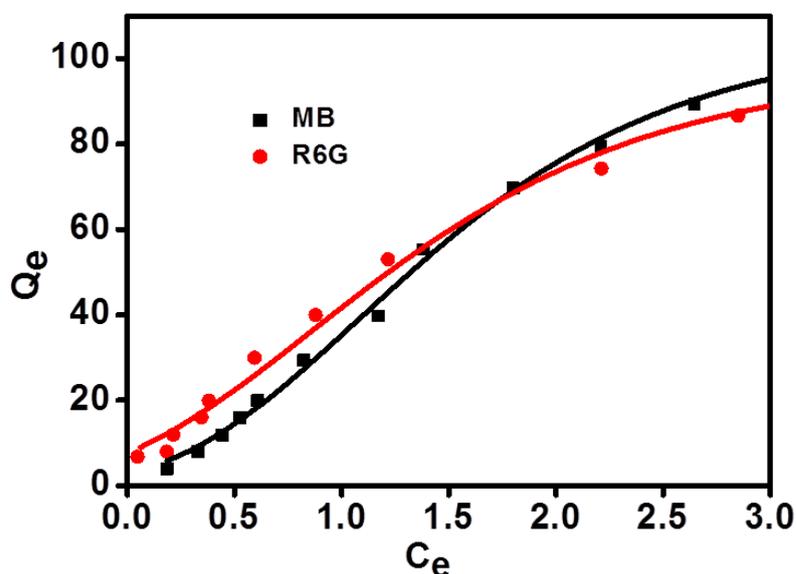
Figure 2.8. Gile's curve for the individual dye solutions of MB and R6G showing S type adsorption (initial dye concentration (20-400 mg/L, adsorption time: 3 days, pH: 7)

The type S- isotherm observed may be originating relatively weak adsorbate-adsorbent interaction compared to adsorbate-adsorbate. The weak adsorbate and adsorbent force will cause the slow uptake of dye components initially. However, once the molecule is adsorbed, the adsorbate- adsorbate interaction which may promote the adsorption of more dye molecules through a cooperative process where the isotherm becomes convex to the concentration axis. These studies show that the adsorption capacity of the gel increases with increase in the concentration of dyes. Gile's curve

showed the high adsorption capacity of PAG hydrogels and revealed that 1g of PAG can adsorb maximum of 100 mg of dye.

Experiments were also performed to study the adsorption capacity of the PAG hydrogels in the mixture of dyes. Representative UV–Visible spectra and the Gile's adsorption curve are shown in Figure 2.9 (a) and (b). Complete decolorization was observed with the mixture of dyes.
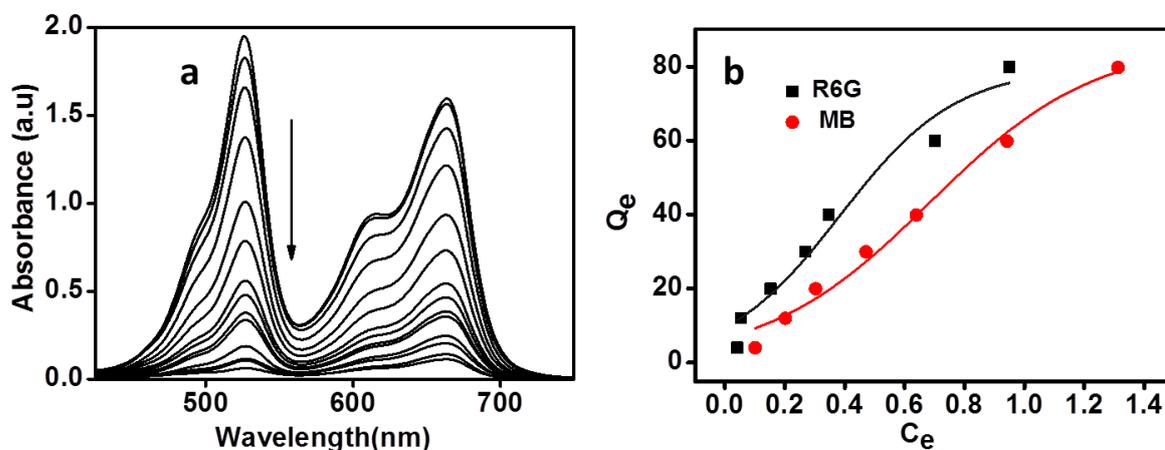
Figure 2.9. Time dependent absorption spectra of mixture of R6G and MB in presence of PAG5 and (b) Gile's adsorption curve for MB and R6G in presence of PAG5

2.3.4. Effect of pH and temperature

The pH of the solution can change the surface charge of the PAG which may suppress or promote the ionization of the adsorbent and dye molecule. Effect of pH on the dye removal efficiency is shown in Figure 2.10 (a). It exhibited an increase in the removal efficiency with increase in the pH of the dye solution. At lower pH value, –COOH groups are in the non-ionized state. On increasing the pH value, –COOH group ionizes, and it generates an electrostatic repulsion among the adjacent ionized groups. This causes an expansion of the polymer chain within the hydrogel network (Paulino et al., 2006). Hence the decolorization efficiency of the PAG hydrogel

increases. Most of the waste water, pH is in the alkaline region and hence PAG hydrogel can be applied effectively in waste water treatment. Figure 2.10 (b) shows the dye removal efficiency of the PAG hydrogel with an increase in the temperature. The rate of diffusion increases with increase in temperature and enhances the dye adsorption.
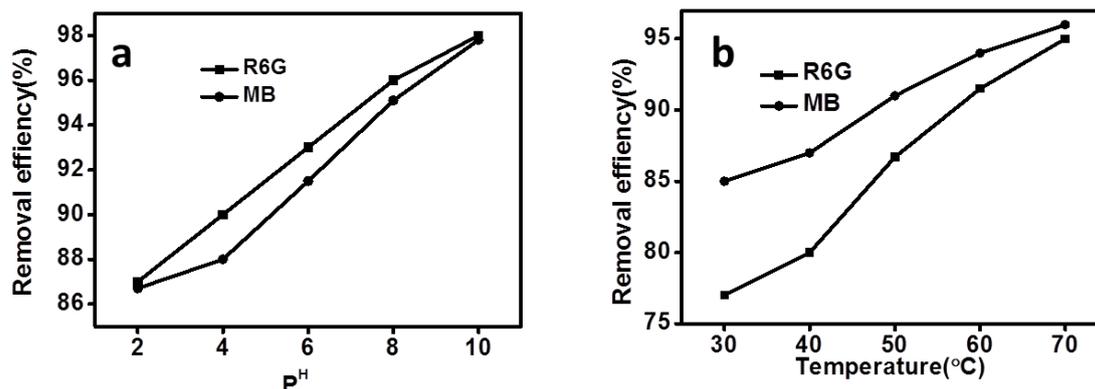
Figure 2.10. (a) Effect of pH and (b) Effect of temperature on the dye adsorption by PAG5

Morphology of the PAG5 was observed as cross-linked fibrillar networks in the xerogel state as shown in Figure 2.11 (a). During swelling, they imbibe large amount of water and the SEM image of swelled network is shown in 2.11 (b). A collapsed morphology of swollen gel observed after the entrapment of dye molecules as shown in 2.11 (c) and 2.11 (d). This may be due to the hydrogen bonding interaction between the amine and carboxyl group of the hydrogel and the amine group and oxygen atom of the dye molecules. Thus, it can be inferred from the morphological analysis that PAG hydrogels are porous functional three-dimensional fibrillar network structures which allow the diffusion of solutes and solvent into the interior network.
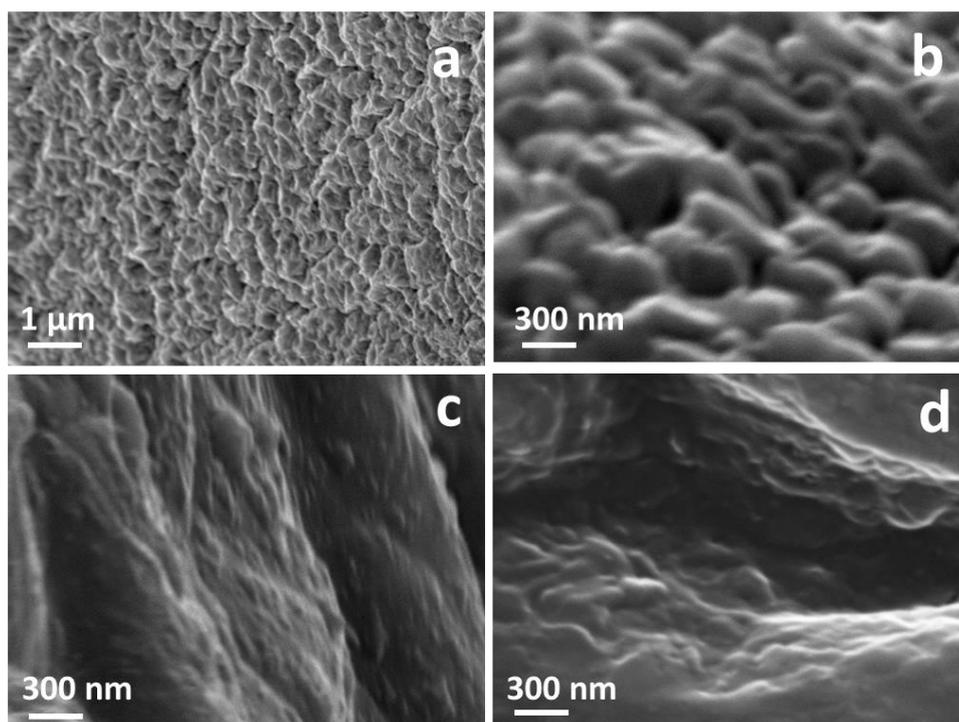
Figure 2.11. SEM images of (a) PAG5 xerogel (b) swelled PAG5 gel and (c and d) PAG5 entrapped with R6G and MB

2.3.5. Real sample analysis

The suitability of the PAG hydrogel for the dye adsorption in real sample was checked by using the mixture of waste water collected from various industries such as food, paper and textiles. 0.5g of PAG hydrogel was dipped in 20 mL of the waste water and stirred for three days. The solution became almost colorless indicating the capability of hydrogel to adsorb dyes and other impurities. Results suggested that PAG hydrogel is an excellent candidate for the color removal of waste water and the various kinetic parameters and adsorption mechanism studied can be exploited for the pilot scale waste water purification process. Moreover, desorption of dye was not observed even after few months. Hence this can be considered as an efficient polymeric filtration membrane for the removal of dyes from aqueous solutions. These studies can be utilized for the removal of other aromatic toxic material present in our environment generated from various industries.

2.4. Conclusion

PAGs were successfully prepared by the insitu polymerization of AA and physical cross – linking with AMD. Rheological studies showed an enhancement in the mechanical strength of the gel with increase in the amount of amidodiol. The dye adsorption was studied with R6G and MB and the adsorption was observed as pseudo second order. Adsorption was investigated with Langmuir and Freundlich isotherm and suggested multilayer adsorption. The adsorbate-adsorbent interaction studied with Gile's classification system showed an S type adsorption and better adsorption efficiency of PAG hydrogels. Morphological studies revealed the porous network of the PAG hydrogel through which dye molecules could effectively diffuse to the fibrillar network of the hydrogel. The adsorption efficiency of the PAG showed an enhancement with increase in the AMD content, pH and temperature and is stable at high pH and temperature.

2.5. Experimental

2.5.1. Materials

Hexamethylenediamine, rhodamine-6G (Sigma Aldrich), γ-butyrolactone [Fluka], isopropanol, APS, acrylic acid (E-Merk, India) and MB (Nice Stains) were used without any further purification.

2.5.2. Preparation of AMD

AMD was prepared by the aminolysis of γ-butyrolactone using 1, 6 hexamethylenediamine as per the earlier reported procedure (Sudha et al., 2000). Typical procedure is as follows: A solution of 0.2 mol (17.2 g) of γ-butyrolactone in 10 mL of isopropanol was taken in a conical flask and cooled in ice bath at 5 °C. A

solution of 11.62 g (0.1mol) of hexamethylenediamine in isopropanol was added drop wise with stirring for two hours (800 rpm) and kept overnight. Formation of the product was checked using TLC in a 7:2:1 benzene, methanol, triethylamine mixture. White crystalline solid formed was filtered and washed several times with isopropanol, then dried in vacuum and further recrystallized from 150 mL of methanol and acetone mixture (Yield : 95%, M.P: 118.5°C).
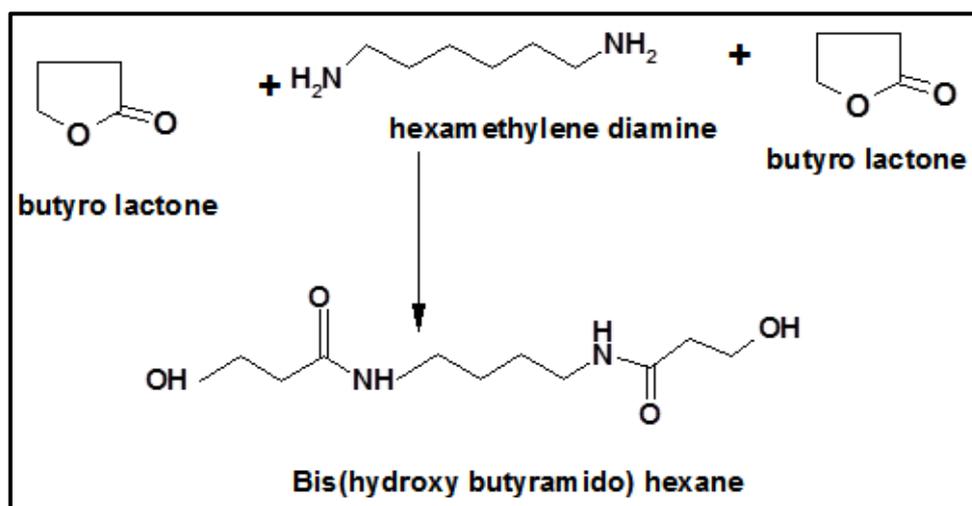
Figure 2.12. Scheme for the synthesis of AMD

2.5.3. Preparation of PAGs

AA (1mL) and 10 % AMD (1mL, in water) were mixed. Two drops of 10 % APS was added to the above mixture. The contents were shaken well and kept at 80 °C for about one hour. The gel formed was washed several times with distilled water to remove residual monomers and ions. Experiments were repeated with different compositions of AMD and the details of preparation of PAG hydrogel are given Table 2.4.

Hydrogel	AMD (moles)	Acrylic acid (moles)	Gelation time (min)	Colour and appearance
PAG1	3.4×10^{-5}	0.0145	50	Transparent and colourless
PAG2	1.04×10^{-4}	0.0145	45	Transparent and colourless
PAG3	1.73×10^{-4}	0.0145	40	Transparent and colourless
PAG4	2.42×10^{-4}	0.0145	35	Transparent and colourless
PAG5	3.4×10^{-4}	0.0145	30	Transparent and colourless

Table 2.4. Experimental details for the preparation of PAGs

2.5.4. Swelling and diffusion studies

Uniform size of dried PAG (0.1g) was immersed in 20 mL of aqueous dye solutions of R6G and MB in a beaker at room temperature. The uptake of solution with respect to time was obtained periodically by weighing the hydrogel. The water present on the surface of the swollen hydrogel was removed by softly wiping the sample with filter paper. The swelling percentage of PAG hydrogel was calculated from the following equation

$$S(\%) = \frac{(m_t - m_0)}{m_0} \ X \ 100$$

Here, m_t is the mass of swollen gel at time t and m_0 is the initial mass of the swollen gel.

2.5.5. Adsorption studies

Aqueous solutions of cationic dyes R6G and MB were prepared in the ranges of 20 to 400 mg/L. The uniform size of dried PAG hydrogel (0.1g) was immersed in 20 mL of each dye solution and stirred for three days at room temperature. The pH of the solution is ~7.5 and the adsorption experiment is performed at room temperature (30 °C). Concentration of the dye present in the filtrate was periodically calculated by

measuring absorption intensity from the UV–Visible spectra at λ_{max} = 665 nm and 525 nm for MB and R6G, respectively. Adsorption isotherm was studied by calculating the amount of dye adsorbed per gram of the hydrogel using the equation

$$q_e = \frac{(C_0 - C_{eq})V}{m}$$

Where C_0 is the initial concentration of dyes, C_{eq} is the equilibrium concentration and V is the volume of solution (L) and m is the mass of the dry hydrogel (g).

Decolorization efficiency of hydrogel was calculated using the equation

Decolorization efficiency $= \frac{C_0 - C}{C_0} \times 100$

Where, C_0 is the initial concentration of dye and C is the concentration of dye at time t

2.5.6. Characterization techniques

Optical properties were studied in the range 300–800 nm using UV–Visible spectrophotometer [Shimadzu model 2100]. For SEM measurements, samples were subjected for thin gold and platinum coating using a JEOL JFC–1200 fine coater. The probing side was inserted into JEOL JSM–5600 LV scanning electron microscope. Rheological properties were measured using Anton Paar Rheometer-MCR-150. Experiments were performed with parallel plate sensor under oscillatory mode in the linear viscoelastic region.FT–IR spectroscopic measurements were made with a fully computerized Nicolet Impact 400D FT–IR spectrophotometer. Materials were mixed thoroughly with potassium bromide and compressed into pellets before recording. All spectra were corrected for the presence of moisture and carbon dioxide in the optical path.

CHAPTER 3

SILVER NANOPARTICLE ENTRAPPED HYDROGEL AS NANOCATALYST FOR THE REDUCTION OF DYES AND NITROPHENOLS

3.1. Abstract

Robust fibrillar networks of hydrogels entrapped with silver nanoparticles (SPAG) were prepared by in-situ polymerization of AA and reduction of silver nitrate in presence of AMD using APS as the radical initiator. SPAGs were characterized by UV-Visible spectroscopy, SEM, TEM, XRD and rheology. Further, catalytic efficiency of SPAGs were demonstrated for the reduction of dyes and nitrophenols.

3.2. Introduction

In recent years, there has been considerable interest in polymer dispersed metal nanocomposites, particularly polymeric hydrogel metal nanocomposites which respond to various stimuli in the bulk phase. They were used in responsive artificial muscles, switches, memory devices, catalysis, tissue engineering, etc. (Wang et al., 2004; Schexnailder et al.,2009; Yoshida et al.,1995; Dong et al.,1991; Fuhrer et al.,2009). Hydrogels are three-dimensional polymeric fibrillar networks which can imbibe a large amount of water with stimuli-responsive swelling and deswelling properties. Various non-covalent interactions such as hydrogen bonding, π- π stacking, and van der Waals' interactions are involved during the organization of these molecules into 3D fibrillar architectures (Zhao et al., 2005; Ramachandran et al., 2005; Xing et al., 2011).

Metal nanoparticles exhibit unique opto-electronic properties different from their bulk counter parts. They find promising applications in the areas such as nanoelectronic devices, catalysis, sensors, biochemical tagging reagents, optical switches and so forth (Li et al., 2009; Wu et al., 2004; Adams et al., 2004; Jin et al., 2000). Among the metal nanoparticles, silver is easily reducible and has high excitation efficiency, SPRE in the visible region and unique electrical, optical and

catalytic properties. They are potential candidates in catalysis because of their high surface area and size-shape dependent catalytic properties. Silver catalyzed reactions such as Diels-Alder reaction, epoxidation, hydrogenation of aldehydes, hydroformylation, carbonylation, reduction of dyes and nitrophenol have been reported earlier (Xu et al., 2006; Jana et al., 2006; Jiang et al., 2005; Zheng et al., 2012; Lu et al., 2007). Metal nanoparticles tend to aggregate during the catalytic process due to their van der Waals' forces of attraction and high surface area. A wide range of capping agents such as block copolymers, polysaccharides, latex particles, hydrogels and surfactants have been used to enhance the stability and dispersion of metal nanoparticles (Himadri et al., 2002; Yu et al.,2004; Berti et al.,2005). Among these stabilizers, polymeric hydrogels with three-dimensional fibrillar networks are receiving importance. The hydrophilic ionic groups present in the hydrogel network can potentially serve as nanoreactors for the synthesis of metal nanoparticles and provide cage effect for its stabilization. Moreover, the fibrillar network can speed up the diffusion of metal ions through the hydrogel networks. Apart from this, the size and shape of metal nanoparticles can be tuned by controlling the amount of monomer, cross-linker and metal ions (Murphy et al., 2002; Wiley et al., 2004; Murali Mohan et al., 2010).

Polymeric hydrogel metal nanocomposites are considered as viable catalysts because they prevent aggregation of nanoparticles, and the loosely bound dynamic structure may give easy access to the nanoparticles. One of the disadvantages of such systems is its poor mechanical stability. The mechanical and chemical properties of the hydrogel can be improved by incorporating inorganic clays, cellulose, carbon nanotubes etc. (Zhou et al., 2011; Xia et al., 2010). Chemical reduction of metal salts with reducing agents such as sodium borohydride, ascorbic acid, lithium aluminium

hydride, sodium citrate etc. is the commonly employed method for the synthesis of metal nanoparticles (Mushran et al., 1974; Li et al., 2014; Gupta et al., 2014). The catalytic performance and stability of metal nanoparticles can enhanced by incorporating functional groups such as –NH_2, –CONH, –SiH (Ren et al., 2004; Li et al., 2004; Guari et al., 2003; White et al., 2009). In this context, development of homogeneously dispersed metal nanoparticles supported in the polymeric hydrogel with enhanced functionalities and their application as a catalyst is receiving a major challenge.

Amino phenols and their derivatives are receiving commercial importance in a wide range of areas such as photographic, pharmaceutical and dye industries. The most facile synthesis of amino phenols is the reduction of the respective nitrophenols. The detailed study of the mechanism for catalytic reduction is important to alter the catalyst for the better output. Saha et al. studied the kinetics of the reduction of nitrophenols by varying the concentration of metal nanoparticles, nitrophenols and sodium borohydride suggested that the reduction is taking place at the surface of the metal nanoparticles (Saha et al., 2009). Zhang et al. provided a mechanistic interpretation for the reduction that both the reactants (nitrophenol and borohydride) will adsorb on the surface of the catalyst and the reaction can be modelled through Langmuir-Hinshelwood mechanism (Zhang et al., 2009). Khalavka et al. reported that only hydrogen species get adsorbed on the surface and the reaction proceeds through Eley - Rideal mechanism (Khalavka et al., 2009).

In this chapter, we are reporting a novel strategy for the preparation of silver nanoparticles entrapped robust polymeric hydrogel by in situ reduction of silver nitrate and simultaneous polymerization of acrylic acid using AMD as a physical cross-

linking cum reducing agent. AMD is expected to exhibit extensive hydrogen bonding to form intermolecular physical cross-links with PAA and act as a reducing agent for the reduction of silver ions. SPAGs were characterized by SEM, TEM, XRD, rheology and UV–Visible spectroscopy. Further, its application is illustrated for the catalytic reduction of organic dyes and nitrophenols using sodium borohydride as the reducing agent. The kinetics and mechanisms of the reduction reactions were studied.

3.3. Results and Discussion

3.3.1. Preparation and characterization of SPAGs

SPAGs were prepared by in-situ reduction of silver ions and polymerization of AA at room temperature using APS as the radical initiator and AMD as reducing agent cum physical cross-linking agent. Thus, AA is polymerized to PAA and physically crosslink with AMD in the presence of radical initiator APS, and simultaneously silver ions present in the system are reduced to silver atoms (Lu et al., 2007; Zhang et al., 2003). AMD exhibited extensive hydrogen bonding with AA and increased the cross-linking density and functionality of the hydrogel attributed to the presence of two hydroxyl and two amide groups. AMD can also acting as reducing agent for the reduction of metal ions and the amide group may interact with metal nanoparticle and imparting stability for the metal nanoparticles in the hydrogel nanocomposite.
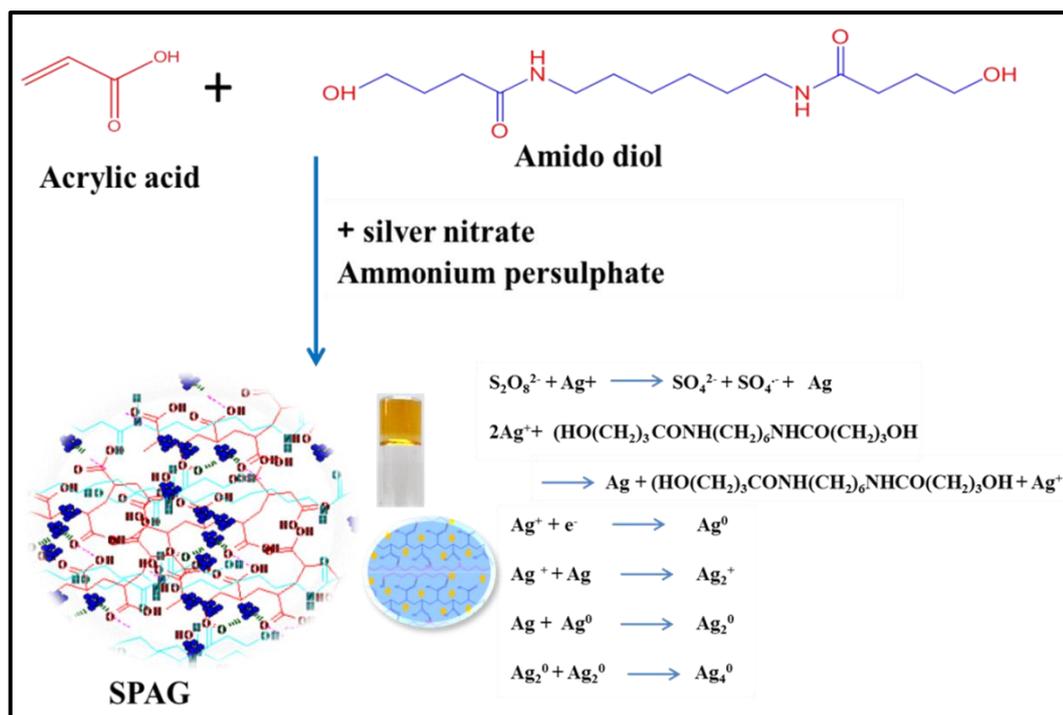
Scheme 3.1. Scheme for the synthesis of SPAG and the mechanism for the formation of silver nanoparticles

The scheme for the formation of SPAG is given in Scheme 3.1. The formation of SPAG was observed as a transformation from colourless low viscous liquid to light yellow transparent gel. The functional groups such as hydroxyl and two amide groups present in AMD can establish extensive hydrogen bonding interaction with PAA to form fibrillar networks. Polymerization reactions were progressed much faster rate in the presence of silver ions than in its absence due to the catalytic activity of silver ions. The dispersed Ag^+ accelerates the generation of the radical anion from persulphate ion and initiates the polymerization of AA at room temperature (House et al., 1962). Simultaneously, the homodispersed Ag^+ ions were reduced by reductive particles, AMD or solvated electrons present in the system. The primary products are silver atoms (Ag^0) which may combine in various fashions to produce progressively larger silver clusters of silver atoms and silver nanoparticles as shown in the inset of Scheme

3.1 (Marignier et al., 1985; Henglein et al., 1992). SPAGs prepared by varying the concentration of silver nitrate at room temperature.
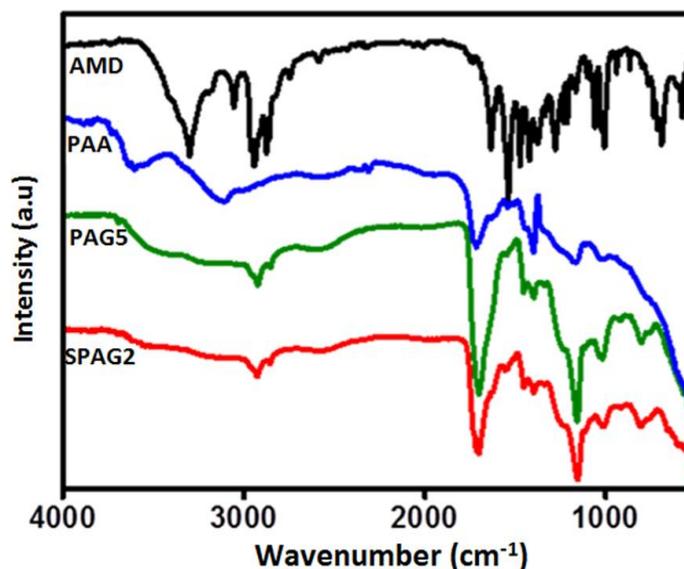
Figure 3.1. FT–IR spectra of AMD, PAA, PAG5 and SPAG2

The various interactions present in SPAG were studied by FT–IR spectroscopy. FTIR spectra of AMD, PAA, PAG5 and SPAG2 are shown in Figure 3.1. The broad band due to the hydroxyl and –NH group observed at 3500 and 3200 cm^{-1} in PAG5 and SPAG2 revealing the formation of extensive hydrogen bonding interaction among –OH and –NH groups present in the hydrogels. The –C=O band shifted to 1700 cm^{-1} in PAG and 1698 cm^{-1} in SPAG attributing from the hydrogen bond formation between PAA and AMD and the weak coordination bond between the oxygen of –C=O and silver. The band observed at 2930 cm^{-1} in both PAG5 and SPAG2 is attributed to the stretching vibrations of –CH$_2$ group present in the AMD moiety. The bands at 1635 cm^{-1} and 1450 cm^{-1} correspond to the –NH bending vibrations of the amide group. Thus, the observed shift in the positions of bands in PAG5 and SPAG2 in comparison with PAA revealed the formation of extensive hydrogen bonding among AA and AMD and also with the silver nanoparticles in the

fibrillar networks of SPAGs. Further, formation of silver nanoparticles entrapped fibrillar network was confirmed by UV–Visible spectroscopy in combination with microscopic observations. Thus, the combination of AMD with PAA form physically cross-linked network through extensive intermolecular hydrogen bonding and the charged carboxyl and hydroxyl groups present in the network is expected to stabilize the silver nanoparticles via cage effect.

3.3.2. Rheological studies

Mechanical stability of hydrogels was studied by measuring viscoelastic properties by rheometry. Rheological properties measured under frequency sweep in the linear viscoelastic region using parallel plate sensor. Storage modulus/loss modulus plotted against angular frequency and the profile of PAG5, SPAG2, and SPAG4 are shown in Figure 3.2 (a). It was observed that at lower frequency region, the variation of G' and G′′ is independent of angular frequency where the applied frequency does not affect considerably the three-dimensional structure of the gels. The gap between storage and loss modulus is in the order PAG5 < SPAG2 < SPAG4. This showed that as the amount of silver ion increases, the elastic modulus also enhanced due to the high extent of cross-linking density present in SPAG. The gap between the storage and loss modulus for SPAG4, SPAG2 and PAG5 are observed as 3470 Pa, 2580 Pa and 2338 Pa, respectively revealing more solid-like nature for SPAG gel. Complex viscosity variation with angular frequency is shown in Figure 3.2 (b). Generally, all the rheograms showed a power law thinning region at lower frequency region. As moving from PAG5 to SPAG4, complex viscosity showed a hike in the values. SPAGs showed an increased storage modulus and complex viscosity values on comparison with PAG are due to the cross-linking effect of silver ions present in the

SPAGs. The initial decrease in viscosity with an increase in frequency attributed to the change in the periodicity of the chains present in gels with increasing frequency. The strength of the SPAGs was observed to be higher (6×10^3 Pa) compared to PAG5 (3×10^3 Pa) due to the higher extent of cross-linking in the presence of silver ions.
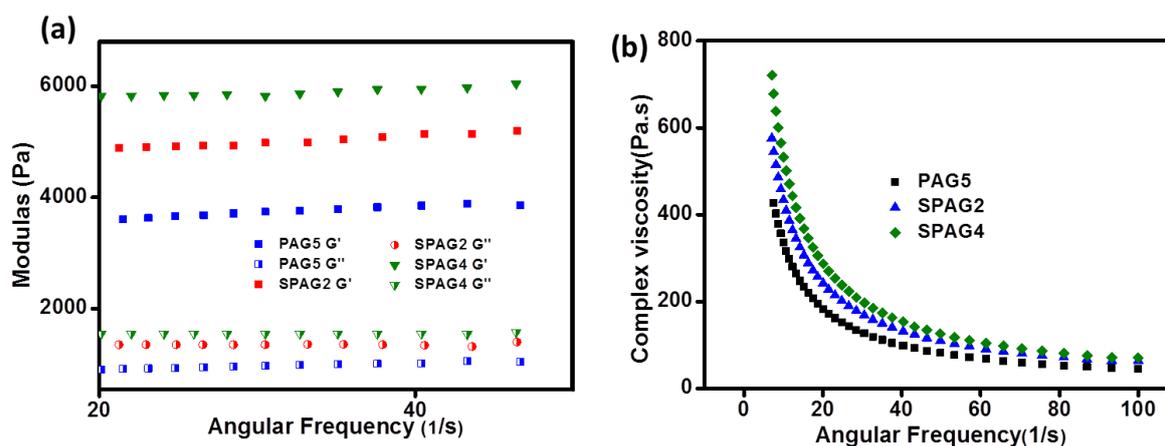
Figure 3.2. (a) Angular frequency versus storage storage modulus (G') of PAG5 (■), SPAG2 (●), and SPAG4 (▼) and loss modulus (G'') of PAG5 (▫) SPAG2 (◑) and SPAG4 (▽) and (b) Angular frequency versus complex viscosity profile (η) of PAG5, SPAG2, and SPAG4

3.3.3. Optical and morphological analysis

Optical properties of silver nanoparticles were studied by recording UV–Visible spectra. Spectra for SPAGs prepared with varying concentration of silver nitrate are given in Figure 3.3. It has been observed that the nature and shape of the band is changed with the amount of silver ion used in the preparation. This can be qualitatively related to the shape and size distribution of the formed silver nanoparticles. UV-Visible spectra of SPAG1 and SPAG2 exhibited a sharp well defined maximum at 315 nm. SEM images of SPAG1 and SPAG2 showed narrow distribution of distorted spherical and cuboidal nanoparticles as shown in Figure 3.4 (a) and (b). SEM picture showed a strong contrast between silver nanoparticles and the polymeric matrix, reflecting the diverse atomic composition of film components.
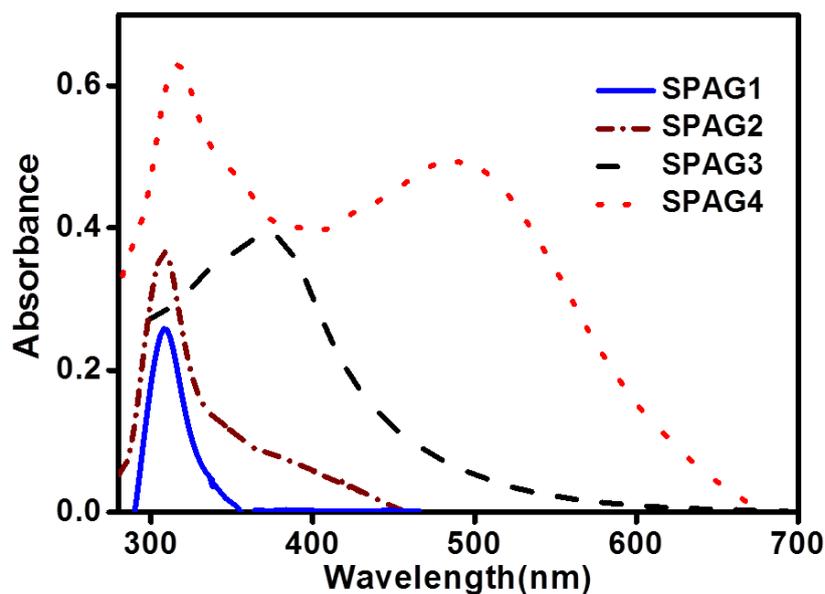
Figure 3.3. Solid state UV–Visible spectra of SPAGs with varying concentration of silver ions

The absorption maxima of SPAG3 showed a broad band at ~373 nm. SEM image of the same showed a mixture of cubes and needles (Figure 3.4 (c)). SPRE of SPAG4 is observed as a bimodal spectrum with two maxima appeared at 316 nm and 488 nm. It was reported that frequency and intensity of SPRE depend on the distribution of polarization charge across the nanoparticles, which is determined by the size and shape of the particles (Itoigawa et al., 1997; Kelly et al., 2002). The SEM image of SPAG4 showed bar/rod like morphology and the same is shown in Figure 3.4 (d). Thus, the two UV–Visible maxima observed are resulting from the polarization of these nanobars along their long axis (longitudinal plasmon resonance) and width (transverse plasmon resonance). Both SPRE bands are quite broad due to the formation of silver nano particles in different length and width scales.
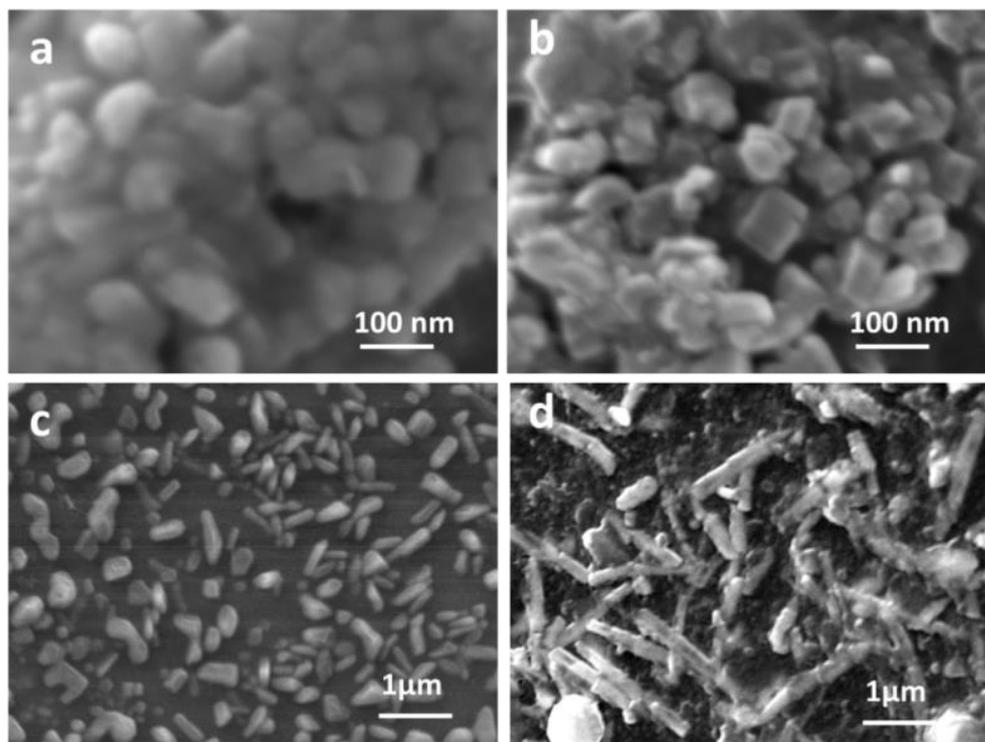
Figure 3.4. SEM images of SPAGs showing the formation of nanospheres and nanocubes of silver particles in (a) SPAG1 (b) SPAG2 (c) mixture of nanocubes and nanoneedles of silver particles in SPAG3 and (d) nanobars and nanorods of silver particles in SPAG4

TEM images of SPAGs are shown in Figure 3.5. SPAG1 and SPAG2 exhibited distorted cuboidal and spherical geometry of silver nanoparticles and are shown in Figure 3.5 (a) and (b). The TEM images of SPAG3 (nanocapsules) and SPAG4 (nanobars and nanorods) are shown in Figure 3.5 (c) and (d) respectively. Thus it could be inferred from the morphological studies that on increasing the amount of silver nitrate, an obvious evolution in the shape and size of the silver nanoparticles from spheres to cubes to bars were observed. Typical EDS spectrum confirming the presence of silver nanoparticles in the SPAG2 system is shown in Figure 3.5 (e).
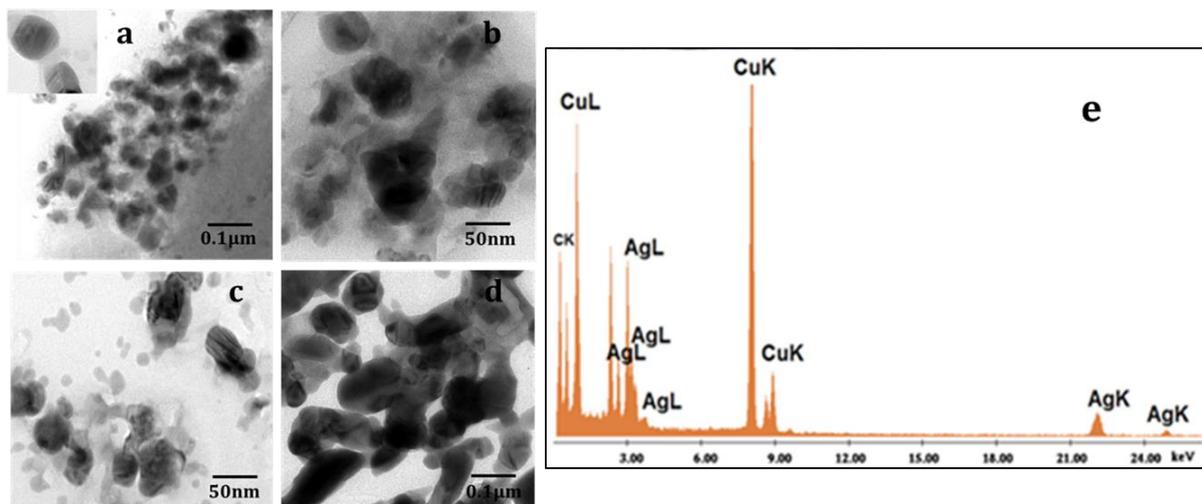
Figure 3.5. TEM images of (a) SPAG1 (b) SPAG2 (c) SPAG3 (d) SPAG4 and (e) EDS spectrum of SPAG2

Formation of silver nanoparticles and their crystalline state in the hydrogel were further confirmed by XRD. The XRD patterns of PAG5, SPAG1, SPAG2, SPAG3 and SPAG4 are shown in Figure 3.6. The broad peak appeared around $2\theta = 17°$ in PAG and SPAGs corresponds to the d-spacing of 3.5Å and is closely related to the lateral distance between the repeating length of PAA units (Xu et al., 1998). The diffractograms of SPAG1, SPAG2, SPAG3 and SPAG4 exhibited diffraction maxima at $2\theta = 30.38°$, 44 ° and 65° which corresponds to (111), (200) and (220) plane of silver crystallites. These maxima correspond to the characteristic diffraction peaks of FCC lattice of the crystalline silver as reported in the literature (Hu et al., 2004; Zhang et al., 2008). The SPAG gel is not completely crystalline and has an amorphous character because of the PAA chains present. Hence, they exhibit broad peaks in the XRD and the crystalline peak of silver nanoparticle is diminished. As we move from SPAG1 to SPAG4, the characteristic reflection peaks of silver become more intense, and decreased the amorphous nature of SPAG.
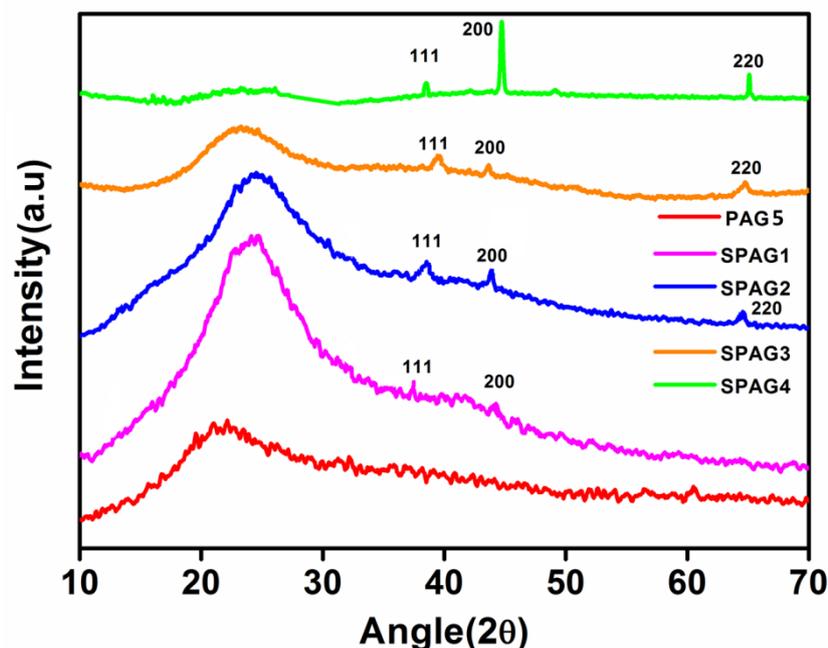
Figure 3.6. XRD spectra of PAG5, SPAG1, SPAG2, SPAG3 and SPAG4

3.3.4. Swelling studies

Swelling properties of SPAGs were conducted in distilled water (pH ~ 7.5) as per the procedure given in the experimental section. It was observed that the presence of silver nanoparticles in the hydrogel caused an enhancement in the swelling index. The increase in the degree of hydration was attributed to the presence of surface charge of silver nanoparticles. The repulsion between silver nanoparticles with identical surface charges resulting an expansion of the hydrogel network, which, in turn, allows more water molecules to diffuse into the gel (Ahmed et al., 2010; Saravanan et al., 2007). Morphological changes during swelling were studied by SEM and the swelled image of SPAG2 is shown in Figure 3.7 (a).
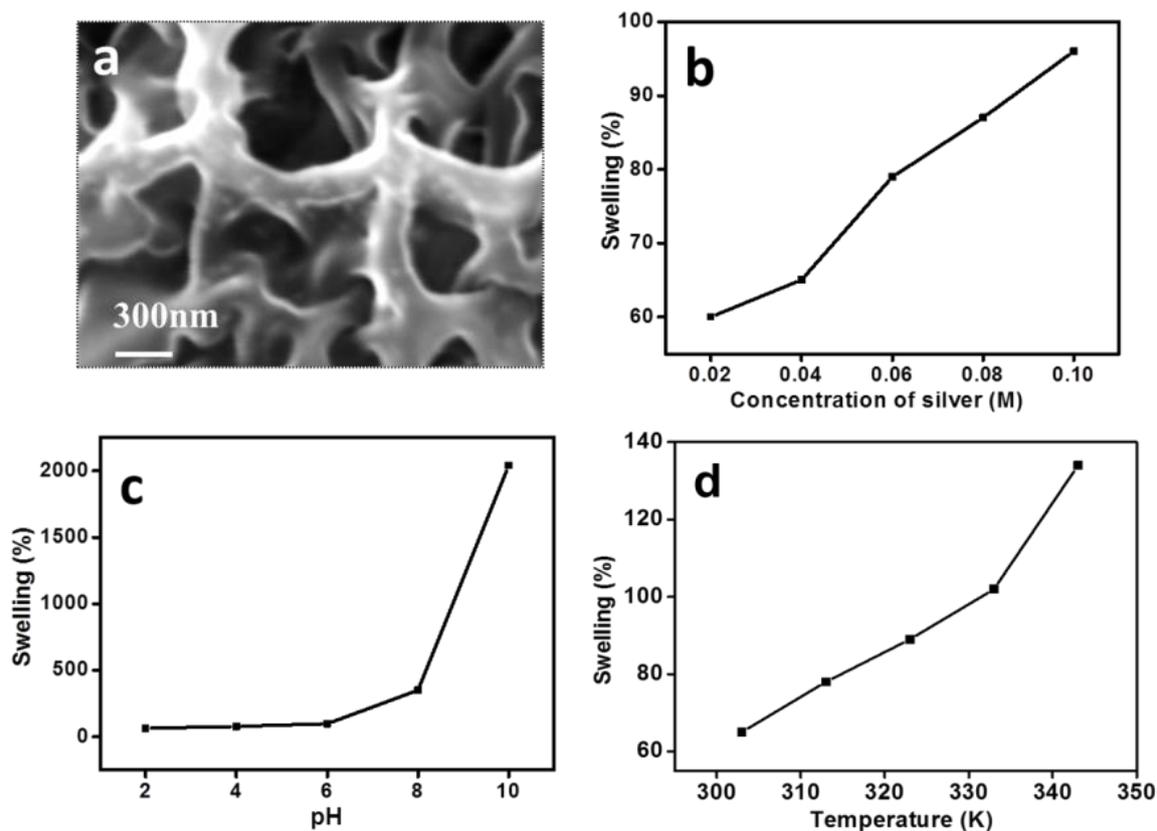
Figure 3.7. (a) SEM image of SPAG2 after swelling (pH ~ 7.5) (b) swelling percentage versus varying concentration of silver (pH ~ 7.5) (c) swelling of SPAG2 at different pH (2-10) and (d) swelling of SPAG2 at different temperature (305K- 345K)

It exhibited highly porous network established by high swelling percentage of the SPAG. The bright portion of SEM image in the fibrillar network revealed the presence of silver nanoparticles. The percentage of swelling index with the increasing amount of silver at pH ~ 7.5 is given in Figure 3.7 (b). Swelling studies were also carried out under different pH conditions (pH 2 to 10) and are shown in Figure 3.7 (c). Enhancement in the swelling index was observed with increase in the pH value due to the salt formation of the free acrylic acid. The increase in the swelling ratio is expected on the basis of AA going from the non-ionized state to the ionized state at pH greater than 4.2. Upon neutralization of the carboxylate groups, the mutual repulsion between these groups causes the molecule to adopt an expanded configuration, leading to

71

higher swelling of the matrix. Swelling studies were also carried out at different temperature (303 K to 343 K) and are shown in Figure 3.7 (d). The swelling percentage increases with increase in temperature is due to the increase in the entropy and internal energy of the solution which leads to a fast diffusion process.

3.3.5. Catalytic reduction of organic dyes and nitrophenols

Catalytic property of SPAG was investigated for the reduction of both dyes and nitrophenols using $NaBH_4$ as the reducing agent.

3.3.6. Catalytic reduction of organic dyes

The decrease in the intensity of UV absorption maxima was noted periodically and the representative diagrams showing the UV-Visible absorption spectra at various intervals of time for MB, R6G and CV in the presence and absence of SPAG2 are shown in Figure 3.8. Reduction of dyes with $NaBH_4$ is incomplete in the absence of the catalyst. The choice of dyes based on the factors, such as the dyes possess different colours in the oxidized and reduced states, and the absorption maxima of the dyes do not overlap with the surface plasmon band of metal nanoparticles which is employing as a catalyst. In the present system, the absorption maxima of silver nanoparticles was observed around 430 nm and the maxima for R6G, CV and MB is 525 nm, 590 nm and 665 nm respectively. The absorption maxima of these bands are distinct from the SPRE of silver nanoparticles present in the SPAGs and hence the precise determination of the catalytic behaviour of the silver nanoparticles is viable. The catalytic reduction was carried out at room temperature and pH~7.5 and was monitored using UV-Visible spectroscopy.
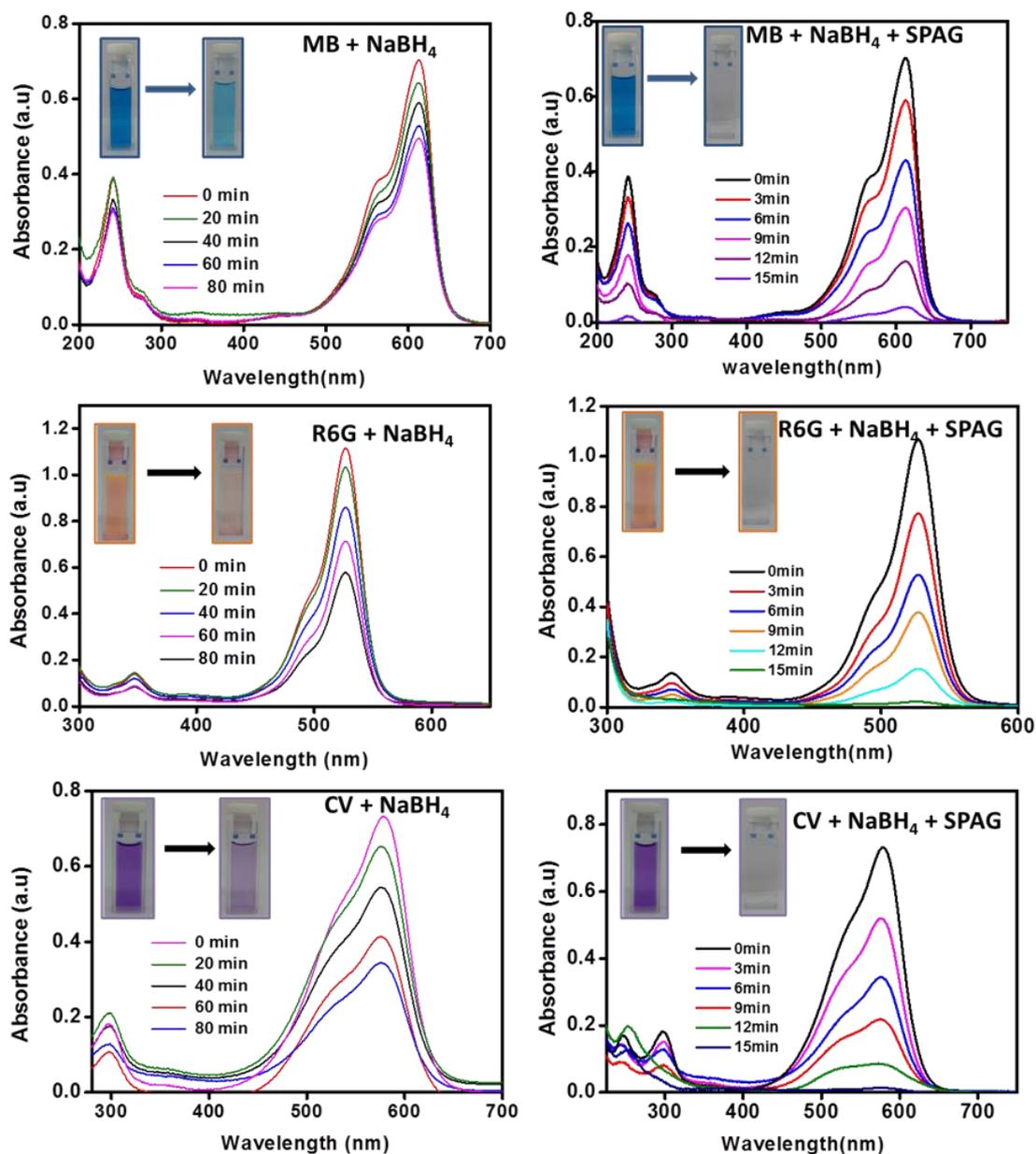
Figure 3.8. The dye reduction studies of MB, R6G and CV (in the absence of SPAG2 (left side) and presence of SPAG2 (right side)) (R6G (240 mg/L), MB (160 mg/L), and CV (200 mg/L), amount of catalyst: 20 mg, temperature: 30 °C, pH: 7.5)

The kinetics of the reduction reaction was studied by periodically measuring the absorption maxima using UV-Visible spectroscopy. A straight line is obtained by fitting the data using first order kinetic equation. ln (a/a_0) versus time is plotted and the rate constant was calculated from the slope of the line, where 'a' is absorbance at time 't' and 'a_o' is initial absorbance and is shown in Figure 3.9. The rate constants of

the uncatalyzed reaction are 0.00014 ± 0.000015, 0.000075 ± 0.0000024 and $0.000142 \pm 0.00001 s^{-1}$ for R6G, MB and CV respectively. The rate constants calculated for the SPAG2 catalyzed reaction are 0.0047 ± 0.0002, 0.0037 ± 0.00016, and 0.0048 ± 0.0002 s^{-1} for R6G, MB and CV, respectively. The increased value for rate constant in the presence of SPAG suggested an enhancement in the rate of reaction. Here, the hydrogel network effectively stabilizes the silver nanoparticles and prevent aggregation of silver nanoparticles during the reaction. The colour of the dye was not retaining in the gels confirmed its complete reduction. Effect of silver concentration on the dye reduction process was monitored. The rate constant values for SPAG1, SPAG2, SPAG3 and SPAG4 are 0.002 ± 0.0001, 0.0047 ± 0.0002, 0.0088 ± 0.00023, 0.024 ± 0.001 for R6G 0.0011 ± 0.0003, 0.0037 ± 0.00016, 0.0074 ± 0.0002, 0.015 ± 0.0021 for MB 0.0023 ± 0.0002, 0.0048 ± 0.0002, 0.0089 ± 0.00014, 0.031 ± 0.0012 for CV. As we move from SPAG1 to SPAG4, there is an increase in the number of silver nanoparticles as evidenced from the UV–Visible spectral area which facilitates the reduction of dye molecules. Apart from these observations, the anisotropic shape with high energy exposed crystalline planes of the silver particles present in SPAG3 and SPAG4 as shown in the XRD patterns also contribute for the high efficiency in the reduction process conducted in presence of SPAG3 and SPAG4. The rate of the reaction is compared with the literature reports, (Jiang et al., 2005; Zheng et al., 2012; Zhu et al., 2013) and SPAG showed a high catalytic efficiency even with high concentration of dye (160 mg/L MB) and the value of rate constant is found to be 0.0037 s^{-1} $(0.22$ $min^{-1})$ with SPAG2 and 0.015 $s^{-1}(0.9$ $min^{-1})$ with SPAG4 which is higher than previous reported values.
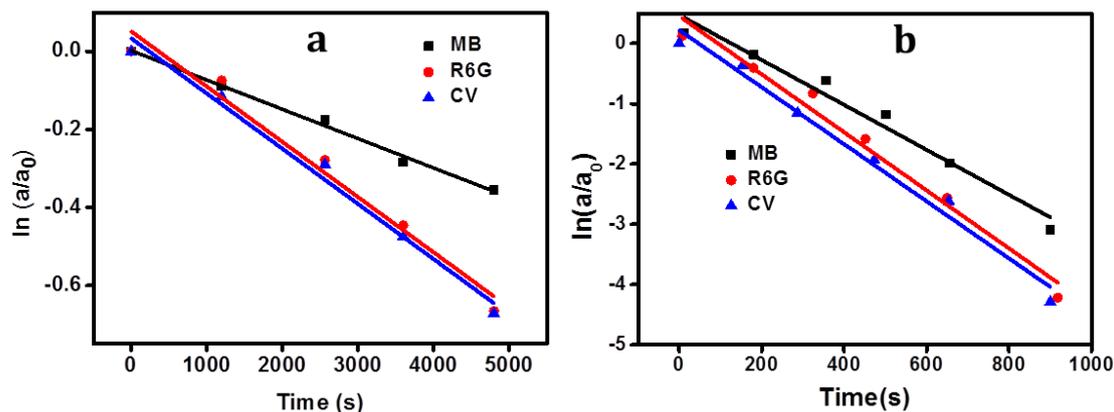
Figure 3.9. The kinetic plots of MB, R6G and CV for (a) uncatalyzed reaction and (b) SPAG2 catalyzed reaction

3.3.7. Catalytic reduction of nitrophenols

Amino phenols synthesized by the reduction of the nitro group using sodium borohydride as the reducing agent. The UV absorption peak of para-nitrophenol (PNP) appeared at 400 nm in alkaline conditions is due to the formation of nitrophenolate ion. In the presence of the catalyst, the reaction starts immediately with the decrease in the intensity of the peak at 400 nm. The new peak at 316 nm gradually emerged indicated the formation of para aminophenol (PAP) (Pozun et al., 2013). The progress of the reaction visually monitored by the disappearance of yellow colour suggested the formation of aminophenol. In the absence of the catalyst, the peak at 400 nm remained unaltered with time showing the absence of reduction to PAP. After the catalytic reduction of PNP is completed (600 s), the peak due to the nitro compound is vanished. The UV absorption profile of PNP in the presence of SPAG2 with respect to time is given in Figure 3.10 (a). Since large amount of sodium borohydride was used for the reduction of PNP, the concentration of sodium borohydride is not taken for consideration. So, first order rate kinetics with respect to the concentration of PNP is used to evaluate the rate of reaction. The rate constant is

calculated from the decrease in the peak intensity at 400 nm. The linear correlation obtained for ln (a/a_0) versus time confirmed the first order reaction kinetics of the catalytic reduction and were shown in the inset of Figure 3.10 (a). The rate constant was calculated from the slope of the line and is obtained as $8.16 \pm 0.04 \times 10^{-3} \, s^{-1}$. As the initial concentration of BH_4^{-} was very high, it remained constant during the reaction. The hydrogen liberated during the reduction will expel out the air and inhibit the areal oxidation of PAP. A catalyst with an intermediate potential between the donor and acceptor may help the electron relay process and metal nanoparticles considered as effective redox catalysts. The silver nanoparticles catalyze the reduction by facilitating the electron relay from the donor sodium borohydride to the acceptor para-nitrophenol. Both borohydride and the para-nitrophenolate are adsorbed on the surface of the SPAG and facilitate the reduction by lowering the activation energy of the reaction. The catalytic activity of SPAG2 s also tested for the reduction of ortho-nitrophenol (ONP) and meta-nitrophenol (MNP). In this case also, in the presence of SPAG2, peak of meta-nitrophenolate (398 nm) and ortho-nitrophenolate (416 nm) is gradually decreased and a new peak of meta-aminophenol (MAP) and ortho-aminophenol (OAP) is appeared with time. The time-dependent UV spectra of ONP and MNP and the corresponding kinetic plots are given in the Figure 3.10 (b) and 3.10 (c).
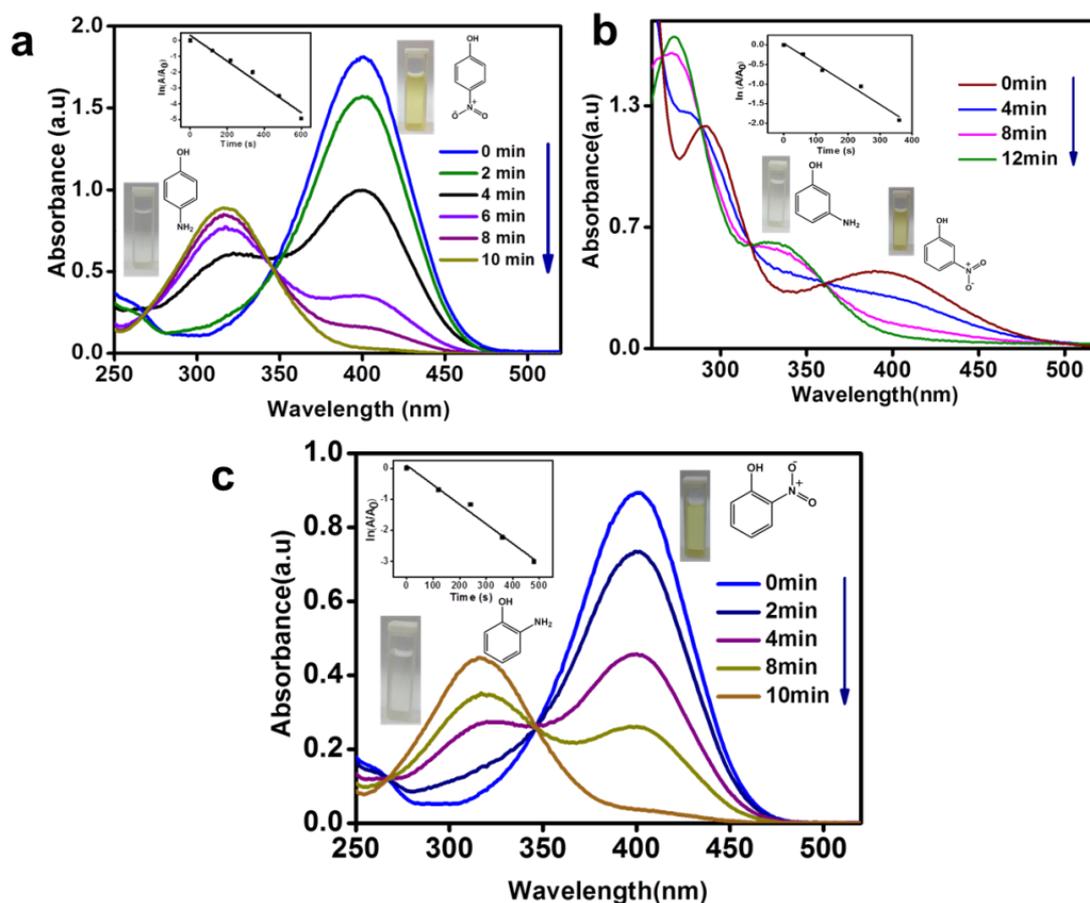
Figure 3.10. Time dependent UV–Visible spectra of nitrophenols and the kinetic plot of ln (a/a_0) versus time for the reduction of nitrophenols (inset) (a) PNP (b) MNP (c) ONP ([PNP]: 1 mM, [MNP]: 1mM, [ONP]: 1 mM, [NaBH$_4$]: 10mM, amount of catalyst: 20 mg, temperature: 30 °c, pH: 7.5)

The ortho and para nitrophenolate is more stable than meta nitrophenolate. The –I effect of nitro group and the resonance effect stabilize ortho and para isomer. Ortho isomer is less stable than para due to the steric hindrance which makes –I effect is less effective comparing with the para isomer. Due to the absence of conjugation, meta isomer is the least stable one. Hence the rate of reduction of nitrophenols followed the order PNP ($8.2 \pm 0.04 \times 10^{-3}$ s^{-1}) >ONP ($6.3 \pm 0.03 \times 10^{-3}$ s^{-1}) >MNP ($5.2 \pm 0.05 \times 10^{-3}$ s^{-1}) (Jana et al., 2007; Pradhan et al., 2002). The catalytic conversion efficiency of the catalyst is 99%, 96% and 95% for PNP, MNP and ONP respectively. The rate constant for the reduction of PNP is compared with the polymeric hydrogel supported silver nanoparticles and found to be higher than that reported in literature

(Lu et al., 2007; Otari et al., 2013; Jana et al., 2007; Pradhan et al., 2002; Hariprasad et al.,2010; Butun et al., 2011; Sengupta et al., 2014; Ai et al., 2012) and is given in Table 3.1. In the present study, 20 mg of SPAG (2.59×10^{-5}g of silver) is employed.

Catalyst	Rate constant	Reference
PVA/PS-PEGMA/Ag	$7.80 \times 10^{-5} s^{-1}$	Lu et al., 2007
PVA/Ag hydrogel	$7.31 \times 10^{-5} s^{-1}$	Otari et al., 2013
Ag–Alg biohydrogel	$0.36\ \text{min}^{-1}$	Jana et al., 2007
PVA/Ag	$3.78 \times 10^{-7} s^{-1}$	Pradhan et al., 2002
Ag–PVA/PVA/Ag–PVA	$5.3 \times 10^{-3} s^{-1}$	Hariprasad et al., 2010
poly-(acrylamide glycolic acid)/Ag composites	$0.0923\ \text{min}^{-1}$	Butun et al., 2011
pyridine–pyrazoletrisamide ligand- Ag hydrogel	$7.8 \pm 1.5 \times 10^{-3} s^{-1}$	Sengupta et al., 2014
alginate–magnetite hybrid biohydrogels	$0.27\ \text{min}^{-1}$	Ai et al., 2012
SPAG	$8.16 \times 10^{-3} s^{-1}$ ($0.489\ \text{min}^{-1}$)	Present work

Table 3.1.Comparative study of the catalytic activity of polymeric hydrogel-supported silver nanoparticle for reduction of nitrophenol

In the present system, silver nanoparticles were stabilized with carboxyl and hydroxyl groups of the fibrous network and are mostly exposed to the solution system and enhance the rate of diffusion of reactants. The absence of induction period during the reduction process of nitrophenol revealed the fast diffusion of reactants and products in and out of the hydrogel. Thus diffusion rate is extremely quick and hence the rate of reduction is very fast. In this situation, limitation due to the diffusion of reactants inside the hydrogel is not taken into consideration (Chtchigrovsky et al., 2012; Liu et al., 2007; Kuroda et al., 2009).

3.3.8. Mechanism of reduction

The proposed mechanism for the SPAG catalyzed reduction of dyes with sodium borohydride as reducing agent is shown in Scheme 3.2. Dye molecules are electrophilic and $NaBH_4$ is nucleophilic compared to silver nanoparticles. Generally, the rate of reduction process depends on the potential difference between the donor and acceptor molecule. Silver nanoparticles are negatively charged in the presence of $NaBH_4$ by the following equation (Ung et al., 1999).

$$BH_4^- + Ag_n + 3H_2O \longrightarrow BO_3^{3-} + Ag_n^{8-} + 10H^+$$
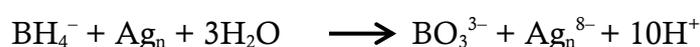
Hence the negatively charged silver particles are more accessible to the positively charged particles due to the electrostatic interaction. Then silver particles may become more attracted to the positively charged dye molecules. Thus the electron transfer between dye molecules and BH_4^- through the silver nanoparticles becomes viable and enhances the rate of reaction. The observed enhancement in the rate of reduction revealed the catalytic efficiency of SPAG. The rate of the reduction of dyes increased when moving from SPAG1 to SPAG4. There is an increase in the number of silver nanoparticles as evidenced from the UV–Visible spectral area which facilitates the reduction of dye molecules. Apart from these observations, it is attributed to the change in the size, shape and crystalline state of silver nanoparticles. Morphological observation of SPAGs made by SEM and TEM showed variation in the shape and size of the silver particles. It exhibited spherical, rod and capsule type particles. XRD results of SPAG3 and SPAG4 suggested the formation planes of (220) and (200) with enhanced intensity compared to SPAG1 and SPAG2 revealing high surface area. This may also enhance the efficiency of the catalyst. The high viscoelastic properties observed during rheological measurements suggested its operational and storage

stability. Even after the ten successive uses, the shape of the catalyst and the efficiency of catalysis remain intact. SPAGs allow the easy diffusion of the solute molecules and enhance the efficiency of the catalyst for the reduction process.
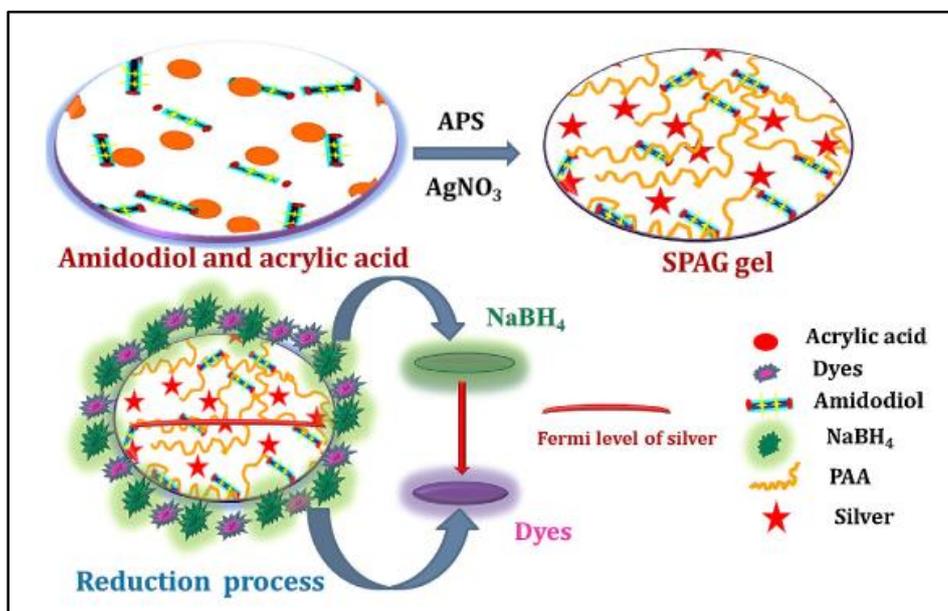
Scheme 3.2. Mechanism for catalytic reduction of dyes in presence of SPAG

The study of the reaction mechanism helps to design a catalyst with better output. The mechanism for the catalytic reduction of nitrophenols is studied with Eley–Rideal model or Langmuir–Hinshelwood studies. In the Eley–Rideal model, only one of the educts will adsorb on the surface of the catalyst and reacts with the other educt in the solution. In the case of Langmuir- Hinshelwood model, both the educts get adsorbed on the surface of the catalyst and react on its surface. The valid reaction mechanism for the reduction of nitrophenols can be suggested by performing two sets of experiments, i.e., by studying the rate constant dependence on the concentration of PNP and sodium borohydride. In Eley–Rideal model, the rate is increasing with an increasing concentration of PNP which is not adsorbed on the surface. According to Langmuir– Hinshelwood model, the rate constant is decreasing with an increasing concentration of PNP whereas for an increasing concentration of

NaBH$_4$, the rate is reaching maximum (Wunder et al., 2010; Herves et al., 2012).The reduction of nitrophenol is taking place only in the presence of metal nanoparticles. If an excess NaBH$_4$ is used for the reaction, the reaction is first order with respect to the concentration of PNP. The apparent rate constant is proportional to the surface area of the nanoparticles. The kinetic constant can be calculated as

$$\frac{dc_{PNP}}{dt} = kc_{PNP} = k_1 Sc_{PNP} \qquad (1)$$

For the quantitative comparison of the data, the catalytic reduction can be modelled in terms of Langmuir–Freundlich isotherm.

$$\theta_i = \frac{(K_i c_i)^{n_i}}{1 + \sum_{j=1}^{N}(K_j c_j)} \qquad (2)$$

Where, θ_i is the surface coverage of the compound i, K_i is the adsorption constant of the respective component and c_i is the concentration in solution and 'n' is related to the heterogeneity of the sorbent. Further rearrangement of the equation (1) leads to equation (3) which can be used to model the catalytic activity.

$$-\frac{dc_{PNP}}{dt} = \frac{kS(K_{PNP}c_{PNP})^n \left(K_{BH_4}c_{BH_4}\right)^m}{(1 + (K_{PNP}c_{PNP})^n + \left(K_{BH_4}c_{BH_4}\right)^m)^2} = k_{app}c_{PNP} \qquad (3)$$

Thus, k_{app} is given by

$$k_{app} = \frac{kSK_{PNP}^n c_{PNP}^{n-1}\left(K_{BH_4}c_{BH_4}\right)^m}{(1 + (K_{PNP}c_{PNP})^n + \left(K_{BH_4}c_{BH_4}\right)^m)^2} = c_{PNP} \qquad (4)$$

Here, k is the molar rate constant per square meter of the catalyst and K_{PNP} is the adsorption coefficient of nitrophenol and K_{BH4} is the adsorption coefficient of BH$_4^-$.
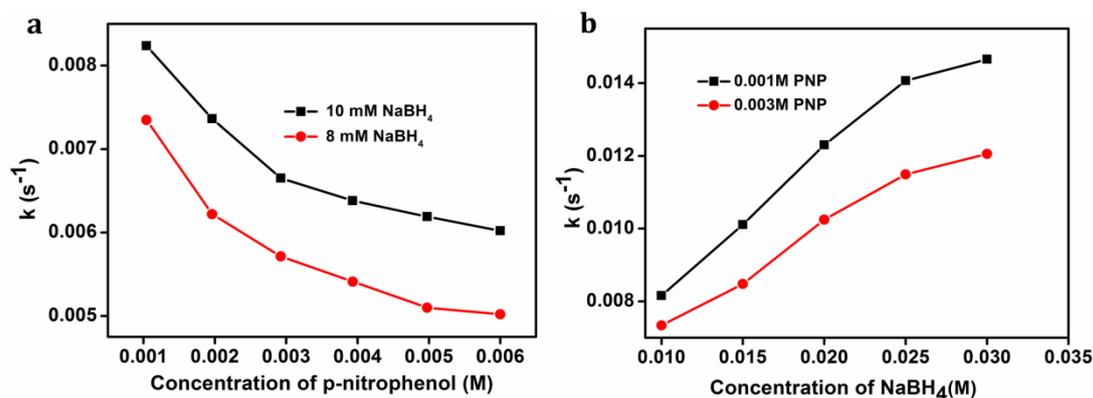
Figure 3.11. Dependence of apparent rate constant on the concentration of (a) PNP and (b) NaBH$_4$

The Figure 3.11. showed the nonlinear dependence of rate constant of both PNP and NaBH$_4$ concentration variation and the solid lines refer to the fit of the experimental data for equation (3) and suggested Langmuir –Hinshelwood model for the reaction. The rate constant is decreasing with an increasing concentration of PNP and augmented with an increasing concentration of NaBH$_4$. According to this mechanism, BH$_4^-$ and PNP adsorb on the surface of the catalyst. The diffusion of the reactants to the nanoparticle surface and the adsorption/desorption equilibrium is assumed to be fast. In the rate determining step, the surface hydrogen and PNP react with each other and PAP desorbs from the surface of the catalyst. Detachment of the product creates a free surface, and the catalytic cycle can start again. A high concentration of nitrophenol molecules leads to the full coverage of the catalytic surface which slows down the reaction. An increasing concentration of NaBH$_4$ leads to an increase in the rate constant because it supplants PNP. Further increase in the concentration of borohydride leads to a maximum rate constant due to the saturation surface area of the catalyst. According to the results, both borohydride ions and PNP simultaneously adsorb on the surface of the catalyst and product PAP is desorbed out. The reduction rate is observed to be very fast, and the diffusion of the reactants and

products in and out of the hydrogel is much quicker. So the diffusion rate inside the hydrogel is ignored while calculating the rate constant (Cussler et al., 1997).

3.3.9. Effect of temperature

The effect of temperature on the catalytic reduction on dyes and nitrophenols were studied using SPAG2. The temperature experiments were conducted in the range of 303–343 K and at the pH of ~7.5. The rate of reduction showed an enhancement with increase in temperature. The degree of swelling of hydrogel increases at high temperature due to the fast diffusion of dye molecules to the surface of hydrogel. As the temperature was increased, the surface area of the catalyst and the diffusion of reactants onto the surface of the catalyst increased. These factors contribute to the enhancement in the rate constant at a higher temperature.

The activation energy of the reduction process was calculated using Arrhenius equation.

$$k = Ae^{-\left(\frac{E_a}{RT}\right)}$$

$$\ln k = \ln A - \frac{E_a}{RT}$$

Where k is the rate constant, A is the pre-exponential factor, E_a is the activation energy, R is the gas constant (8.314 $Jmol^{-1}K^{-1}$) and T is the temperature.

A straight line is obtained by plotting ln k versus 1/T for the SPAG2 catalyzed reduction of dyes and nitrophenols is given in Figure 3.12 (a) and (b). The activation energy of the SPAG2 catalyzed reduction reaction is 28, 30.7, 33.8, 54, 45 and 44 KJ/mol for MB, R6G, CV, PNP, ONP and MNP respectively.
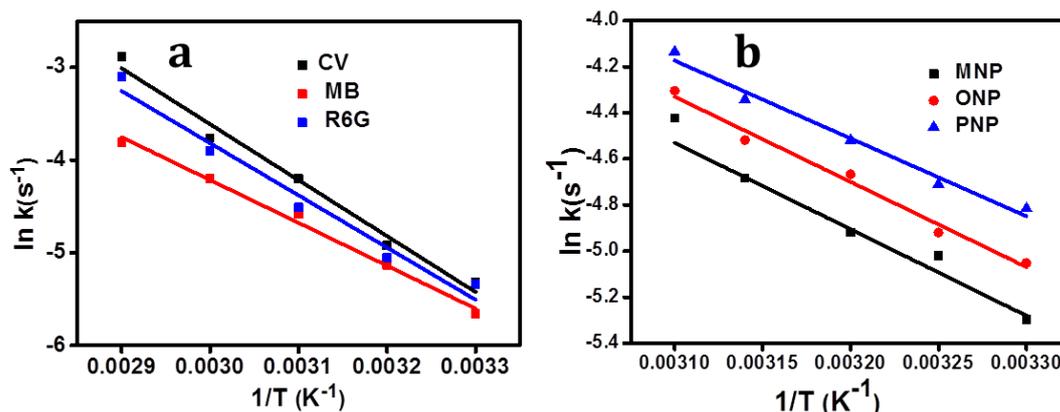
Figure 3.12. Effect of temperature on the reduction (a) Arrhenius plot of R6G, MB and CV (dye concentration: R6G (240 mg/L), MB (160 mg/L), CV (200 mg/L), amount of catalyst: 20 mg, temperature: 30 - 70 °c, pH: 7.5) (b) Arrhenius plot for the reduction of nitrophenols ([PNP]: 1mM, [ONP]: 1mM, [MNP]: 1mM, [NaBH4]: 10mM, amount of catalyst: 20 mg, temperature: 30 °c, pH: 7.5)

3.3.10. Reusability and storage stability

The reusability of the SPAG for the catalytic reduction was studied for the reduction of PNP and as shown in Figure 3.13. There was only a slight decrease in the catalytic efficiency as evidenced from the rate of reaction even after 20 cycles, which suggests that SPAG as an efficient catalyst for the reduction of nitrophenols. The high rate constant, high reusability, good storage stability, easy separation and the absence of induction period suggest SPAG as an efficient catalyst for the reduction of organic molecules, and the process is rapid, efficient and economical.
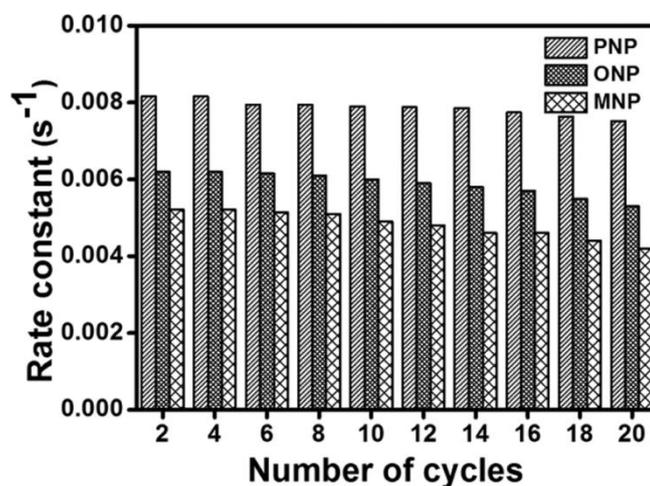
Figure 3.13. The variation of rate constant for 20 cycles for SPAG2 catalyzed reduction of PNP

Long-term stability of the catalyst was monitored by measuring the efficiency of catalyst up to six months after storing the gel at 4°C in a sealed covers. The storage stability of the SPAG for the reduction process was checked with SPAG2 at room temperature and pH ~7.5 up to six months. The graph showing the variation of rate constant with time (up to 6 months) for the SPAG2 catalyzed the reduction of MB, R6G and CV, PNP, MNP and ONP is given in Figure 3.14 (a) to (c). The SPAG catalyst is stable up to six months without any appreciable loss in catalytic efficiency.
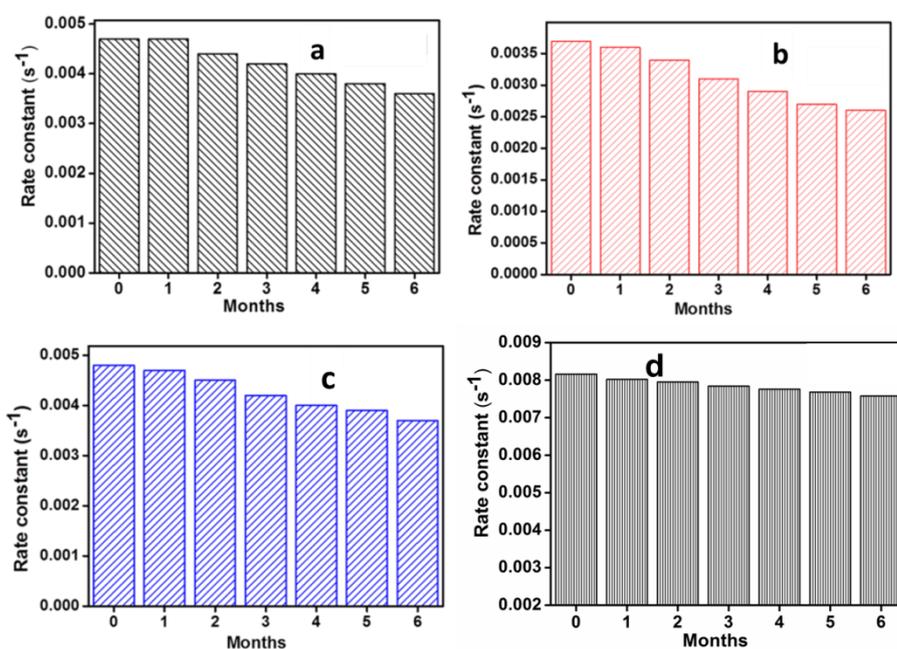
Figure 3.14. The variation of rate constant with respect to time (upto 6 months) for the SPAG2 catalyzed reduction of (a) R6G (b) MB (c) CV and (d) PNP

3.4. Conclusions

SPAGs were prepared by in situ reduction and polymerization approach. Morphological studies revealed the formation of nanospheres, nanocubes and nanorods depending on the amount of silver nitrate. The catalytic activity of SPAG was checked with organic dyes and nitrophenols, the activation energy for the reduction process is found to be reduced by ~ 10 kJ. The reduction reaction is fitted

with Langmuir–Hinshelwood model and is suggested that both the reactants are adsorbed on the surface of the catalyst. The SPAG catalyst exhibit high storage modulus, reusability, storage stability, sludge free operation, absence of induction period and high rate constant (PNP: $8.2 \pm 0.04 \times 10^{-3}$ s^{-1}, ONP: $6.3 \pm 0.03 \times 10^{-3}$ s^{-1} and MNP: $5.2 \pm 0.05 \times 10^{-3}$ s^{-1}) during the reduction process. Hence, SPAG can be considered as an efficient catalyst for the reduction of organic molecules and the process is rapid, efficient and economical.

3.5. Experimental

3.5.1. Materials

Hexamethyelene diamine, R6G (Sigma Aldrich), γ-butyrolactone (Fluka, Germany), isopropanol, acrylic acid, silver nitrate, sodium borohydride, ammonium persulphate (E-Merk, India), MB, CV (Nice Stains, India).

3.5.2. Preparation of SPAGs

AA (1mL) and 10 % AMD (1mL) in water were mixed with 0.2 mL of 0.02M silver nitrate. Two drops of 10 % APS was added to the mixture. The content was shaken well and kept at room temperature for 10-20 minutes for gel formation. It was washed several times with distilled water to remove residual monomers and ions. The prepared gel was kept at 70 ^{o}C for 12 hours to ensure the complete reduction of silver nanoparticles. Experimental details of the preparation of SPAGs are given in Table 3.2.

Hydrogel	Acrylic acid (ml)	AMD 10% in water (ml)	APS (10% in water)	Silver nitrate ($\times 10^{-3}$ g)	Gel formation time (min)	Colour and appearance
SPAG1	1	1	2 drops	0.068	10	Transparent yellow
SPAG2	1	1	2 drops	1.36	8	Transparent yellow
SPAG3	1	1	2 drops	2.04	7	Transparent yellowish brown
SPAG4	1	1	2 drops	2.72	5	Transparent brownish yellow

Table 3.2: Experimental details for the preparation of SPAGs

3.5.3. Swelling studies

Definite amount SPAG hydrogels were accurately dried and transferred into 20 mL of water in a beaker at room temperature for 24 hours. The sample was taken out at definite time intervals and the water present on the surface of the swollen hydrogel were removed by soft pressing the sample between the folds of a filter paper before weighing. The uptake of water with respect to time was calculated by periodically weighing the hydrogel. The swelling percentage of SPAGs was calculated using the following equation.

$$S(\%) = \frac{(m_t - m_0)}{m_0} \text{ X } 100$$

Here, m_0 is the initial mass and m_t is the mass of swollen gel at time t.

3.5.4. Catalytic reduction studies

Aqueous solutions of cationic dyes such as R6G (240 mg/L), MB (160 mg/L) and CV (200 mg/L) and nitrophenols such as ONP, MNP and PNP (1 mM) were

prepared. The catalytic reduction was carried out by taking 20 mL of each dye/nitrophenol solution, 2 mL of 10 mM $NaBH_4$ solution and 20 mg of SPAG catalyst. The progress of the reaction was monitored by measuring the periodic decrease in the absorbance with small aliquots of solution from the reaction mixture. Effect of silver concentration, pH and temperature on the catalytic reduction was studied.

3.5.5. Characterization techniques

X-ray diffraction studies were done with X-ray diffractometer (Philips X'pert Pro) with CuKα radiation (λ~0.154 nm) employing X'celarator detector and a monochromator at the diffraction beam side. The d-spacing of the nanocomposite was calculated from the angular positions 2θ of the observed d001 reflection peaks based on the Bragg's formula nλ = 2d sin θ, where λ is the wavelength of the X-ray beam and θ is the diffraction angle. Averaged 2θ was used with the 2θ resolution of 0.002 degree from 2 to 70°. TEM measurements were carried out using FEI (TECNAI G2 30 S-TWIN) with an accelerating voltage of 100 kV. For TEM measurements, the samples were casted on a carbon coated copper grid and dried in vacuum at room temperature before observation.

CHAPTER 4

DEVELOPMENT OF FUNCTIONAL LIQUID CRYSTALLINE LAPONITE- AMIDODIOL GEL THROUGH SELF-ASSEMBLY APPROACH
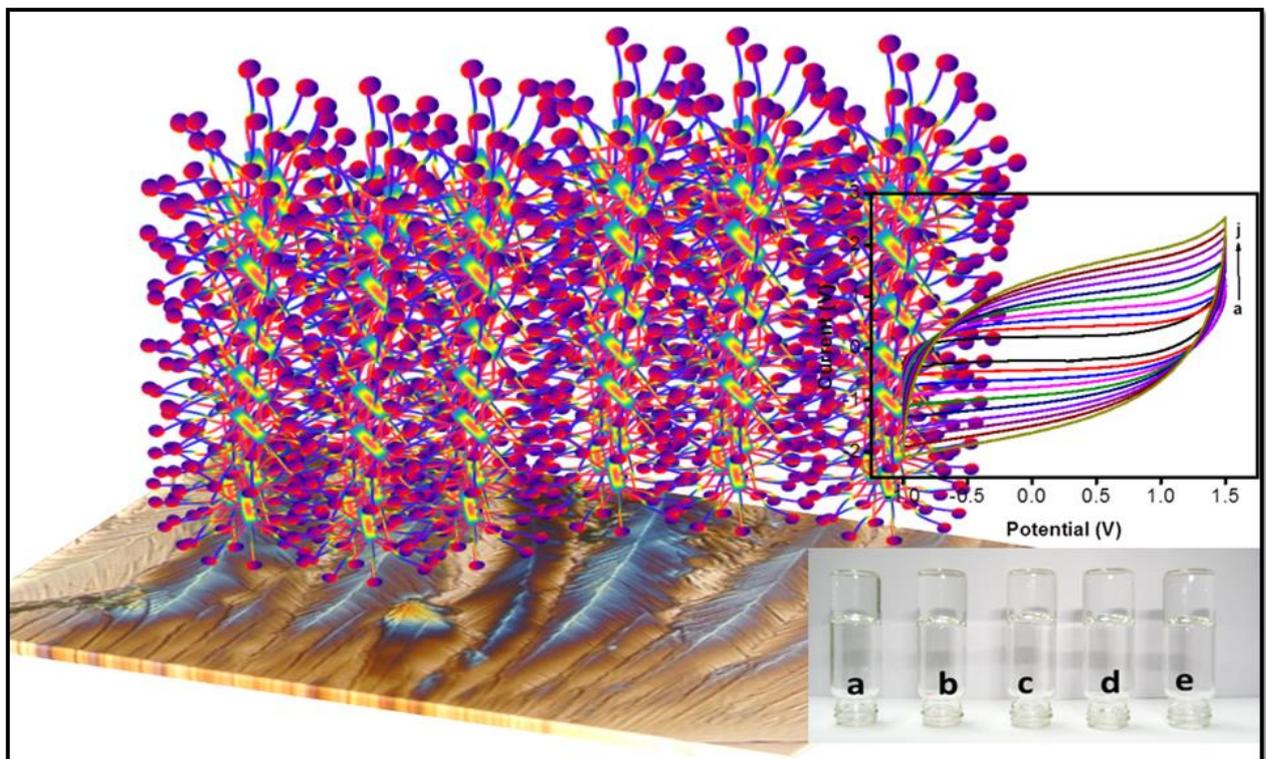
4.1. Abstract

In this chapter, we have demonstrated the design and synthesis of liquid crystalline gels through multi-scale hierarchical self-assembly of laponite and AMD (FLAG) in water. They interact with each other through various non-covalent interactions such as hydrogen bonding and ion-dipole interactions to form highly ordered super structures in different dimensions and length scales. Effect of concentration of AMD and time scale on the specific modes of packing was studied using various techniques such as PLM, SEM, TEM, XRD, rheology and FT–IR spectroscopy. The amount of hydroxyl functional groups in FLAG was estimated by chemical analysis. A plausible mechanism is proposed for the formation of superstructures in FLAG. Electrochemical impedance studies of the FLAG showed low charge transfer resistance (245Ω) with a stable electrochemical window ($-0.4V - 1V$). Galvanostatic studies revealed good cycling stability with a specific capacitance of 1856 mF/g. Results suggested that FLAGs can exploited as an efficient gel electrolyte in energy storage devices.

4.2. Introduction

Hybrid liquid crystalline materials having self-assembled superstructures with specific modes of packing along with desired functionalities are reported for potential applications in drug delivery, sensors, display devices, energy storage, etc. (Kanie et al., 2003; Walcarius et al., 2001; Nguyen et al.,2015; Qasim et al., 2015; Tunkara et al., 2014). Development of liquid crystalline functional gels through self–organization of organic–inorganic molecular systems is recently emerging and they find applications in many technological areas (Ungar et al., 2011; Kato et al., 2006). Supramolecular self-assembly approach through non-covalent interactions such as hydrogen bonding, van der Waals interactions, ionic bonding, charge transfer and electrostatic interactions have growing significance for the design of functional liquid

crystalline materials (Paleos et al., 1995; Daly et al., 2013). Tuning the interaction anisotropy through non-covalent interactions has shown enormous implications on the functional properties of formed superstructures. Among these, studies on soft materials formed by the self–organization of low molecular weight organic molecules and layered inorganic materials such as laponite are receiving importance for many biochemical applications (Hirst et al., 2008; Juggernauth et al., 2011).

Laponite is a synthetic hectorite clay, made up of discoid platelets of lithium magnesium silicate ($Si_8[Mg_{5.5}Li_{0.4}O_{24.0}]H_4O_{24}Na_{0.7}$) with a thickness of about 1 nm, and diameter of about 30 nm as shown in Figure 4.1 (Bonn et al., 1999; Willenvacher et al.,1996). In laponite, sodium ions between the negatively charged silicates may exchange for other ions (exchange capacity 50.8 meq/g). They possess high surface area (370 m/g) and very small particle size. Nanoscale dimension and high aspect ratio of laponite clay is capable for the development of functional devices. They readily expand in water by osmotic swelling and hydration of interlayer cations balance the negative electrical charge. Laponite discs are endowed with structural features such as hydroxyl groups, Lewis and Bronsted acidity, exchangeable interlayer cations, and nano dimensions of the individual layers. The silanol groups located at the edges of the laponite sheets can be modified with organic compounds, such as thiol, amine, or long hydrocarbon chains (Herrera et al., 2005; Teng et al., 2015). The modification of laponite clay platelets with polyelectrolytes finds application in the area of sensors, permeation barriers, coatings etc. Ruzicka and Gabriel et al. extensively studied the laponite water interaction and the lyotropic liquid crystalline phases of laponite gels (Ruzicka et al., 2004; Gabriel et al., 1996; Ruzicka et al., 2011). The use of ultra-thin electrolyte expected to reduce the overall resistance of the system even in the low conductivity.
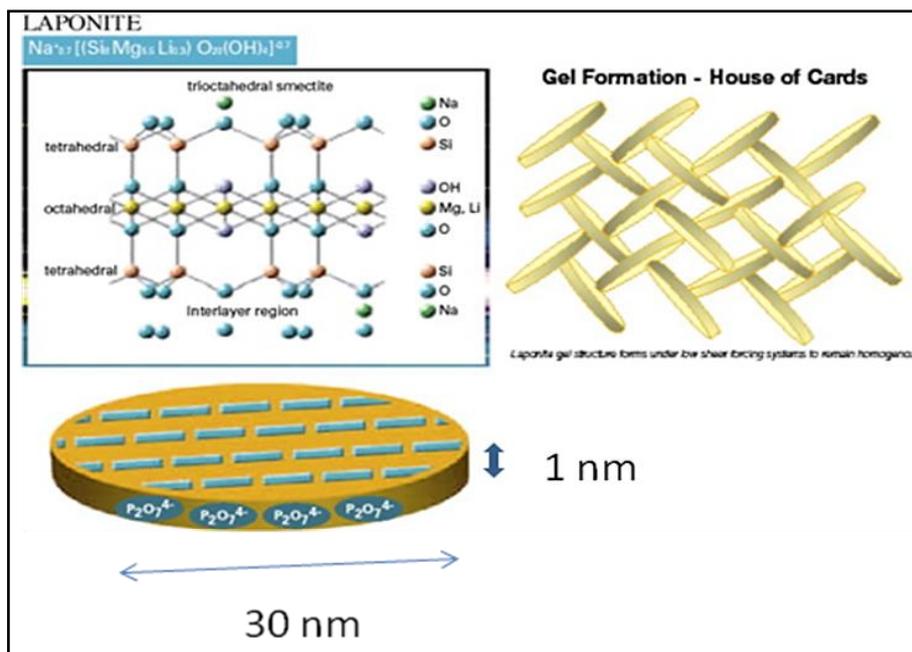
Figure 4. 1. Structure of laponite

Laponite clay particles have an asymmetric charge distribution as there is a net negative charge on the surface and a partial positive charge on the edges. Hence, they will not interact with all the neighbours, but they can lock together in lower densities. Laponite gel is stable for a long time, and aging problem is not observed. Such a low-density gel can act as gel electrolyte and could be employed in energy storage devices. Park et al. reported water based thixotropic polymer xanthan gum gel electrolyte in DSSCs. They suggested that owing to the thixotropic property, the gel electrolyte can infiltrate into the mesoporous titania electrodes with sufficient penetration and exhibited good power conversion efficiency (Park et al., 2013). It was reported that the high aspect ratio of laponite clay platelets favors superior transport property. Naturally occurring clays are difficult to purify and process. The synthetic laponite RD can be obtained in the high degree of structural regularity and in pure form. It was reported that sodium ions present in laponite clay can be exchanged with lithium ions, and the conductivity can be increased to a large extent and find application in energy storage devices (Lutkenhaus et al., 2007; Riley et al., 2002).

The basic requirements of a material to suggest as an electrolyte material are good ionic conductivity, mechanical stability, suitable for fabrication, electrochemical and thermal stability and lack of leakage of electrolyte (Xue et al., 2015). A variety of electrolytes consisting of liquids, gels, and polymers have been developed. However, liquid electrolytes have good ionic conductivity but it has a fundamental limitation for long-term operation due to their evaporation and leakage (Tarascon et al., 2001; Goodenough et al., 2010). Solid electrolytes in comparison with liquid electrolytes possess unique features like compactness, portability, reliability and lack of leakage. Solid electrolytes received considerable attention due to superior mechanical properties and long-term stability but have limitations such as low ionic conductivity and slow rate of diffusion. Gel electrolytes combine the merit of the liquid electrolyte (high ionic conductivity) and the solid electrolyte (good mechanical stability). They are considered to be superior candidates as electrolytes due to their three-dimensional gel network which facilitates the ion transportation (Manuel et al., 2006; Wang et al., 2015). On comparison with organogels, hydrogels provide an environment-friendly green approach and low-cost route for the preparation of electrolyte materials (Choudhury et al., 2009). The infiltration ability of gel polymer electrolyte is less favourable and hence the development of water based environmentally friendly, highly reliable supramolecular hydrogel electrolyte that resists solvent leakage and good mass transport is receiving importance. The self-assembled liquid crystalline materials forming well defined anisotropic conductive pathways can be considered as an attractive alternative for the electrolyte material. Liquid crystalline materials exhibit both temperature or solution induced 1D, 2D and 3D ordered mesophases with typical textures such as columnar, smectic and bicontinuous cubic phases having anisotropic channels which are capable of forming conductive pathways for the transport of

charges and ions (Yoshio et al., 2002; Högberg et al., 2014; Feng et al., 2015; Sakuda et al., 2015). Liquid crystalline hydrogels are considered as better candidates as electrolytes for energy storage systems because of their special features such as compactness, portability, reliability, lack of leakage and green approach in addition to the well-defined anisotropic pathway for the charge conduction.

The design of liquid crystalline functional materials using tailor-made molecular gelators containing amide and hydroxyl linkages offers new features (VanGorp et al., 2002; Yabuuchi et al., 2003). Inter and intramolecular hydrogen bonds between amide linkages are reported to be responsible for the functional properties of proteins and synthetic polyamides (Kato et al., 1899; Ringsdorf et al., 1989; Praefcke et al., 1991; Yamuchi et al., 2008). AMD possess amide and hydroxyl groups and is expected to form self-organized macroscopic structures through extensive intermolecular hydrogen bond interactions. By combining the advantageous of laponite and AMD, the development of a promising hybrid liquid crystalline supramolecular hydrogel which may expect to form self-assembled anisotropic structures can be considered as an alternative for gel electrolyte in energy storage devices.

The present work demonstrates the design of liquid crystalline functional gel through non-covalent interactions among laponite and AMD by multi-scale hierarchical self-assembly approach. Effect of time and concentration of AMD in the design of liquid crystalline functional gels was studied. They were characterized using various techniques such as PLM, SEM, TEM, rheology, XRD and FT-IR spectroscopy. Finally, the cyclic voltammetric and galvanostatic charge-discharge studies were carried out to demonstrate its application as an electrolyte for energy storage devices.

4.3.   Results and Discussion

4 .3.1. Preparation and characterizations of FLAGs

FLAGs of varying compositions and designs were prepared by mixing aqueous solutions of laponite and AMD at room temperature and are designated as FLAG1, FLAG2, FLAG3 and FLAG4 and the details are provided in the experimental section. Studies showed that gelation time and gel strength of FLAGs depended on the composition of the components and time. It has been observed that dilute aqueous laponite solution (< 2 weight %) initially appeared as a sol and later it changed into a transparent gel. However, when the laponite concentration is increased to > 5 weight %, it immediately transform into an opaque gel. Observation of laponite gels (LAP) under PLM showed the formation of nematic texture and is depicted in Figure 4.2 (a). This observation is strengthened by the studies made by Ruzicka and Gabriel et al. Liquid crystalline phase formation is favoured by the ordered arrangement of the discs in a particular direction and gelation attributed due to the three-dimensional network formation of discs. SEM image of laponite sol before functionalization exhibited isolated disc like morphology and is provided in Figure 4.2 (b).
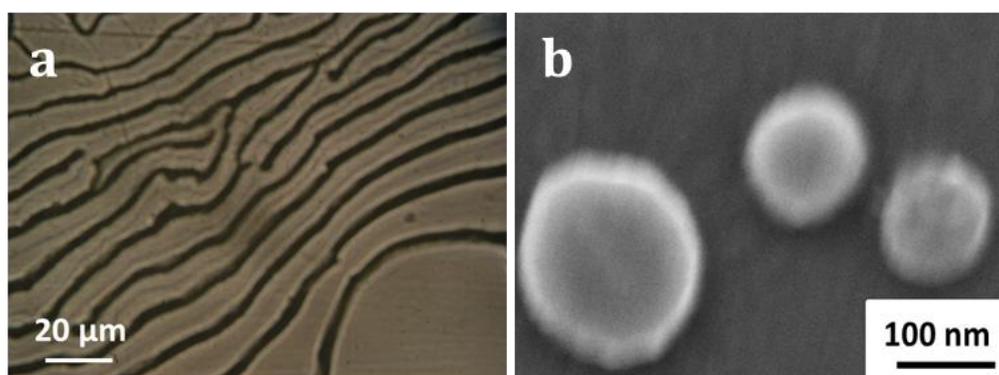
Figure 4.2. (a) Schleiren nematic texture of laponite gel and (b) SEM image of laponite exhibiting isolated disc like morphology

Effect of AMD on the gel strength and formation of liquid crystalline phase formation were studied. It has been observed that there is an increase in the gel strength in the presence of AMD. This may be due to the network formation established by the combined effect of various non-covalent interactions among the partial charges, Mg–OH, Si–OH groups present on the surface and edges of the laponite discs with diamide and dihydroxyl group contributed by AMD.
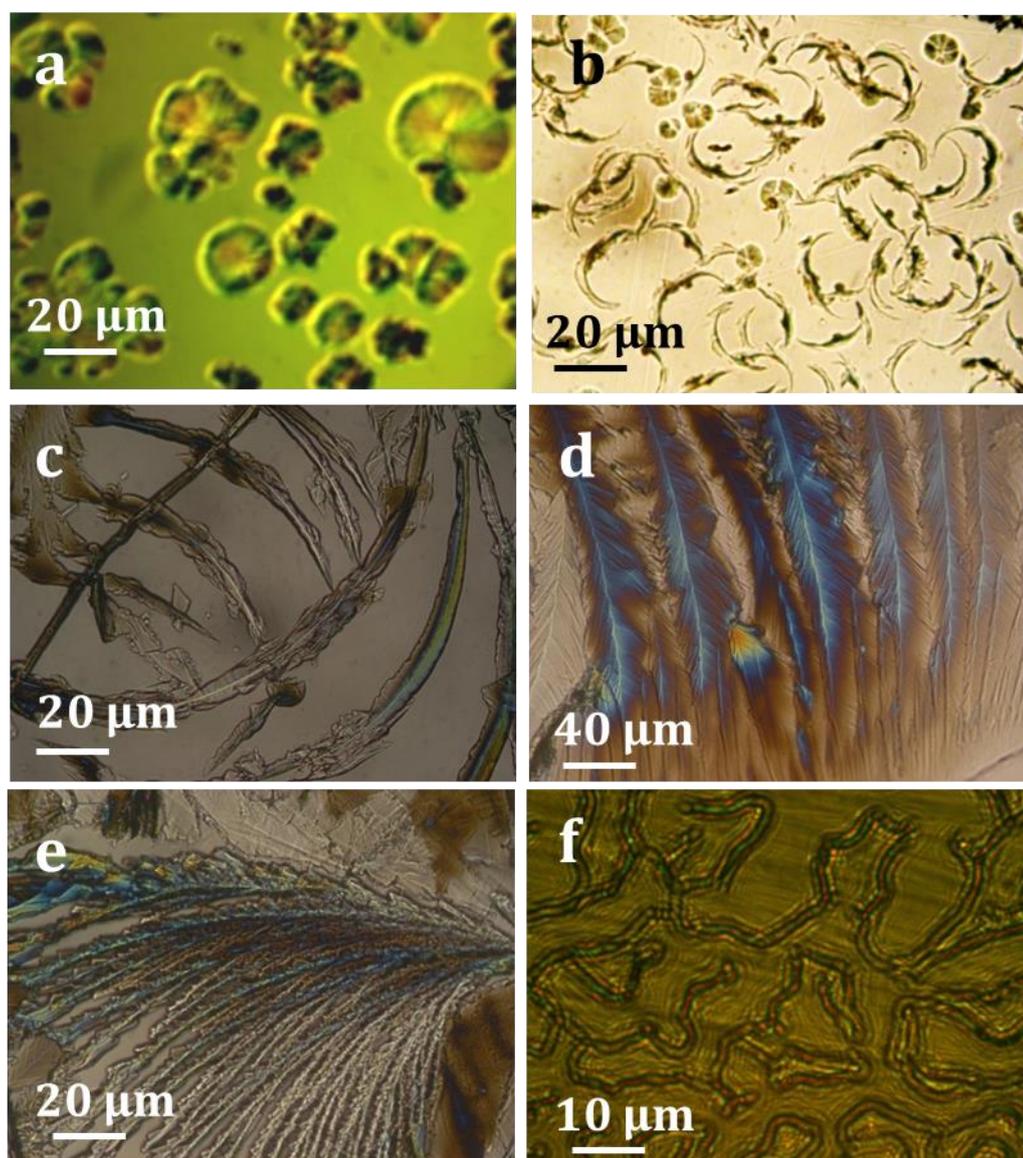
Figure 4.3. PLM images of FLAGs (a) spherullites in the initial stage of FLAG1 (b) self- assembling and co-structuring of FLAG1 (c) FLAG2 (d & e) feather and quill like morphology of FLAG3 and (f) branched tape like morphology of FLAG4

Evolutions of morphological changes in FLAGs were studied using various microscopic techniques such as PLM, SEM and TEM. FLAGs exhibited different mesophases depending upon the amount of AMD, laponite and time and as shown in Figure 4.3. The initial stage of FLAG1 observed as birefringent distorted spherullites dispersed in an isotropic medium under PLM and is shown in Figure 4.3 (a). Then, these discs were self- assembled to form specific texture as shown in Figure 4.3 (b). Later, these domains were observed to be elongated through edge to edge interaction to form branched structures in FLAG2 as shown in Figure 4.3 (c). Here, the self-assembled bilayer of AMD is co-structuring with the laponite discs in various fashions. The branched quill and feather morphology of FLAG3 is shown in Figure 4.3 (d) and (e). With increasing amount of AMD, branched nematic tapes were observed in FLAG4 as shown in Figure 4.3 (f).

Further morphology of the FLAGs was studied by SEM and the images are shown in Figure 4.4. Figure 4.4 (a) showed SEM image of single disc having flowery edges of self-assembled AMD and laponite in FLAG1. SEM image of freshly prepared FLAG2 exhibited as thick edged isolated discs and later, these discs piled up hierarchically by edge to edge ordering as shown in Figure 4.4 (b). These observations were further supported by the results observed during PLM studies. As the amount of AMD increased, these domains transformed into feathers/plume and tape like morphology in FLAG3 and FLAG4 as shown in Figure 4.4 (c) and (d) respectively. Thus by controlling the experimental conditions, the multiscale hierarchical arrangement of the domains can be obtained for various liquid crystalline phases.
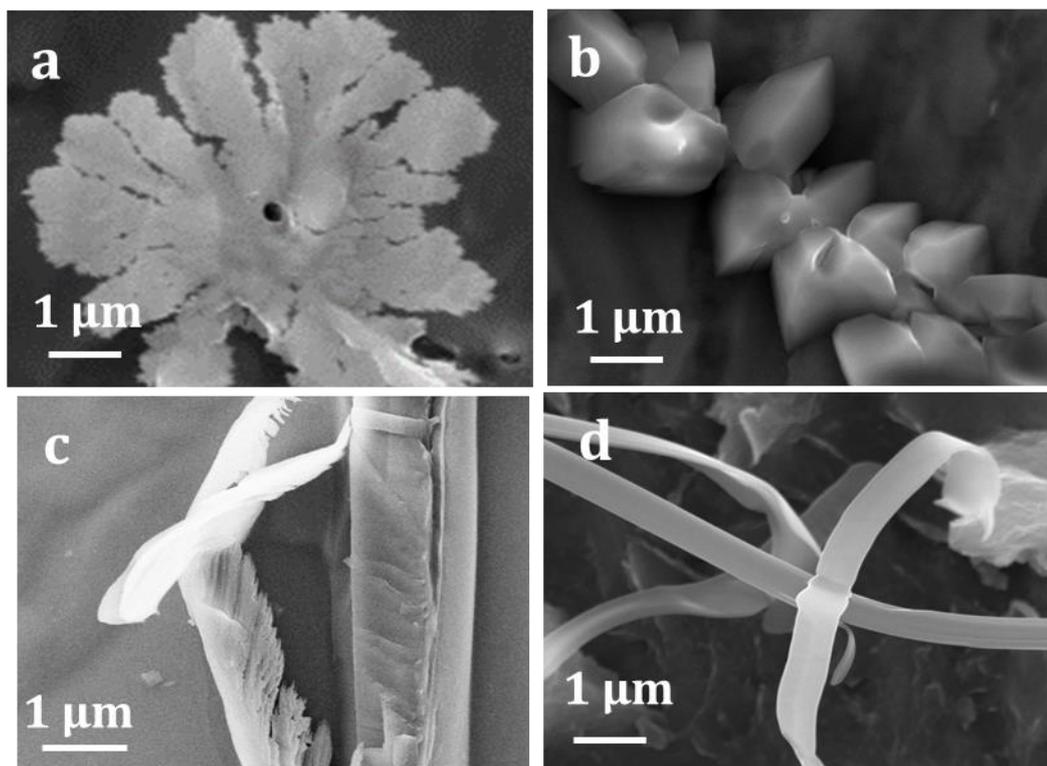
Figure 4.4. SEM images (a) freshly prepared FLAG1 (b) FLAG2 (c) branched morphology of FLAG3 and (d) the fibrillar tape like morphology of FLAG4

TEM image of FLAG4 taken under different magnifications are shown in Figure 4.5 (a) and (b). It exhibited tape like morphology and a number of well-defined dark fringes were observed inside the tape. The contrast in the TEM image is strongly depending on their orientation with respect to the electron beam. Diffraction contrast is strong when the laponite nano discs are seen with their basal plane parallel to the electron beam. Pronounced Fresnel fringes appeared on each side of the diffracting platelets and are shown in Figure 4.5 (b). These fringes are considered to be originated from the development of various interactions among the individual moieties present in FLAG4. The dimensions of the fringes are measured to be ~30–40 nm and are almost matching with the theoretical dimension of the functionalized monodiscs of laponites.
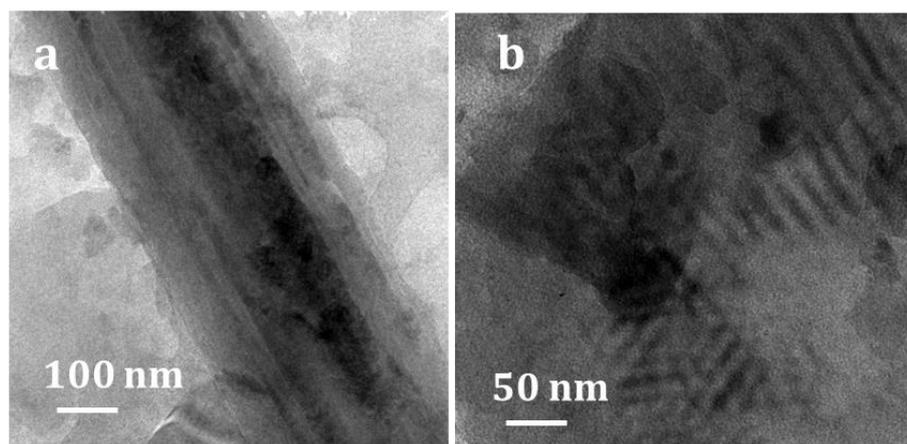
Figure 4.5. (a) TEM image of FLAG4 showing tape morphology and (b) Magnified image of tape like morphology in FLAG4 showing the Fresnel fringes of laponite discs

The non-covalent interactions between laponite and AMD during the self-assembly process leading to the formation of supramolecular structures in FLAGs were evidenced from the results obtained by FT–IR spectroscopy and XRD. The FT–IR spectra of LAP, AMD and FLAG4 are shown in Figure 4.6. Spectrum of LAP exhibited two sharp bands at 3630 cm^{-1} and 3685 cm^{-1}, attributed to the presence of Si–OH and Mg–OH stretching vibrations which are distinct to the varying micro environments in the laponite structure. It exhibited bands at 3465 cm^{-1} (–OH stretching), 1640 cm^{-1} (physisorbed water), 1007 cm^{-1} (stretching vibration of Si–O and Si–O–Si moieties), and 640 cm^{-1} (stretching vibration of Mg–O linkage). FT–IR spectrum of AMD exhibited characteristic amide I and amide II bands at 1636 cm^{-1} (–C = O stretching) and 1545 cm^{-1} (–C–N stretching in combination with –N–H bending). The band at 3300 cm^{-1} is attributed to –OH and –NH stretching vibrations of the AMD and the band at 2896 cm^{-1} is corresponds to the stretching vibrations of the –CH$_2$ moiety. The characteristic spectral bands of Mg–O (1007 cm^{-1}) and Si–O–Si (640 cm^{-1}) which was observed in LAP is shifted to 963 cm^{-1} and 591 cm^{-1} and the distinctive vibrations corresponds to amide bands present in AMD observed at 1636 and 1545 cm^{-1} are measured to be shifted to 1585 cm^{-1} and 1480 cm^{-1} in FLAG4. Further, the

characteristic bands of –OH and –NH stretching vibrations in LAP (3630 cm^{-1} and 3685 cm^{-1}) and AMD (3300 cm^{-1}) was appeared as a broad band at 3000–3500 cm^{-1} in FLAG4 confirmed the extensive hydrogen bonding interaction between the laponite and AMD.   The shifts in the characteristic bands of AMD and LAP in FLAG4 revealed extensive hydrogen bonding and the non-covalent interactions between these two moieties induce the formation of self-assembled aggregates of mesophase and stable gel phase.
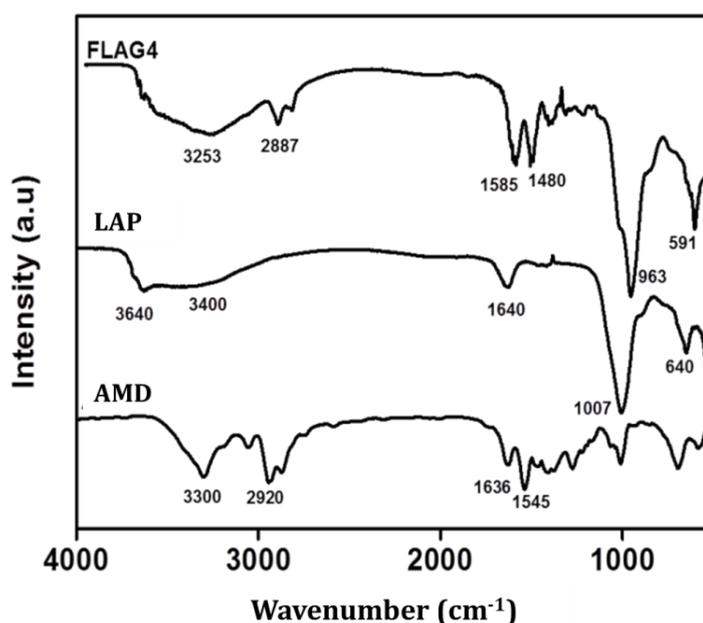
Figure 4.6. FT–IR spectra of LAP, AMD and FLAG4

Functional hydroxyl groups in FLAGs were estimated by chemical analysis. Results showed that the FLAG4 has high hydroxyl value (3.04 mmol/g) when compared to LAP (0.94 mmol/g) which confirmed the presence of amide and hydroxyl functional groups in FLAGs apart from the unreacted charges.

The d-spacing between the laponite discs and dimension of the aggregates in FLAG was studied by XRD. The XRD spectra of AMD, LAP and FLAGs are shown in Figure 4.7.
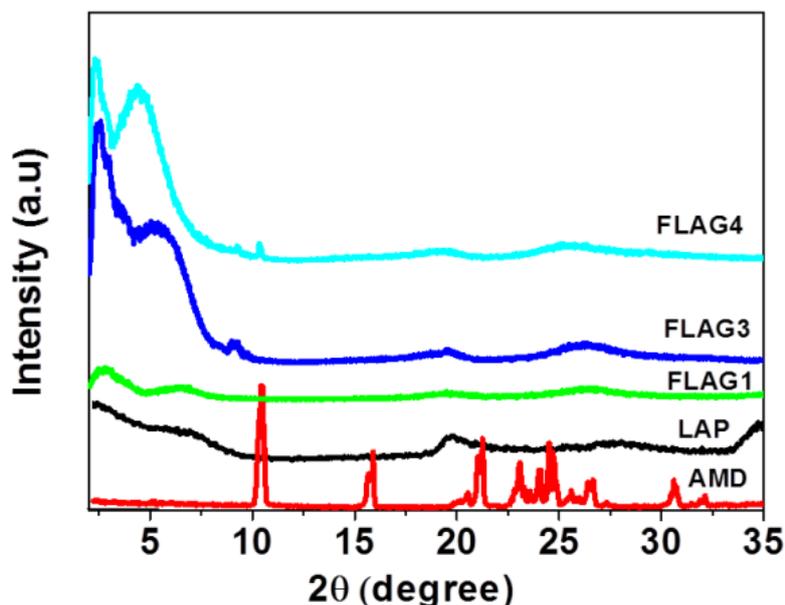
Figure 4.7. XRD of AMD, LAP, FLAG1, FLAG3 and FLAG4

The diffraction pattern of LAP exhibited broad diffraction peak at $2\theta = 6.64°$ corresponding to inter planar d spacing of ~13.3 Å which can be related to the d001 basal plane oriented parallel to the substrate surface. The exact position of this peak may vary as a function of relative humidity. XRD of AMD exhibited well-defined peaks at $2\theta = 10°, 15°, 21°, 23°, 26°, 30°$ and $32°$ revealing its highly crystalline nature. Nevertheless, the XRD plot of FLAGs exhibited entirely different diffractograms in terms of shape and position of peaks in comparison with LAP and AMD suggesting the formation of supramolecular structure. FLAGs exhibited two peaks at lower angles between 2θ ~2 to 6° revealing the formation of highly ordered supramolecular ensembles with dimension of 30–40 Å and shift in the d spacing of the laponite disc. The nature and position of this peak varied with the amount of AMD in FLAGs. FLAG1 showed peaks at $2\theta = 6.2°$ (15.4 Å shift in the d-spacing of laponite) and $2\theta = 2.8°$ (32.08 Å related to the dimension of the supramolecular ensemble) agree with the dimension of the supramolecular ensembles. FLAG3 showed broad peak at $2\theta = 5.2°$ (17.11 Å– shift in the d-spacing of laponite) and a sharp peak at $2\theta = 2.54°$

(35.84 Å related to the dimension of the supramolecular ensemble). FLAG4 exhibited peaks at 2θ = 4.3° (20.53 Å - shift in the d-spacing of laponite) and 2θ = ~ 2.2° (40.52Å) agree with the dimension of the ensembles. The peaks corresponding to AMD is diminished in the XRD spectra FLAGs due to the amorphous nature of gels. The formation of these supramolecular ensembles was further supported by PLM and SEM.

Rheological properties of composites rely on the size, shape, entanglement and periodicity of the components. Viscoelastic properties of gels are functions of critical oscillatory strain, phase angle, storage modulus, loss modulus and viscosity (Zhang et al., 2005; Xu et al., 2015).
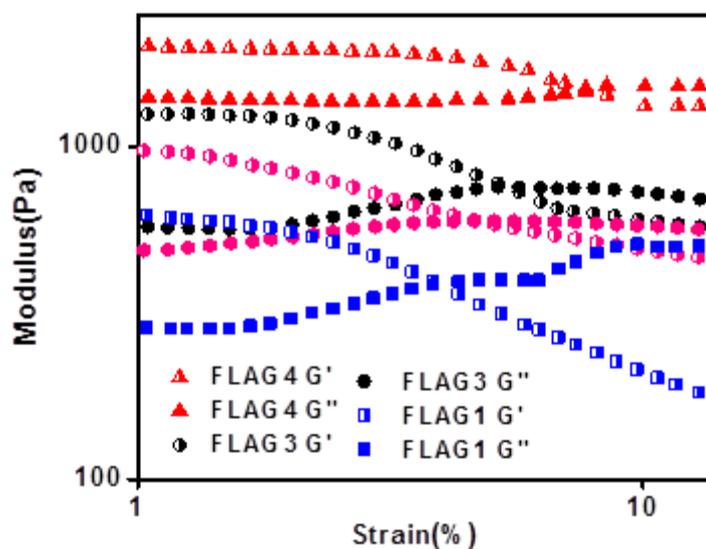
Figure 4.8. Amplitude sweep of FLAG1, FLAG3 and FLAG4

The linear viscoelastic regime is identified by performing experiments at constant frequency under strain sweep. The stress-strain curve was plotted and the linear region is observed at strain values of ~1–2 %. The storage/loss modulus versus amplitude strain sweep profile of FLAGs is shown in Figure 4.8. The cross over point indicates the elastic nature of gel is changed into its viscous nature. The cross over

point obtained for FLAG1, FLAG2, FLAG3 and FLAG4 is 3.5 %, 4.2 %, 5.6 %, and 6.9 % respectively confirmed the role of AMD for establishing robust nature for FLAGs.

The angular frequency dependent storage modulus and loss modulus of FLAGs and LAP were studied at constant strain (1%). Typical plots showing angular frequency versus storage modulus (G′) and loss modulus (G″) is shown in Figure 4.9 (a). At lower frequency region, the variation of G′ and G″ is independent of angular frequency where the applied frequency does not considerably affect the three-dimensional structure of the gels which is the signature for the true gel formation. The gap between storage and loss modulus increases with increase in the concentration of AMD revealed that as the amount of AMD increases, the elastic modulus is enhanced due to the high extent of crosslinking density. The difference in the modulus for LAP, FLAG1, FLAG2, FLAG3 and FLAG4 are observed to be 730 Pa, 938 Pa, 984 Pa, 1073 Pa, and 1290 Pa respectively. Time-dependent rheological studies were carried out to study and predict the effect of aging on the gel strength. Freshly prepared gel samples showed storage modulus of 831.3, 1193.7, 1295.26, 1552.12, and 2085.3 Pa for LAP, FLAG1, FLAG2, FLAG3, and FLAG4 respectively. However, storage modulus values found to be increased with time attributed to the establishment of more hydrogen bond interactions between these two entities in various fashions. Time-dependent changes in the storage modulus of FLAG4 is measured as 2341, 2784, 3321, 3890, 4512, 4514, 4515 Pa, which is quite high elastic and solid like behaviour compared with the freshly prepared sample. After one week, the storage modulus was observed to be making an only small variation in the storage modulus.
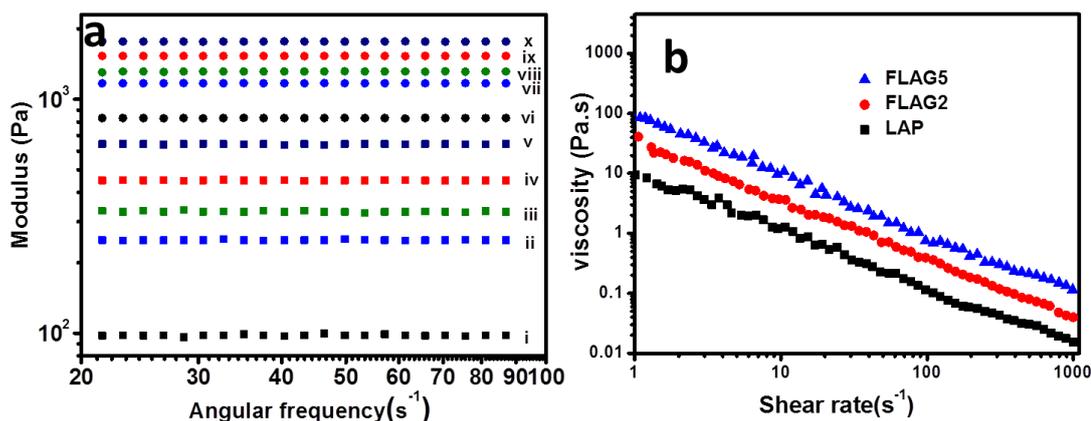
Figure 4.9. (a) Double logarithmic plot of angular frequency versus loss and storage modulus profile for LAP and FLAGs (i) LAP G′ (ii) FLAG1 G′ (iii) FLAG2 G′ (iv) FLAG3 G′ (v) FLAG4 G′ (vi) LAP G″ (vii) FLAG1 G″ (viii) FLAG2 G″ (ix) FLAG3 G″ (x) FLAG4 G″and (b) Double logarithmic plot of shear rate versus viscosity of FLAGs showing shear thinning behaviour

It has been reported in Ericksen's theory that liquid crystalline materials may exhibit the high degree of structural ordering, and the domains will be arranged in specific fashion to obtain molecular orientation. Under shear flow, structural rearrangement may occur in the internal polydomain structure of liquid crystalline materials. Each domain is having high degree of molecular orientation. With increasing shear rate, there is a successive destruction of the polydomain structure into smaller domains. Accordingly, the lamellar liquid crystalline phase of FLAGs is also composed of ordered hierarchical structures of polydomains. With increasing shear force, they slide upon one another to form smaller domains and a sudden decrease in the viscosity value. The double logarithmic plot of shear rate versus viscosity is given in Figure 4.9 (b), viscosity decreased with increase in shear rate according to the power law behaviour, $\eta = K\gamma^n$. This observation also supports the shear thinning behaviour and supported by the observation made by Onogi and Asada in the rheological studies of liquid crystalline materials (Onogi et al., 1980; Viola et al., 1986).

4.3.2. Mechanism for the formation of mesophases

A plausible mechanism for the formation of various mesophases was manifested from the studies made by FT–IR, microscopic analysis, XRD and rheology. FLAG comprises highly exfoliated nanodiscs with negative charges on the surface, the partial positive charge on the edges and Mg–OH and Si–OH groups at the broken edges. AMD contains two amide groups and two hydroxyl groups. Hence, there is a competition of various non-covalent interactions among laponite-laponite, laponite - AMD and AMD - AMD via hydrogen bonding, dipole-dipole and electrostatic interactions of hydroxyl groups, amide groups and ionic charges. Apart from this laponite–AMD–water interaction also plays a crucial role in the liquid crystalline phase formation. When laponite is in contact with water, water molecules may penetrate into the interlaminar space and push the laponite discs apart. At high concentration of laponite, the suspension spontaneously turns into an opaque gel. Under PLM, the formation of schlieren liquid crystalline phase was observed. Schlieren liquid crystalline phase formation is due to the periodicity arising from the face to face mutual orientation among the functional laponite discs. Formation of various liquid crystalline phases on increasing AMD concentration in FLAGs can be explained due to changes in the periodicity, defect formation, molecular packing and nano-segregation during the mesophase formation which varies with the experimental conditions. FLAGs are observed as transparent gels and the photograph of the same are given in Figure 4.10.
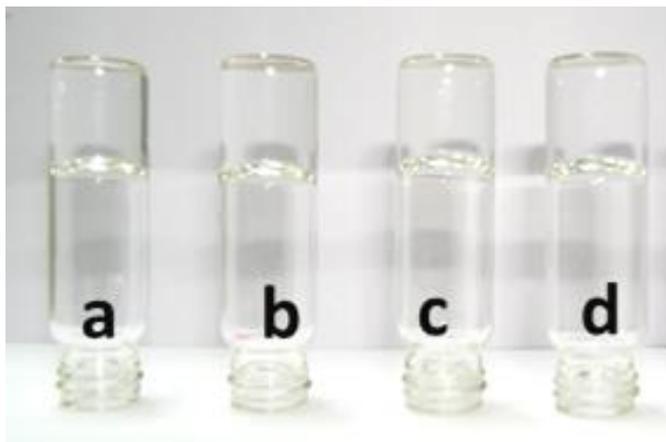
Figure 4.10. Photographs of FLAGs (a) FLAG1, (b) FLAG2, (c) FLAG3 and (d) FLAG4

The supramolecular interactions among laponite and AMD form spherullites in the isotropic medium. Slowly these spherullites elongated by a growth process of etching and self-assembling. It self-assembles in two ways, either zigzag to form bush or edge to edge etching to form feather/plume type structures. Later, in presence of excess AMD, more amount of self-assembled AMD adhere on the surface of the branched stems (templates) to form arrays of highly birefringent feathers or leaves and multiwalled tapes by co-structuring and self-assembly process among functionalized laponites and AMD. This observation is supported by our earlier studies made on laponite based nanocomposites (Sudha et al., 2011). The various liquid crystalline phases formed by FLAGs are further supported by the work reported earlier (Dufour et al., 2001). They suggested that organo-modified laponites can undergo various structural transformations such as star,vesicular and more disorganized bundle-like structures based on the experimental conditions (Mourchid et al., 1998; Jeroen et al., 2005). Thus, by controlling the concentration and time parameters in FLAG, we can design stable mesophases through non-covalent interactions by self-assembly approach. This synthetic design can be exploited for the development of multi-scale and hierarchical functional materials from low molecular weight organic molecules.

Schematic representation showing various supramolecular structural organizations among the components in the FLAG is depicted in scheme 4.1.
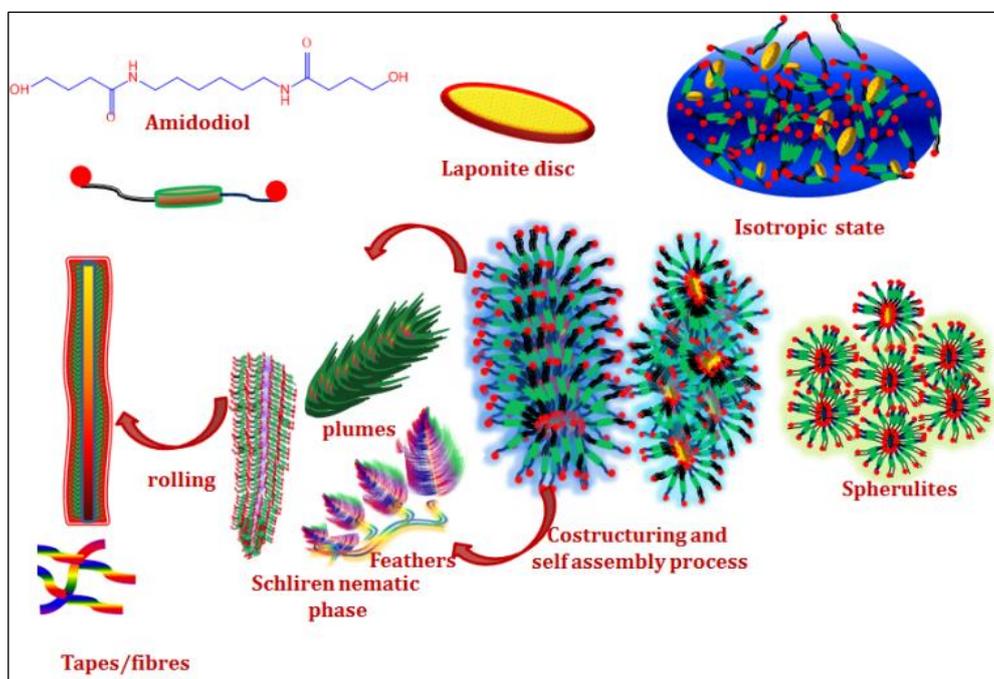
Scheme 4.1. Schematic representation for the formation of various mesophases via supramolecular self-assembly of laponite and AMD

4.3.3. Electrochemical studies

The electrochemical impedance spectroscopic (EIS) analyses were carried out to study the electron transfer process of the surface modified electrodes. The Nyquist plots of GCELAP/GCE and FLAG/GCE with $Fe(CN)_6^{3-/4-}$ are shown in Figure 4.11 (a). The circuit diagram used to fit the data is shown in the inset. The equivalent circuit diagram is composed of solution resistance (R_s), constant phase element (CPEQ), charge transfer resistance (R_{ct}) and Warburg impedance (W). The graph showing imaginary impedance versus real impedance showed two regions, initially a semicircle region lying in the Z'' axis followed by a straight line. The typical Nyquist plot consists of semicircle region at higher range of frequencies corresponds to the

charge transfer kinetics and the linear part at the lower range of frequencies representing diffusion limited electron transfer process (Barsoukov et al., 2005).
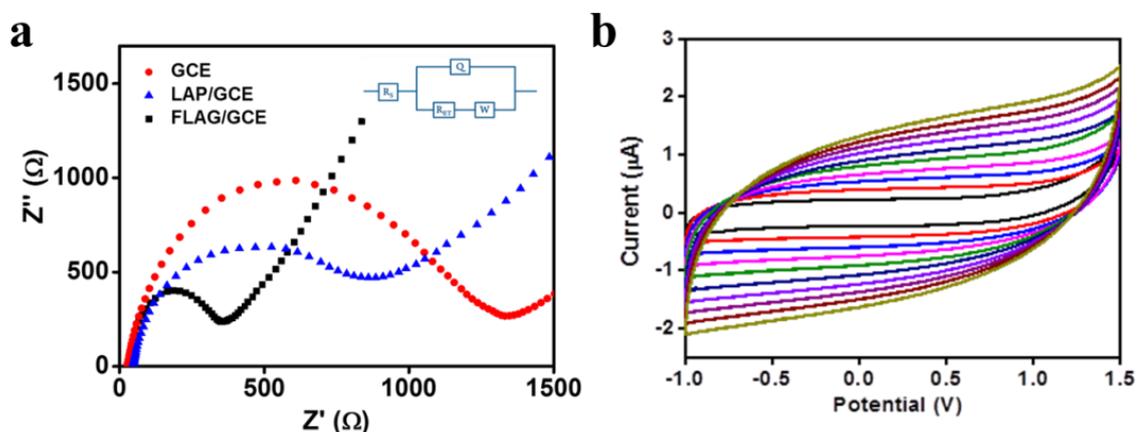
Figure 4.11. (a) Nyquist plots of GCE, LAP/GCE and FLAG/GCE and (b) Cyclic voltammogram of FLAG/GCE with scan rate ranging from 0.01 to 0.1V

The diameter of the semicircle region decreased in FLAG/GCE on comparison with GCE and LAP/GCE. The R_{ct} values of bare GCE, LAP/GCE, and FLAG/GCE are 1124 Ω, 640 Ω and 245 Ω respectively. The high conductivity of FLAG/GCE may be suggested due to high anisotropic liquid crystalline ordering of FLAG. The cyclic voltammograms of FLAG4 is shown in the Figure 4.11 (b). They showed a good rectangular electrochemical window between -0.4 to 1 V and hence these gel electrolytes are suitable for the application in capacitors and batteries. The stability of electrochemical window is retained even at higher scan rates with high current density.

The galvanostatic charge-discharge measurements were carried out within the potential window of -0.4 to 1.5 V at various current densities ranging from 0.02 to 0.41A/g is shown in Figure 4.12 (a). Galvanostatic charge-discharge studies showed symmetrical charge-discharge profile which suggests that the FLAG4 exhibit ideal electrical double layer capacitive behaviour without any redox reaction involved. For

a constant current density of 0.02A/g, the specific capacitance of the cell has calculated as 1856 mF/g illustrating the excellent energy storage capability of the material. The specific capacitances of FLAG4 is calculated as 1856, 1799, 1676, 1640, 1610 and 1598 mF/g at current densities of 0.02, 0.04, 0.06, 0.08, 0.16 and 0.41 mF/g, respectively. On increasing the current density, there observed a steady lowering of specific capacitances due to faster discharging.
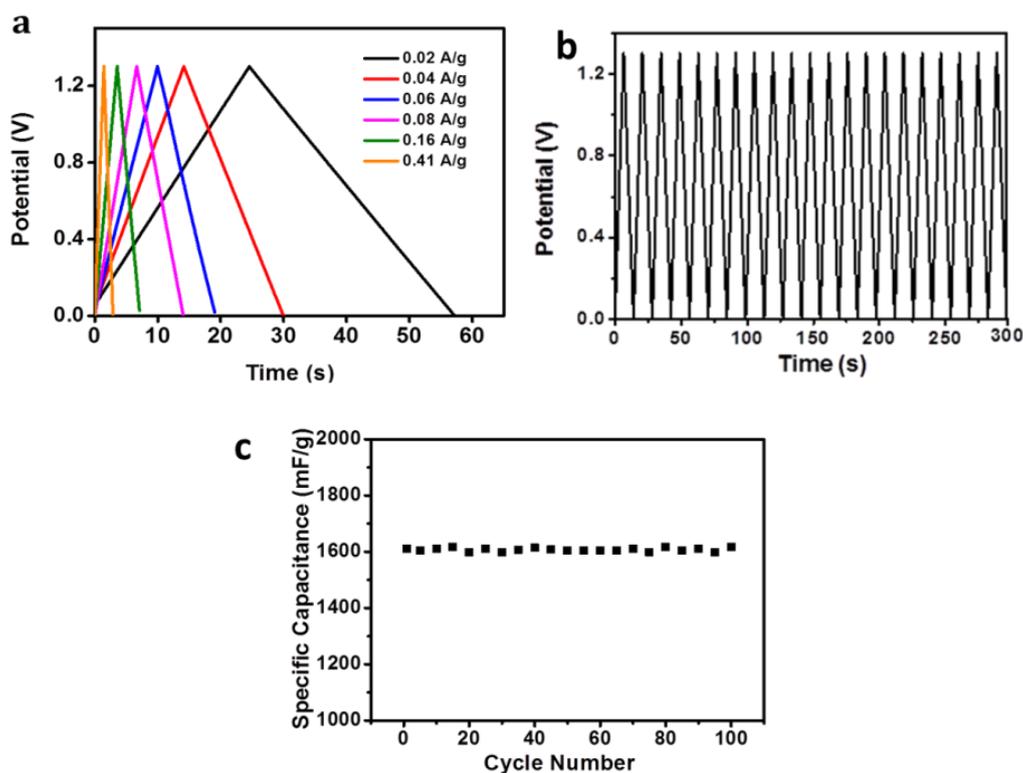
Figure 4.12. (a) Charge–discharge voltage profiles at various current densities ranging from 0.005 to 0.2 A/g (b) Cycling performance of FLAG4 for 100 cycles at a current density of 0.1 A/ g and (c) Variation of specific capacitance with cycle number at a current density of 0.1 A/g

Cycling performance plays an important role in determining the efficiency of the super capacitors for real life applications (Choudhury et al., 2009; Masarapu et al., 2009). Capacity retention of the device was analyzed by carrying out repetitive charging and discharging for 100 cycles. The device gave 99% retention of specific capacitance even after 100th cycle indicating its high cycling stability. Cycling

performance of FLAG4 for 100 cycles at a current density of 0.1 A/g shown in Figure 4.12 (b). The variation of specific capacitance with cycle number is given in Figure 4.12 (c).

FLAG exhibit conductivity 540 µS/cm and is attributed to the presence of Na$^+$ ions. The sodium ions which are present in the interlayer gallery dissociate and may responsible for the ionic conductivity. The AMD moiety can induce an anisotropic liquid crystal ordering in the gel and leads to low impedance and ideal capacitive behaviour. It has been reported earlier that liquid crystalline ordering can enhance the conductivity by augmenting mobility of ions through the ordered channels which are present in between the domains (Cheng et al., 2014; Zhou et al., 2011). The high ionic conductivity and the viscoelastic properties of the FLAG, revealed its utility as prospectable gel electrolyte for energy storage systems.

4.4. Conclusion

Supramolecular functional liquid crystalline gel with tape like morphology was prepared by the self-assembly process through various non-covalent interactions among the laponite and AMD entities. Spectroscopic, microscopic and rheological studies revealed that gelation, morphology, viscoelastic properties are functions of the concentration of components and time. The various mesophases phases observed can be related to the change in the periodicity of self-assembled aggregates which depend on the non-covalent interactions among laponite and AMD. The electrochemical studies showed a stable electrochemical window (-0.4V to 1.5V) and galvanostatic studies showed a specific capacitance of 1856 mF/g and good cycling stability which suggested its application as a gel electrolyte in capacitors and batteries. These

functional soft tapes were endowed with functional groups like amide and hydroxyl groups and can be exploited for many applications in high technological areas.

4.5. Experimental

4.5.1. Materials

Laponite RD (Southern Clay Products) was used as received. It is having cation exchange capacity of 60 meq/100g. γ–butyrolactone purchased from Fluka, hexamethylene diamine, isopropanol, acetone, methanol, were purchased from s.d. fine chem. Ltd, Bombay, India and were used without further purification. All solutions were prepared in Milli–Q purified water.

4.5.2. Preparation of FLAGs

0.05 g of laponite was dissolved in 1 ml of distilled water and then it was thoroughly mixed with 1 ml of 1% AMD solution at 60 ^{0}C for 5 minutes. Then the sample kept undisturbed at room temperature. After 24 hours, transparent soft gel was obtained. FLAGs were prepared by varying the percentage of AMD (0.4 to 1.5) and are designated as FLAG1, FLAG2, FLAG3 and FLAG4 respectively. Control sample was prepared with the same procedure in the absence of AMD and designated as LAP.

Sample	Weight of laponite(g)	Weight of AMD(g)	Water (ml)	Appearance
FLAG1	0.05	0.004	2	Soft transparent gel
FLAG2	0.05	0.006	2	Soft transparent gel
FLAG3	0.05	0.008	2	Soft transparent gel
FLAG4	0.05	0.01	2	Soft transparent gel
LAP	0.05	----	2	Soft transparent gel

Table 4.1. Experimental details of FLAGs

4.5.3. Estimation of hydroxyl value

The hydroxyl value of laponite and FLAGs were estimated by chemical analysis. Hydroxyl number is the milligrams of potassium hydroxide equivalent to the hydroxyl content of 1 g of material. The substance (w ~0.5 g) was taken in a dry and pure stoppered conical flask. To this 20 mL of acetylating mixture (1 volume of acetic anhydride and 8 volume of pyridine) was added, shaken well and kept in a water bath. A blank was also prepared. It was kept for 5 hours under reflux. After acetylation, 50 ml of water was added and titrated to phenolphthalein with 0.5N NaOH. From the volume of blank titration (A) and sample titration (B) will give the amount of acetyl bound to the hydroxyl group.

$$\text{Hydroxyl number} = \frac{(A - B) \times N \times 56.1}{w}$$

Where, N is the normality and w is the weight of sample

4.5.4. Electrochemical studies

The ITO plates were cut into pieces of 2×2 cm using glass cutter and were subjected to 5-minutes cleaning in acetone, isopropanol, and distilled water by ultra-sonication and were dried. The test cells fabricated by sandwiching FLAG hydrogel between transparent conducting ITO coated glass electrodes were used for cyclic voltammetric and galvanostatic charge-discharge (GCD) studies. The specific capacitance values were calculated from the below equation using GCD results

$$\text{Specific capacitance} = \frac{4I \, \Delta t}{m \, \Delta v}$$

Where, I, is discharge current in ampere, Δt, is the discharging time, Δv, is the potential window during the discharge process, and m, is the mass of the material in gram.

4.5.5. Characterization techniques

Wide angle X-ray diffraction (WAXD) measurements were performed using XEUSS SAXS/WAXS system by Xenocs. Cu Kα with a wavelength, $\lambda \sim 1.54$ Å is used as the source. All the measurements were carried out in the transmission mode. The d-spacing of the nanocomposite was calculated from the angular positions 2θ of the observed d001 reflection peaks based on the Bragg's formula $n\lambda = 2d \sin \theta$, where λ is the wavelength of the X-ray beam and θ is the diffraction angle. Liquid crystalline phase formation was observed under polarized light microscope (PLM) (Olympus BX51 equipped with camera). The electrochemical impedance measurements were performed at a frequency range of 0.1 Hz to 10 kHz at an open circuit potential of 1V in a three electrode one compartment electrochemical cell in which glassy carbon electrode served as working electrode and a platinum wire used as a counter electrode. All the potential were recorded using Ag/AgCl as the reference electrode. Prior to electrochemical experiments, GCE was polished with 0.03 mM alumina and ultrasonically cleaned for about 5 minutes in doubly distilled water. Finally the electrode was washed thoroughly with double distilled water. All the experiments were carried out at 25 ± 5 °C. Before performing the experiments, the solution was purged with nitrogen gas for 10 minutes. Ionic conductivity is measured with JENWAY 3540 pH and conductivity meter.

CHAPTER 5

DEVELOPMENT OF NANOSILVER PATTERNED LIQUID CRYSTALLINE GEL AND ITS APPLICATION AS ELECTROCHEMICAL SENSOR
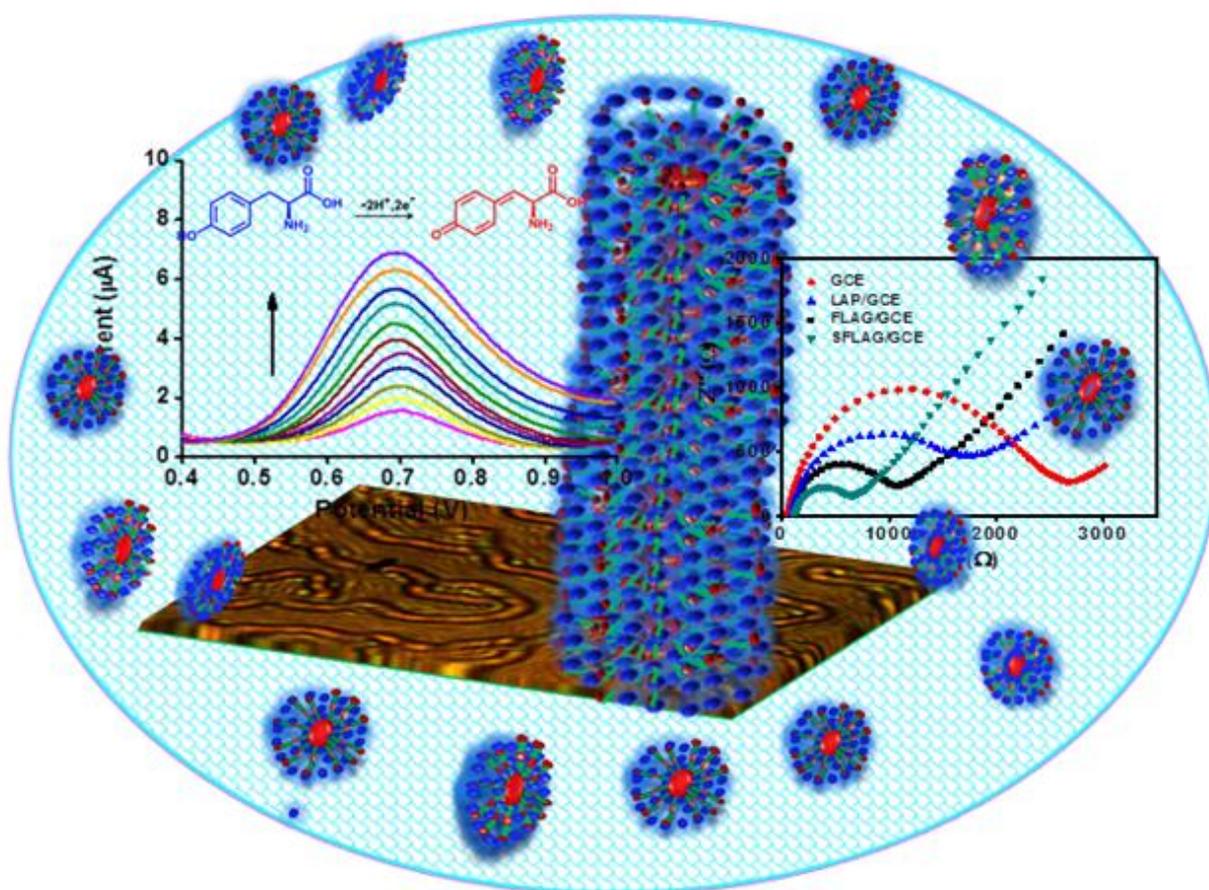
5.1. Abstract

In this chapter, we have prepared silver nanoparticle patterned laponite – AMD hydrogels (SFLAG) through self-assembly process. Formation of liquid crystalline gel phase was studied by microscopic techniques and rheology. The surface plasmon energy of SFLAGs was observed at ~400 nm and the FCC lattices of silver particles were confirmed with XRD. The low R_{ct} (96 Ω) values measured from electrochemical impedance spectra revealed high conductivity of the SFLAG modified glassy carbon electrode (SFLAG/GCE). Further, SFLAG/GCE is demonstrated as an electrochemical sensor for L–tyrosine with a high current response and lower detection limit of 10 nM. Electrochemical sensor performances such as interference, selectivity, reproducibility, repeatability, storage stability and the real sample analysis with human blood serum were studied. All these excellent results suggested its application for the clinical diagnosis of L–tyrosine.

5.2. Introduction

Developments of noble metal nanoparticles patterned liquid crystalline hydrogels are receiving importance in many technological areas such as sensors, catalysis, drug delivery, actuators, etc. because of the ordered arrangement. Low molecular weight organic molecules such as amino acids, peptides and cholic acid can self-assemble to form liquid crystalline supramolecular hydrogels. Synthesis of nanoparticles in hydrogel matrix is gaining importance due to the better stabilization and easy access of nanoparticles within the porous 3D hydrogel network (Mitra et al., 2008; Yang et al., 2006; Kobayashi et al., 2002). The preparation of ordered nanoparticles in patterned arrays using liquid crystalline phases are reported to be excellent strategy. Liquid crystalline template based synthesis of inorganic nanostructures were reported earlier (Asghar et al., 2015; Sharma et al., 2014; Atard et

al., 1995). Liquid crystalline phase can also act as structure directing agents and also stabilizes the nanoparticles at the interface between hydrophobic and hydrophilic domains of mesophase separated environment. Hierarchically structured liquid crystalline molecules offer more flexibility in tailoring the functionality and mechanical properties of the gels. Optimal properties can be tuned using the liquid crystalline gelator which can self-assemble in a nanometer scale and capable of generating ion-conducting network. The microphase segregation and the interaction between the components play crucial role in the anisotropic ordering and the formation of liquid crystalline phases. The liquid crystalline gels exhibit anisotropy which significantly enhances the conduction and finds application in electrochemical devices (Tunkara et al., 2014; Firestone et al., 2002). Stabilization of metal nanoparticles in the liquid crystalline soft molecular hydrogels significantly enhance the electrical and thermal conductivity, faster response and mechanical strength (Zhou et al.,2012; Senyuk et al., 2012; Nguyen et al., 2014; Mirzaei et al.,2014; Ji et al.,2012; Xue et al., 2015; Nguyen et al., 2015).

Among the noble metal nanoparticles, silver nanoparticles are easily reducible, exhibit strong SPRE in the visible region, high excitation efficiency, unique optical, and electronic properties. They find application in electrochemical devices, plasmonic waveguides, as well as in biomedical and chemical sensing via surface-enhanced Raman scattering and surface-enhanced fluorescence (Daniel et al., 2013; Varaprasad et al., 2011; Zheng et al., 2012). The development of low molecular weight liquid crystalline gelators that itself can reduce silver ions and stabilizes nanoparticles in patterned arrays is a challenge. The high surface area and anisotropic long range electron conduction pathway of nanoparticles synthesized in a liquid crystalline

hydrogel is expected to enhance its efficiency in applications such as catalysis, sensors, batteries due to efficient mass transport and interfacial processes.

L–tyrosine is considered as a biomarker and is used in the early detection of cancers. L–tyrosine concentration analysis helps in the study of metabolism and for the pathological staging for the classification of diseases. The lower concentration of L–tyrosine is responsible for albinism and a higher dosage may result in Parkinson's disease, atherosclerosis and cancer (Li et al., 2006; Quintana et al., 2010). Hence, a rapid and selective detection of L–tyrosine is of great significance. Several instrumental techniques are developed for the detection of L–tyrosine such as luminescence, fluorescence, high performance liquid chromatography and surface enhanced Raman spectroscopy (Lee et al., 2006: Letellier et al., 1997). These methods suffer drawbacks such as complicated pre-sampling, high cost, wastage of a large amount of chemicals, etc. The electrochemical method is a good alternative for the detection of L–tyrosine because of its good sensitivity, selectivity, rapid response, low cost, fast, simple and convenient to operate (Heli et al.,2014: Sheng et al.,2014). A large number of electrochemical methods are reported using modified electrodes such as gold nanoparticles, metal oxide nanoparticles, nafion/TiO_2 film, graphene oxide, single and multiwalled carbon tubes for the electrocatalytic oxidation of L–tyrosine (Cheng et al.,2009; Fan et al., 2011: Yu et al., 2008; Tang et al.,2010; Liu et al.,2012). The silver nanoparticle patterned liquid crystalline hydrogel can be considered as an efficient material for the electrode modification and for the sensing of L–tyrosine.

Ruzicka and Gabriel et al. extensively studied the nematic lyotropic liquid crystalline phases of laponite gels (Gabriel et al., 1996; Ruzicka et al., 2004). In the chapter IV, we have reported the synthesis of FLAG by the self-assembly between

laponite and AMD. The well-defined channels exposed with functional groups of FLAG can reduce silver ions to form patterned arrays of silver nanoparticles. The high surface area and surface energy of silver within the ordered channels is expected to enhance the conductive pathways for electrocatalytic activity. In the present programme, a liquid crystalline hydrogel is developed by the self-assembly of laponite and AMD and employed for the reduction of silver ions. The silver nanoparticles entrapped functionalized laponite amidodiol gels (SFLAG) were characterized by PLM, SEM, TEM, XRD, FT-IR and rheology. The electrochemical conductivity was studied with impedance spectroscopy. SFLAG modified GCE (SFLAG/GCE) expected to enhance the electrochemical performance and is demonstrated for the electrochemical sensing of L–tyrosine. The analytical performance of SFLAG/GCE validated using blood serum samples.

5.3. Results and discussion

5.3.1. Prepearation and characterizations of SFLAGs

Laponite interact with AMD to form FLAGs through various non-covalent interactions as reported in the chapter 4. By varying the concentration of AMD, the self-assembled functional tapes like morphology have been reported in FLAG4. The functional tapes were endowed with groups such as amide and hydroxyl apart from the free partial positive and negative charges present in laponite. All these functional groups can be effectively exploited for the synthesis of metal nanoparticles and utilized for the synthesis of silver entrapped functionalized laponite-AMD gels (SFLAGs). SFLAGs were synthesized by varying the concentration of silver and are designated as SFLAG1, SFLAG2, SFLAG3 and SFLAG4. The transparent to brown colour of the SFLAG gel indicates the formation of silver nanoparticles. The photograph of FLAG4

and SFLAGs are shown in Figure 5.1 (a) to (e). Apart from reduction of silver ion to silver, the functional groups such as the carbonyl groups are expected to enhance the stability of silver nanoparticles through partial coordination bonding. It was also observed that an increasing concentration of silver decreased the time of gelation and also enhanced the strength of the gel due to the crosslinking of self–assembled molecular layers through silver nanoparticles.
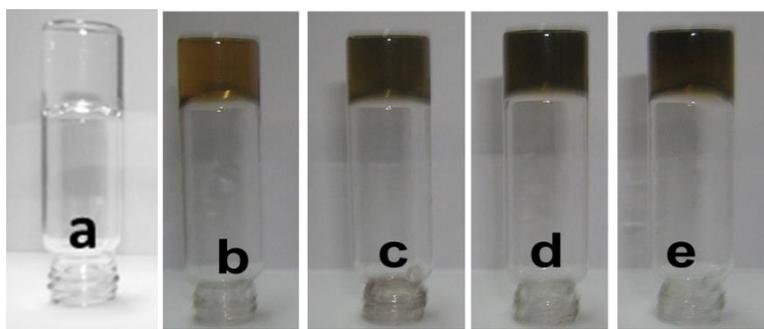
Figure 5.1. Photographs of (a) FLAG4, (b) SFLAG1, (c) SFLAG2, (d) SFLAG3 and (e) SFLAG4

The FT–IR spectra of AMD, LAP, FLAG4 and SFLAG2 are shown in Figure 5.2. The characteristic spectral bands of Mg–O (1007 cm^{-1}) and Si–O–Si (640 cm^{-1}) observed in LAP is shifted to 960 cm^{-1} and 606 cm^{-1} in FLAG4 and the distinctive vibrations corresponds to amide bands present in AMD at 1636 and 1533 cm^{-1} are shifted to 1592 cm^{-1} and 1494 cm^{-1}. Further, the characteristic bands of –OH stretching vibrations in LAP (3400 cm^{-1}) and AMD (3300 cm^{-1}) was appeared as a broad band at 3000–3500 cm^{-1} in FLAG4 confirmed the extensive hydrogen bonding interaction between the laponite and AMD. In SFLAG2, a broad band appeared at 3000–3500 cm^{-1} confirmed the presence of the hydrogen bonding. The Mg–O (960 cm^{-1}) and Si–O–Si (606 cm^{-1}) band observed in FLAG4 is shifted to 953 cm^{-1} and 593 cm^{-1} in SFLAG2. The distinctive bands of amide observed at 1592 and 1494 cm^{-1} in FLAG4 shifted to 1580 cm^{-1} and 1485 cm^{-1}. The shift in the peaks of SFLAG2 showed the partial coordinate bond between the carboxyl group, Mg–O and Si–O–Si with silver.

The extensive hydrogen bonding and the shifts in peaks confirmed the non-covalent interactions between these two moieties and also induce the formation of self-assembled aggregates and stable gel phase.
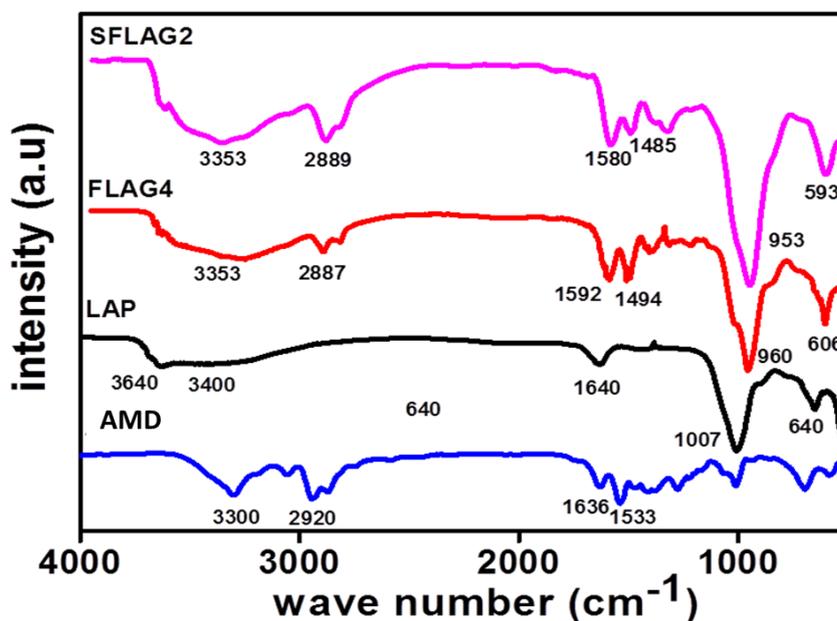
Figure 5.2. FTIR spectra of AMD, LAP, FLAG4 and SFLAG2

Typical diagrams showing angular frequency versus storage modulus (G') and loss modulus (G") is shown in Figure 5.3. The storage modulus is the characteristic of elastic or solid like behaviour and loss modulus (G") is correspond to the liquid like behaviour of the gel. The gap between the storage and loss modulus for FLAG4, SFLAG2 and SFLAG4 are observed to be 1270 Pa, 2288 Pa and 3077 Pa respectively. The difference in the modulus increases with the incorporation of silver indicating the enhancement of elastic modulus due to the efficient cross-linking of silver in the gel which increases the gel strength.
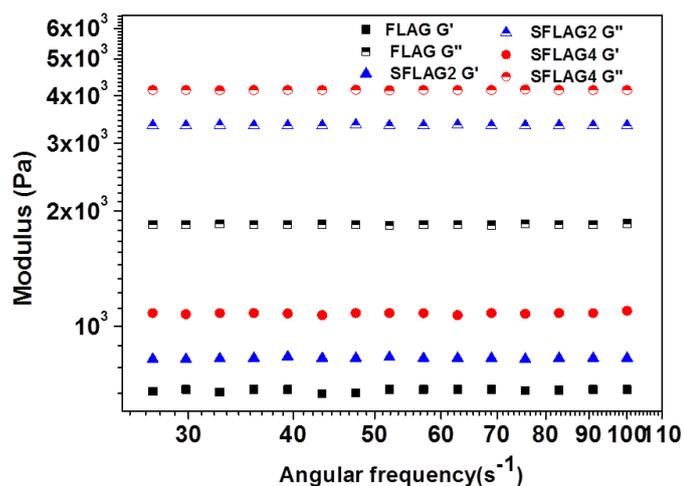
Figure 5.3. Double logarithmic plot of angular frequency versus storage modulus (G') and loss modulus (G'') of FLAG4, SFLAG2 and SFLAG4

The SEM images of SFLAGs are shown in Figure 5.4. The spherical and cuboidal silver nanoparticles were entrapped on the functional gel network of FLAG. Silver entrapped functional tape of SFLAG1 and SFLAG2 is shown in Figure 5.4 (a) and 5.4 (b). With increasing the concentration of silver nanoparticles, they form branched morphologies in SFLAG3 (Figure 5.4 (c)) and SFLAG4 (Figure 5. 4 (d)).
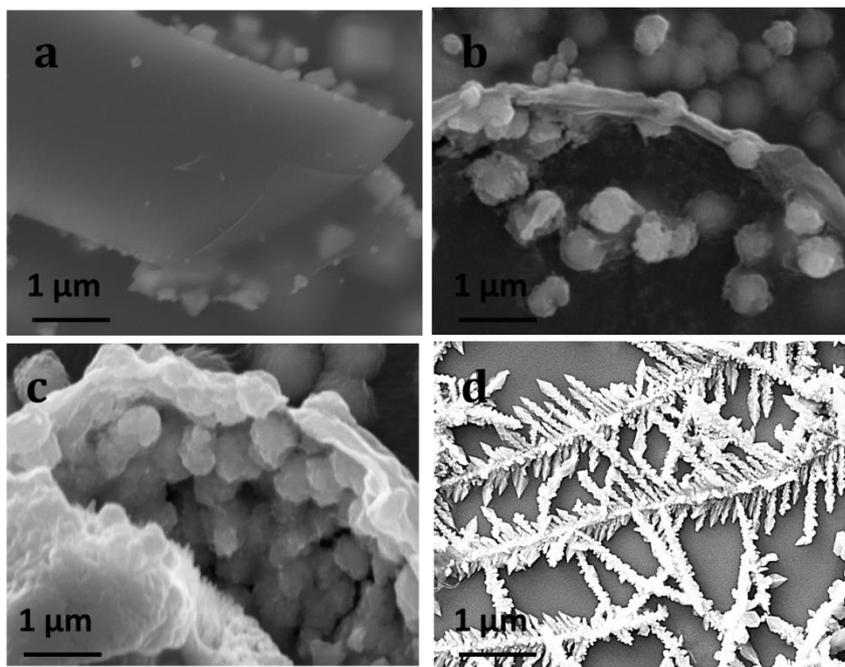
Figure 5.4. SEM images of SFLAGs. Silver nanoparticle entrapped tapes of (a) SFLAG1 (b) SFLAG2 (c) SFLAG3 and (d) branched morphology of SFLAG4

The TEM images also confirmed the formation of silver nanoparticle entrapped tapes in SFLAGs. Figure 5.5 (a) showed the formation of silver nanoparticle entrapped tapes in SFLAG1 and the magnified image of silver nanoparticles in these tapes is given in the inset. The silver entrapped tape of SFLAG2 is shown in Figure 5.5 (b).The branched morphology of SFLAG3 and its magnified image is shown in Figure 5.5 (c) and highly branched and aggregated morphology of SFLAG4 is given in Figure 5.5 (d). The EDS spectrum of SFLAG2 is given in Figure 5.5 (e) confirmed the presence of silver nanoparticles in the nanocomposite gels.
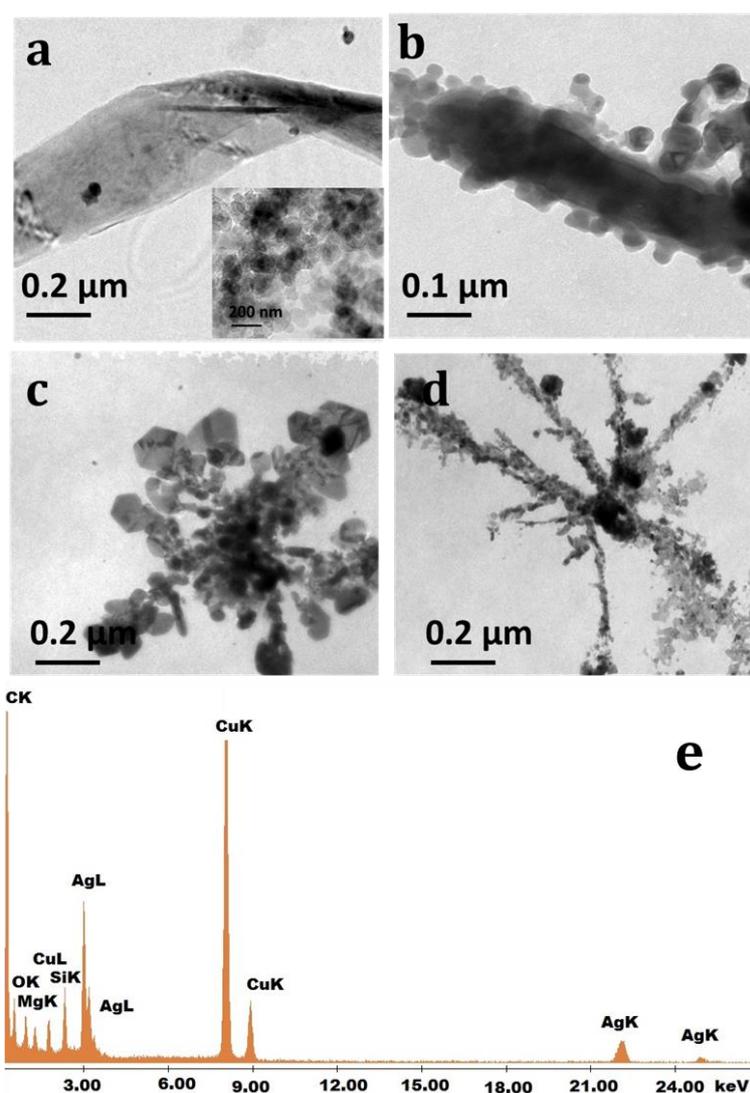
Figure 5.5. TEM images of SFLAGs. Silver nanoparticle entrapped tapes of (a) SFLAG1; the inset showed the magnified image (b) SFLAG2 (c) SFLAG3 (d) SFLAG4 and (e) EDS spectrum of SFLAG2

The formation nematic liquid crystalline texture of SFLAG is confirmed by the PLM studies. The PLM images of the silver nanoparticle entrapped gels of SFLAG1, SFLAG2, SFLAG3 and SFLAG4 are shown in Figure 5.6 (a) to (d) respectively. AMD self-assemble with laponite to form spherullites, and the hydroxyl group present reduces silver ions to silver nanoparticles. Initially, it forms vesicles and then the non–covalent interaction between laponite and AMD leads to a tape like morphology and silver nanoparticles were adhering on to the surface of these tapes and formed birefringent branched network. The high birefringent nature of the gel network is due to the patterning of silver nanoparticle in the gel network. As the silver content increases, more thick and multiwalled tapes were observed in SFLAG3 and SFLAG4.
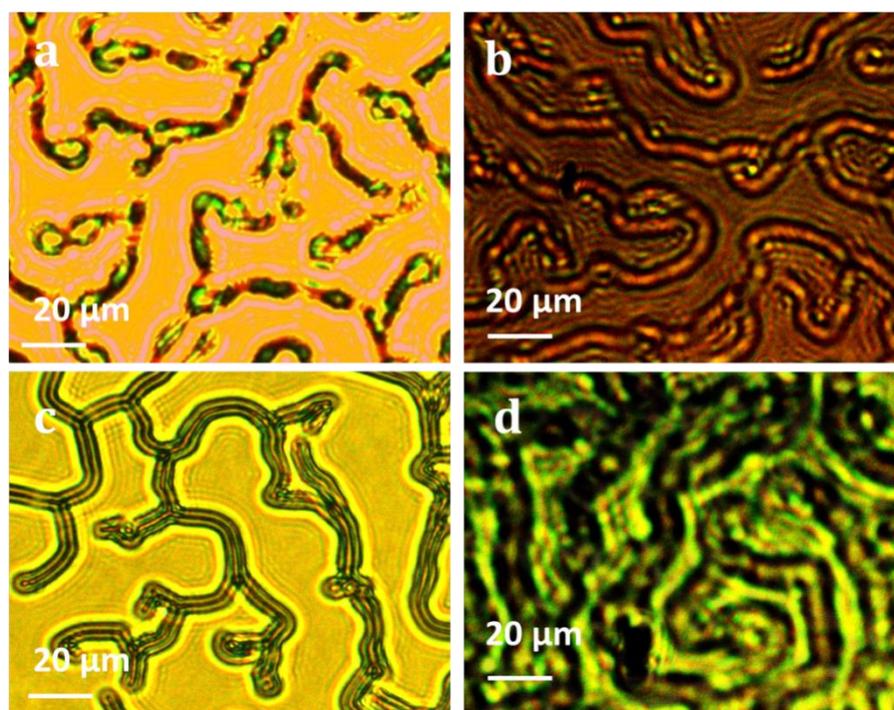
Figure 5.6. PLM images of SFLAGs. (a) SFLAG1 (b) SFLAG2 (c) SFLAG3 and (d) SFLAG4

The optical properties of the SFLAGs were studied by recording the UV–Visible spectroscopy and are shown in Figure 5.7 (a). The UV–Visible spectra of SFLAGs showed absorption maximum in the range of 400–450 nm indicating the

surface resonance energy of silver particles. The spectrum showed an enhanced intensity with increasing concentration of silver due to the increased population of silver nanoparticles with similar size. Effect of aging on the optical property of SFLAGs was studied by recording the UV-Visible spectra of SFLAG2 at particular intervals and is shown in Figure 5.7 (b). The hike in the intensity of spectral lines shows the formation of more silver nanoparticles with time. After one week, the formation of silver nanoparticle reached a plateau and the intensity, and the position of wavelength of absorption maxima remained unaltered. After one month, the intensity of absorption maxima decreased and spectral shape slightly broadened and blue shifted showing the aggregation of nanoparticles in the system.
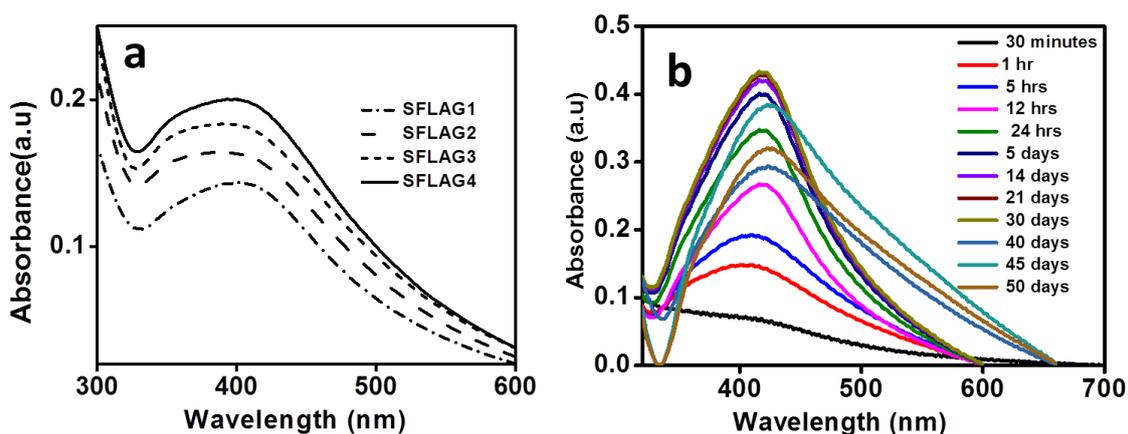
Figure 5.7 (a) The UV−Visible spectra of SFLAGs and (b) The aging studies of SFLAG2

XRD is used for studying the periodicity, variation in the d-spacing in the SFLAG, dimension of the self-assembled layers and to study the crystalline phase of silver nano crystallites in the SFLAG. The diffractogram of AMD, laponite, FLAG and SFLAG2 between $2\theta = 2$ to $35°$ were shown in Figure 5.8 (a). AMD exhibited well -defined sharp intense peaks at $2\theta = 10°$, $15°$, $21°$, $23°$, $26°$, $30°$ and $32°$ revealing its highly crystalline nature. The diffraction pattern of laponite exhibited broad diffraction peak at $2\theta = 6.64°$ corresponding to interplanar d spacing of ~13.3 Å

which can be related to the d001 basal plane oriented parallel to the substrate surface. The peaks corresponding to AMD is diminished in the FLAG showing the amorphous nature of the gel sample. The XRD of FLAG4 exhibited the peak $2\theta = 4.3°$ (d-spacing 20.53 Å corresponds to the shift in laponite d-spacing) and the peak at $2\theta = \sim 2.2°$ (40.52Å) agrees with the formation of highly ordered supramolecular ensembles. SFLAG2 exhibited a peak $2\theta = 4.2°$ (d-spacing 20.95 Å corresponds to the shift in laponite d-spacing) and the peak at $2\theta = \sim 2.08°$ (42.5 Å).The diffractograms of SFLAG2 and SFLAG4 are shown in Figure 5.8 (b) exhibited peaks at $2\theta = 38.1^0$, 44^0, 61.6^0 corresponds to the characteristic diffraction peaks of (111), (200) and (220) planes FCC lattices of silver respectively.
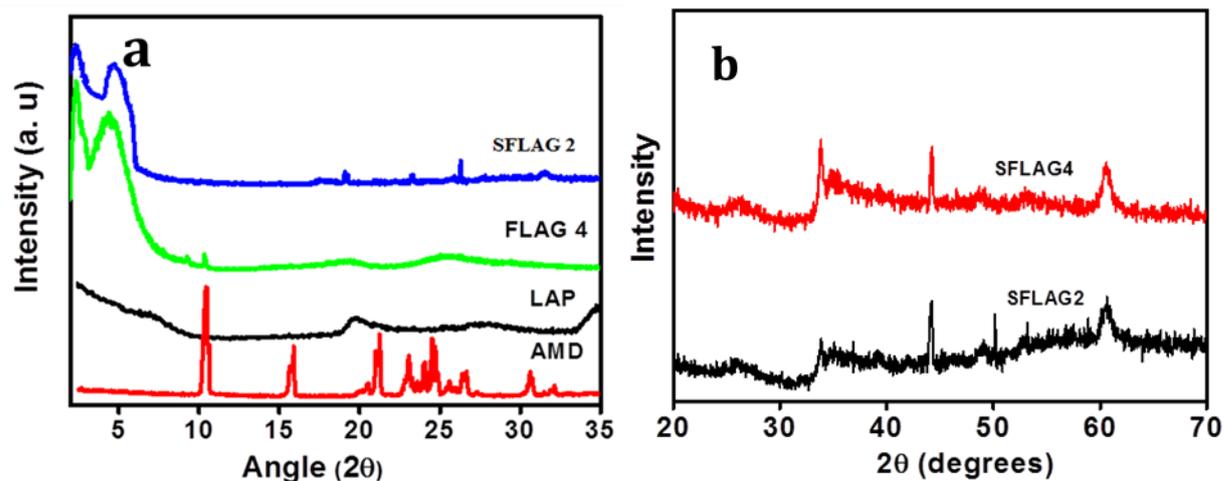
Figure 5.8. (a) XRD of AMD, LAP, FLAG4 and SFLAG2 ($2\theta = 2$ to $35°$) and (b) XRD spectra of SFLAG2 and SFLAG4 ($2\theta = 20$ to $70°$)

5.3.2. The electrochemical studies of modified electrodes

The electrochemical studies were used to study the electron transfer and electrochemical properties of the surface modified electrodes. The electrochemical impedance spectroscopy (EIS) measurements were carried out in a frequency range of 0.1 Hz to 10 kHz. Nyquist plots of GCE, LAP/GCE, FLAG/GCE and

SFLAG/GCE are shown in Figure 5.9. GCE exhibited a semicircle at higher frequency region showing significant resistance towards the electron transfer process at the electrode surface. While going from LAP/GCE, FLAG/GCE to SFLAG/GCE, the diameter of the semicircle region decreases indicating the very low impedance of the SFLAG gel. The charge transfer resistance (R_{ct}) of GCE, LAP/GCE, FLAG/GCE and SFLAG/GCE is measured as 1124, 640, 245 and 96 Ω respectively. The very low impedance value of SFLAG/GCE revealed the high conducting nature, good electrocatalytic activity which proposes it as an excellent electron mediator for redox reactions.
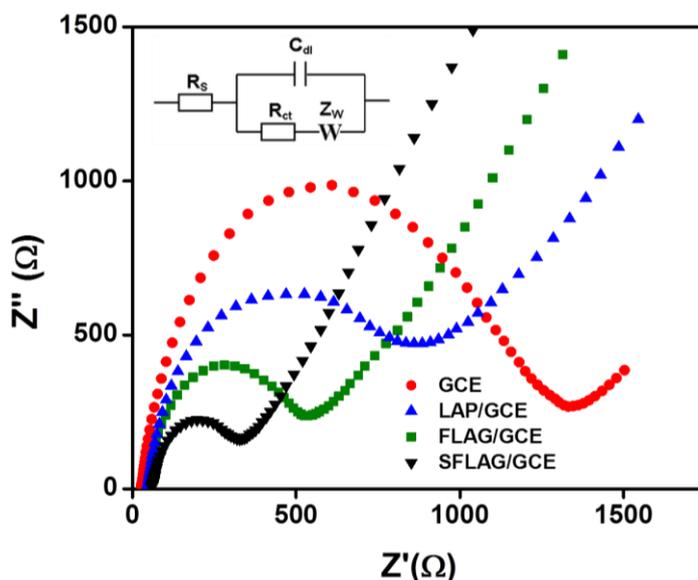
Figure 5.9. Nyquist plots of GCE, LAP/GCE, FLAG/GCE and SFLAG/GCE

The electroactive surface area of GCE and the modified electrodes are calculated using cyclic voltammetry. The cyclic voltammetric studies of the SFALG/GCE was carried out using $K_3Fe(CN)_6$ as an electrochemical probe. The electroactive surface area of GCE, LAP/GCE, FLAG/GCE and SFLAG/GCE was determined by cyclic voltammetry in 1 mM $K_3Fe(CN)_6$ solution containing 0.1 M KCl as the supporting electrolyte at different scan rates (v). A linear response is

obtained for the peak currents (I_p) versus the square root of scan rate as shown in Figure 5.10 (a)–(d) and the respective cyclic voltammetric profiles at different scan rate is given in the inset.
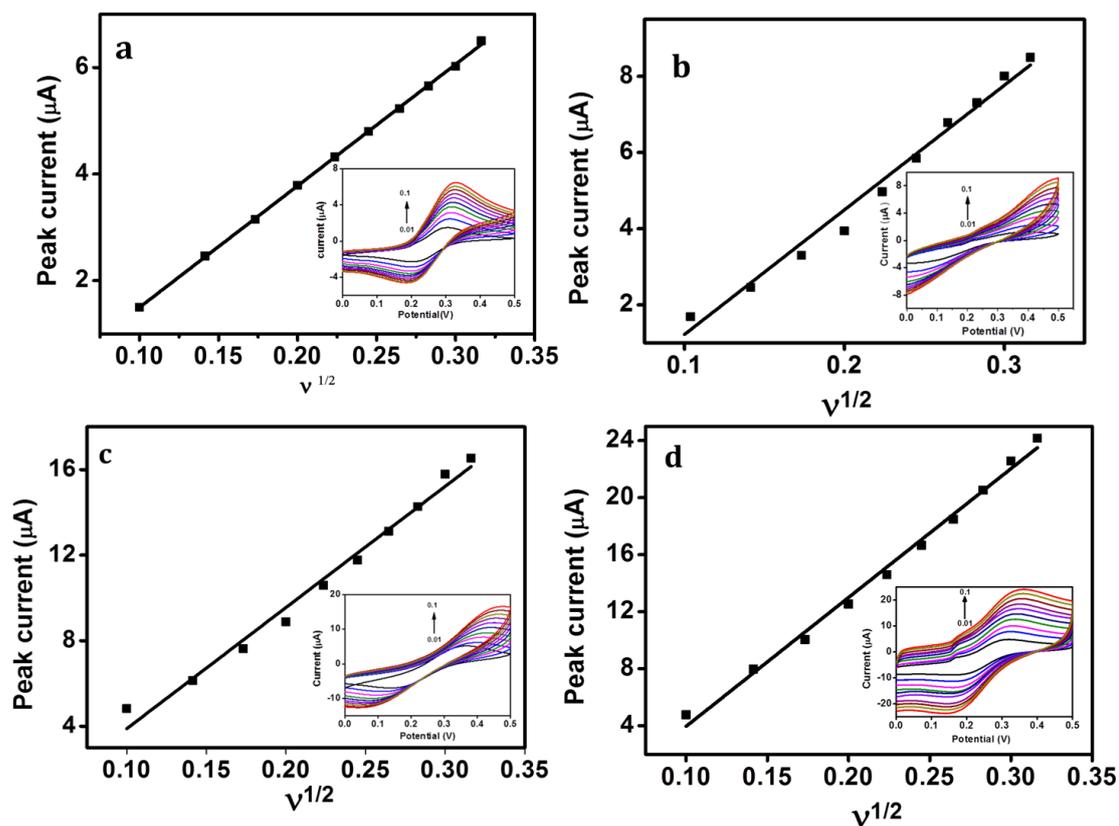
Figure 5.10. The linear response of the peak currents (Ip) versus the square root of scan rate with modified electrodes (a) GCE, (b) LAP/GCE, (c) FLAG/GCE and (d) SFLAG/GCE and the respective cyclic voltammetric profiles are shown in the inset

Approximate value of electrochemical area is calculated using Randles-Sevcik equation (Bard et al., 2009)

$$I_p = 2.687 \times 10^5 \, n^{3/2} \, D^{1/2} \, v^{1/2} \, AC$$

Where, I_p refers to the peak current, n is the number of electrons involved, A is the surface area of the electrode, D is the diffusion coefficient, C is the concentration of $K_3Fe(CN)_6$ and v is the scan rate. For $K_3Fe(CN)_6$, n =1 and D = 7.6×10^{-6} cm^2 S^{-1}. The electroactive surface area was calculated as 0.022, 0.034, 0.049 and 0.085 cm^2 for

GCE, LAP/GCE, FLAG/GCE and SFLAG/GCE respectively. This suggests that SFLAG/GCE can effectively accelerate the diffusion of ions towards the electrode surface which is strengthened by the higher current density observed for SFLAG/GCE.

5.3.3. Electrocatalytic oxidation of L–tyrosine

The electrocatalytic performance of SFLAG/GCE was probed for the oxidation of L–tyrosine by three electroanalytical techniques such as cyclic voltammetry, differential pulse voltammetry (DPV) and chronoamperometry (CA). The cyclic voltammetric studies of GCE, FLAG/GCE and SFLAG/GCE in phosphate buffer solution (pH 7.4) are shown in Figure 5.11. The cyclic voltammetric profile of GCE and FLAG/GCE exhibit silent signals in buffer solution whereas the cyclic voltammetric profile of SFLAG/GCE exhibited oxidation (0.441V) and reduction (0.075V) peaks of silver in the buffer solution. The electrochemical behaviour of colloidal silver nanoparticle in the buffer solution is reported elsewhere (Giovanni et al., 2012).
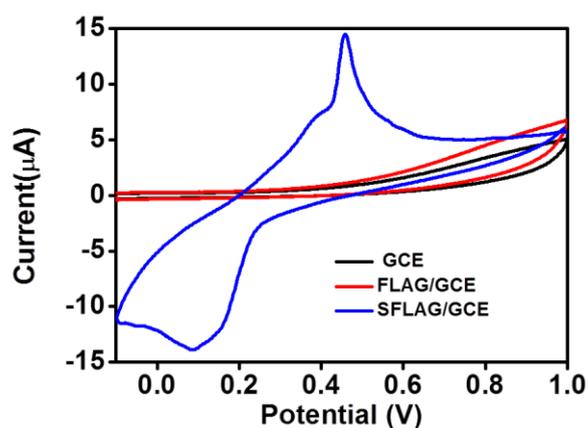
Figure 5.11. The cyclic voltammogram of GCE, FLAG/GCE and SFLAG/GCE in phosphate buffer solution (pH 7.4) at a scan rate of 50 mV/s

The cyclic voltammogram for the oxidation of L–tyrosine at GCE, FLAG/GCE and SFLAG/GCE in phosphate buffer solution (pH 7.4) in presence of 1 × 10^{-6} M L–tyrosine is shown in the Figure 5.12. The oxidation of L–tyrosine at GCE was observed as a diffused peak at a higher potential 0.75V and with lower peak current 2.04 μA. The oxidation potential of L–tyrosine is found to be shifted to 0.69 V at SFLAG/GCE with a hike in the peak current of 6.4 μA which evidenced the better electrocatalytic property of SFLAG/GCE.
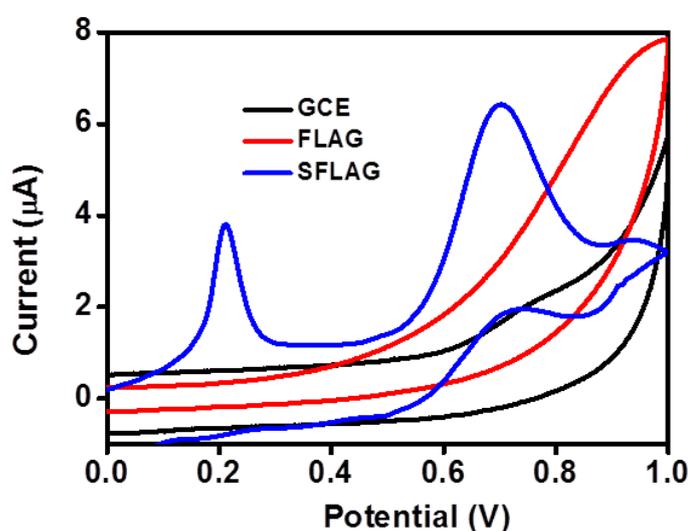
Figure 5.12. The cyclic voltammogram for the oxidation of L–tyrosine at GCE, FLAG/GCE and SFLAG/GCE in phosphate buffer solution (pH 7.4) in presence of 1 × 10^{-6} M L–tyrosine

DPV is a rapid and effective electroanalytical technique which can improve the sensitivity and detection limit due to its minimization of the background effects. Figure 5.13 (a) showed the DPV responses on the successive addition of L–tyrosine to the buffer solution. The differential pulse voltammogram of SFLAG/GCE recorded after the addition of L–tyrosine exhibited a well-resolved peak at 0.68 V. The DPV responses on the successive addition of L–tyrosine and the peak current is proportional to the concentration of L–tyrosine is shown in Figure 5.13 (b). SFLAG/GCE showed

a linear relationship with increasing L–tyrosine in the concentration range of 0.001μM to 1mM. The limit of detection is measured as 10 nM.
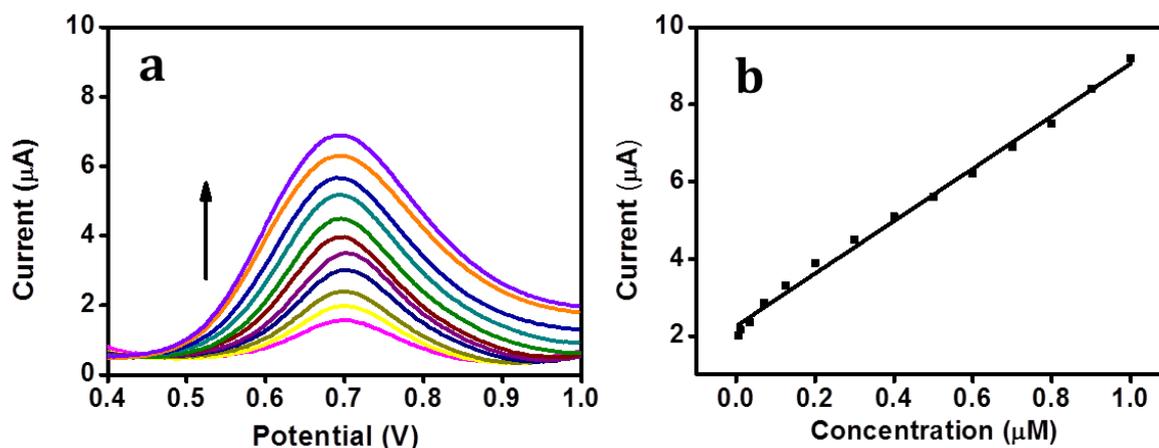
Figure 5.13. (a) DPV responses on the successive addition of L–tyrosine in the phosphate buffer solution (0.2 μM to 2.2μM) (b) The linear plot of peak current with respect to the concentration of L–tyrosine

The pH of the electrolyte affects the oxidation of the L–tyrosine, which in turn affects the redox potential and initial electrochemical oxidation processes. The DPV responses for the oxidation of L–tyrosine varying the pH from 2 to 11 were carried out. The variation of peak current versus pH is shown in Figure 5.14 (a). The peak current has the maximum value at pH 2 and then started decreasing up to pH 6. Above pH 6, the peak current was raised till pH 8 and thereafter decreased. The pH sensitive groups present in the L–tyrosine may affect the electrochemical oxidation. In the acidic medium, the potential is shifted to a more positive value with enhanced current intensity. This may be suggested that, at lower pH, L–tyrosine have a protonated amino group, i.e., R-NH$_3^+$, the oxidation of this monocation occurs at higher potential with enhanced current density due to the electrostatic interaction between the electrode surface and the molecule. In the basic pH, the carboxylic group is deprotonated and acquires a negative charge which in turn can enhance the current

density. In the highly basic medium, the –OH group of the L–tyrosine begins to dissociate and cannot be oxidized in a strongly basic medium. In the pH ~6, the zwitterion form of the L–tyrosine was suggested, which carries no net electric charge and the electrostatic interaction between the electrode surface and L–tyrosine is ruled out and showed a decrease in the current intensity.
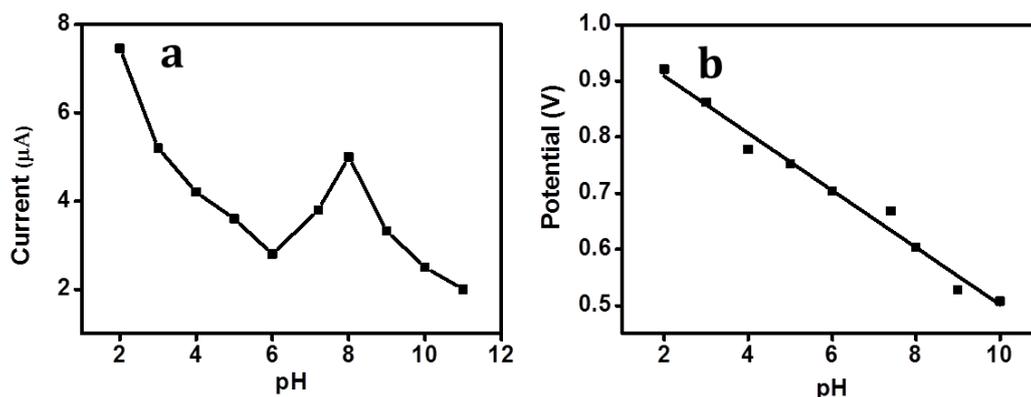
Figure 5.14. (a) Effect of pH on the peak current of the oxidation of L–tyrosine and (b) Effect of peak potential on the peak current of the oxidation of L–tyrosine

With the increase in pH, the oxidation potential of L–tyrosine was shifted to less positive side indicates that protons are directly involved in the reaction. The dependence of pH with peak potential is depicted using a linear regression equation, $E_p = -0.051pH + 1.012$ with a linear regression coefficient, $R^2 = 0.98$ and is shown in Figure 5.14 (b). A slope of -0.051 indicates that an equal number of protons and electrons were involved in the oxidation of L–tyrosine (Baig et al., 2015; Roeser et al., 2010). Acidic pH can be considered as more favourable pH for the oxidation of L–tyrosine. At physiological pH (~7.4), the oxidation of L–tyrosine occurs at 0.668 V with an enhanced current intensity of 4.5 µA. Accounting the advantage of physiological pH, pH ~ 7.4 has been chosen for the further electrochemical oxidation studies of L–tyrosine.

5.3.3.1. Kinetic studies

Kinetics of electrochemical oxidation of L–tyrosine was studied using cyclic voltammetry with SFALG/GCE in 10^{-5} M solution of L–tyrosine in phosphate buffer at different scan rate and is shown in Figure 5.15.
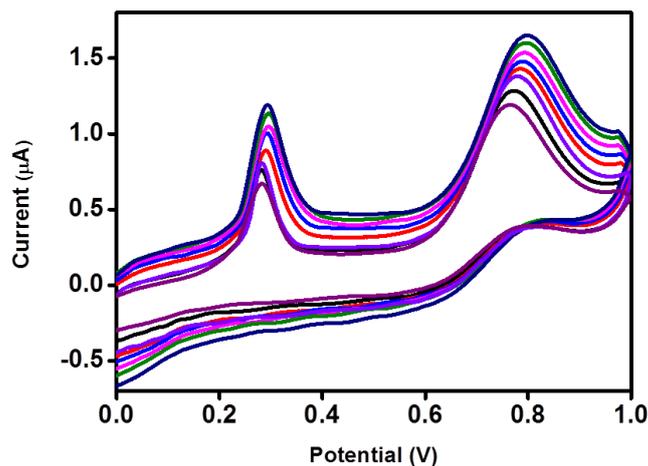
Figure 5.15. Cyclic voltammograms of SFALG/GCE in 10^{-5} M solution of L–tyrosine in phosphate buffer at different scan rate

The oxidation potential of L–tyrosine is shifted to more positive potential with increasing scan rate. The anodic peak current varies linearly with $v^{1/2}$ as shown in Figure 5.16 (a) confirmed the diffusion controlled nature of the reaction.
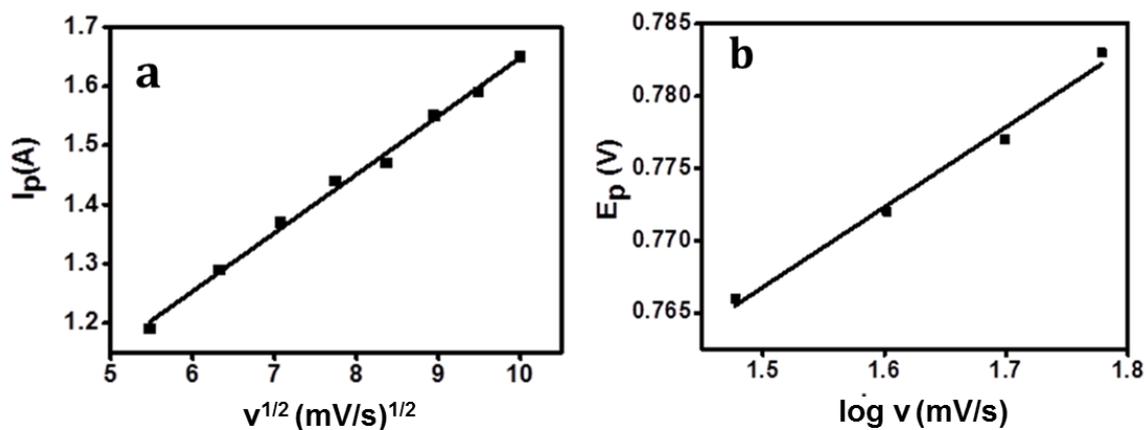
Figure 5.16. (a) Plot of peak current versus $v^{1/2}$ (b) Plot of Ep versus log v in 10^{-5} M solution of L–tyrosine in phosphate buffer at different scan rate

The information about the rate determining step of the reaction can be studied with Tafel plot. The Tafel equation for a diffusion controlled process is

$$Ep = (2.303 RTln\alpha F) \log \nu + constant$$

Where, Ep is oxidation potential, ν is scan rate, R is universal gas constant, T is temperature, F is Faraday's constant and α is the charge transfer coefficient. The linear response of variation of peak potential with log ν given in Figure 5.16 (b) suggests the reaction is totally irreversible. The charge transfer coefficient (α) is calculated as 0.53 from the slope of Ep versus log ν plot, indicated a two electron process in the rate determining step for the oxidation of L–tyrosine. The mechanism for the electrochemical oxidation of L–tyrosine is suggested and is given in Figure 5.17.
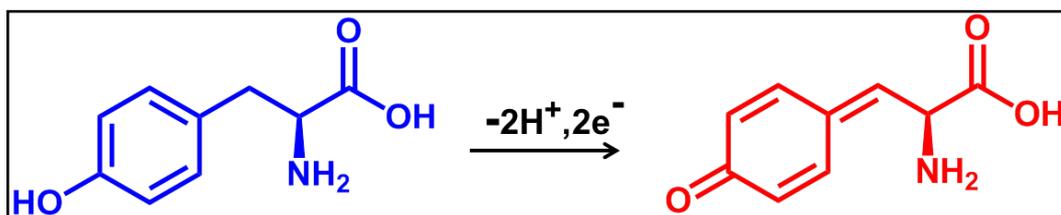
Figure 5.17. The mechanism for the electrochemical oxidation of L–tyrosine

Further, electrocatalytic property of SFLAG/GCE is studied for the electrochemical oxidation of L–tyrosine using chronoamperometric technique at 0.69V in the presence and absence of L–tyrosine was studied. The chronoamperometric response on the successive addition of 20 μL from 10^{-5} M L–tyrosine to 10 mL of the buffer is given in Figure 5.18 (a). The graph showed a linear response with concentration and is shown in Figure 5.18 (b).
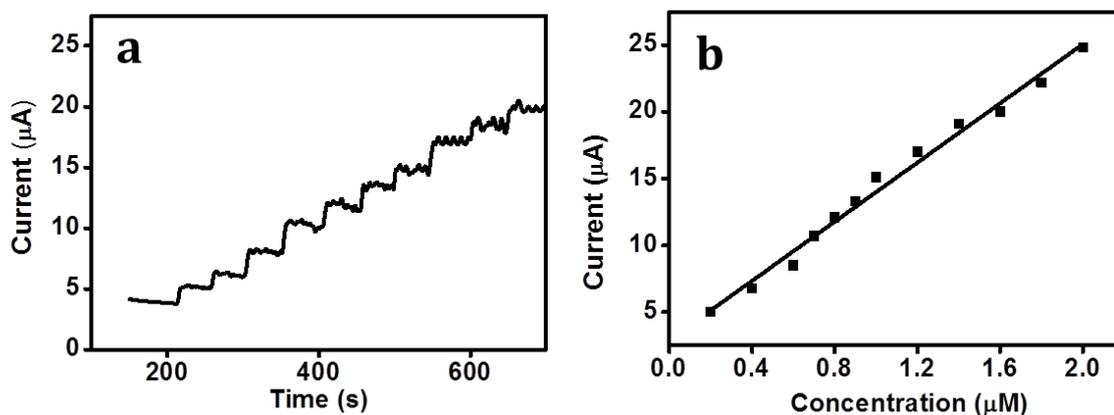
Figure 5.18. (a) Chronoamperometric response of SFLAG/GCE at a potential of 0.69V in phosphate buffer on the successive addition of L–tyrosine (b) The linear response of peak current with respect to the concentration of L–tyrosine

The current obtained for electrochemical reaction is due to the diffusion of electroactive species towards the surface of the electrode which can be described by Cottrell equation

$$I = nFACD1^{/2}/\pi^{1/2}t^{1/2} = Kt^{-1/2}$$

Where, D is the diffusion coefficient, C is the bulk concentration in mol/cm^3, n is the number of electrons involved, F is the Faraday constant and A is the electroactive surface area. In a diffusion control reactions, I versus t$^{-1/2}$ will be linear, and the diffusion coefficient can be calculated from the slope.
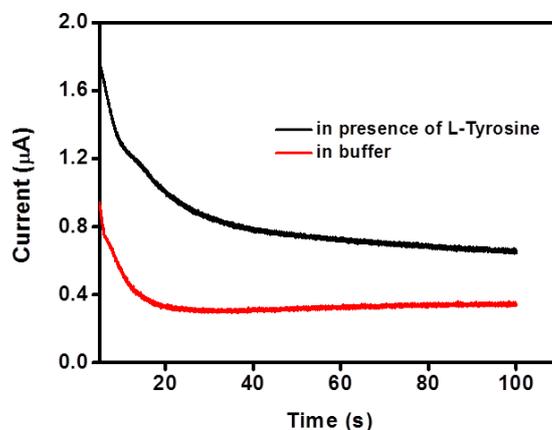
Figure 5.19. The chronoamperometric response of SFLAG/GCE at a potential step of 0.69 V in phosphate buffer solution in the presence and absence of L-Tyrosine

132

The Figure 5.19 showed the chronoamperometric response of SFLAG/GCE in phosphate buffer solution at pH 7.4 at a potential step of 0.69V in the presence and absence of L–tyrosine. The Figure 5.20 (a) showed the linear plot of I versus $t^{-1/2}$ plot with the best fitting of data ($R^2 \sim 99.2$). From the slope of the plot, the diffusion coefficient is calculated as 4.8×10^{-5} $cm^2 s^{-1}$.
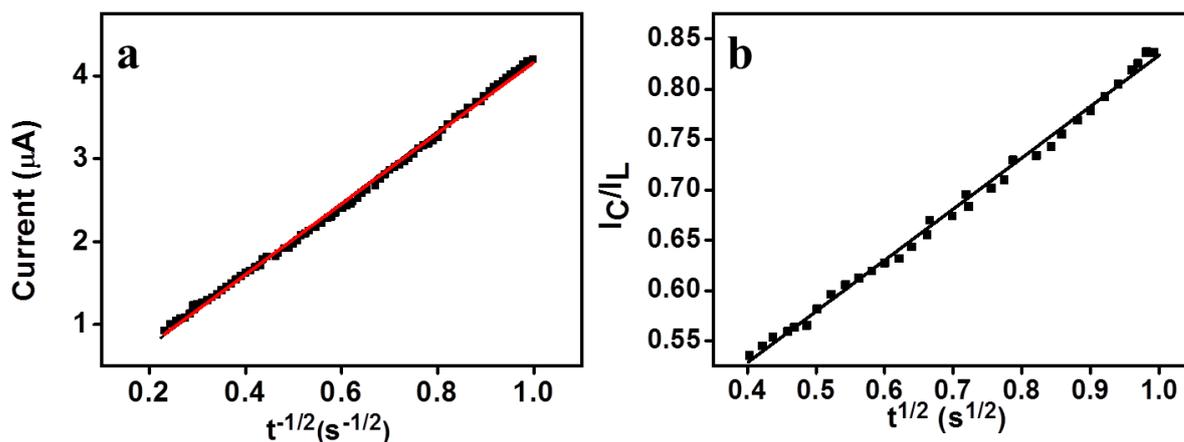
Figure 5.20. (a) The plot of peak current versus $t^{-1/2}$ and (b) The plot of I_C/I_L versus $t^{1/2}$

The catalytic rate constant K_h can be calculated using Galus method, i.e.,

$$I_c/I_L = \pi^{1/2}\gamma^{1/2} = \pi^{1/2}(k_h C_b t)^{1/2}$$

Where, k_h is the catalytic rate constant, t is the time elapsed, I_C is the catalytic current and I_L is the current in the absence of L–tyrosine. From the linear plot of I_C/I_L versus $t^{1/2}$ as shown in Figure 5.20 (b), the rate constant (k_h) can be calculated using Galus equation. The catalytic rate constant for the oxidation of L–tyrosine at SFLAG/GCE is calculated as 3.1435×10^4. The high value of the catalytic rate constant confirmed the good catalytic efficiency of SFALG/GCE for the oxidation of L–tyrosine.

5.3.4. The Interference studies, reusability and storage stability

The selectivity of the proposed electrochemical sensor was evaluated in the presence of common interfering analytes such as L-cysteine, dopamine, ascorbic acid, glucose, uric acid, alanine and phenyl alanine using chronoamperometry at an applied potential of 0.69V and is shown in Figure 5.21 (a). The chronoamperometric responses of the SFLAG/GCE were measured upon subsequent additions of 0.1 mM of each L-cysteine, dopamine, ascorbic acid, glucose, uric acid, alanine and phenyl alanine. The experimental results showed that hundred-fold of L-cysteine, dopamine, ascorbic acid, glucose and uric acid is not interfered with the detection of L–tyrosine and had no influence on the current response for the oxidation of L–tyrosine. The long-term stability of the SFLAG/GCE is checked for one month after storing in a dry and cool place. The DPV response for the oxidation of 1×10^{-5} L–tyrosine is retained 95% even after one month indicated the good storage stability and durability of the proposed sensor.
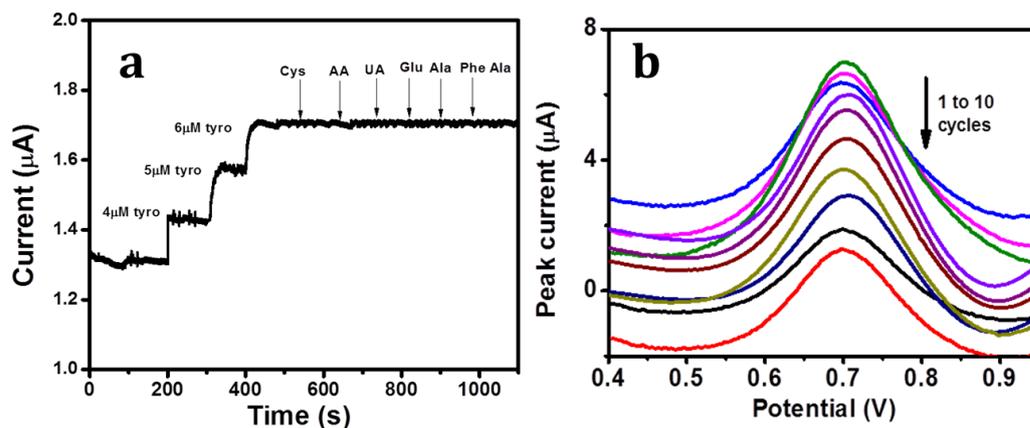
Figure 5.21. (a) Chronoamperogram measured in the presence of interfering analytes and (b) The repeatability studies of SFLAG/GCE upto 10 times

The repeatability was checked by recording the DPV responses during 10 cycles using the same electrode. The current remains same for the first four use and then

current intensity decreases. A small decrease in the current density of the oxidation of L–tyrosine up to 5 cycles and then decreased to a slight extent even after 10 repeated cycles confirmed its potential for reuse and is shown in Figure 5.21 (b). The reproducibility was checked with 5 different glassy carbon electrodes modified with SFLAG using DPV analyses. The value of peak current and peak potential obtained for the replicate measurements showed a relative standard deviation of 4.8 % and 1.8% respectively suggested a good reproducibility of the sensor.

5.3.5. Real sample analysis

The analytical performance of the proposed modified electrode is validated by the recovery experiments performed using DPV. The human blood serum samples were collected from the laboratories is diluted 50 times with 0.1M phosphate buffer (pH7.4) using the standard addition method. The results are given in Table 5.1 which showed the recoveries varied from 96% –103%. The results were suggested that the proposed method can be employed for the quantification of L-Tyrosine in real samples.

Sl No.	Sample	L–tyrosine added(μM)	L–tyrosine found (μM)	Recovery (%)
1	Blood serum1	60	58.11	96.85
		80	83.53	104.41
		100	95.83	95.83
2	Blood serum2	60	59.88	99.8
		80	73.64	92.05
		100	96.93	96.93

Table 5.1. Quantitative and recovery analysis of L–tyrosine in blood serum samples

5.4. Conclusion

SFLAGs were prepared through the self-assembly of laponite – amidodiol. The functional groups like amide and hydroxyl groups present in soft tapes can be exploited for the formation of silver nanoparticles. Morphological studies using various microscopic techniques revealed the formation of spherical and cuboidal silver nanoparticles are embedded in these tapes. The electrochemical impedance spectroscopic studies showed an enhancement in the conductivity (GCE = R_{et} ~1124 Ω, SFLAG/GCE = R_{et} ~ 96Ω). The SFLAG/GCE was demonstrated as an electrochemical sensor for the detection of L–tyrosine. The lower detection limit of L–tyrosine observed as 10 nM. SFLAG/GCE exhibited excellent selectivity, reproducibility, storage stability; high current response and lower detection limit (10 nM). The recovery values ranging from 96–103% for blood serum samples suggested it as a better candidate in clinical diagnostics.

5. 5. Experimental

5.5.1. Materials

Laponite RD (Southern Clay Products) was used as received. γ-butyrolactone (Fluka, Germany), silver nitrate, potassium ferricyanide, potassium ferrocyanide, potassium dihydrogen phosphate, sodium hydroxide, hydrochloric acid, L–tyrosine, ascorbic acid, glucose, urea, L–cysteine (Merck, India). Hexamethylene diamine, isopropanol, acetone and methanol (s.d. fine chem. limited, Bombay, India) were purchased and used without further purification.

5.5.2. Preparation SFLAGs

0.05 g of laponite was dissolved in 1 ml of hot distilled water and then it was thoroughly mixed with 1 ml of 1 % AMD solution at 60 °C for 5 minutes. To this, 0.2 ml of 20 to 70 mM concentrations of silver nitrate solution is added, stirred well and kept undisturbed. The nanocomposite gel was formed within 30 minutes. They were designated as SFLAG1, SFLAG2, SFLAG3 and SFLAG4 respectively with varying concentration of silver nitrate. Control samples were prepared with the same procedure in the absence of silver nitrate and with laponite alone and are designated as FLAG and LAP respectively.

5.5.3. Fabrication of modified electrodes

The glassy carbon electrodes were modified with LAP, FLAG and SFLAG and were designated as LAP/GCE, FLAG/GCE and SFLAG/GCE.

5.5.4. Electrochemical studies

The electrochemical detection of L–tyrosine was carried out with modified electrodes in phosphate buffer (pH 7.4) and sweeping the voltage between 0V and 1 V using cyclic voltammetry and DPV. Real sample analysis was carried out in human serum samples. The unknown concentrations of L–tyrosine were determined by referring to the calibration graph prepared by plotting the peak current values for different standard concentrations of L–tyrosine. The electrochemical impedance measurements were performed with potassium ferrocyanide/ ferricyanide solution for GCE, LAP/GCE, FLAG/GCE and SFLAG/GCE.

5.5.5. Characterization Techniques

Electrochemical measurements were performed using CHI6211B electrochemical analyzer, in a three electrode one compartment system consisting of GCE as working electrode, platinum wire as counter electrode and Ag/AgCl reference electrode. The experiments were performed at 25 ± 5 °C. Prior to electrochemical analysis, GCE was polished with 0.05 micron alumina powder and then ultrasonically cleaned successively with acetone, ethanol and double distilled water and allowed to dry at room temperature. The electrochemical impedance spectroscopy (EIS) measurements were carried out in a frequency range of 0.1 Hz to 10 kHz at an open circuit potential of 0.2V.

Summary

There has been considerable interest in the development of hydrogel stabilized metal nanoparticles which may find applications in responsive artificial muscles, switches, memory devices, catalysis, tissue engineering, sensors, energy storage systems and so forth. The incorporation of metal nanoparticles in hydrogels expected to exhibit synergistic properties of hydrogels and metal nanoparticles such as stimuli responsive optoelectronic, catalytic and sensor properties. Hydrogels can be prepared by in situ radical polymerization of hydrophilic monomers containing functional group such as hydroxyl, amide, carboxyl group etc. These functional groups can be exploited for the in situ reduction of metal ions and formation of metal nanoparticle entrapped hydrogel nanocomposites. The viscoelastic property of the hydrogel can be enhanced by cross linking with low molecular weight gelators. In the present programme we have successfully prepared two sets of hydrogel/silver entrapped hydrogel nanocomposites and investigated its properties and applications.

The salient results of the present research programm are summarized below.

Polymeric hydrogels based on AA and AMD (PAGs) were prepared by varying the amount of AMD via in situ radical polymerization of AA at room temperature and evaluated their properties. The viscoelastic property of PAG hydrogel is enhanced by crosslinking with AMD and the maximum value of storage modulus was observed as 3130 Pa. The swelling and diffusion studies of PAG in distilled water and dye solutions were studied and the value of diffusional exponent (n) was obtained as 0.54, 0.72 and 0.74 for water, MB solution and R6G solution respectively, suggesting non–Fickian character. The equilibrium swelling percentage of hydrogel was measured as 76%, 120% and 140% in water, MB solution and R6G solution respectively. The dye

adsorption is followed a pseudo second order kinetics and the rate constant was found to be 7.78×10^{-3} and 1.05×10^{-5} for R6G and MB. The high value of the correlation coefficient obtained in the Freundlich isotherm for MB (0.98) and R6G (0.99) suggested multilayer adsorption behaviour of PAGS. The adsorbate-adsorbent interaction showed an S type Gile's adsorption and better dye adsorption efficiency of PAGs. The dye adsorption capacity of PAG is increased with increase in AMD content, pH and temperature. PAGs can be employed for the dye removal from waste water.

SPAGs were prepared by in-situ reduction of silver ions and polymerization of AA at room temperature using APS as the radical initiator and AMD as reducing agent cum physical cross-linking agent and further demonstrated its application as a catalyst for the reduction of dyes and nitrophenols. Morphological studies revealed the formation of spherical, cuboid and rods of silver nanoparticles depending upon the amount of silver nitrate. SPAG can be employed as an effective catalyst in the reduction of dyes and nitrophenols. The rate constant for the reduction of nitrophenols are $(8.2 \pm 0.04) \times 10^{-3} \ s^{-1}$, $(6.3 \pm 0.03) \times 10^{-3} \ s^{-1}$, $(5.2 \pm 0.05) \times 10^{-3} \ s^{-1}$ for PNP, ONP and MNP respectively. The catalytic conversion efficiency of the catalyst is 99%, 96% and 95% for PNP, MNP and ONP, respectively.The SPAG exhibit high storage stability up to six and better reusability upto 20 cycles. Hence, SPAG can be considered as an efficient catalyst for the reduction of organic molecules and the process is rapid, efficient and economical.

The second type of hydrogel is prepared using of laponite and AMD in presence of water via supramolecular self-assembly approach. The liquid crystalline phase formation and various specific modes of packing were depending on the composition

of constituents. Further its application is envisaged as a gel electrolyte in super capacitors (ITO/FLAG/ITO). Highly birefringent super structures were formed by the self-assembly of laponite and AMD. They exhibit AMD-concentration dependent birefringent super structures such as tapes/fibre like morphology. The viscoelastic property of FLAG ids enhanced with increasing amount of AMD. The difference in the storage and loss modulus for LAP, FLAG1, FLAG2, FLAG3 and FLAG4 are observed to be 730 Pa, 938 Pa, 984 Pa, 1073 Pa, and 1290 Pa respectively revealing the cross–linking nature of AMD in FLAGs. The cross over point obtained for FLAG1, FLAG2, FLAG3 and FLAG4 is 3.5%, 4.2%, 5.6%, and 6.9% respectively confirmed the role of AMD for establishing robust nature for FLAGs. Electrochemical impedance studies of the FLAG/GCE showed low charge transfer resistance (245Ω).The cyclic voltammetric studies showed stable electrochemical window (-0.4V– 1.5V). The GCD studies showed specific capacitance of 1856 mF/g and good cycling stability. All these results showed that FLAG can be exploited as a gel electrolyte in the energy storage devices.

Silver nanoparticle patterned liquid crystalline hydrogel is prepared by in situ reduction and cross–linking of laponite and AMD in presence of silver ions. Further, SFLAG/GCE was studied for its application in the electrochemical sensing of L-tyrosine. The surface plasmon energy of SFLAGs was observed at ~ 400 nm and the formation of silver in FCC lattices is confirmed by XRD. The morphological studies revealed the formation of spherical and cuboidal silver nanoparticles are embedded on the functional tapes of FLAG. The low R_{ct} (96 Ω) values measured by electrochemical impedance spectra revealed high conductivity of the SFLAG. The electroactive surface area was calculated as 0.022, 0.034, 0.049 and 0.085 cm^2 for bare GCE, LAP/GCE, FLAG/GCE and SFLAG/GCE respectively. SFLAG was demonstrated

as an electrochemical sensor for L–tyrosine with high current response and lower detection limit of 10 nM. The diffusion coefficient of L–tyrosine was calculated from the Tafel plot as 4.8 X 10^{-5} cm^2s^{-1} and catalytic rate constant was calculated using Cottrell equation as 3.1435 X 10^4. The real sample analysis showed 96% –103% recovery values and suggested the analytical application for the detection of L-tyrosine in real samples. Excellent selectivity, reproducibility, storage stability, high current response and nanomolar detection suggest its application as an excellent electrochemical sensor for L–tyrosine.

Future perspectives

➤ The developed novel strategy of simultaneous polymerization and in situ reduction approach can be widely applied as a low-cost one pot process for the preparation of metal nanoparticle entrapped polymeric hydrogel nanocomposites.

➤ In the present program, we have used a tailor made gelator which can enhance the mechanical stability and functionality of the PAG hydrogel. The observed enhanced dye adsorption characteristics of PAG can be exploited for waste water purification.

➤ The hydrogel stabilized metal nanoparticles are widely employed in the catalytic applications because of the easy access and better stabilisation of the porous three dimensional networks. The SPAG hydrogels can be used for the reduction of various commercially and technologically important organic molecules.

➤ The good storage stability, reusability, easy separation and better rate constant of SPAG suggests that it could be used as an alternative for the homogeneous Pd or Pt catalysed reactions.

➤ The SPAG can also be used for the stabilization of Pd, Pt and Au nanoparticles for a broad range of applications.

➤ The well-ordered anisotropic channels of liquid crystalline hydrogel can improve the optoelectronic properties of the material. So FLAG can be employed as a gel electrolyte for batteries and super capacitors.

> The conductivity of FLAG can be enhanced by the exchange of sodium with lithium ions and also the mechanical strength can be increased by the addition of polymers such as PVA and can be employed as a thin film electrolyte.

> The excellent electrochemical sensor performances of SFLAG/GCE suggested its application in the clinical diagnostics of L- tyrosine.

REFERENCES

Abou El-Nour, K. M. M.; Eftaiha, A.; Al-Warthan, A.; Ammar, R. A. A. Synthesis and Applications of Silver Nanoparticles. *Arab. J. Chem.* **2010**, *3*, 135–140.

Adams, R. D.; Captain, B.; Zhu, L. Platinum Participation in the Hydrogenation of Phenylacetylene by $Ru_5(CO)_{15}(C)[Pt(PBut_3)]$. *J. Am. Chem. Soc.* **2004**, *126*, 3042-3043.

Agnihotri, S.; Mukherji, S.; Mukherji, S. Immobilized Silver Nanoparticles Enhance Contact Killing and Show Highest Efficacy: Elucidation of the Mechanism of Bactericidal Action of Silver. *Nanoscale* **2013**, 5, 7328-7340.

Ahmed, A. E.-S. I. Hydrogels for Water Filters: Characterization and Regeneration. *J. Appl. Polym. Sci.* **2012**, *123*, 1889–1895.

Ahmed, E. M. Hydrogel: Preparation, Characterization, and Applications. *J. Adv. Res.* **2013**, *6*, 105–121.

Ahmed, E. M.; Aggor, F. S. Swelling Kinetic Study and Characterization of Crosslinked Hydrogels Containing Silver Nanoparticles. *J. Appl. Polym. Sci.* **2010**, *117*, 2168-2174.

Ai, L.; Jiang, J. Catalytic Reduction of 4-Nitrophenol by Silver Nanoparticles Stabilized on Environmentally Benign Macroscopic Biopolymer Hydrogel. *Bioresour. Technol.* **2013**, *132*, 374–377.

Ai, L.; Yue, H.; Jiang, J. Environmentally Friendly Light-Driven Synthesis of Ag Nanoparticles Insitu Grown on Magnetically Separable Biohydrogels as Highly Active and Recyclable Catalysts for 4-nitrophenol Reduction. *J. Mater. Chem.* **2012**, *22*, 23447-23453.

Akpomie, G. K.; Ogbu, I. C.; Osunkunle, A. A.; Abuh, M. A.; Abonyi, M. N. Equilibrium Isotherm Studies on the Sorption of Pb(II) from Solution by Ehandiagu Clay *J. Emerg. Trends Eng. Appl. Sci.* **2012**, *3*, 354

Al-Qodah, Z. Adsorption of Dyes Using Shale Oil Ash. *Water Res.* **2000**, *34*, 4295-4303.

Asghar, K. A.; Rowlands, D. A.; Elliott, J. M.; Squires, A. M. Predicting Sizes of Hexagonal and Gyroid Metal Nanostructures from Liquid Crystal Templating. *ACS Nano* **2015**, *9*, 10970-10978.

Atala, A.; Lanza, R. P. *Methods of Tissue Engineering*; Academic Press, 2002.

Attard, G. S.; Glyde, J. C.; Goltner, C. G. Liquid-Crystalline Phases as Templates for the Synthesis of Mesoporous Silica. *Nature* **1995**, *378*, 366-368.

Bai, J.; Li, Y.; Du, J.; Wang, S.; Zheng, J.; Yang, Q.; Chen, X. One-Pot Synthesis of Polyacrylamide-Gold Nanocomposite. *Mater. Chem. Phys.* **2007**, *106*, 412–415.

Baig, N.; Kawde, A.-N. A Novel, Fast and Cost Effective Graphene-Modified Graphite Pencil Electrode for Trace Quantification of L-Tyrosine. *Anal. Methods* **2015**, *7*, 9535-9541.

Bajpai, S. K.; Bajpai, M.; Gautam, D. In Situ Formation of Silver Nanoparticles in Regenerated Cellulose-Polyacrylic Acid (RC-PAAc) Hydrogels for Antibacterial Application. *J. Macromol. Sci. Part A* **2013**, *50*, 46–54.

Bajpai, S. K.; Bajpai, M.; Sharma, L. In Situ Formation of Silver Nanoparticles in Poly(N-Isopropyl Acrylamide) Hydrogel for Antibacterial Applications. *Des. Monomers Polym.* **2011**, *14*, 383–394.

Bajpai, S. K.; Kumari, M. A Green Approach to Prepare Silver Nanoparticles Loaded Gum Acacia/poly(acrylate) Hydrogels. *Int. J. Biol. Macromol.* **2015**, *80*, 177–188.

Bard, A. J.; Faulkner, L. R. Electrochemical Methods: Fundamentals and Applications. Wiley: 2000.

Barsoukov, E.; Macdonald, J. R. Impedance Spectroscopy: Theory, Experiment, and Applications. Wiley: 2005.

Berti, L.; Alessandrini, A.; Facci, P. DNA-Templated Photoinduced Silver Deposition. *J. Am. Chem. Soc.* **2005**, *127*, 11216-11217.

Bocos, E.; Pazos, M.; Sanromán, M. A. Electro-Fenton Decolourization of Dyes in Batch Mode by the Use of Catalytic Activity of Iron Loaded Hydrogels. *J. Chem. Technol. Biotechnol.* **2014**, *89*, 1235–1242.

Bonn, D.; Kellay, H.; Tanaka, H.; Wegdam, G.; Meunier, J. Laponite: What Is the Difference between a Gel and a Glass? *Langmuir* **1999**, *15*, 7534-7536.

Bosetti, M.; Massè, A.; Tobin, E.; Cannas, M. Silver Coated Materials for External Fixation Devices: In Vitro Biocompatibility and Genotoxicity. *Biomaterials* **2002**, *23*, 887–892.

Butun, S.; Sahiner, N. A Versatile Hydrogel Template for Metal Nano Particle Preparation and Their Use in Catalysis. *Polymer* **2011**, *52*, 4834–4840.

Chatzoudis, G. K.; Rigas, F. Macroreticular Hydrogel Effects on Dissolution Rate of Controlled-Release Fertilizers. *J. Agric. Food Chem.* **1998**, *46*, 2830–2833.

Chaudhari, V. R.; Samant, K. M.; Ingole, P. P.; Hassan, P. A.; Haram, S. K. Catalytic Activity and Stability of Silver Supported on Multiwalled Carbon Nanotubes. *Int. J. Nanotechnol.* **2012**.

Chavan, A. A.; Li, H.; Scarpellini, A.; Marras, S.; Manna, L.; Athanassiou, A.; Fragouli, D. Elastomeric Nanocomposite Foams for the Removal of Heavy Metal Ions from Water. *ACS Appl. Mater. Interfaces* **2015**, *7*, 14778–14784.

Chen, C.-Y.; Chen, C.-T. A PNIPAM-Based Fluorescent Nanothermometer with Ratiometric Readout. *Chem. Commun. (Camb).* **2011**, *47*, 994–996.

Chen, Y.; Xu, W.; Zeng, G. The Preparation and Characteristic of Robust Inorganic/organic IPN Nanocomposite Hydrogels with Fast Response Rate. *J. Mater. Sci.* **2014**, *49*, 7360–7370.

Cheng, H.; Chen, C.; Zhang, S. Electrochemical Behaviour and Sensitive Determination of L-Tyrosine with a Gold Nanoparticles Modified Glassy Carbon Electrode. *Anal. Sci.* **2009**, *25*, 1221-1225.

Cheng, S.; Smith, D. M.; Li, C. Y. How Does Nanoscale Crystalline Structure Affect Ion Transport in Solid Polymer Electrolytes? *Macromol.* **2014**, *47*, 3978-3986.

Cho, M.; Chung, H.; Choi, W.; Yoon, J. Different Inactivation Behaviour s of MS-2 Phage and Escherichia Coli in TiO2 Photocatalytic Disinfection. *Appl. Environ. Microbiol.* **2005**, *71*, 270–275.

Choudhury, N. A.; Sampath, S.; Shukla, A. K. Hydrogel-polymer electrolytes for electrochemical capacitors: an overview. *Energy Environ. Sci.* **2009**, *2*, 55-67.

Chtchigrovsky, M.; Lin, Y.; Ouchaou, K.; Chaumontet, M.; Robitzer, M.; Quignard, F.; Taran, F. Dramatic Effect of the Gelling Cation on the Catalytic Performances of Alginate-Supported Palladium Nanoparticles for the Suzuki–Miyaura Reaction. *Chem. Mater.* **2012**, *24*, 1505-1510.

Contreras-Cáceres, R.; Pastoriza-Santos, I.; Alvarez-Puebla, R. A.; Pérez-Juste, J.; Fernández-Barbero, A.; Liz-Marzán, L. M. Growing Au/Ag Nanoparticles within Microgel Colloids for Improved Surface-Enhanced Raman Scattering Detection. *Chem. - A Eur. J.* **2010**, *16*, 9462–9467.

Crane, R. S.; Barton, P.; Cartmell, E.; Coulon, F.; Hillis, P.; Judd, S. J.; Santos, A.; Stephenson, T.; Lester, J. N. Fate and Behaviour of Copper and Zinc in Secondary Biological Wastewater Treatment Processes: I. Evaluation of Biomass Adsorption Capacity. *Environ. Technol.* **2010**, *31*, 705–723.

Crini, G. Non-conventional Low-Cost Adsorbents for Dye Removal: A Review. *Bioresour. Technol.* **2006**, *97*, 1061-1085.

Cussler, E. L. Diffusion: Mass Transfer in Fluid Systems. Cambridge University Press: 2009.

Daly, R.; Kotova, O.; Boese, M.; Gunnlaugsson, T.; Boland, J. J. Chemical Nano-Gardens: Growth of Salt Nanowires from Supramolecular Self-Assembly Gels. *ACS Nano* **2013**, *7*, 4838-4845.

Daniel, L.; Gaël, G.; Céline, M.; Caroline, C.; Daniel, B.; Jean-Pierre, S. Flexible Transparent Conductive Materials Based on Silver Nanowire Networks: A Review. *Nanotechnol.* **2013**, *24*, 452001.

Dong, L.; Hoffman, A. S. A Novel Approach for Preparation of pH-Sensitive Hydrogels for Enteric Drug Delivery. *J. Control. Release* **1991**, *15*, 141–152.

Dong, R.; Pang, Y.; Su, Y.; Zhu, X. Supramolecular Hydrogels: Synthesis, Properties and Their Biomedical Applications. *Biomater. Sci.* **2015**, *3*, 937–954.

Dufour, B.; Rannou, P.; Fedorko, P.; Djurado, D.; Travers, J.-P.; Pron, A. Effect of Plasticizing Dopants on Spectroscopic Properties, Supramolecular Structure, and Electrical Transport in Metallic Polyaniline. *Chem. Mater.***2001**, *13*, 4032-4040.

Elias, W. C.; Eising, R.; Silva, T. R.; Albuquerque, B. L.; Martendal, E.; Meier, L.; Domingos, J. B. Screening the Formation of Silver Nanoparticles Using a New Reaction Kinetics Multivariate Analysis and Assessing Their Catalytic Activity in the Reduction of Nitroaromatic Compounds. *J. Phys. Chem. C* **2014**, *118*, 12962–12971.

Esumi, K.; Tano, T.; Meguro, K. Preparation of Organo Palladium Particles from Thermal Decomposition of Its Organic Complex in Organic Solvents. *Langmuir* **1989**, *5*, 268–270.

Evanoff, D. D.; Chumanov, G. Synthesis and Optical Properties of Silver Nanoparticles and Arrays. *ChemPhysChem.* **2005**, *6*, 1221–1231.

Fan, Y.; Liu, J.-H.; Lu, H.-T.; Zhang, Q. Electrochemistry and Voltammetric Determination of L-Tryptophan and L-Tyrosine Using a Glassy Carbon Electrode Modified With a Nafion/TiO$_2$-Graphene Composite Film. *Microchim. Acta* **2011**, *173*, 241-247.

Fateixa, S.; Daniel-da-Silva, A. L.; Nogueira, H. I. S.; Trindade, T. Raman Signal Enhancement Dependence on the Gel Strength of Ag/Hydrogels Used as SERS Substrates. *J. Phys. Chem. C* **2014**, *118*, 10384–10392.

Feng, X.; Sosa-Vargas, L.; Umadevi, S.; Mori, T.; Shimizu, Y.; Hegmann, T. Discotic Liquid Crystal-Functionalized Gold Nanorods: 2- and 3D Self-Assembly and Macroscopic Alignment as well as Increased Charge Carrier Mobility in Hexagonal Columnar Liquid Crystal Hosts Affected by Molecular Packing and π–π Interactions. *Adv. Funct. Mater.* **2015**, *25*, 1180-1192.

Firestone, M. A.; Dzielawa, J. A.; Zapol, P.; Curtiss, L. A.; Seifert, S.; Dietz, M. L. Lyotropic Liquid-Crystalline Gel Formation in a Room-Temperature Ionic Liquid. *Langmuir* **2002**, *18*, 7258-7260.

Fuhrer, R.; Athanassiou, E. K.; Luechinger, N. A.; Stark, W. J. Crosslinking Metal Nanoparticles into the Polymer Backbone of Hydrogels Enables Preparation of Soft, Magnetic Field-Driven Actuators with Muscle-like Flexibility. *Small* **2009**, *5*, 383–388.

Gabriel, J.-C. P.; Sanchez, C.; Davidson, P. Observation of Nematic Liquid-Crystal Textures in Aqueous Gels of Smectite Clays. *J. Phys. Chem.* **1996**, *100*, 11139–11143.

Geary, C. D.; Zudans, I.; Goponenko, A. V; Asher, S. A.; Weber, S. G. Electrochemical Investigation of Pb^{2+} Binding and Transport through a Polymerized Crystalline Colloidal Array Hydrogel Containing Benzo-18-Crown-6. *Anal. Chem.* **2005**, *77*, 185–192.

Gholam Reza Mahdavinia, R. Z. Removal Kinetic of Cationic Dye Using Poly (Sodium Acrylate)-Carrageenan/Na-Montmorillonite Nanocomposite Superabsorbents *J. Mater. Environ. Sci.* **2012,** *3*, 895–906

Giovanni, M.; Pumera, M. Size Dependant Electrochemical Behaviour of Silver Nanoparticles with Sizes of 10, 20, 40, 80 and 107 nm. *Electroanal.* **2012**, *24*, 615-617.

Gong, Z.; Wang, C.; Wang, C.; Tang, C.; Cheng, F.; Du, H.; Fan, M.; Brolo, A. G. A Silver Nanoparticle Embedded Hydrogel as a Substrate for Surface Contamination Analysis by Surface-Enhanced Raman Scattering. *Analyst* **2014**, *139*, 5283–5289.

Goodenough, J. B.; Kim, Y. Challenges for Rechargeable Li Batteries. *Chem. Mater.* **2010**, *22*, 587-603.

Guari, Y.; Thieuleux, C.; Mehdi, A.; Reyé, C.; Corriu, R. J. P.; Gomez-Gallardo, S.; Philippot, K.; Chaudret, B. In Situ Formation of Gold Nanoparticles within Thiol Functionalized HMS-C16 and SBA-15 Type Materials via an Organometallic Two-Step Approach. *Chem. Mat.* **2003**, *15*, 2017-2024.

Gundiah, G.; Mukhopadhyay, S.; Tumkurkar, U. G.; Govindaraj, A.; Maitra, U.; Rao, C. N. R. Hydrogel Route to Nanotubes of Metal Oxides and Sulfates. *J. Mater. Chem.* **2003**, *13*, 2118.

Guo, B.-L.; Gao, Q.-Y. Preparation and Properties of a pH/temperature-Responsive Carboxymethyl chitosan/poly(N-Isopropylacrylamide)semi-IPN Hydrogel for Oral Delivery of Drugs. *Carbohydr. Res.* **2007**, *342*, 2416–2422.

Gupta, A.; Silver, S. Silver as a Biocide: Will Resistance Become a Problem? *Nat. Biotechnol.* **1998**, *16*, 888.

Gupta, N. R.; Prasad, B. L. V.; Gopinath, C. S.; Badiger, M. V. A Nanocomposite of Silver and Thermo-associating Polymer by a Green Route: A Potential Soft-Hard Material for Controlled Drug Release. *RSC Adv.* **2014**, *4*, 10261-10268.

Güven, D. Ş. M. Ş. Z. K. M. T. O. Adsorption of Some Dyes on Cationic Poly(N,N – Dimethyl Amino Ethylmethacrylate) Hydrogels. *Hacettepe J. Biol. Chem.***2009**,*7*,233.

Hacker, M. C.; Mikos, A. G. Chapter 33 - Synthetic Polymers. *In Principles of Regenerative Medicine (2ⁿᵈ Ed.)*, Atala, A. Lanza, R. P. Thomson, J.A. Nerem, R.M. Eds., Elsevier Academic Press: San Diego, **2011**, 587-622.

Haraguchi, K.; Takehisa, T. Nanocomposite Hydrogels: A Unique Organic–Inorganic Network Structure with Extraordinary Mechanical, Optical, and Swelling/De-swelling Properties. *Adv. Mater.* **2002**, *14*, 1120-1124.

Haraguchi, K.; Uyama, K.; Tanimoto, H. Self-Healing in Nanocomposite Hydrogels. *Macromol. Rapid Commun.* **2011**, *32*, 1253–1258.

Hari, P. R.; Chandy, T.; Sharma, C. P. Chitosan/calcium-alginate Beads for Oral Delivery of Insulin. *J. Appl. Polym. Sci.* **1996**, *59*, 1795–1801.

Hariprasad, E.; Radhakrishnan, T. P. A Highly Efficient and Extensively Reusable "Dip Catalyst" Based on a Silver-Nanoparticle-Embedded Polymer Thin Film. *Chem. Eur. J* **2010**, *16*, 14378-14384.

Heli, H.; Sattarahmady, N.; Hajjizadeh, M. Electrocatalytic Oxidation and Electrochemical Detection of Guanine, L-Arginine And L-Lysine at a Copper Nanoparticles-Modified Electrode. *Anal. Methods* **2014**, *6*, 6981-6989.

Henglein, A. Colloidal Silver Nanoparticles: Photochemical Preparation and Interaction with O 2 , CCl 4 , and Some Metal Ions. *Chem. Mater.* **1998**, *10*, 444–450.

Henglein, A. Physicochemical Properties of Small Metal Particles in Solution: "microelectrode" reactions, Chemisorption, Composite Metal Particles, and the Atom-to-Metal Transition. *J. Phys. Chem.* **1993**, *97*, 5457–5471.

Henglein, A.; Janata, E.; Fojtik, A. Reduction of lead(2+) in aqueous solution: early steps and colloid formation, and the atom metal transition. *J. Phys. Chem.* **1992**, *96*, 4734-4736.

Herrera, N. N.; Letoffe, J.-M.; Reymond, J.-P.; Bourgeat-Lami, E. Silylation of Laponite Clay Particles with Monofunctional and Trifunctional Vinyl Alkoxysilanes. *J. Mater. Chem.* **2005**, *15*, 863-871.

Herves, P.; Perez-Lorenzo, M.; Liz-Marzan, L. M.; Dzubiella, J.; Lu, Y.; Ballauff, M. Catalysis by Metallic Nanoparticles in Aqueous Solution: Model Reactions. *Chem. Soc. Rev.* **2012**, *41*, 5577-5587.

Himadri, B. B.; Paul, D.; Yoshihito, O. Polymer Gels. American Chemical Society: 2002; Vol. 833, p 388.

Hirst, A. R.; Coates, I. A.; Boucheteau, T. R.; Miravet, J. F.; Escuder, B.; Castelletto, V.; Hamley, I. W.; Smith, D. K. Low-Molecular-Weight Gelators: Elucidating the Principles of Gelation Based on Gelator Solubility and a Cooperative Self-Assembly Model. *J. Am. Chem. Soc.* **2008**, *130*, 9113-9121.

Ho, Y. S.; McKay, G. Pseudo-Second Order Model for Sorption Processes. *Process Biochem.* **1999**, *34*, 451-465.

Högberg, D.; Soberats, B.; Uchida, S.; Yoshio, M.; Kloo, L.; Segawa, H.; Kato, T. Nanostructured Two-Component Liquid-Crystalline Electrolytes for High-Temperature Dye-Sensitized Solar Cells. *Chem. Mater.* **2014**, *26*, 6496-6502.

House, D. A. Kinetics and Mechanism of Oxidations by Peroxydisulfate. *Chem. Rev.* **1962**, *62*, 185-203.

Hu, D. S.-G.; Chou, K. J.-N. Kinetics of Water Swelling and Development of Porous Structure in Ionic Poly(Acrylonitrile-Acrylamide-Acrylic Acid) Hydrogels. *Polymer* 1996, 37, 1019-1025.

Hu, H.; Xin, J. H.; Hu, H. PAM/graphene/Ag ternary hydrogel: synthesis, characterization and catalytic application. J. Mater. Chem.A 2014, 2, 11319-11333.]

Hu, J. Q.; Chen, Q.; Xie, Z. X.; Han, G. B.; Wang, R. H.; Ren, B.; Zhang, Y.; Yang, Z. L.; Tian, Z. Q. A Simple and Effective Route for the Synthesis of Crystalline Silver Nanorods and Nanowires. *Adv. Funct. Mat.* **2004**, *14*, 183-189.

Huang, C.; Chen, C.; Ye, X.; Ye, W.; Hu, J.; Xu, C.; Qiu, X. Stable Colloidal Boron Nitride Nanosheet Dispersion and Its Potential Application in Catalysis. *J. Mater. Chem. A* **2013**, *1*, 12192–12197.

Imae, T.; Hayashi, N.; Matsumoto, T.; Tada, T.; Furusaka, M. Structures of Fibrous Supramolecular Assemblies Constructed by Amino Acid Surfactants: Investigation by AFM, SANS, and SAXS. *J. Colloid Interface Sci.* **2000**, *225*, 285–290.

Imae, T.; Takahashi, Y.; Muramatsu, H. Formation of Fibrous Molecular Assemblies by Amino Acid Surfactants in Water. *J. Am. Chem. Soc.* **1992**, *114*, 3414–3419.

Itoigawa, H.; Kamiyama, T.; Nakamura, Y. Ag Precipitation and Optical Behaviour in $Na_2O\Box B_2O_3$ Glasses. *J. Non-Cryst. Solids* **1997**, *220*, 210-216.

Jackowska, K.; Krysinski, P. New Trends in the Electrochemical Sensing of Dopamine. *Anal. Bioanal. Chem.* **2012**, *405*, 3753–3771.

Jain, P.; Pradeep, T. Potential of Silver Nanoparticle-Coated Polyurethane Foam as an Antibacterial Water Filter. *Biotechnol. Bioeng.* **2005**, *90*, 59–63.

Jana, S.; Ghosh, S. K.; Nath, S.; Pande, S.; Praharaj, S.; Panigrahi, S.; Basu, S.; Endo, T.; Pal, T. Synthesis of silver nanoshell-coated cationic polystyrene beads: A solid phase catalyst for the reduction of 4-nitrophenol. *Appl. Catal. A: Gen.* **2006**, *313*, 41-48.

Jana, S.; Pal, T. Synthesis, Characterization and Catalytic Application of Silver Nanoshell Coated Functionalized Polystyrene Beads. *J. Nanosci. Nanotechnol.* **2007**, *7*, 2151-2156.

Jeon, Y. S.; Lei, J.; Kim, J.-H. Dye Adsorption Characteristics of Alginate/Polyaspartate Hydrogels. *J. Ind. Eng. Chem.* **2008**, *14*, 726-731.

Jeroen, S. v. D.; Susanne, K.; Edward, L.; Claire, P.; Robert, M. R. Large Scale Structures in Liquid Crystal/Clay Colloids. *J. Phys.: Condens. Matter* **2005**, *17*, 2255.

Ji, Y.; Marshall, J. E.; Terentjev, E. M. Nanoparticle-Liquid Crystalline Elastomer Composites. *Polymers* **2012**, *4*, 316.

Jiang, Z.-J.; Liu, C.-Y.; Sun, L.-W. Catalytic Properties of Silver Nanoparticles Supported on Silica Spheres. *J. Phys. Chem. B* **2005**, *109*, 1730–1735.

Jiang, Z.-J.; Liu, C.-Y.; Sun, L.-W. Catalytic Properties of Silver Nanoparticles Supported on Silica Spheres. *J. Phys.Chem.B* **2005**, *109*, 1730-1735.

Jian-xiao, L.; Guo-hong, X.; Qing-ling, Y.; Li, Z.; Jian-min, L.; Ying, C. H_2O_2-Assisted photolysis of reactive dye BES golden yellow simulated wastewater. *Water Sci. Technol.* **2009**, *60*, 2329-2336.

Jiao, T.; Guo, H.; Zhang, Q.; Peng, Q.; Tang, Y.; Yan, X.; Li, B. Reduced Graphene Oxide-Based Silver Nanoparticle-Containing Composite Hydrogel as Highly Efficient Dye Catalysts for Wastewater Treatment. *Sci. Rep.* **2015**, *5*, 11873.

Jiao, T.; Zhao, H.; Zhou, J.; Zhang, Q.; Luo, X.; Hu, J.; Peng, Q.; Yan, X. Self-Assembly Reduced Graphene Oxide Nanosheet Hydrogel Fabrication by Anchorage of Chitosan/Silver and Its Potential Efficient Application toward Dye Degradation for Wastewater Treatments. *ACS Sustain. Chem. Eng.* **2015**, *3*, 3130–3139.

Jin, R.; Cao, Y.; Mirkin, C. A.; Kelly, K. L.; Schatz, G. C.; Zheng, J. G. Photoinduced Conversion of Silver Nanospheres to Nanoprisms. *Science* **2001**, *294*, 1901-1903.

Jing, G.; Wang, L.; Yu, H.; Amer, W. A.; Zhang, L. Recent Progress on Study of Hybrid Hydrogels for Water Treatment. *Colloids Surfaces A Physicochem. Eng. Asp.* **2013**, *416*, 86–94.

Juggernauth, K. A.; Gros, A. E.; Meznarich, N. A. K.; Love, B. J. In Situ Photogelation Kinetics of Laponite Nanoparticle-Based Photorheological Dispersions. *Soft Matter* **2011**, *7*, 10108–10115.

Jung, J. H.; John, G.; Masuda, M.; Yoshida, K.; Shinkai, S.; Shimizu, T. Self-Assembly of a Sugar-Based Gelator in Water: Its Remarkable Diversity in Gelation Ability and Aggregate Structure. *Langmuir* **2001**, *17*, 7229–7232.

Kanie, K.; Sugimoto, T. Organic−Inorganic Hybrid Liquid Crystals: Hybridization of Calamitic Liquid-Crystalline Amines with Monodispersed Anisotropic TiO2 Nanoparticles. *J. Am. Chem. Soc.* **2003**, *125*, 10518-10519.

Kato, T.; Frechet, J. M. J. A New Approach to Mesophase Stabilization Through Hydrogen Bonding Molecular Interactions in Binary Mixtures. *J. Am. Chem. Soc.***1989**, *111*, 8533-8534.

Kato, T.; Hirai, Y.; Nakaso, S.; Moriyama, M. Liquid-Crystalline Physical Gels. *Chem. Soc. Rev.* **2007**, *36*, 1857–1867.

Kato, T.; Mizoshita, N.; Kishimoto, K. Functional Liquid-Crystalline Assemblies: Self-Organized Soft Materials. *Angew. Chem. Int. Ed. Engl.* **2005**, *45*, 38–68.

Kelly, K. L.; Coronado, E.; Zhao, L. L.; Schatz, G. C. The Optical Properties of Metal Nanoparticles: The Influence of Size, Shape, and Dielectric Environment. *J. Phys. Chem. B* **2003**, *107*, 668-677.

Khalavka, Y.; Becker, J.; Sönnichsen, C. Synthesis of Rod-Shaped Gold Nanorattles with Improved Plasmon Sensitivity and Catalytic Activity. *J.Am.Chem. Soc.***2009**, *131*, 1871-1875.

Khan, F.; Tanaka, M.; Ahmad, S. R. Fabrication of Polymeric Biomaterials: A Strategy for Tissue Engineering and Medical Devices. *J. Mat. Chem. B* 2015, 3, 8224-8249.

Kim, B.; La Flamme, K.; Peppas, N. A. Dynamic Swelling Behaviour of pH-Sensitive Anionic Hydrogels Used for Protein Delivery. *J. Appl. Polym. Sci* **2003**, *89*, 1606-1613.

Kim, S. J.; Kim, H. Il; Park, S. J.; Kim, I. Y.; Lee, S. H.; Lee, T. S.; Kim, S. I. Behaviour in Electric Fields of Smart Hydrogels with Potential Application as Bio-Inspired Actuators. *Smart Mater. Struct.* **2005**, *14*, 511–514.

Klaus, T.; Joerger, R.; Olsson, E.; GranqVisiblet, C.-G. Silver-Based Crystalline Nanoparticles, Microbially Fabricated. *Proc. Natl. Acad. Sci.* **1999**, *96*, 13611–13614.

Kobayashi, S.; Hamasaki, N.; Suzuki, M.; Kimura, M.; Shirai, H.; Hanabusa, K. Preparation of Helical Transition-Metal Oxide Tubes Using Organogelators as Structure-Directing Agents. *J. Am. Chem. Soc.* **2002**, *124*, 6550-6551.

Kundakcı, S.; Üzüm, Ö. B.; Karadağ, E. Behaviour s of Polyelectrolyte AAm/AMPS/bentonite Composite Hydrogels in Uptake of Uranyl Ions from Aqueous Solutions. *Polym. Compos.* **2011**, *32*, 994–1001.

Kuroda, K.; Ishida, T.; Haruta, M. Reduction of 4-nitrophenol to 4-aminophenol Over Au Nanoparticles Deposited on PMMA. *J. Mol. Catal. A: Chem.* **2009**, *298*, 7-11.

Lee, C.-J.; Yang, J. α-Cyclodextrin-Modified Infrared Chemical Sensor for Selective Determination of Tyrosine in Biological Fluids. *Anal. Biochem.* **2006**, *359,* 124-131.

Leeuwenburgh, S. C. G.; Jansen, J. A.; Mikos, A. G. Functionalization of Oligo(poly(ethylene Glycol)fumarate) Hydrogels with Finely Dispersed Calcium Phosphate Nanocrystals for Bone-Substituting Purposes. *J. Biomater. Sci. Polym. Ed.* **2012**, *18*, 1547–1564.

Letellier, S.; Garnier, J. P.; Spy, J.; Bousquet, B. Determination of The L-DOPA/L-Tyrosine Ratio in Human Plasma by High-Performance Liquid Chromatography: Usefulness as a Marker in Metastatic Malignant Melanoma. *J. Chromatogr. B: Biomed. Sci. Appl.* **1997**, *696*, 9-17.

Li, C. Voltammetric Determination of Tyrosine Based on an L-Serine Polymer Film Electrode. *Colloids Surf. B Biointerf.* **2006**, *50*, 147-151.

Li, C.; Mu, C.; Lin, W.; Ngai, T. Gelatin Effects on the Physicochemical and Hemocompatible Properties of Gelatin/PAAm/Laponite Nanocomposite Hydrogels. *ACS Appl. Mater. Interfaces* **2015**, *7*, 18732–18741.

Li, J.; Zhu, J.; Liu, X. Ultrafine Silver Nanoparticles Obtained from Ethylene Glycol at Room Temperature: Catalyzed by Tungstate ions. *Dalton Trans.***2014**, *43*, 132-137.

Li, L.; Shi, J.-l.; Yan, J.-n. A Highly Efficient Heterogeneous Catalytic System for Heck Reactions with A Palladium Colloid Layer Reduced In Situ in the Channel of Mesoporous Silica Materials. *Chem. Comm.* **2004**, 1990-1991.

Li, P.; Siddaramaiah; Kim, N. H.; Heo, S.-B.; Lee, J.-H. Novel PAAM/Laponite Clay Nanocomposite Hydrogels with Improved Cationic Dye Adsorption Behaviour . *Composites Part B* **2008**, *39*, 756-763.

Li, S. j.; Gong, S. A Substrate-Selective Nanoreactor Made of Molecularly Imprinted Polymer Containing Catalytic Silver Nanoparticles. *Adv. Funct. Mater.* **2009**, *19*, 2601-2606.

Li, Y.; Maciel, D.; Tomás, H.; Rodrigues, J.; Ma, H.; Shi, X. pH Sensitive Laponite/alginate Hybrid Hydrogels: Swelling Behaviour and Release Mechanism. *Soft Matter* **2011**, *7*, 6231-6238.

Liang, H.; Li, Z.; Wang, W.; Wu, Y.; Xu, H. Highly Surface-Roughened â€œFlower-Likeâ€• Silver Nanoparticles for Extremely Sensitive Substrates of Surface-Enhanced Raman Scattering. *Adv. Mater.* **2009**, *21*, 4614–4618.

Lin, Y.-J.; Hsu, F.-C.; Chou, C.-W.; Wu, T.-H.; Lin, H.-R. Poly(acrylic Acid)–chitosan–silica Hydrogels Carrying Platelet Gels for Bone Defect Repair. *J. Mater. Chem. B* **2014**, *2*, 8329–8337.

Liu, B.; Deng, Y.; Hu, X.; Gao, Z.; Sun, C. Electrochemical Sensing of Trichloroacetic Acid Based on Silver Nanoparticles Doped Chitosan Hydrogel Film Prepared with Controllable Electrodeposition. *Electrochim. Acta* **2012**, *76*, 410–415.

Liu, P.; Jiang, L.; Zhu, L.; Guo, J.; Wang, A. Synthesis of Covalently Crosslinked Attapulgite/poly(acrylic Acid-Co-Acrylamide) Nanocomposite Hydrogels and Their Evaluation as Adsorbent for Heavy Metal Ions. *J. Ind. Eng. Chem.* **2015**, *23*, 188–193.

Liu, W.; Yang, X.; Xie, L. Size-Controlled Gold Nanocolloids on Polymer Microsphere-Stabilizer via Interaction Between Functional Groups and Gold Nanocolloids. *J. Colloid Interf. Sci.* **2007**, *313*, 494-502.

Liu, X.; Luo, L.; Ding, Y.; Kang, Z.; Ye, D. Simultaneous Determination of L-Cysteine and L-Tyrosine Using Au-Nanoparticles/Poly-Eriochrome Black T Film Modified Glassy Carbon Electrode. *Bioelectrochem.* **2012**, *86*, 38-45.

Liu, X.; Wang, X.; Zha, L.; Lin, D.; Yang, J.; Zhou, J.; Zhang, L. Temperature- and pH-Tunable Plasmonic Properties and SERS Efficiency of the Silver Nanoparticles within the Dual Stimuli-Responsive Microgels. *J. Mater. Chem. C* **2014**, *2*, 7326.

Liu, Y.; Zheng, Y.; Wang, A. Enhanced Adsorption of Methylene Blue from Aqueous Solution by Chitosan-G-Poly (Acrylic Acid)/Vermiculite Hydrogel Composites. *J. Environ. Sci.* **2010**, *22*, 486-493.

Lu, Y.; Mei, Y.; Schrinner, M.; Ballauff, M.; Möller, M. W.; Breu, J. In Situ Formation of Ag Nanoparticles in Spherical Polyacrylic Acid Brushes by UV Irradiation. *J. Phys. Chem. C* **2007**, *111*, 7676-7681.

Lu, Y.; Spyra, P.; Mei, Y.; Ballauff, M.; Pich, A. Composite Hydrogels: Robust Carriers for Catalytic Nanoparticles. *Macromol. Chem. Phys.* **2007**, *208*, 254–261.

Lutkenhaus, J. L.; Olivetti, E. A.; Verploegen, E. A.; Cord, B. M.; Sadoway, D. R.; Hammond, P. T. Anisotropic Structure and Transport in Self-Assembled Layered Polymer−Clay Nanocomposites. *Langmuir* **2007**, *23*, 8515-8521.

Ma, C.; Li, T.; Zhao, Q.; Yang, X.; Wu, J.; Luo, Y.; Xie, T. Supramolecular Lego Assembly towards Three-Dimensional Multi-Responsive Hydrogels. *Adv. Mater.* **2014**, *26*, 5665–5669.

Ma, Y.-Q.; Yi, J.-Z.; Zhang, L.-M. A Facile Approach to Incorporate Silver Nanoparticles into Dextran-Based Hydrogels for Antibacterial and Catalytical Application. *J. Macromol. Sci. Part A* **2009**, *46*, 643–648.

Manuel Stephan, A. Review on gel polymer electrolytes for lithium batteries. *Eur. Polym. J.* **2006**, *42*, 21-42.

Mao, Q.; Shi, S.; Wang, H. Biomimetic Nanowire Structured Hydrogels as Highly Active and Recyclable Catalyst Carriers. *ACS Sustain. Chem. Eng.* **2015**, *3*, 1915–1924.

Maretti, L.; Billone, P. S.; Liu, Y.; Scaiano, J. C. Facile Photochemical Synthesis and Characterization of Highly Fluorescent Silver Nanoparticles. *J. Am. Chem. Soc.* **2009**, *131*, 13972–13980.

Marignier, J. L.; Belloni, J.; Delcourt, M. O.; Chevalier, J. P. Microaggregates of Non-noble Metals and Bimetallic Alloys Prepared by Radiation-Induced Reduction. *Nature* **1985**, *317*, 344-345.

Masarapu, C.; Zeng, H. F.; Hung, K. H.; Wei, B. Effect of Temperature on the Capacitance of Carbon Nanotube Supercapacitors. *ACS Nano* **2009**, *3*, 2199-2206.

Mayol, L.; Serri, C.; Menale, C.; Crispi, S.; Piccolo, M. T.; Mita, L.; Giarra, S.; Forte, M.; Saija, A.; Biondi, M.; *et al.* Curcumin Loaded PLGA-Poloxamer Blend Nanoparticles Induce Cell Cycle Arrest in Mesothelioma Cells. *Eur. J. Pharm. Biopharm. Off. J. Arbeitsgemeinschaft für Pharm. Verfahrenstechnik e.V* **2015**, *93*, 37–45.

Mehl, G. H. Quasi-Periodic Organization in Soft Self-Assembling Matter. *Angew. Chem. Int. Ed. Engl.* **2005**, *44*, 672–673.

Mendizábal, I. K. a. E. Swelling Properties of New Hydrogels Based on the Dimethyl Amino Ethyl Acrylate Methyl Chloride Quaternary Salt with Acrylic Acid and 2-Methylene Butane-1,4-Dioic Acid Monomers in Aqueous Solutions. *Mater. Sci. Appl.* **2010**, *1*, 162-167.

Mie, G. Beiträge Zur Optik Trüber Medien, Speziell Kolloidaler Metallösungen. *Ann. Phys.* **1908**, *330*, 377–445.

Mirzaei, J.; Urbanski, M.; Kitzerow, H.-S.; Hegmann, T. Synthesis of Liquid Crystal Silane-Functionalized Gold Nanoparticles and Their Effects on the Optical and Electro-Optic Properties of a Structurally Related Nematic Liquid Crystal. *Chem. Phys. Chem.* **2014**, *15*, 1381-1394.

Mitra, R. N.; Das, P. K. In situ Preparation of Gold Nanoparticles of Varying Shape in Molecular Hydrogel of Peptide Amphiphiles. *J. Phys. Chem.C* **2008**, *112*, 8159-8166.

Mourchid, A.; Lécolier, E.; Van Damme, H.; Levitz, P. On Viscoelastic, Birefringent, and Swelling Properties of Laponite Clay Suspensions: ReVisibleited Phase Diagram. *Langmuir* **1998**, *14*, 4718-4723.

Mundargi, R. C.; Patil, S. A.; Kulkarni, P. V; Mallikarjuna, N. N.; Aminabhavi, T. M. Sequential Interpenetrating Polymer Network Hydrogel Microspheres of Poly(methacrylic Acid) and Poly(vinyl Alcohol) for Oral Controlled Drug Delivery to Intestine. *J. Microencapsul.* **2008**, *25*, 228–240.

Murali Mohan, Y.; Vimala, K.; Thomas, V.; Varaprasad, K.; Sreedhar, B.; Bajpai, S. K.; Mohana Raju, K. Controlling of Silver Nanoparticles Structure by Hydrogel Networks. *J. Colloid Interface Sci.* **2010**, *342*, 73–82.

Murphy, C.J.; Jana, N. R. Controlling the Aspect Ratio of Inorganic Nanorods and Nanowires. *Adv. Mater.* **2002**, *14*, 80-82.

Murthy, P. S. K.; Murali Mohan, Y.; Varaprasad, K.; Sreedhar, B.; Mohana Raju, K. First Successful Design of Semi-IPN Hydrogel-Silver Nanocomposites: A Facile Approach for Antibacterial Application. *J. Colloid Interface Sci.* **2008**, *318*, 217–224.

Mushran, S. P.; Agrawal, M. C.; Mehrotra, R. M.; Sanehi, R. Kinetics and Mechanism of Reduction of Silver(I) by Ascorbic acid. *J. Chem. Soc., Dalton Trans.* 1974, 1460-1462.

Nagahama, K.; Kawano, D.; Oyama, N.; Takemoto, A.; Kumano, T.; Kawakami, J. Self-Assembling Polymer Micelle/clay Nanodisk/doxorubicin Hybrid Injectable Gels for Safe and Efficient Focal Treatment of Cancer. *Biomacromolecules* **2015**, *16*, 880–889.

Nguyen, C. T.; Kasi, R. M. Nanocomposite Hydrogels Based on Liquid Crystalline Brush-Like Block Copolymer-Au Nanorods and their Application in H_2O_2 Detection. *Chem. Comm.* **2015**, *51*, 12174-12177.

Nguyen, C. T.; Tran, T. H.; Lu, X.; Kasi, R. M. Self-assembled nanoparticles from thiol functionalized liquid crystalline brush block copolymers for dual encapsulation of doxorubicin and gold nanoparticles. *Polym. Chem.* **2014**, *5*, 2774-2783.

Nho, Y.-C.; Park, S.-E.; Kim, H.-I.; Hwang, T.-S. RETRACTED: Oral Delivery of Insulin Using pH-Sensitive Hydrogels Based on Polyvinyl Alcohol Grafted with Acrylic Acid/Methacrylic Acid by Radiation. *Nucl. Instrum. Methods B* **2005**, *236*, 283-288.

Ogoshi, T.; Takashima, Y.; Yamaguchi, H.; Harada, A. Chemically-Responsive Sol-Gel Transition of Supramolecular Single-Walled Carbon Nanotubes (SWNTs) Hydrogel Made by Hybrids of SWNTs and Cyclodextrins. *J. Am. Chem. Soc.* **2007**, *129*, 4878–4879.

Ohde, H.; Hunt, F.; Wai, C. M. Synthesis of Silver and Copper Nanoparticles in a Water-in-Supercritical-Carbon Dioxide Microemulsion. *Chem. Mater.* **2001**, *13*, 4130–4135.

Oliveira, M. M.; Ugarte, D.; Zanchet, D.; Zarbin, A. J. G. Influence of Synthetic Parameters on the Size, Structure, and Stability of Dodecanethiol-Stabilized Silver Nanoparticles. *J. Colloid Interface Sci.* **2005**, *292*, 429–435.

Ong, S.-T.; Keng, P.-S.; Lee, W.-N.; Ha, S.-T.; Hung, Y.-T. Dye Waste Treatment. *Water* **2011**, *3*, 157.

Onogi, S.; Asada, T. Rheology and Rheo-Optics of Polymer Liquid Crystals. In Rheology, Astarita, G.; Marrucci, G.; Nicolais, L., Eds. Springer US: 1980; pp 127-147.

Oral, E.; Peppas, N. A. Responsive and Recognitive Hydrogels Using Star Polymers. *J. Biomed. Mater. Res. A* **2004**, *68*, 439–447.

Otari, S. V; Patil, R. M.; Waghmare, S. R.; Ghosh, S. J.; Pawar, S. H. A Novel Microbial Synthesis of Catalytically Active Ag-Alginate Biohydrogel and Its Antimicrobial Activity. *Dalton Trans.* **2013**, *42*, 9966–9975.

Pal, K.; Banthia, A. K.; Majumdar, D. K. Polymeric Hydrogels: Characterization and Biomedical Applications. *Des. Monomers Polym.* **2009**, *12*, 197–220.

Paleos, C. M.; Tsiourvas, D. Thermotropic Liquid Crystals Formed by Intermolecular Hydrogen Bonding Interactions. *Angew. Chem. Int. Ed. Engl.* **1995**, *34*, 1696-1711.

Panswad, T.; Luangdilok, W. Decolorization of Reactive Dyes with Different Molecular Structures Under Different Environmental Conditions. *Water Res.* **2000**, *34*, 4177-4184.

Park, S. J.; Yoo, K.; Kim, J.-Y.; Kim, J. Y.; Lee, D.-K.; Kim, B.; Kim, H.; Kim, J. H.; Cho, J.; Ko, M. J. Water-Based Thixotropic Polymer Gel Electrolyte for Dye-Sensitized Solar Cells. *ACS Nano* **2013**, *7*, 4050-4056.

Park, T. G. Temperature Modulated Protein Release from pH/temperature-Sensitive Hydrogels. *Biomaterials* **1999**, *20*, 517–521.

Pastoriza-Santos, I.; Liz-Marzán, L. M. Synthesis of Silver Nanoprisms in DMF. *Nano Lett.* **2002**, *2*, 903–905.

Patwadkar, M. V.; Gopinath, C. S.; Badiger, M. V. An Efficient Ag-Nanoparticle Embedded Semi-IPN Hydrogel for Catalytic Applications. *RSC Adv.* **2015**, *5*, 7567–7574.

Paulino, A. T.; Guilherme, M. R.; Reis, A. V.; Campese, G. M.; Muniz, E. C.; Nozaki, J. Removal of Methylene Blue Dye from an Aqueous Media Using Superabsorbent Hydrogel Supported on Modified Polysaccharide. *J. Colloid Interface Sci.* **2006**, *301*, 55-62.

Peppas, N. Hydrogels in Pharmaceutical Formulations. *Eur. J. Pharm. Biopharm.* **2000**, *50*, 27–46.

Perju, M. M.; Dragan, E. S. Removal of Azo Dyes from Aqueous Solutions Using Chitosan Based Composite Hydrogels. *Ion Exch. Lett.* **2010**, *3*, 7-11.

Petelin, M.; Šentjurc, M.; Stolič, Z.; Skalerič, U. EPR Study of Mucoadhesive Ointments for Delivery of Liposomes into the Oral Mucosa. *Int. J. Pharm.* **1998**, *173*, 193–202.

Pozun, Z. D.; Rodenbusch, S. E.; Keller, E.; Tran, K.; Tang, W.; Stevenson, K. J.; Henkelman, G. A Systematic Investigation of p-Nitrophenol Reduction by Bimetallic Dendrimer Encapsulated Nanoparticles. *J. Phys. Chem. C* **2013**, *117*, 7598-7604.

Pradhan, N.; Pal, A.; Pal, T. Silver Nanoparticle Catalyzed Reduction of Aromatic Nitro Compounds. *Colloids Surfaces A* **2002**, *196*, 247-257.

Praefcke, K.; Singer, D.; Kohne, B.; Ebert, M.; Liebmann, A.; Wendorff, J. H. Charge Transfer Induced Nematic Columnar Phase in Low Molecular Weight Disc-Like Systems. *Liq. Cryst.* **1991**, *10*, 147-159.

Pujala, R. K.; Joshi, N.; Bohidar, H. B. Spontaneous Evolution of Self-Assembled Phases from Anisotropic Colloidal Dispersions. *Colloid Polym. Sci.* **2015**, *293*, 2883–2890.

Qasim, M. M.; Khan, A. A.; Kostanyan, A.; Kidambi, P. R.; Cabrero-Vilatela, A.; Braeuninger-Weimer, P.; Gardiner, D. J.; Hofmann, S.; Wilkinson, T. D. Hybrid Graphene Nematic Liquid Crystal Light Scattering Device. *Nanoscale* **2015**, *7*, 14114-14120.

Qu, F.; Zhang, Y.; Rasooly, A.; Yang, M. Electrochemical Biosensing Platform Using Hydrogel Prepared from Ferrocene Modified Amino Acid as Highly Efficient Immobilization Matrix. *Anal. Chem.* **2014**, *86*, 973–976.

Quintana, C.; Suárez, S.; Hernández, L. Nanostructures on Gold Electrodes for the Development of an L-Tyrosine Electrochemical Sensor Based on Host–Guest Supramolecular Interactions. *Sens. Actuators B: Chem.* **2010**, *149*, 129-135.

Raghavan, S. R.; Douglas, J. F. The Conundrum of Gel Formation by Molecular Nanofibers, Wormlike Micelles, and Filamentous Proteins: Gelation Without Cross-Links. *Soft Matter,* **2012**, 8, 8539-8546.

Ramachandran, S.; Tseng, Y.; Yu, Y. B. Repeated Rapid Shear-Responsiveness of Peptide Hydrogels with Tunable Shear Modulus. *Biomacromolecul.* **2005**, *6*, 1316-1321.

Ramanujan, R. V; Lao, L. L. The Mechanical Behaviour of Smart Magnet–hydrogel Composites. *Smart Mater. Struct.* **2006**, *15*, 952–956.

Rao, C. N. R.; Kulkarni, G. U.; Thomas, P. J.; Edwards, P. P. Metal Nanoparticles and Their Assemblies. *Chem. Soc. Rev.* **2000**, *29*, 27–35.

Ravindra, S.; Varaprasad, K.; Rajinikanth, V.; Mulaba-Bafubiandi, A. F.; Venkata Surya Ramam, K. Studies on Curcumin Loaded Poly(N -Isopropylacrylamide) Silver Nanocomposite Hydrogels for Antibacterial and Drug Releasing Applications. *J. Macromol. Sci. Part A* **2013**, *50*, 1230–1240.

Reetz, M. T.; Helbig, W. Size-Selective Synthesis of Nanostructured Transition Metal Clusters. *J. Am. Chem. Soc.* **1994**, *116*, 7401–7402.

Reetz, M. T.; Winter, M.; Breinbauer, R.; Thurn-Albrecht, T.; Vogel, W. Size-Selective Electrochemical Preparation of Surfactant-Stabilized Pd-, Ni- and Pt/Pd Colloids. *Chemistry* **2001**, *7*, 1084–1094.

Ren, N.; Dong, A.-G.; Cai, W.-B.; Zhang, Y.-H.; Yang, W.-L.; Huo, S.-J.; Chen, Y.; Xie, S.-H.; Gao, Z.; Tang, Y. Mesoporous Microcapsules with Noble Metal or Noble Metal Oxide Shells and their Application in Electrocatalysis. *J. Mater. Chem.* **2004**, *14*, 3548-3552.

Riley, M.; Fedkiw, P. S.; Khan , S. A. Transport Properties of Lithium Hectorite-Based Composite Electrolytes. *J. Electrochem. Soc.***2002**, *149*, A667-A674.

Ringsdorf, H.; Wüstefeld, R.; Zerta, E.; Ebert, M.; Wendorff, J. H. Induction of Liquid Crystalline Phases: Formation of Discotic Systems by Doping Amorphous Polymers with Electron Acceptors. *Angew. Chem. Int. Ed. Engl.***1989**, *28*, 914-918.

Roeser, J.; Permentier, H. P.; Bruins, A. P.; Bischoff, R. Electrochemical Oxidation and Cleavage of Tyrosine- and Tryptophan-Containing Tripeptides. *Anal. Chem.* **2010**, *82*, 7556-7565.

Rong, Q.; Han, H.; Feng, F.; Ma, Z. Network Nanostructured Polypyrrole hydrogel/Au Composites as Enhanced Electrochemical Biosensing Platform. *Sci. Rep.* **2015**, *5*, 11440.

Rosa, S.; Laranjeira, M. C. M.; Riela, H. G.; Fávere, V. T. Cross-Linked Quaternary Chitosan as an Adsorbent for the Removal of the Reactive Dye from Aqueous Solutions. *J. Hazard. Mater.* **2008**, *155*, 253-260.

Rudzinski, W. E.; Dave, A. M.; Vaishnav, U. H.; Kumbar, S. G.; Kulkarni, A. R.; Aminabhavi, T. M. Hydrogels as Controlled Release Devices in Agriculture. *Des. Monomers Polym.* **2002**, *5*, 39–65.

Ruel-Gariépy, E.; Leroux, J.-C. In Situ-Forming Hydrogels--Review of Temperature-Sensitive Systems. *Eur. J. Pharm. Biopharm.* **2004**, *58*, 409–426.

Ruzicka, B.; Zaccarelli, E.; Zulian, L.; Angelini, R.; Sztucki, M.; Moussaïd, A.; Narayanan, T.; Sciortino, F. Observation of Empty Liquids and Equilibrium Gels in a Colloidal Clay. *Nat. Mater.* **2011**, *10*, 56-60.

Ruzicka, B.; Zulian, L.; Ruocco, G. Routes to Gelation in a Clay Suspension. *Phys. Rev. Lett.* **2004**, *93*, 258301.

Saez, S.; Fasciani, C.; Stamplecoskie, K. G.; Gagnon, L. B.-P.; Mah, T.-F.; Marin, M. L.; Alarcon, E. I.; Scaiano, J. C. Photochemical Synthesis of Biocompatible and Antibacterial Silver Nanoparticles Embedded within Polyurethane Polymers. *Photochem. Photobiol. Sci.* **2015**, *14*, 661–664.

Saha, S.; Pal, A.; Kundu, S.; Basu, S.; Pal, T. Photochemical Green Synthesis of Calcium-Alginate-Stabilized Ag and Au Nanoparticles and Their Catalytic Application to 4-Nitrophenol Reduction. *Langmuir* **2010**, *26*, 2885-2893.

Sakuda, J.; Hosono, E.; Yoshio, M.; Ichikawa, T.; Matsumoto, T.; Ohno, H.; Zhou, H.; Kato, T. Liquid-Crystalline Electrolytes for Lithium-Ion Batteries: Ordered Assemblies of a Mesogen-Containing Carbonate and a Lithium Salt. *Adv. Funct. Mater.* **2015**, *25*, 1206-1212.

Sangeetha, N. M.; Balasubramanian, R.; Maitra, U.; Ghosh, S.; Raju, A. R. Novel Cationic and Neutral Analogues of Bile Acids: Synthesis and Preliminary Study of Their Aggregation Properties †. *Langmuir* **2002**, *18*, 7154–7157.

Saravanan, P.; Padmanabha Raju, M.; Alam, S. A Study on Synthesis and Properties of Ag Nanoparticles Immobilized Polyacrylamide Hydrogel Composites. *Mater. Chem. Phys.* **2007**, *103*, 278-282.

Saraydin, D.; Karadağ, E.; Güven, O. Acrylamide/Maleic Acid Hydrogels. *Polym. Adv. Technol.* **1995**, *6*, 719-726.

Saraydin, D.; Karadağ, E.; Güven, O. Use of Superswelling Acrylamide/Maleic Acid Hydrogels for Monovalent Cationic Dye Adsorption. *J. Appl. Polym. Sci.* **2001**, *79*, 1809-1815.

Sarkar, S.; Jana, A. D.; Samanta, S. K.; Mostafa, G. Facile Synthesis of Silver Nano Particles with Highly Efficient Anti-Microbial Property. *Polyhedron* **2007**, *26*, 4419–4426.

Schexnailder, P.; Schmidt, G. Nanocomposite Polymer Hydrogels. *Colloid Polym. Sci.* **2008**, *287*, 1–11.

Sengupta, S.; Goswami, A.; Mondal, R. Silver-Promoted Gelation Studies of an Unorthodox Chelating Tripodal Pyridine-Pyrazole-Based Ligand: Templated Growth of Catalytic Silver Nanoparticles, Gas and Dye Adsorption. *New J. Chem.* **2014**, *38*, 2470-2479.

Senyuk, B.; Evans, J. S.; Ackerman, P. J.; Lee, T.; Manna, P.; Vigderman, L.; Zubarev, E. R.; Lagemaat, J. v. d.; Smalyukh, I. I. Shape-Dependent Oriented Trapping and Scaffolding of Plasmonic Nanoparticles by Topological Defects for Self-Assembly of Colloidal Dimers in Liquid Crystals. *Nano Lett.* **2012**, *12*, 955-963.

Sharma, A.; Mori, T.; Lee, H.-C.; Worden, M.; Bidwell, E.; Hegmann, T. Detecting, Visibleualizing, and Measuring Gold Nanoparticle Chirality Using Helical Pitch Measurements in Nematic Liquid Crystal Phases. *ACS Nano* **2014**, *8*, 11966-11976.

Shen, M.; Li, L.; Sun, Y.; Xu, J.; Guo, X.; Prud'homme, R. K. Rheology and Adhesion of Poly(acrylic Acid)/laponite Nanocomposite Hydrogels as Biocompatible Adhesives. *Langmuir* **2014**, *30*, 1636–1642.

Sheng, Q.; Liu, R.; Zhang, S.; Zheng, J. Ultrasensitive Electrochemical Cocaine Biosensor Based on Reversible DNA Nanostructure. *Biosens. Bioelectron.***2014**, 51, 191-194.

Shikinaka, K.; Aizawa, K.; Fujii, N.; Osada, Y.; Tokita, M.; Watanabe, J.; Shigehara, K. Flexible, Transparent Nanocomposite Film with a Large Clay Component and Ordered Structure Obtained by a Simple Solution-Casting Method. *Langmuir* **2010**, *26*, 12493–12495.

Starowicz, M.; Stypuła, B.; Banaś, J. Electrochemical Synthesis of Silver Nanoparticles. *Electrochem. commun.* **2006**, *8*, 227–230.

Stempfle, B.; Große, A.; Ferse, B.; Arndt, K.-F.; Wöll, D. Anomalous Diffusion in Thermoresponsive Polymer-Clay Composite Hydrogels Probed by Wide-Field Fluorescence Microscopy. *Langmuir* **2014**, *30*, 14056–14061.

Strachota, B.; Matějka, L.; Zhigunov, A.; Konefał, R.; Spěváček, J.; Dybal, J.; Puffr, R. Poly(N-Isopropylacrylamide)-Clay Based Hydrogels Controlled by the Initiating Conditions: Evolution of Structure and Gel Formation. *Soft Matter* **2015**, *11*, 9291–9306.

Sudha, J. D. Synthesis and Characterization of Hydrogen-Bonded Thermotropic Liquid Crystalline Aromatic-Aliphatic Poly(Ester–Amide)S from Amido Diol. *J. Polym. Sci. Part A: Polym. Chem.* **2000**, *38*, 2469-2486.

Sudha, J. D.; Pich, A.; Reena, V. L.; Sivakala, S.; Adler, H.-J. P. Water-Dispersible Multifunctional Polyaniline-Laponite-Keggin Iron Nanocomposites through a Template Approach. *J. Mater. Chem.***2011**, *21*, 16642-16650.

Sun, K.; Raghavan, S. R. Thermogelling Aqueous Fluids Containing Low Concentrations of Pluronic F127 and Laponite Nanoparticles. *Langmuir* **2010**, *26*, 8015–8020.

Tan, Z.; Ohara, S.; Naito, M.; Abe, H. Supramolecular Hydrogel of Bile Salts Triggered by Single-Walled Carbon Nanotubes. *Adv. Mater.* **2011**, *23*, 4053–4057.

Tang, X.; Liu, Y.; Hou, H.; You, T. Electrochemical Determination of L-Tryptophan, L-Tyrosine and L-Cysteine Using Electrospun Carbon Nanofibers Modified Electrode. *Talanta* **2010**, *80*, 2182-2186.

Tarascon, J. M.; Armand, M. Issues and Challenges Facing Rechargeable Lithium Batteries. *Nature* **2001**, *414*, 359-367.

Teng, C.; Qiao, J.; Wang, J.; Jiang, L.; Zhu, Y. Hierarchical Layered Heterogeneous Graphene-poly(N-isopropylacrylamide)-clay Hydrogels with Superior Modulus, Strength, and Toughness. *ACS Nano* **2016**, *10*, 413-420.

Thomas, J. R. Preparation and Magnetic Properties of Colloidal Cobalt Particles. *J. Appl. Phys.* **1966**, *37*, 2914-2915.

Thomas, V.; Yallapu, M. M.; Sreedhar, B.; Bajpai, S. K. A Versatile Strategy to Fabricate Hydrogel-Silver Nanocomposites and Investigation of Their Antimicrobial Activity. *J. Colloid Interface Sci.* **2007**, *315*, 389–395.

Thoniyot, P.; Tan, M. J.; Karim, A. A.; Young, D. J.; Loh, X. J. Nanoparticle-Hydrogel Composites: Concept, Design, and Applications of These Promising, Multi-Functional Materials. *Adv. Sci.* **2015**, *2*, n/a – n/a.

Tomatsu, I.; Peng, K.; Kros, A. Photoresponsive Hydrogels for Biomedical Applications. *Adv. Drug Deliv. Rev.* **2011**, *63*, 1257–1266.

Tunkara, E.; Albayrak, C.; Polat, E. O.; Kocabas, C.; Dag, Ö. Highly Proton Conductive Phosphoric Acid–Nonionic Surfactant Lyotropic Liquid Crystalline Mesophases and Application in Graphene Optical Modulators. *ACS Nano* **2014**, *8*, 11007-11012.

Ung, T.; Liz-Marzán, L. M.; Mulvaney, P. Redox Catalysis Using Ag@SiO$_2$ Colloids. *J. Phys. Chem. B* **1999**, *103*, 6770-6773.

Ungar, G.; Tschierske, C.; Abetz, V.; Holyst, R.; Bates, M. A.; Liu, F.; Prehm, M.; Kieffer, R.; Zeng, X.; Walker, M.; *et al.* Self-Assembly at Different Length Scales: Polyphilic Star-Branched Liquid Crystals and Miktoarm Star Copolymers. *Adv. Funct. Mater.* **2011**, *21*, 1296–1323.

Valdés, H.; Godoy, H. P.; Zaror, C. A. Heterogeneous Catalytic Ozonation of Cationic Dyes Using Volcanic Sand. *Water Sci. Technol.* **2010**, *61*, 2973-2978.

van Gorp, J. J.; Vekemans, J. A. J. M.; Meijer, E. W. C3-Symmetrical Supramolecular Architectures: Fibers and Organic Gels from Discotic Trisamides and Trisureas. *J. Am. Chem. Soc.* **2002**, *124*, 14759-14769.

Varaprasad, K.; Mohan, Y. M.; Vimala, K.; Mohana Raju, K. Synthesis and Characterization of Hydrogel-Silver Nanoparticle-Curcumin Composites for Wound Dressing and Antibacterial Application. *J. Appl. Polym. Sci.* **2011**, *121*, 784-796.

Vigneshwaran, N.; Ashtaputre, N. M.; Varadarajan, P. V.; Nachane, R. P.; Paralikar, K. M.; Balasubramanya, R. H. Biological Synthesis of Silver Nanoparticles Using the Fungus Aspergillus Flavus. *Mater. Lett.* **2007**, *61*, 1413–1418.

Vimala, K.; Kanny, K.; Varaprasad, K.; Kumar, N. M.; Reddy, G. S. M. Novel-Porous-Ag0 Nanocomposite Hydrogels via Green Process for Advanced Antibacterial Applications. *J. Biomed. Mater. Res. A* **2014**, *102*, 4616–4624.

Viola, G. G.; Baird, D. G. Studies on the Transient Shear Flow Behaviour of Liquid Crystalline Polymers. *J. Rheol.* **1986**, *30*, 601-628.

Wadkar, M. M.; Chaudhari, V. R.; Haram, S. K. Synthesis and Characterization of Stable Organosols of Silver Nanoparticles by Electrochemical Dissolution of Silver in DMSO. *J. Phys. Chem. B* **2006**, *110*, 20889–20894.

Walcarius, A. Electrochemical Applications of Silica-Based Organic−Inorganic Hybrid Materials. *Chem. Mater.* **2001**, *13*, 3351-3372.

Wang, C.; Flynn, N. T.; Langer, R. Controlled Structure and Properties of Thermoresponsive Nanoparticle–Hydrogel Composites. *Adv. Mater.* **2004**, *16*, 1074–1079.

Wang, Q.; Mynar, J. L.; Yoshida, M.; Lee, E.; Lee, M.; Okuro, K.; Kinbara, K.; Aida, T. High-Water-Content Mouldable Hydrogels by Mixing Clay and a Dendritic Molecular Binder. *Nature* **2010**, *463*, 339–343.

Wang, S.; Ang, H. M.; Tadé, M. O. Novel Applications of Red Mud as Coagulant, Adsorbent and Catalyst for Environmentally Benign Processes. *Chemosphere* **2008**, *72*, 1621-1635.

Wang, Y.; Zhong, W.-H. Development of Electrolytes towards Achieving Safe and High-Performance Energy-Storage Devices: A Review. *ChemElectroChem* **2015**, *2*, 22-36.

Webb, A. R.; Kumar, V. A.; Ameer, G. A. Biodegradable Poly(diol Citrate) Nanocomposite Elastomers for Soft Tissue Engineering. *J. Mater. Chem.* **2007**, *17*, 900–906.

White, R. J.; Luque, R.; Budarin, V. L.; Clark, J. H.; Macquarrie, D. J. Supported Metal Nanoparticles on Porous Materials. Methods and Applications. *Chem. Soc. Rev.* **2009**, *38*, 481-494.

Wichterle, O.; Lim, D. Hydrophilic Gels for Biological Use. *Nature* **1960**, *185*, 117–118.

Wiley, B.; Herricks, T.; Sun, Y.; Xia, Y. Polyol Synthesis of Silver Nanoparticles: Use of Chloride and Oxygen to Promote the Formation of Single-Crystal, Truncated Cubes and

Tetrahedrons. *Nano Lett.* **2004**, *4*, 1733–1739.

Willenbacher, N. Unusual Thixotropic Properties of Aqueous Dispersions of Laponite RD. *J. Colloid Interface Sci.* **1996**, *182*, 501-510.

Wong, Y. C.; Szeto, Y. S.; Cheung, W. H.; McKay, G. Sorption Kinetics for the Removal of Dyes From Effluents onto Chitosan. *J. Appl. Polym. Sci.* **2008**, *109*, 2232-2242.

Wong, Y.; Yu, J. Laccase-Catalyzed Decolorization of Synthetic Dyes. *Water Res.* **1999**, *33*, 3512-3520.

Woo, H.; Lee, K.; Park, S.; Park, K. H. Magnetically Separable and Recyclable Fe3O4-Supported Ag Nanocatalysts for Reduction of Nitro Compounds and Selective Hydration of Nitriles to Amides in Water. *Molecules* **2014**, *19*, 699–712.

Wu, Y.; Xiang, J.; Yang, C.; Lu, W.; Lieber, C. M. Single-Crystal Metallic Nanowires and Metal/Semiconductor Nanowire Heterostructures. *Nature* **2004**, *430*, 61-65.

Wunder, S.; Polzer, F.; Lu, Y.; Mei, Y.; Ballauff, M. Kinetic Analysis of Catalytic Reduction of 4-Nitrophenol by Metallic Nanoparticles Immobilized in Spherical Polyelectrolyte Brushes. *J. Phys. Chem. C* **2010**, *114*, 8814-8820.

Xia, L.-W.; Ju, X.-J.; Liu, J.-J.; Xie, R.; Chu, L.-Y. Responsive Hydrogels with Poly(N-Isopropylacrylamide-co-Acrylic Acid) Colloidal Spheres as Building Blocks. *J. Colloid Interface Sci.* **2010**, *349*, 106-113.

Xing, Y.; Cheng, E.; Yang, Y.; Chen, P.; Zhang, T.; Sun, Y.; Yang, Z.; Liu, D. Self-Assembled DNA Hydrogels with Designable Thermal and Enzymatic Responsiveness. *Adv. Mater.* **2011**, *23*, 1117-1121.

Xu, D.; Bhatnagar, D.; Gersappe, D.; Sokolov, J. C.; Rafailovich, M. H.; Lombardi, J. Rheology of Poly (N-isopropylacrylamide)–Clay Nanocomposite Hydrogels. *Macromol.* **2015**, *48*, 840-846.

Xu, R.; Wang, D.; Zhang, J.; Li, Y. Shape-Dependent Catalytic Activity of Silver Nanoparticles for the Oxidation of Styrene. *Chem. Asian J.* **2006**, *1*, 888–893.

Xu, X.; Yin, Y.; Ge, X.; Wu, H.; Zhang, Z. γ-Radiation Synthesis of Poly(acrylic acid)–Metal Nanocomposites. *Mater. Lett.* **1998**, *37*, 354-358.

Xue, C.; Kung, C.-C.; Gao, M.; Liu, C.-C.; Dai, L.; Urbas, A.; Li, Q. Facile Fabrication of 3D Layer-By-Layer Graphene-Gold Nanorod Hybrid Architecture for Hydrogen Peroxide Based Electrochemical Biosensor. *Sens. Bio-Sens. Res.* **2015**, *3*, 7-11.

Xue, Z.; He, D.; Xie, X. Poly(ethylene oxide)-Based Electrolytes for Lithium-ion Batteries. *J. Mater. Chem.* A **2015**, *3*, 19218-19253.

Yabuuchi, K.; Marfo-Owusu, E.; Kato, T. A New Urea Gelator: Incorporation of Intra- and Intermolecular Hydrogen Bonding for Stable 1D Self-Assembly. *Org. Biomol. Chem.* **2003**, *1*, 3464-3469.

Yamauchi, K.; Takashima, Y.; Hashidzume, A.; Yamaguchi, H.; Harada, A. Switching between Supramolecular Dimer and Nonthreaded Supramolecular Self-Assembly of Stilbene Amide-α-Cyclodextrin by Photoirradiation. *J. Am. Chem. Soc.* **2008**, *130*, 5024-5025.

Yang, Y.; Suzuki, M.; Fukui, H.; Shirai, H.; Hanabusa, K. Preparation of Helical Mesoporous Silica and Hybrid Silica Nanofibers Using Hydrogelator. *Chem. Mater.* **2006**, *18*, 1324-1329.

Yin, B.; Ma, H.; Wang, S.; Chen, S. Electrochemical Synthesis of Silver Nanoparticles under Protection of Poly(N -Vinylpyrrolidone). *J. Phys. Chem. B* **2003**, *107*, 8898–8904.

Yoshida, R.; Ichijo, H.; Hakuta, T.; Yamaguchi, T. Self-Oscillating Swelling and Deswelling of Polymer Gels. *Macromol. Rapid Commun.* **1995**, *16*, 305–310.

Yoshii, T.; Ikeda, M.; Hamachi, I. Two-Photon-Responsive Supramolecular Hydrogel for Controlling Materials Motion in Micrometer Space. *Angew. Chem. Int. Ed. Engl.* **2014**, *53*, 7264–7267.

Yoshio, M.; Mukai, T.; Kanie, K.; Yoshizawa, M.; Ohno, H.; Kato, T. Layered Ionic Liquids: Anisotropic Ion Conduction in New Self-Organized Liquid-Crystalline Materials. *Adv. Mater.* **2002**, *14*, 351-354.

Yoza, K.; Amanokura, N.; Ono, Y.; Akao, T.; Shinmori, H.; Takeuchi, M.; Shinkai, S.; Reinhoudt, D. N. Sugar-Integrated Gelators of Organic Solvents—Their Remarkable Diversity in Gelation Ability and Aggregate Structure. *Chem. - A Eur. J.* **1999**, *5*, 2722–2729.

Yu, S.-H.; Colfen, H. Bio-inspired crystal morphogenesis by hydrophilic polymers. *J. Mater. Chem.* **2004,** *14*, 2124-2147.

Yu, X.; Mai, Z.; Xiao, Y.; Zou, X. Electrochemical Behaviour and Determination of L-Tyrosine at Single-walled Carbon Nanotubes Modified Glassy Carbon Electrode. *Electroanal.* **2008**, *20*, 1246-1251.

Zaarour, M.; El Roz, M.; Dong, B.; Retoux, R.; Aad, R.; Cardin, J.; Dufour, C.; Gourbilleau, F.; Gilson, J.-P.; Mintova, S. Photochemical Preparation of Silver Nanoparticles Supported on Zeolite Crystals. *Langmuir* **2014**, *30*, 6250–6256.

Zendehdel, M. B., M.; Alikhani, H.; Hekmat, A.;. Removal of Methylene Blue Dye from Wastewater by Adsorption onto Semi-Inpenetrating Polymer Network Hydrogels Composed of Acrylamide and Acrylic Acid Copolymer and Polyvinyl Alcohol, *Iran. J. Environ. Health Sci. Eng.* **2010**, *7*, 423-428.

Zendehdel, M.; Zendehnam, A.; Hoseini, F.; Azarkish, M. Investigation of Removal of Chemical Oxygen Demand (COD) Wastewater and Antibacterial Activity of Nanosilver Incorporated in Poly (Acrylamide-Co-Acrylic acid)/NaY Zeolite Nanocomposite. *Polym. Bull.* **2015**, *72*, 1281–1300.

Zhang, E.; Wang, T.; Zhao, L.; Sun, W.; Liu, X.; Tong, Z. Fast Self-Healing of Graphene Oxide-Hectorite Clay-poly(N,N-Dimethylacrylamide) Hybrid Hydrogels Realized by near-Infrared Irradiation. *ACS Appl. Mater. Interfaces* **2014**, *6*, 22855–22861.

Zhang, H.; Li, X.; Chen, G. Ionic Liquid-Facilitated Synthesis and Catalytic Activity of Highly Dispersed Ag Nanoclusters Supported on TiO_2. *J. Mater. Chem.* **2009**, *19*, 8223-8231.

Zhang, J.; Daubert, C.; Foegeding, E. A. Characterization of Polyacrylamide Gels as an Elastic Model for Food Gels. *Rheol. Acta* **2005**, *44*, 622-630.

Zhang, L.; Zheng, S.; Kang, D. E.; Shin, J. Y.; Suh, H.; Kim, I. Synthesis of Multi-Amine Functionalized Hydrogel for Preparation of Noble Metal Nanoparticles: Utilization as Highly Active and Recyclable Catalysts in Reduction of Nitroaromatics. *RSC Adv.* **2013**, *3*, 4692.

Zhang, W. C.; Wu, X. L.; Chen, H. T.; Gao, Y. J.; Zhu, J.; Huang, G. S.; Chu, P. K. Self-organized Formation of Silver Nanowires, Nanocubes and Bipyramids via a Solvothermal Method. *Acta Mater.* 2008, 56, 2508-2513.

Zhang, Z.; Han, M. One-Step Preparation of Size-Selected and Well-Dispersed Silver Nanocrystals in Polyacrylonitrile by Simultaneous Reduction and Polymerization. *J. Mater. Chem.* **2003**, *13*, 641-643.

Zhao, Y.; Su, H.; Fang, L.; Tan, T. Superabsorbent Hydrogels from Poly(aspartic acid) with Salt-, Temperature- and pH-responsiveness Properties. *Polymer* **2005**, *46*, 5368-5376.

Zheng, Y.; Wang, A. Ag Nanoparticle-Entrapped Hydrogel as Promising Material for Catalytic Reduction of Organic Dyes. *J. Mater. Chem.* **2012**, *22*, 16552–16559.

Zhou, C.; Wu, Q.; Yue, Y.; Zhang, Q. Application of Rod-Shaped Cellulose Nanocrystals in Polyacrylamide Hydrogels. *J. Colloid Interface Sci.* **2011**, *353*, 116-123.

Zhou, J.; Du, X.; Gao, Y.; Shi, J.; Xu, B. Aromatic-Aromatic Interactions Enhance Interfiber Contacts for Enzymatic Formation of a Spontaneously Aligned Supramolecular Hydrogel. *J. Am. Chem. Soc.* **2014**, *136*, 2970–2973.

Zhou, Y.; Ahn, S.-k.; Lakhman, R. K.; Gopinadhan, M.; Osuji, C. O.; Kasi, R. M. Tailoring Crystallization Behaviour of PEO-Based Liquid Crystalline Block Copolymers through Variation in Liquid Crystalline Content. *Macromolecules* **2011**, *44*, 3924-3934.

Zhou, Y.; Sharma, N.; Deshmukh, P.; Lakhman, R. K.; Jain, M.; Kasi, R. M. Hierarchically Structured Free-Standing Hydrogels with Liquid Crystalline Domains and Magnetic Nanoparticles as Dual Physical Cross-Linkers. *J. Am. Chem. Soc.* **2012**, *134*, 1630-1641.

Zhu, M.; Wang, C.; Meng, D.; Diao, G. In Situ Synthesis of Silver Nanostructures on Magnetic Fe_3o_4@C Core-Shell Nanocomposites and their Application in Catalytic Reduction Reactions. *J. Mater. Chem. A* **2013**, *1*, 2118-2125.

Zhu, X.; Jiang, X.; Cheng, S.; Wang, K.; Mao, S.; Fan, L.-J. Preparation of High Strength Ultrafine Polyvinyl Chloride Fibrous Membrane and Its Adsorption of Cationic Dye. *J. Polym. Res.* **2009**, *17*, 769-777.

Zidane, F.; Drogui, P.; Lekhlif, B.; Bensaid, J.; Blais, J.-F.; Belcadi, S.; kacemi, K. E. Decolourization of Dye-Containing Effluent Using Mineral Coagulants Produced by Electrocoagulation. *J. Hazard. Mater.* **2008**, *155*, 153-163.

Zou, X.; Zhao, X.; Ye, L. Synthesis of Cationic Chitosan Hydrogel with Long Chain Alkyl and Its Controlled Glucose-Responsive Drug Delivery Behaviour. *RSC Adv.* **2015**, *5*, 96230–96241.

List of Publications

1. Percolated conductive polyaniline-clay nanocomposite in polyvinyl chloride through the combined approach porous template and self-assembly. J. D. Sudha*, S. Sivakala, C. K. Chandrakanth, K. S. Neethu, **K. N. Rohini,** R. Ramakrishnan, *eXPRESS Polym. Lett.* **2014**, *8*, 107–115.

2. Electrically conducting silver nanoparticle-polyacrylic acid hydrogel by in situ reduction and polymerization approach Sudha J. D., **Rohini K. N**., Sivakala S. *Mater. Lett.* **2014**,*116*,135-138.

3. Robust polymeric hydrogel using rod-like amidodiol as crosslinker: studies on adsorption kinetics and mechanism using dyes as adsorbate **Rohini K. N.**, Navya K. N., Sudha J. D., Rao T. P. *J. Appl. Polym. Sci.* **2014**, *131*, 40908.

4. Design of a Nanostructured Electromagnetic Polyaniline–Keggin Iron–Clay Composite Modified Electrochemical Sensor for the Nanomolar Detection of Ascorbic Acid, Reena V. L., Sudha J. D., **Rohini K. N.**, Neethu K. S. *J. Appl. Polym. Sci.* **2014***, 131,* 40936.

5. Robust fibrillar nanocatalysts based on silver nanoparticle-entrapped polymeric hydrogels **Rohini K. N.,** Sudha J. D., Rao T. P. *Appl. Catal. A* **2014**, *483*, 31–40.

6. Brawny silver-hydrogel based nanocatalyst for reduction of nitrophenols: studies on kinetics and mechanism **Rohini K. N.** and Sudha J. D. *Ind. Eng. Chem. Res*. **2015**, *54*, 1197−1203.

7. Electrochemically patterned transducer with anisotropic pedot through liquid crystalline template polymerization Neethu K. S., Sudha J. D., **Rohini K. N.** and Molji C., *ACS Appl. Mater. Interfaces* **2015**, *7*, 18028−18037.

Cover page

1. Cover page accepted for *J. Appl. Polym. Sci.* **2014**, *131*, 40908. Robust polymeric hydrogel using rod-like amidodiol as crosslinker: studies on adsorption kinetics and mechanism using dyes as adsorbate **Rohini K. N.**, Navya K. N., Sudha J. D., Rao T. P.

Conference Proceedings

1. Facile approach for the development of burly starch- silver hydrogel nanocomposites for antimicrobial applications. Reshma L. R., Sudha J. D, **Rohini K. N.** *Mater. Sci. Forum* **2015,** Vols. *830-831*, 616-619.

Papers presented at conferences (Posters/Oral)

1. "Formation of electrically conducting silver nanoparticle poly acrylic acid hydrogel nanocomposite by insitu reduction and polymerization approach" **Rohini. K. N**., Navya K. N., Prasada Rao and Sudha J.D., Poster presented in *Nano India* 2013 held at CSIR-NIIST Thiruvananthapuram on February 19-20, 2013.

2. "Silver nanoparticle entrapped fibrillar hydrogel based robust nanoreactors" **Rohini. K. N**., Navya K. N., Prasada Rao and Sudha J.D., Poster presented in international conference 3rd *FAPS Polymer Congress and MACRO-2013* held at Bangalore on May 15-18, 2013.

3. "Silver nanoparticle entrapped polymeric hydrogel as robust fibrillar nanoreactors" **Rohini. K. N**., J.D. Sudha and Prasada Rao, Poster presented in *International Conference on Nanoscience & Technology* (ICONSAT-2015) held at Institute of Nanoscience and Technology, Mohali, at Punjab University, Chandigarh on March 02 - 05, 2014.

4. "Silver nanoparticle entrapped polymeric hydrogel as robust fibrillar nanoreactors" **Rohini. K. N**., J.D.Sudha and Prasada Rao, Poster presented in *International Conference on Nanoscience & Technology Polymer Conference for Young Researchers* (PCYR 2014), held at CSIR-NIIST on October 18, 2014.

5. "Silver nanoparticle-entrapped polymeric hydrogels as robust fibrillar nanocatalyst for the reduction of nitrophenols" **Rohini. K. N**., Prasada Rao, and J.D. Sudha, Poster presented in *International Conference on Mid CRSI Symposium in Chemistry* held at NIT-T, Trichy on July 23- 25, 2015.

6. "Silver nanoparticle-entrapped polymeric hydrogels as robust fibrillar nanocatalysts for the reduction of nitrophenols" **Rohini. K. N.** and J.D. Sudha oral presentation in *National seminar on polymers and composites* held at Nirmalagiri College, Kannur on September 9-10th, 2015.